ENTATION PAGE

Form Approved
OMB No. 0704-0188

PORT DATE	3. REPORT TYPE AND DATES COVERED
1993	THESIS/DISSERTATION

4. TITLE AND SUBTITLE
Ultrasonic Wave Propagation Model for Nondestructive Evaluation of Solid Rocker Motor Propellant

5. FUNDING NUMBERS

6. AUTHOR(S)
Rosario Nici

7. PERFORMING ORGANIZATION NAME(S) AND ADDRESS(ES)
AFIT Student Attending: Univ of Colorado

8. PERFORMING ORGANIZATION REPORT NUMBER
AFIT/CI/CIA-93-17D

9. SPONSORING/MONITORING AGENCY NAME(S) AND ADDRESS(ES)
DEPARTMENT OF THE AIR FORCE
AFIT/CI
2950 P STREET
WRIGHT-PATTERSON AFB OH 45433-7765

10. SPONSORING/MONITORING AGENCY REPORT NUMBER

11. SUPPLEMENTARY NOTES

12a. DISTRIBUTION/AVAILABILITY STATEMENT
Approved for Public Release IAW 190-1
Distribution Unlimited
MICHAEL M. BRICKER, SMSgt, USAF
Chief Administration

12b. DISTRIBUTION CODE

13. ABSTRACT *(Maximum 200 words)*

14. SUBJECT TERMS

15. NUMBER OF PAGES
252

16. PRICE CODE

17. SECURITY CLASSIFICATION OF REPORT	18. SECURITY CLASSIFICATION OF THIS PAGE	19. SECURITY CLASSIFICATION OF ABSTRACT	20. LIMITATION OF ABSTRACT

DISCLAIMER NOTICE

THIS DOCUMENT IS BEST QUALITY AVAILABLE. THE COPY FURNISHED TO DTIC CONTAINED A SIGNIFICANT NUMBER OF PAGES WHICH DO NOT REPRODUCE LEGIBLY.

ULTRASONIC WAVE PROPAGATION MODEL FOR NONDESTRUCTIVE EVALUATION OF SOLID ROCKET MOTOR PROPELLANT

BY

ROSARIO NICI

B.S., United States Air Force Academy, 1977

M.S.S.M., University of Southern California, 1983

M.S., Air Force Institute of Technology, 1984

M.S., University of Colorado, 1991

A thesis submitted to the

Faculty of the Graduate School of the

University of Colorado in partial fulfillment

of the requirement for the degree of

Doctor of Philosophy

Department of Aerospace Engineering Sciences

1993

This dissertation for the Doctor of Philosophy degree by

Rosario Nici

has been approved for the

Department of

Aerospace Engineering Sciences

by

George W Morgenthaler

George W. Morgenthaler

Leonard J Bond

Leonard J. Bond

Date 7-14-93

Nici, Rosario (Ph. D., Aerospace Engineering Sciences)

Ultrasonic Wave Propagation Model For Nondestructive Evaluation Of Solid Rocket Motor Propellant

Thesis directed by Proffessor George W. Morgenthaler

The detection of voids in SRM propellant is critical to the safety of Launch Vehicles. Currently this is done with the use of x-rays as an NDE technique. It is hoped to supplant this technique with the use of ultrasonic NDE methods for reasons of reduced cost, increased mobility of the NDE set-up, automated accept/reject criteria, to name a few. To be feasible the ultrasonic NDE methods must be able to differentiate between a through-transmission signal from an SRM propellant segment with a void, and a signal from a segment without a void. The ability of ultrasonic NDE to penetrate one meter of propellant has already been demonstrated with sufficient signal-to-noise ratio. The crux of the ultrasonic NDE method will be in using the information present in the received signal to detect, locate, and size voids. This research embarks in this direction by showing the ultrasonic NDE technique received signal indicates a viscoelasticity of the SRM propellant, and therefore viscoelasticity must be included in any wave propagation model of the SRM propellant.

Ultrasonic NDE was used on a sample of inert propellant at the fifth and eleventh month after casting. A matched pair of 50 kHz transducers, wavelength in the material of 3.2 cm, were used in over 100 tests. Attenuation and velocity versus frequency profiles were obtained. A

simple numerical simulation, based on the Kelvin-Voigt mechanical approximation of the stress-strain relationship, guided by a scalar expression, determined a viscoelastic damping coefficient, which is a measure of viscosity. This characterized the propellant sample for bulk viscoelastic material properties, and matched the experimental attenuation over the limited frequency band of the transducer.

Ultrasonic NDE on specimen with inclusions showed excess attenuation over what one would expect without inclusions. Numerical simulations showed like excess attenuation.

Ultrasonic NDE on SRM propellant segments shows promise as a technique for future use to detect, locate, and size voids. Further, as an ancillary benefit, the characterization of propellant sample for bulk viscoelastic material properties also allows the periodic tracking of attenuation, velocity and VDC to determine the changes over time. This should provide a quantitative means of determining service life in SRM propellant and possibly in other viscoelastic material.

ACKNOWLEDGMENTS

And though I have the gift of prophecy, and understand all mysteries, and all knowledge; and though I have all faith, so that I could remove mountains, and have not love, I am nothing. -- 1 Corinthians 13:2

I wish to thank my loving wife Jane, daughter Lindsay, and son Michael, for the support they gave to me during trying times.

Dr. George W. Morgenthaler is an honorable and just man, whose help and support ensured the completion of this work. For this and his friendship, I will always be thankful.

The guidance I received from Dr. Leonard Bond was invaluable. I commend him for his knowledge and patience. To the rest of my committee: Dr. B. Boro Djordjevic, Dr. Allan Mord, Dr. Wayne Rogers, and Dr. Howard Snyder, I wish to thank each individual for their insight and contribution.

I would like to thank Dr. B. Boro Djordjevic, Mr. Michael Rooney, and Mr. William Ferrell for their assistance, guidance, and help during and after the conducting of experiments. Finally, I would like to thank the Martin Marietta Corporation for allowing me such a generous use of their manpower and equipment, NASA Marshall Space Flight Center and the Atlantic Research Corporation for the use of the inert samples.

CONTENTS

CONTENTS (continued)

TABLES

TABLES (continued)

Table

FIGURES

Figure

FIGURES (continued)

Figure

FIGURES (continued)

Figure

FIGURES (continued)

Figure

FIGURES (continued)

Figure

FIGURES (continued)

Figure

FIGURES (continued)

Figure

FIGURES (continued)

Figure

FIGURES (continued)

Figure

CHAPTER I

INTRODUCTION

1.1 The Importance of Testing in the Space Exploration Initiative Area

In 1985, the Space Exploration Initiative (SEI) program was created to further US efforts in space. The goals outlined in this program include Moon missions, Mars exploration by humans, and eventually space colonies. But before any of these endeavors can be undertaken, several key technological areas need to be furthered. Morgenthaler and Nici (1991) pointed out the need for in-space testing and development of a Testing and Evaluation philosophy for SEI. In addition, there will also be a need for increased testing of the Launch Vehicles that will lift these missions and carry the payloads into orbit. Space logistics support requires a Heavy Lift Launch Vehicle (HLLV) for the SEI missions to succeed. There will also be an increased requirement for large Solid Rocket Motors (SRMs) to supplement the large liquid rocket launch vehicles that will comprise the HLLV fleet.

1.2 The Requirement for High Multiple Solid Rocket Motor Utilization.

With an increased rate of SRM utilization, there will obviously be an increased production requirement. In general, there is a limit on the current production rate which cannot be exceeded without further facility

construction. The current maximum production limit for the Titan IV SRM segments is 72 per year (Hercules Aerospace Corporation, 1993). Once this is reached, production of SRM segments will be on the critical path in the flow of SEI missions sequencing. Several economic factors influence the decision as to how much production capability is necessary. Industry will naturally be reluctant to build excess production capacity. According to the industry, there is a limit to the ability to stock-pile SRMs because the shelf-life of an SRM segment is five years (Martin Marietta, 1992a). This last statement implies dependence of a SEI mission launch rate on the SRM, among other things, and the dependence of timely SEI programs on the success of the SRMs. This success is directly related to the SRM reliability and safety, both of which rely on establishing a high quality, efficient SRM production process.

1.3 Reliability and Safety Depend on a Quality Production Process

A controlled quality production process is necessary to produce a product that can meet or exceed requirements. As a part of such a production process the SRM segment must be inspected. If a critical flaw is not detected, a launch failure is likely to occur.

1.4 NDE can be Used to Ensure that Defect Limits are not Breached

Non-Destructive Evaluation (NDE) techniques can be used to find SRM critical defects. First, the proper inspection methods and tools must

be used to detect, locate and evaluate flaws. Then defects must be characterized. The size of the critical flaw must also be determined. Again, previous workmanship in production, as far as quality is concerned, can be used as an indicator of defect size. Procedures can give indications as to the location of probable faults. The different companies that produce SRMs utilize several methods in the inspection of SRM segments.

1.5 Flaws in SRM propellant segments

There are several types of flaws in SRM propellant segments. This research effort characterizes the flaws based on the time of occurrence. Specifically manufacturing flaws, those occurring when the segment was cast, and service-history flaws, those occurring subsequent to casting.

Manufacturing flaws consist of voids, inclusions, cracks, unbonds, kissing bonds, delaminations, porosity, as well as variances in density, uneven distribution of fuel (settling), binder rich areas and so on. Since the SRM segment is cast in a vacuum, until the last portion is trowelled in, most voids are created when the propellant folds on itself or folds against a section of liner. The internal voids are usually spherical or spheroidal due to the surface tension of the propellant. The inclusions could be any deposit that entered during the steps in the production process. The other defects are self-explanatory.

Service-history flaws are caused by temperature cycles, shock, vibration, propellant sagging under its own weight, and the exposure to the environment over time (Sutton, 1986). Dewetting, crazing,

microvoids, chain slippage, cracks -- surface and radial, shrinkage, and fluid migration are defects occurring during the service-history of SRM segments (Nielsen, 1974). Moisture, dust, and oxygen from the atmosphere contribute to the breakdown of SRM propellants (Daniels, 1989). Eventually the SRM propellant segment reaches its service-life.

The volumetric flaws, remote from the boundaries, are the critical flaws this research is focusing on. The possibility of a burn through failure created by an early arrival of the flame front at the steel case, under combustion pressure, increases with the size, number, and location of voids in SRM propellant. The catastrophic failure of a launch vehicle with such an event places a high priority on the detection, location, and sizing of voids in SRM propellant.

1.6 Current Inspection Methods of SRMs

The Shuttle SRM segment is four meters in diameter with a propellant annulus one meter thick and 9 meters long (Johnston, 1987). The steel case, primer, adhesive, and insulation are only 1-2 cm thick, in total. The typical SRM segment is approximately three meters long with advanced versions projected to be ten meters long (Martin Marietta, 1992a).

Rooney (1990) provided an overview of SRM NDE in his masters thesis which considered the NDE of SRM structural bonds. Inspections considered include both in-process NDE and final product/pre-flight verification. The in-process NDE includes techniques used to determine surface contamination, cure monitoring, thickness and coverage, as well

as moisture content. The final product NDE includes ultrasonic pulse echo testing, radiographic imaging, visual inspections, and thermographic methods. Both through-body and tangential inspections are performed with x-rays. The current NDE programs for SRM inspection can be summarized in Table 1.1 and Figure 1.1 which are data taken from Rooney (1990).

Table 1.1. Current NDE Programs for Titan 34D and Space Shuttle, (Rooney, 1990, p36)

		TITAN 34D			SHUTTLE		
Case-to-Insulation Bond		**IO Plant**	**FL Plant**	**FL Launch**	**IO Plant**	**FL Plant**	**FL Launch**
JOINT:	Compression face test	x		x	x	x	x
	Video-visual	x,FG		x,FG	x,FG	x,FG	x,FG
	Ultrasonic	PE-s		PE-s	PE-s	PE-s	
MEMBRANE:	Ultrasonic	PE-s		PE-s	PE-r	PE-s	PE-s
	Thermography			x			
Insulation-to-Propellant Bond			**FL Plant**	**FL Launch**		**FL Plant**	**FL Launch**
INHIBITOR:	Video-visual			x		x	x
	Ultrasonic			CW		PE	
	Radial X-ray			15°			
	Tangential X-ray			15°		3°	
BOOT/FLAP:	Video-visual		x	x		NA	NA
	Radial X-ray			15°		120°	
	Tangential X-ray			15°		3°	
MEMBRANE:	Ultrasonic					PE-s	
	Thermography			x			
Other Regions			**FL Plant**	**FL Launch**		**FL Plant**	**FL Launch**
PROPELLANT:	Bore visual		x	x		x	x
	Radial X-ray			15°		120°	
	Tangential X-ray			15°		3°	
POTTING:	Radial X-ray			15°		NA	NA
	Tangential X-ray			15°		NA	NA

Legend:
- IO Plant - Inspections at the plant of insulated-only segments
- FL Plant/Launch - Inspections at either the plant or launch site of fully-loaded segments
- x - inspection performed
- (blank) - no inspection of this type performed
- FG - Feeler gage inspection
- PE-x - 2.25 MHz pulse-echo UT from either rubber side (-r) or steel side (-s)
- CW - Low-frequency continuous wave UT

a) Tang

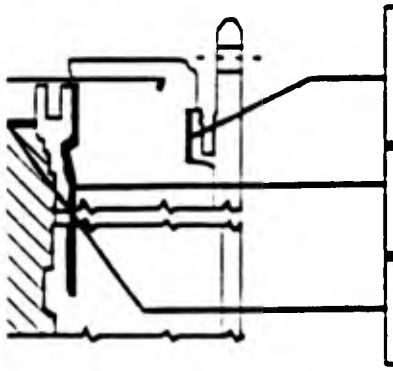

Titan 34D Program	Shuttle NDE Program
Compression face test Video-visual- feeler gauge 2.25 MHz PE UT	Compression face test Video-visual-feeler gauge 2.25 MHz PE UT
15 MeV Tangential X-ray 15 MeV Radial X-ray	15 MeV Tangential X-ray
-NA-	Pulse-echo UT Video-visual

b) Body

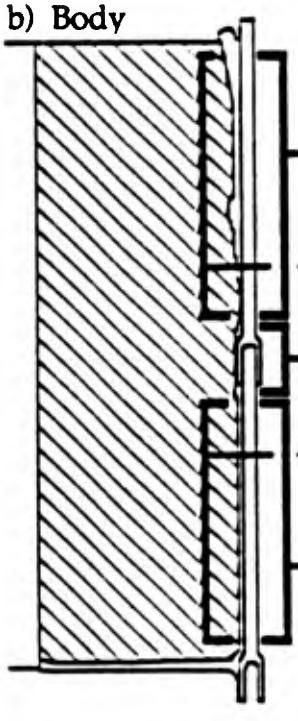

2.25 MHz PE UT Thermography	2.25 MHz PE UT (rubber) 2.25 MHz PE UT (steel)
Thermography	2.25 MHz PE UT (steel) 15 MeV Tangential X-ray
2.25 MHz PE UT (rubber)	2.25 MHz PE UT (rubber)
Thermography	2.25 MHz PE UT (steel) 15 MeV Tangential X-ray
2.25 MHz PE UT Thermography	2.25 MHz PE UT (rubber) 2.25 MHz PE UT (steel)

c) Clevis

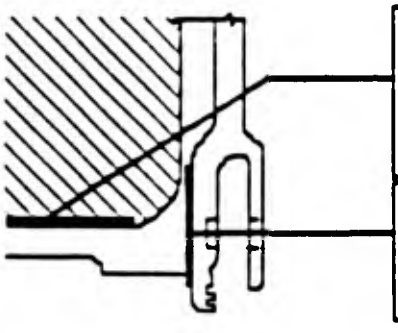

CW P/C UT Video-visual 15 MeV Tangential X-ray 15 MeV Radial X-ray	2.25 MHz PE UT Video-visual
Compression face test Video-visual-feeler gauge 2.25 MHz PE UT	Compression face test Video-visual-feeler gauge 2.25 MHz PE UT

Figure 1.1. Current NDE Programs for the Titan 34D and Space Shuttle Solid Rocket Motors: a) Tang, b) Body, c) Clevis.
(Rooney, 1990, p37, PE- pulse echo, UT- ultrasonic transducer, CW P/C- continuous wave pitch catch)

The NDE which is summarized in Table 1.1 and Figure 1.1 focus on the bonds between propellant-liner and liner-case. However, the primary interest in the work related to this thesis is in NDE of the propellant. In the Propellant section of Table 1.1, the purpose of using radial radiography is not for bondline inspection, but it is used to look for cracks and voids. Rooney further points out that a void of approximately 1.5 cm diameter can be detected through two meters of propellant at current sensitivity levels using radial x-rays.

The bond between the steel case and the rubber insulation was the primary focus of Johnston (1987), especially on the NDE of the Shuttle SRM tang and clevis joints. The Clevis is shown in the top part of Figure 1.1c. In this case a 500 kHz surface wave transmitter was used to produce a Rayleigh wave on the surface of the Clevis to detect debonds between steel-insulation interface based on the amount of energy transmitted into the propellant. The more energy transmitted the better the bond.

Dean and Young (1974) provide examples of rocket motor inspection systems in the UK utilizing ultrasonic transmission for debonds and propellant defect detection. The motors were up to 1.1 meters in diameter and up to seven meters long. They noted that the relatively coarse granular structure of the propellant resulted in an attenuation of about 5 db/cm at 500 kHz, which leads to the requirement of a lower frequency ultrasonic transmission technique. This last item is an important fact.

Shimizu, et al (1989) discuss a swept frequency ultrasonic inspection method and its application to the Japanese H-II SRMs for debond detection.

Gammell (1990) investigates the use of air-coupled transducers for ultrasonic transmission inspections of SRM segments as an alternative to

contact transducers. The frequencies used are in the range of 35-50 kHz.

Djordjevic (1987) reported on tests of actual Titan SRM segments at frequencies between 30-100 kHz using the through-transmission method, and had no trouble differentiating the ultrasonic gated signal transmitted through 1 m of propellant. Djordjevic (1990) reports on the current use of dry-coupled surface mounted transducers in the 20-60 kHz range which provide a signal-to-noise fidelity of better than 60 db in the through-transmission mode. Djordjevic also extolled the use of an optical interferometer that could extend the fidelity of ultrasonic NDE. He reported that the amplitude sensitivity was three angstroms peak-to-peak thereby allowing the detection of very weak signals. A similar probe was reported by Kroll and Djordjevic (1982). Figures 1.2 and 1.3, show the ultrasonic through-transmission technique utilized by Djordjevic.

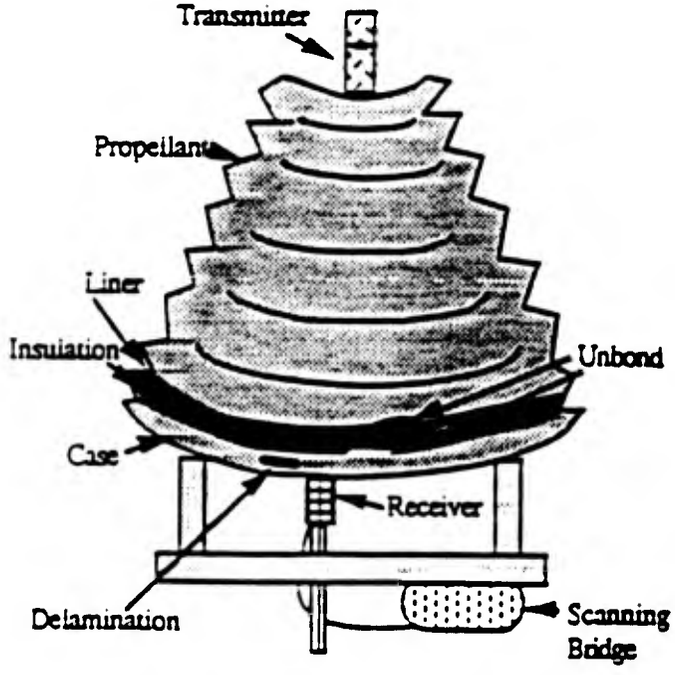

Figure 1.2. Detection of Bondline and Bulk Defects in SRM Segments Using Ultrasonic Testing. (Djordjevic, 1990, p 998)

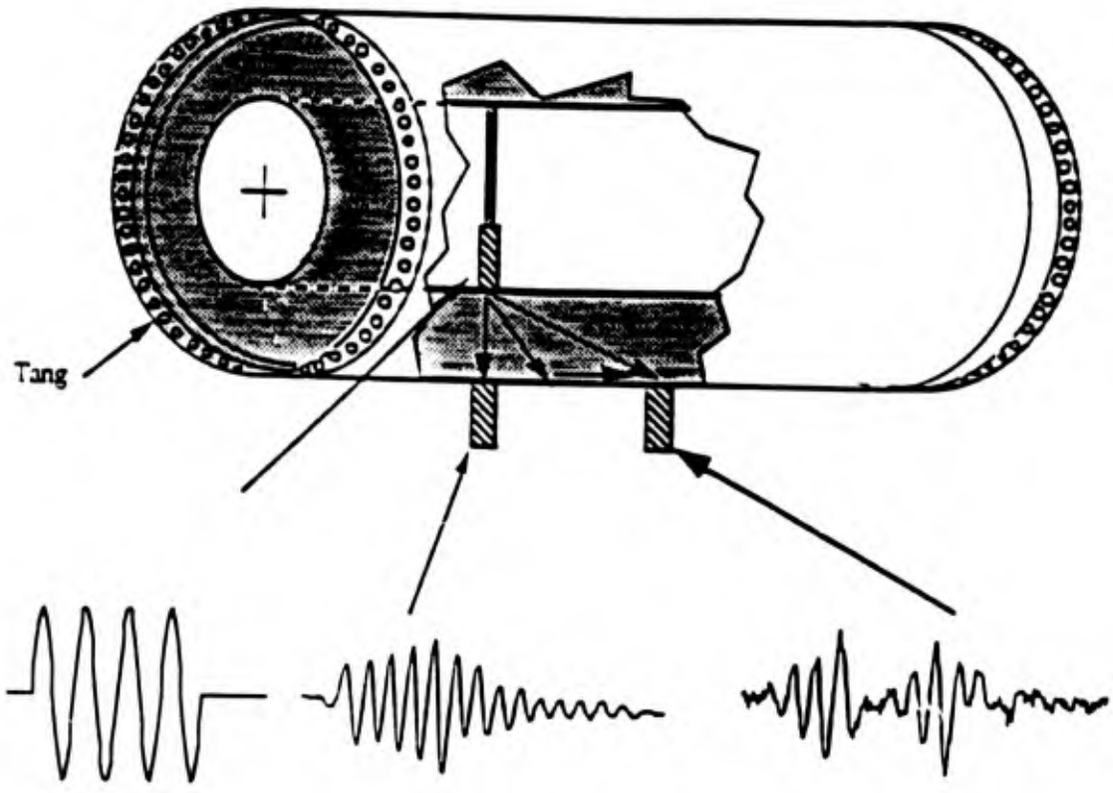

Figure 1.3. Ultrasonic Survey of Large SRM Including Plate Wave Mode Generation. (Djordjevic, 1990, p 999)

If the weak received signals are to be detected then a high intensity source is required. Martin Marietta Internal Research and Development report R-619R describes a gated drive signal of high power that can give a 90 db gain over a spike pulse source. This 90 db gain is important in multilayered structures, such as SRMs, because of the high attenuation of signals traversing these structures. Another example of the through-transmission technique is shown in Figures 1.4 from Djordjevic (1991). However in this Figure, the attenuation of signal intensity is also depicted as the ultrasonic wave propagates from the transmitter, through the

graphite/epoxy (Gr/E) , foam, Kevlar/epoxy (K/E) and finally to the receiver. The important observations from this Figure are:

- The stronger the source intensity, the higher the received signal intensity.

- The attenuation is frequency dependent.

- Conventional Pulsar Drive signals are attenuated below conventional detection limits.

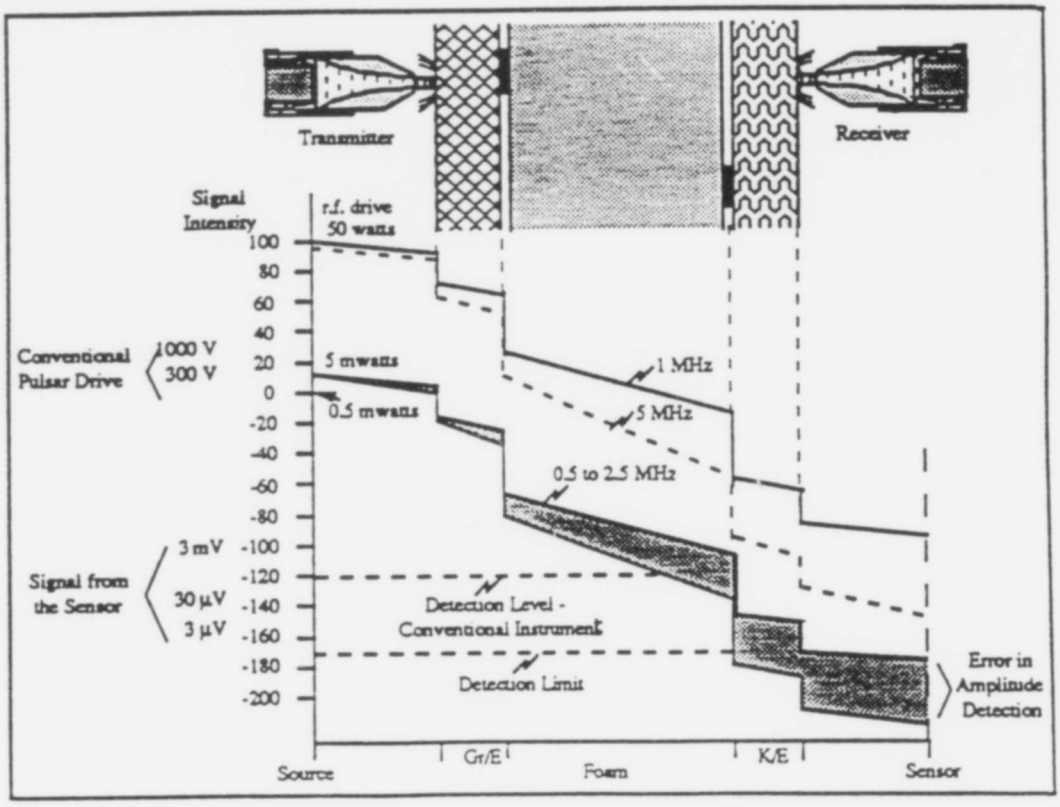

Figure 1.4. Ultrasonic Through-Transmission Signal Intensity Loss in a Multilayer Structure for Conventional and High-Intensity Ultrasonic Signals. (Djordjevic, 1991, p96)

In discussions with Mr. Ward Rummel, at Martin Marietta Astronautics Group in Denver, (Martin Marietta, 1992a), concerning current inspection methods, the author learned about the use of radial x-rays to detect voids in the bottom third of a SRM four meter segment. These voids are similar to the ones referenced by Rooney (1990), and they would be imaged as various standing wave intensity levels on a surface, i.e. a 2-D representation. Defect characterization, such as size, location, and nearest neighbor displays would be lacking because the x-rays only have 2-D information available. This is evident in the NDE method outlined below.

Morton Thiokol's guide STW7-3179A, "Radiographic Inspection Of Space Shuttle SRM Segments, Requirements for," is a standard which applies to all flight production Space Shuttle SRM segments. Section 4.4.1.2.1, entitled "Acceptable voids and regions of porosity in center and aft segments," sets out three criteria:

- All singular voids must be < 2.5 cm in the longitudinal or circumferential direction;

- A maximum of 20 singular voids can exist, with a reduction of propellant between 2.5 and 10 cm, in the longitudinal or circumferential direction in the entire segment;

- No more than one 3.75 cm reduction can exist in the thickness of the propellant in the radial direction due to a single void, cumulative voids, or regions of porosity.

These criteria are used to determine the critical flaws which determine the acceptance or rejection of a SRM propellant segment. The Titan SRM segments have similar criteria, rejecting voids of roughly 6 cm diameter limits, (Hercules Aerospace Corporation, 1991). The definitions

and limitations of a void and region of porosity and their depiction on the radiograph according to STW7-3179A are important parts of this NDE method. The void "is an absence of propellant in a localized region of propellant grain. It has a shape characteristic of an air bubble and appears on a radiograph as a rather poorly defined region of wispy shading of increased film density." The region of porosity is "an anomaly within the propellant grain consisting of a honeycomb-like structure of many small voids close together. Porosity appears on a radiograph as a poorly defined region of wispy shading of increased film density." The author can understand how the reading of the radiograph can be considered an art as much as a science. The problem of determining the dimensions of a "poorly defined region of wispy shading of increased film density," is critical in determining the safety of each SRM segment.

Since the location or alignment of the said voids can be a critical factor in the safe and successful operation of the SRM, another NDE technique is required for complete detection, characterization and evaluation of voids between 2.5 and 10 cm. The choice of using ultrasonic through-transmission techniques to replace x-ray techniques for NDE of SRM propellant would seem appropriate. The ultrasonic signal can be detected after the transmission through almost 1 m of propellant. The difficulty would involve the interpretation of the received signals or the differentiating between a signal with and without a void, which has not been addressed concerning Ultrasonic through-transmission NDE of SRM propellant.

Before continuing the above discussion, answering the question "What is propellant?", can provide an explanation justifying the direction of this research effort, allowing the limitation of the scope of research, and

clearly outlining this contribution toward the replacement of x-ray techniques with Ultrasonic through-transmission NDE of SRM propellant.

1.7 SRM propellant

Propellant is comprised of about 10% binder (polymer), that has 30% fuel (aluminum), 50% oxidizer (ammonium perchlorate) and 10% plasticizer by weight. By volume these percentages are 20, 25, 40, 15 % with additives, such as curing agents, also included. Table 1.2 presents the representative propellant ingredients and their functions.

Table 1.2. Representative Propellant Ingredients and Their Function. (Sutton, 1986, Table 11-2, p294)

Fuels
Aluminum powder (Al)
Beryllium powder (Be)
Oxidizers
Ammonium perchlorate (AP)
Cyclotetramethylene tetranitramine (HMX)
Cyclotrimethylene trinitramine (RDX)
Ammonium nitrate (AN)
Binders (polymers)
Polybutadiene-acrylonitrile-acrylic acid (PBAN)
Polybutadiene-acrylic acid (PBAA)
Carboxy-terminated polybutadiene (CTPB)
Hydroxy-terminated polybutadiene (HTPB)
Polysulfide (PS)
Polypropylene glycol (PPG)
Polyurethane polyether (PU)
Nitrocellulose (plastisol grade) (PNC)
Plasticizers (solvents)
Nitroglycerin (NG)
Triethyleneglycol dinitrate (TEGDN)
Trimethylolethane trinitrate (TMETN)
Curing agents
Tolylene diisocyanate (TDI)
Hexamethylene diisocyanate (HMDI)
Aziridines
Epoxide resins

The SRM propellant may or may not be completely homogeneous. In fact some propellants are a heterogeneous mixture (Sutton, 1986). The migration of fluid substances are common in some formulations. There may be sections that are fuel rich or fuel poor. The processing method can be either extruded, solvent cast, or cast to make the SRM segment. Sutton (1986) stresses "an important objective in the processing is to produce a propellant grain free of cracks, low-density areas, voids, or other flaws." This may seem obvious, however, experience says the flaws were a problem in the past. The author learned from the Senior Staff Engineer of Propulsion Systems, that the first few castings of the SRMU, which were rejected on other grounds, contained numerous voids that were determined to be caused by the casting techniques and contributed to the revision of those same techniques (Martin Marietta, 1993). In a previous interview, (Martin Marietta, 1992a), the propellant was described as tacky and thicker than cake batter when cast. It is a mixture that requires an elevated temperature and controlled conditions to cast. One can understand the need for NDE methods to detect the inevitable flaws. Further, the types and formulations of solid propellant are diverse, see Table 1.3. The polymer, which is used as a binder, is characterized as being in either a glassy or rubber state based on the temperature, (Daniels, 1989). The glass transition temperature is affected by any factor which influences the free volume of the polymer. The ingredients of the propellant penetrate the polymer as opposed to diffusing through it. Therefore the material properties of the SRM propellant depend on the mix, as well as, the time since casting.

Table 1.3 Selected Characteristics of Some Operational Propellants, (Derived from Sutton, 1986, Table 11-1, p 293).

Propellant Type	I_s Range (sec)	Flame Temperature (°F)	Density (lb/in.^{3})	Metal Content (wt %)	Stress/Strain (psi) (%) − 60°F	Stress/Strain (psi) (%) +150°F	Processing Method
DB	220–230	4100	0.058	0	4600/2	490/60	Extruded
DB/AP/Al	260–265	6500	0.065	20–21	2750/5	120/50	Extruded
DB/AP-HMX/Al	265–270	6700	0.065	20	2375/3	50/33	Solvent cast
PVC/AP	230–240	4600	0.061	0	369/150	38/220	Solvent cast
PVC/AP/Al	260–265	5600	0.064	21	369/150	38/220	Cast or extruded
PS/AP	230–240	4700	0.062	0	620/35	120/70	Cast or extruded
PS/AP/Al	240–250	5000	0.062	3	320/11	99/42	Cast
PU/AP/Al	260–265	5400–6000	0.064	16–20	1170/6	75/33	Cast
PBAN/AP/Al	260–263	5800	0.064	16	520/16 (at −10°F)	71/28	Cast
CTPB/AP/Al	260–265	5600–5800	0.064	15–17	325/26	88/75	Cast
HTPB/AP/Al	260–265	5600–5800	0.067	4–17	910/50	90/33	Cast
PBAA/AP/Al	260–265	5400–6000	0.064	14	500/13	41/31	Cast

Acronyms and symbols:
Al, aluminum
AP, ammonium perchlorate
CTPB, carboxy-terminated polybutadiene
DB, double base
HMX, cyclotetramethylene tetranitramine
HTPB, hydroxy-terminated polybutadiene
PBAA, polybutadiene–acrylic acid polymer
PBAN, polybutadiene–acrylic acid–acrylonitrile terpolymer
PS, polysulfide
PU, polyurethane
PVC, polyvinyl chloride
* See Section 3

The generic SRM propellant is basically a rubbery substance with fine, medium and course particles mixed together that requires careful handling. The material properties depend on the composition and age of the mixture.

1.8 The reason for Ultrasonic NDE

Figure 1.3 depicts the ultrasonic NDE on a SRM propellant segment. This was done and it resulted in a received signal with a 60 db signal-to-noise ratio (Djordjevic, 1990). The signal-to-noise ratio was achieved, as shown in Figure 1.4, because there exists components that can withstand

the high signal intensity, roughly 50 watts, and other new detection components that have an increased sensitivity and lower detection limit (Djordjevic, 1991). These two capabilities make using ultrasonic NDE on SRM propellant possible. But these, in themselves, do not demand the transition away from x-ray inspection techniques. There are various technical and non-technical reasons for switching, but using both methods may also be an option.

The preliminary capabilities of an ultrasonic NDE method are investigated in this research, with the potential for great benefits in the future being evident. One important aspect of ultrasonic NDE, is its ability to characterize the SRM propellant's bulk material properties. This enables one to investigate the aging of SRM propellant. Determining the service-life based on a quantitative basis rather than a time basis diminishes the need to track service history, i.e. temperature cycles, shock, humidity, and vibration. Parameters can be established which relate directly to the bulk material properties of the propellant, and the measurement of which are flexible enough to accommodate each batch of propellant which may have slight variations in composition. During this research, progress was made in this area.

The non-technical reasons to be debated are issues such as cost, reliability, automation, safety, environmental impacts, mobility. These are not addressed here, and most likely will have to be evaluated after an ultrasonic NDE system is fully functional. Another important aspect which must be considered is the degree of judgment required of the operators of the inspection methods. One must answer the questions: Which method requires more human judgment?, Does this judgment affect reliability?, Can any parts of the inspection method be automated?

Clearly the decision to use x-ray instead of ultrasonic NDE, vice versa, or both, must be made in context of the entire launch vehicle system perspective. However, one can not choose to use ultrasonic NDE if the same is not investigated and developed. It is in this spirit that this research effort was begun.

1.9 Contribution of this Work to SRM Inspection

Presently 2.5 to 10 cm voids in SRM propellant are detected by means of x-ray techniques. This establishes the critical flaw size that an ultrasonic NDE technique must detect, locate, and size.

In order to reach the goal of establishing a new reliable ultrasonic NDE technique several sub-tasks must be accomplished. This work limited the scope of the research to the beginning parts of the many varied sub-tasks, focusing on certain assumptions critical to those sub-tasks. Any experimental ultrasonic NDE tests on flight hardware or live propellant would be impossible because of cost and safety considerations. This research effort uses samples cast of inert propellant for safety considerations. The oxidizer in the live propellant was replaced with an inert compound in the inert propellant. A numerical model would have to be developed and it would have to be based on propellant experimental tests. This would allow voids at various locations, combinations, of different sizes, to be investigated for a model based inversion system that would be used on the live propellant.

Therefore, the contributions of this research effort are:

A. Developing an acoustical wave propagation model in propellant type material by utilizing viscoelastic effects for the quantitative analysis of ultrasonic Nondestructive Evaluation (NDE) measurements in Solid Rocket Motor (SRM) propellants;

B. Utilizing high intensity equipment at 50 kHz, to determine if the viscoelastic effect is significant in ultrasonic measurements of propellant type material;

C. Determining if a signature of a defect (2.5 cm inclusion) can be detected in the ultrasonic NDE measurements;

D. Presenting a methodology to characterize bulk material properties of an SRM propellant segment, which found the Kelvin-Voigt model an accurate representation of viscoelastic behavior;

E. Realizing that the methodology which incorporated the acoustical wave propagation model could also track the change in bulk viscoelastic properties of SRM propellant over time . This could possibly quantify the useful service-life span in terms of ranges of these bulk viscoelastic properties , in lieu of tracking service history, thereby reducing failure due to old age.

Hopefully, this work will provide insight and a means of comparison with SRM segments inspected by radial x-ray and actual ultrasonic through-transmission. The ultimate goal is to provide a rapid, highly reliable indication of defects (voids) by ultrasonic NDE that would be critical to safe, reliable SRM operation. The ancillary benefit is to be able to characterize the age of the SRM propellant, regardless of service life. It

may prove that ultrasonic NDE will be part of an ongoing safety program more critical than the manufacturing defect detection use for which it was first envisioned.

1.10 Outline of The Research.

A literature search covering viscoelastic models and the selected finite difference numerical methodology will follow in Chapter II. Chapter III provides the theoretical development of the viscoelastic equations of motion which will be used to model the acoustical wave propagation in the SRM inert propellant. A specific finite difference viscoelastic SRM propellant numerical model is outlined in Chapter IV. The experimental results from the collaboration with Martin Marietta Laboratories and the data showing the model verification by ultrasonic NDE are presented in Chapter V, with preliminary numerical results to follow in Chapter VI. The final Chapter VII includes conclusions, lists some ancillary benefits, and makes suggestions for future work.

CHAPTER II

BACKGROUND ON WAVE PROPAGATION, VISCOELASTIC REPRESENTATIONS, AND NUMERICAL MODELS

2.0 Overview

This chapter forms the basis of a literature review covering wave propagation, viscoelastic representations, and numerical models. Starting with the elastic wave propagation model of Hooke's law, a two-dimensional, homogeneous, isotropic equation of motion is developed. Viscoelastic wave propagation is addressed next, followed by several representations of the viscoelastic stress-strain relationship. Finally, a finite difference numerical model is presented and compared to other methods for scattering and wave propagation.

2.1 Elastic Wave Propagation

Before the viscoelastic model, for solids, of stress-strain behavior is introduced, a small explanation of the more common elastic model is in order. Higdon, et al (1985) provides a basic understanding of Hooke's law and introduces the usual equation

$$\sigma = E\varepsilon \qquad \text{(Hooke's Law)} \qquad (1)$$

where (E) is Young's modulus, (σ) is stress, and (ε) is strain .

The relationship between stress and strain beyond the linear or elastic model is covered in Section 2.2, the viscoelastic portion of the background. The focus of this research is on the displacement as it relates to stress and strain from the above relationship and how it changes with viscoelasticity. Equation (1) can also be generalized as shown in equation (2) and explained by Thompson and Wadley (1989) in their review article.

$$\sigma_{ij} = C_{ijkl}\varepsilon_{ij} \tag{2}$$

This covers the case of differing stress/strain relations in various directions. The stress and strain are as before and the C_{ijkl} are elements of the fourth-rank elastic stiffness tensor. In an earlier article Pao (1983) provides a brief history of elastodynamics and mentions five reference-textbooks on elastodynamics. Graff (1975), as well as Boore (1972), Alterman and Leowenthal (1972), Bond (1978), Pao (1983), Chang (1987), Thompson and Wadley (1989), Sullivan, Ludwig, and Geng (1990), and others provide an equation of wave propagation for isotropic, homogeneous elastic solids, namely:

$$(\lambda + \mu)\nabla\nabla\cdot\mathbf{u} + \mu\nabla^2\mathbf{u} + \rho\mathbf{f} = \rho\ddot{\mathbf{u}} \tag{3}$$

with $$\nabla = \frac{\partial}{\partial x}\hat{i} + \frac{\partial}{\partial y}\hat{j} + \frac{\partial}{\partial z}\hat{k} \qquad \nabla^2 = \frac{\partial^2}{\partial x^2} + \frac{\partial^2}{\partial y^2} + \frac{\partial^2}{\partial z^2}.$$

Here **u** is the vector displacement, **f** is the vector body force, $\ddot{\mathbf{u}}$ is the second derivative of **u** with respect with time, ρ is the density and λ and μ

are the Lamé constants. The latter are related to the stiffness tensor in equation (4), with δ the Kronecker delta, from Pao (1983):

$$C_{ijkl} = \lambda\delta_{ij}\delta_{kl} + \mu\left(\delta_{ik}\delta_{jl} + \delta_{il}\delta_{jk}\right) \tag{4}$$

The relationships between the Lamé constants λ, μ and the shear (μ) and bulk (κ) moduli are explained in Hall (1968) and are shown below in equations (5) and (6):

$$\text{Lamé } \lambda = \kappa - 2\mu/3 \tag{5}$$

$$\text{Lamé } \mu = \mu \tag{6}$$

In a Cartesian coordinate system the strain is related to the displacement as shown in Fredrickson (1964), Thompson and Wadley (1989) and below in equation (7).

$$2\varepsilon_{kl} = \frac{\partial u_k}{\partial x_l} + \frac{\partial u_l}{\partial x_k} \tag{7}$$

Finally, Sullivan, Ludwig and Geng (1990) provide the expression between the stress tensor and the displacement as shown in equation (8):

$$\nabla \cdot \sigma = \mu\nabla^2\mathbf{u} + (\lambda + \mu)\nabla\nabla\cdot\mathbf{u} \tag{8}$$

Boore (1972), Alterman and Leowenthal (1972) and Bond (1978) reduce equation (3) to a 2-D model and ignore body forces ρf. The Cartesian form of the 2-D equations of motion (EOM), with v, u the

displacements in the x, y direction respectively, no displacement in the z direction, and t as time, are shown in equations (9) and (10):

$$\frac{\partial^2 v}{\partial t^2} = V_s^2 \frac{\partial^2 v}{\partial x^2} + \left(V_c^2 - V_s^2\right)\frac{\partial^2 u}{\partial x \partial y} + V_c^2 \frac{\partial^2 v}{\partial y^2} \quad , \tag{9}$$

$$\frac{\partial^2 u}{\partial t^2} = V_c^2 \frac{\partial^2 u}{\partial x^2} + \left(V_c^2 - V_s^2\right)\frac{\partial^2 v}{\partial x \partial y} + V_s^2 \frac{\partial^2 u}{\partial y^2} \quad . \tag{10}$$

The longitudinal velocity (V_c) and the transverse velocity (V_s) are related to the Lamé constants as shown in equation (11) and (12) below:

$$V_c^2 = (\lambda + 2\mu) / \rho, \tag{11}$$

$$V_s^2 = \mu / \rho. \tag{12}$$

The equation of motion can be solved numerically using a finite difference method, subject to some boundary and initial conditions. The changes required in all of the above equations to describe viscoelastic effects are discussed in the next section.

2.2 Viscoelastic Wave Propagation

The stress-strain relationship changes from a linear one (equation (1)), to a nonlinear system as a model of the viscoelastic material is developed. Four sets of methods which are used to describe viscoelastic media, are grouped together below in the general categories of dashpots

and springs, complex variables, relaxation and creep functions and other types. Before the explanation of the several methods are presented one should define what constitutes a "viscoelastic" material.

2.2.1 Viscoelastic Material

Several authors define the material properties and the classification of a material based on the results of dynamic or static testing. Most individuals are familiar with "Silly-Putty", a type of children's play material; this is a viscoelastic material. Fredrickson (1964) defines this class of materials as having a behavior which is partly fluid-like and partly solid-like. He further explains that in a viscoelastic material "shearing deformation is not completely conserved, as in solids, nor is it completely dissipated, as in fluids." Hall (1968) poses the definition in terms of the stress-strain relationship and its change over time. If, given a fixed stress, as the strain is measured over time and as it varies, the strain is not uniquely determined by the stress, the material is called viscoelastic. Cooke (1988) refers to a broad description of a viscoelastic material as one which has the following properties:

1. Creeps under constant stress; 2. Relaxes under a constant strain or deformation; 3. Instantaneously recovers a portion of its original shape after removal of the load; 4. Exhibits a delayed recovery from a load over time; 5. Develops a permanent set after removal of load.

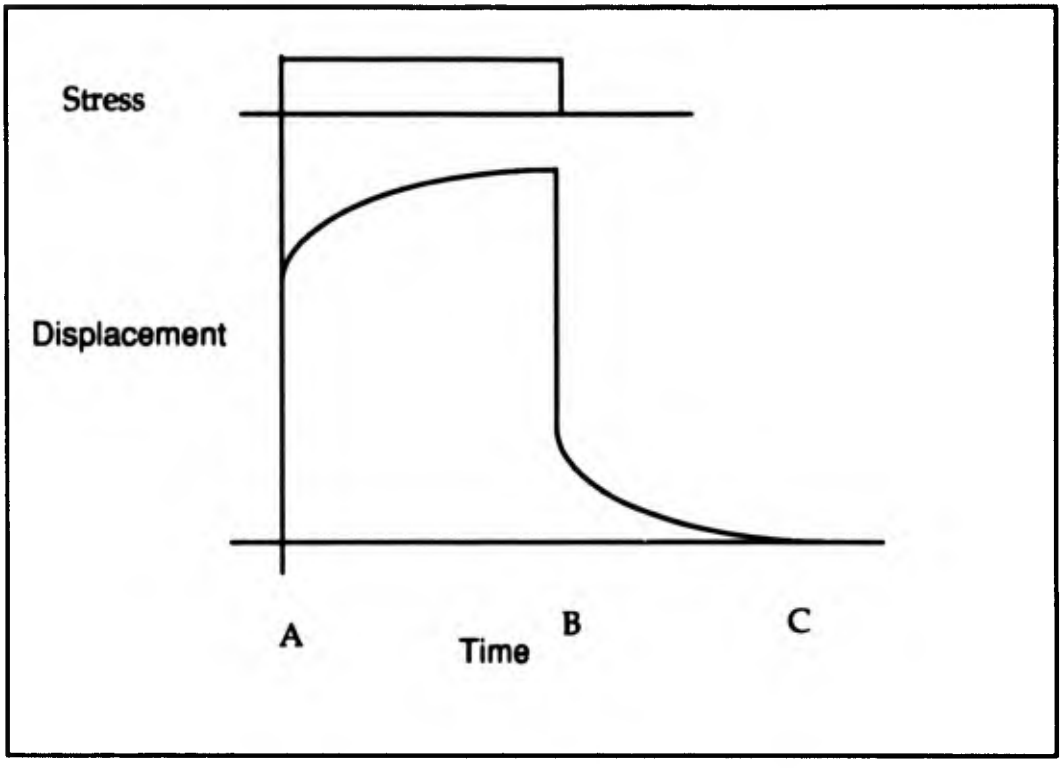

Figure 2.1. Displacement vs Time in a Viscoelastic Material, First Under Constant Stress (AB), and then After the Removal of the Stress (BC). (Note that the time axis can be extremely long.), (Hall, 1968, p 176)

Material properties are also temperature dependent and may also vary based on loading history. In this research effort the temperature dependence will not be included. It was assumed that all ultrasonic NDE would be done at the same controlled room temperature and that the SRM had been brought to that temperature. The viscoelastic material is rubbery and is a good representation for the SRM propellant segment. The next four subsections will explain methods previously used to model viscoelastic material.

2.2.2 Dashpots and Springs

Before explaining each mechanical approximation to the stress-strain relationship Figure 2.2 is shown as a summary.

Depiction	Model	Stress σ - Strain ε relationship	Comments
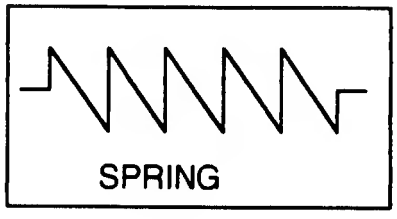	Hooke's	$\sigma = E\varepsilon$	Elastic
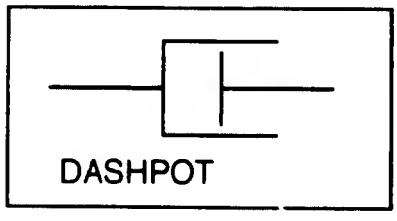	Newtonian Fluid	$\sigma = \eta\dot{\varepsilon}$	Viscosity
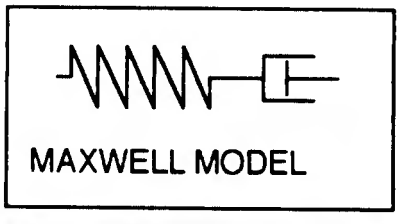	Maxwell	$\dot{\sigma} / E + \sigma/\eta = \dot{\varepsilon}$	Viscoelastic 2 element model
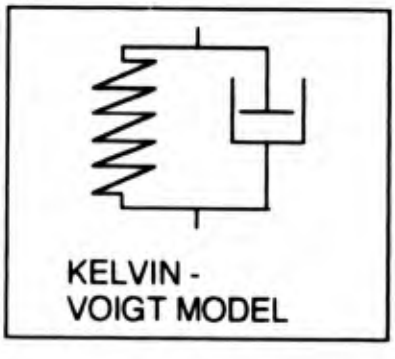	Kelvin-Voigt	$\sigma = E\varepsilon + \eta\dot{\varepsilon}$	Viscoelastic 2 element model

Figure 2.2. Mechanical Representations of Approximations to the Stress-Strain relationship.

Figure 2.2 is a truncated list, upon the addition of more elements, more complex stress-strain relationships could be modeled.

One of the first models of the stress-strain relationship, equation (1), is a simple spring shown in Figure 2.3 below. The basis for this section can be found in Hall (1968), Hudson (1980), Blake, Bond and Cooke (1988), and Mourad (1990) as well as many other places.

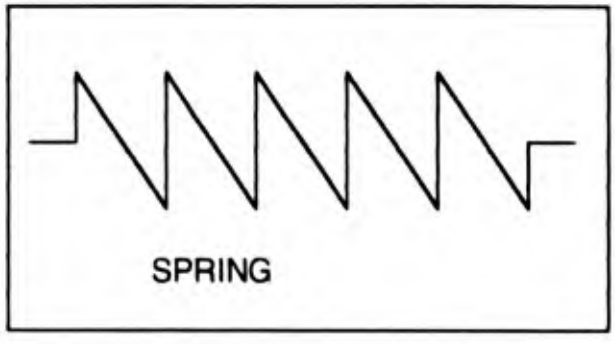

Figure 2.3. A Spring Representing the Linear Relationship Between Stress and Strain as in Hooke's Law.

The viscoelastic model needs some energy dissipating elements. Therefore, the next element included in a model between the stress and strain is the dashpot, shown in Figure 2.4. Equation (13) relates the stress σ to strain ε, with the η related to the viscosity of the dashpot.

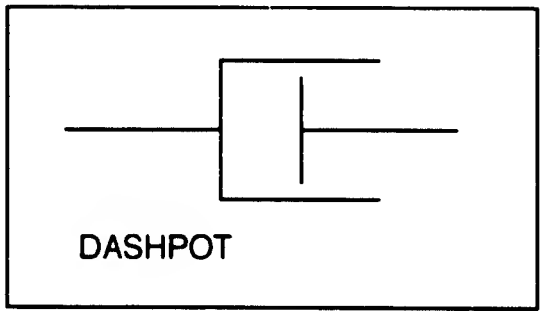

Figure 2.4. A Dashpot Representing the Newtonian Viscosity Model Relationship Between Stress and Strain. (Equation (13))

$$\sigma = \eta\dot{\varepsilon} \qquad (13)$$

From the simple elements presented, more complex relationships between the stress and strain can be developed. The Maxwell model combines the spring and dashpot in series, Figure 2.5. Equation (14) relates the stress to strain in the Maxwell model, E as in equation (1).

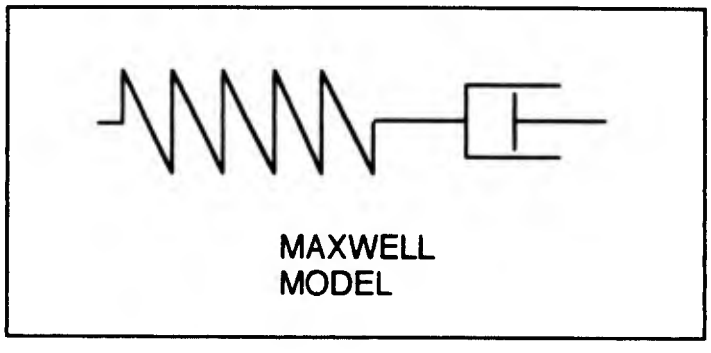

Figure 2.5. Maxwell Viscoelastic Model, a Spring and Dashpot in Series.

$$\dot{\sigma} / E + \sigma/\eta = \dot{\varepsilon} \qquad \text{(Maxwell Model)} \qquad (14)$$

Hall (1968) states that the Maxwell model demonstrates all of the observed experimental behavior of a viscoelastic material except creep recovery. Instead of Figure 2.1's displacement vs time histories from the application and removal of a constant stress, the Maxwell Model produces the relationship given as Figure 2.6.

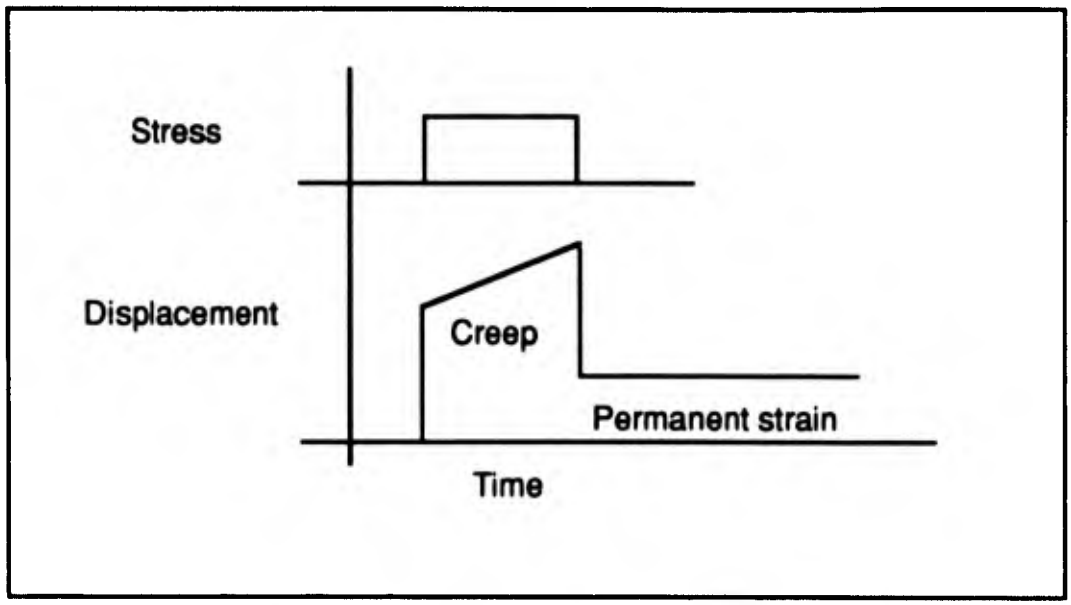

Figure 2.6. Displacement vs Time in a Maxwell Model showing the Application and Removal of a Constant stress. Hall (1968, p 181)

The Kelvin-Voigt model, found in Hudson (1980), connects a spring and dashpot in parallel, Figure 2.7, is described by equation (15).

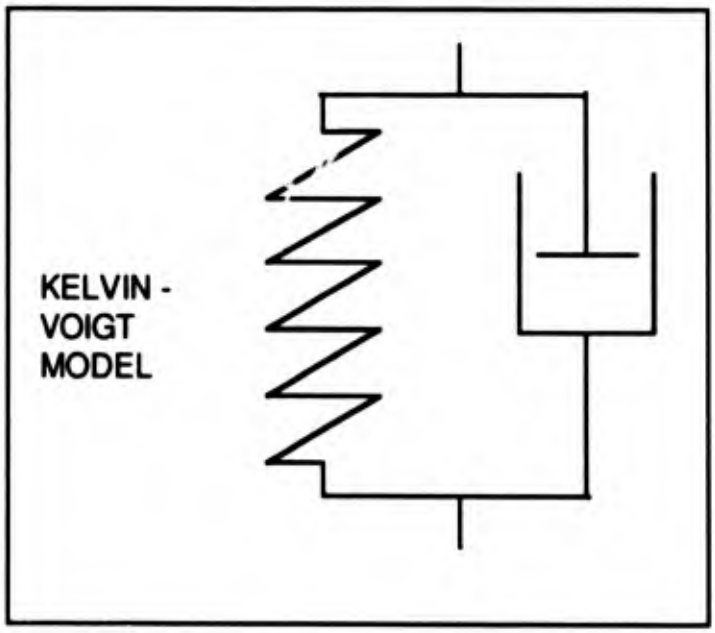

Figure 2.7. Kelvin-Voigt Viscoelastic Stress-Strain Model.

$$\sigma = E\varepsilon + \eta\dot{\varepsilon} \qquad \text{(Kelvin-Voigt Model)} \qquad (15)$$

The Kelvin-Voigt model demonstrates creep and creep recovery, Hall (1968), but does not show instantaneous recovery or extension from an applied or removed constant stress as shown in Figure 2.8.

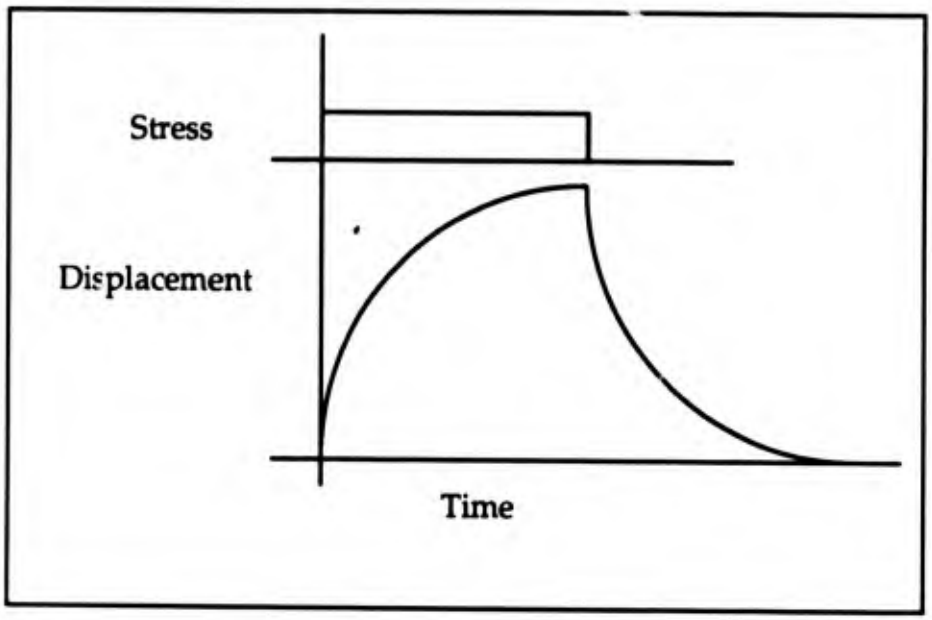

Figure 2.8. Displacement vs Time in the Kelvin-Voigt Model due to the Application (A) and Removal (B) of a Constant Stress in a Viscoelastic Material. (Hall, 1968, p 182)

By the combination of more springs and dashpots responses like those in Figure 2.1 can be produced. The Wiechert model consists of an infinite number of parallel Maxwell elements. In general the models describe the behavior at a single frequency. The material may be modeled by ascribing to it different properties and characteristics at different frequencies.

Several authors have utilized one or more elements to model the viscoelastic behavior of the material under study. Lawrence (1973) used a

Maxwell constitutive relation for the stress-strain model to calculate the response of homogeneous viscoelastic solids. Yang, Fernandez and Reed (1974) used the Kelvin-Voigt Model to develop a one-dimensional equations of continuity and momentum, to include energy loss by structural damping. Tung, Connor and Antoniadis (1988) used a Maxwell model to relate stress and strain. Cooke (1988) uses the Kelvin-Voigt model, as well as the complex variable method discussed in the next section, to compare results with a fairly new model, fractional derivative representation of viscoelastic behavior, which will be discussed later. Mourad (1990) also uses a five parameter (element) viscoelastic model, of springs and dashpots, to describe the behavior of an earplug in a coupled viscoelastic-acoustic system. You et al (1991), describe lossy solid media by "incorporating a term containing the time derivative of the strain tensor" into Hooke's law. This is akin to the Kelvin-Voigt model and equation (15). You et al (1991), define η "as a fourth-rank viscosity tensor whose constants can only be obtained empirically", which is understandable since they are describing anisotropic materials.

The next section, Description Using Complex Variables, is much simpler to detail, if not to understand.

2.2.3 Description Using Complex Variables

Two constants can be used to describe the behavior of an isotropic, homogeneous elastic material. However, there are five constants commonly referenced in the literature:

- E, the modulus of elasticity or Young's modulus, in equation (1)
- λ, the first of the Lamé constants
- μ, the shear modulus and the second of the Lamé constants
- κ, the bulk modulus, related to the Lamé constants in equation (5)
- ν, Poisson's ratio .

The interrelations among the five elastic constants can be found in Table 2.1, (Mal and Singh, 1991). Poisson's ratio is also related to the Lamé constants by equation (16) below, and is the ratio of lateral unit deformation to linear unit deformation within the elastic limit.

$$\nu = \frac{\lambda}{2(\lambda+\mu)} \tag{16}$$

Table 2.1. Interrelations Among the Elastic Constants of an Isotropic Solid. (Mal and Singh, 1991, Table 1-1, p 16)

	Basic Pair			
Constant	λ, μ	μ, κ	μ, E	E, ν
λ	λ	$\kappa - \frac{2\mu}{3}$	$\frac{\mu(E-2\mu)}{3\mu-E}$	$\frac{E\nu}{(1+\nu)(1-2\nu)}$
μ	μ	μ	μ	$\frac{E}{2(1+\nu)}$
κ	$\lambda + \frac{2\mu}{3}$	κ	$\frac{\mu E}{3(3\mu-E)}$	$\frac{E}{3(1-2\nu)}$
E	$\frac{\mu(3\lambda+2\mu)}{\lambda+\mu}$	$\frac{9\kappa\mu}{3\kappa+\mu}$	E	E
ν	$\frac{\lambda}{2(\lambda+\mu)}$	$\frac{3\kappa-2\mu}{2(3\kappa+\mu)}$		ν

Only two of the five elastic constants are independent. In modeling the behavior of viscoelastic material, one method is to just assume the elastic "constants" are now complex. For the case of Young's modulus, equation (17) is generally used and the E_1 and E_2 are referred to as the storage or dynamic modulus and loss or dissipation modulus, respectively, with $i = \sqrt{-1}$.

$$E = E_1 + iE_2 \tag{17}$$

Young's modulus may also be frequency dependent.

Meer (1969) uses a complex Young's modulus to investigate the longitudinal wave propagation of linear viscoelastic bars of slowly varying cross-section. Caille (1988) uses the complex E to model a viscoelastic coating of a cylindrical shell. Cooke (1988) used the complex E viscoelastic model as the second comparison with results of the fractional derivative viscoelastic model. Piché (1989) uses a complex modulus similar to a complex E method in the study of ultrasonic waves in polymers. Mourad (1990) not only uses a five parameter model of springs and dashpots, but also uses a complex E in modeling the viscoelastic-acoustic system under study.

In Bagley and Torvik (1986), the development of the fractional derivative model, the Lamé constants, as well as Young's modulus are assumed to be complex. Kline and Egle (1986) use complex Lamé "constants" which are also frequency dependent in the ultrasonic materials characterization of viscoelastic behavior. Schmidt and Jensen (1984) model the viscoelastic attenuation of horizontally stratified ocean environments by "letting the Lamé constants be complex." Weaver, Sachse and Niu (1989a) explain the viscoelastic plate theory of transient ultrasonic waves with the understanding that the μ, V_c and V_s defined in equations (6), (11), and (12), respectively, are to be complex and frequency dependent. Madigosky and Scharnhorst (1990) define a complex μ, κ and M (compressional modulus).

Weaver, Sachse and Niu (1989b), in a companion paper to the previous citation, note two important points in connection with the viscoelastic model and actual experimentation: " geometric correction terms can be highly significant and should not be ignored, and that beam pattern uncertainties related to finite aperture receivers can be highly problematic." This is mentioned as a reminder that a given model may be accurate or inaccurate, but experimental results can mask observations and prevent one from reaching any conclusions.

The third viscoelastic model introduces relaxation and creep functions to the stress-strain relationship.

2.2.4 Relaxation and Creep Functions

The model involving creep and relaxation uses convolution integral equations to relate the stress to the strain. Pipkin (1986) uses the symbol G(t) to describe the linear stress relaxation modulus and J(t) as the linear creep compliance. Christensen (1971) uses the same notation. Both Christensen (1971) and Pipkin (1986) explain the behavior of the viscoelastic material under a constant stress, then a constant strain. The constant stress condition produces a creep in the material, represented by J(t), which increases until the material fails under the constant stress. The function G(t) is the analog to J(t) under constant strain. Eventually the viscoelastic material will relax under a constant strain and there will be zero stress. The relationship between J(t) and G(t) is found in Pipkin (1986) and below in equation (18):

$$G(t)J(t) = \frac{\sin[p(t)\pi]}{p(t)\pi}, \qquad \text{where} \tag{18}$$

$$p(t) = \frac{d(\log J)}{d(\log t)}. \tag{19}$$

Figure 2.9 portrays G(t) and Figure 2.10 portrays J(t). The function p(t) is the slope at t on the plot of log J vs log t (see Figure 2.10).

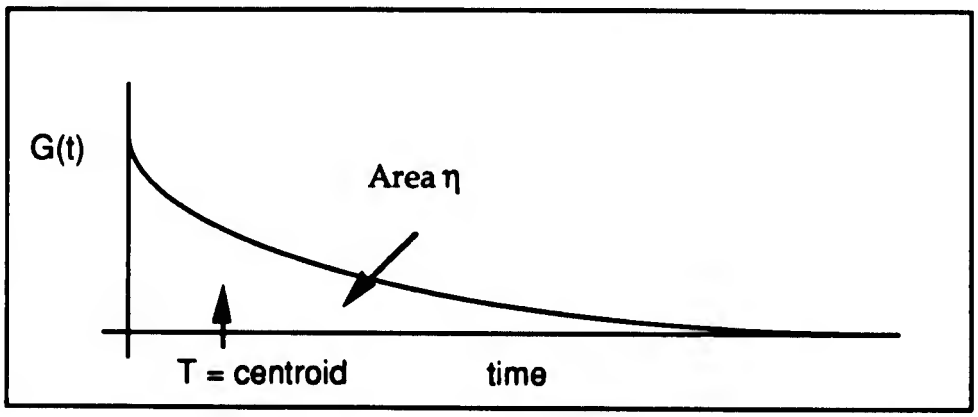

Figure 2.9. The Linear Stress Relaxation Modulus. (Pipkin 1986)

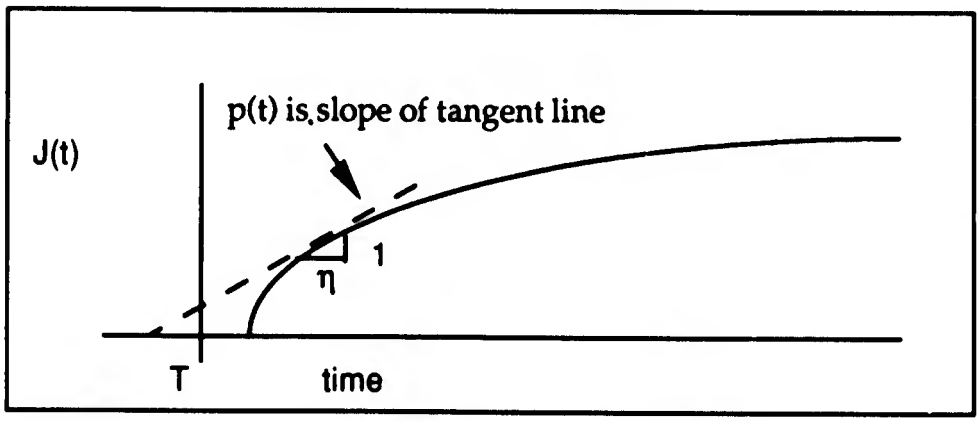

Figure 2.10. The Linear Creep Compliance Modulus. (Pipkin 1986)

The symbol T refers to the mean relaxation time and is the centroid of G(t), while h is the area under the G(t) curve and the inverse of the slope of J(t) that intersects the negative time axis at a distance T. Christensen (1971) suggests Figure 2.11 as a typical creep function.

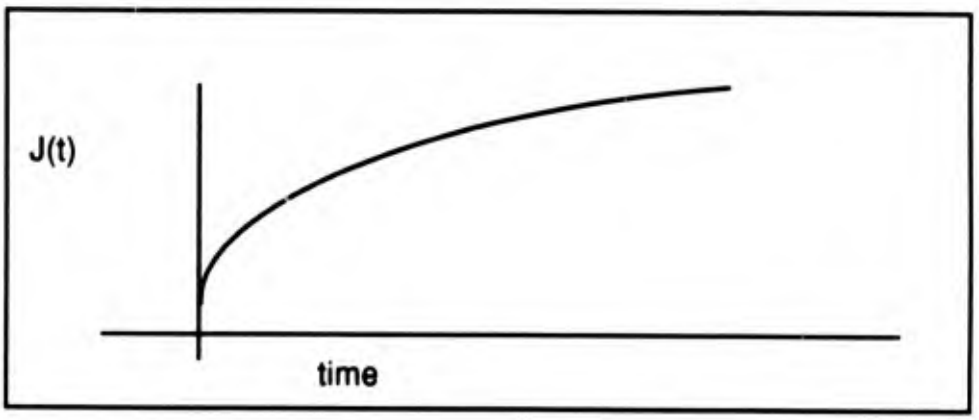

Figure 2.11. Typical Creep Function. (Christensen 1971, p 19)

Wu and Sackman (1974) relate stress to strain using a creep function, equation (20), to investigate transient waves in semi-linear viscoelastic media. Equation (20) is in a nondimensionalized form.

$$J(T) = 2.0 - e^{-T} \qquad (20)$$

Sutherland (1979) derived material characteristics for homogeneous isotropic polymers. Sutherland identified two independent moduli to be the "longitudinal relaxation modulus and the shear relaxation modulus" which "constitute a complete mechanical description."

The last section of the viscoelastic models, Special Considerations, is a collection of different models that do not exactly fit into one of the previous sections.

2.2.5 Special Considerations

This section will present the methods outlined by several authors in characterizing the behavior of viscoelastic material. Bagley and Torvik (1986), describe the Fractional Derivative Model to relate stress to strain.

$$D^{\gamma}(\sigma) = D^{\gamma}(\varepsilon) \tag{21}$$

$$\text{with } D^{\gamma}[x(t)] = \frac{1}{\Gamma(1-\gamma)}\frac{d}{dt}\int_0^t \frac{x(t-\tau)}{\tau^{\gamma}}d\tau$$

Where D^{γ} is a fractional derivative operator defined in Bagley and Torvik (1986) with $0 < \gamma < 1$. This method is similar to the methods outlined in Springs and Dashpots, but there the derivative operators used integer numbers. Cooke (1988) used this fractional derivative technique to model a polypropylene rod's viscoelastic behavior. His conclusion was that "the fractional derivative model represents a viable alternative for representing the transient response of viscoelastic beams."

Other authors outlined methods for including viscoelastic behavior in different fashions. Blake, Bond and Downie (1982) proposed the use of a combination of Maxwell and Kelvin-Voigt models including the Lamé parameters with a time differential operator. Brockman (1984) describes a method of obtaining the required stress-strain relationship analytically. Brockman presumes the viscoplastic strain rates to be functions of the current stresses and relates the time rate of stress to the time rate of strain. Sheen, Reiman, Lawrence and Raptis (1988) investigate ultrasonic techniques for measurements of coal slurry viscosity, noting that the shear

viscosity varies with shear rate. Dassios and Zafiropoulos (1990) note that the "energy behavior of a viscoelastic wave is closer to the corresponding behavior of a purely elastic rather than a thermoelastic wave." Their method employs Lamé constants which fade exponentially and a general equipartition of energy.

This concludes the discussion of the viscoelastic models of behavior outlining several stress-strain relationships. The next section, A Finite Difference Method, solves the partial differential equations representing wave propagation numerically.

2.3 A Finite Difference Method

The hyperbolic partial differential equation (3) can be solved numerically. The method explained is one that is explicit and requires a minimum of analytical effort, as Aki and Richards (1980) states. Smith (1985) explains the forward, backward and centered difference formulas with the help of Figure 2.12. The difference formula is just a Taylor series approximation truncated to the appropriate order. This implies a grid coordinate system which may be Cartesian, cylindrical or any other system, as required. The grid spacing is important as it relates to accuracy, stability, and convergence.

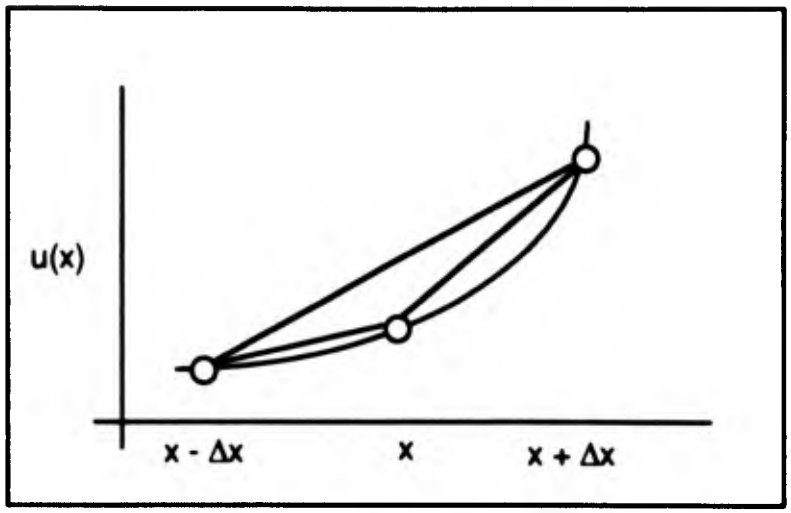

Figure 2.12. Slope of u(x) at x Approximated Using Finite Difference Formulas. (Smith 1985, p 7)

The forward-difference formula is just the approximation of the slope of the function u at x, using points u(x) and u(x + Δx):

$$\frac{\partial u}{\partial x} \cong \frac{u(x+\Delta x)-u(x)}{\Delta x}. \tag{22}$$

The backward-difference formula also approximates the slope of u at x, using points u(x) and u(x - Δx):

$$\frac{\partial u}{\partial x} \cong \frac{u(x-\Delta x)-u(x)}{\Delta x}. \tag{23}$$

Both the forward and backward difference formulas are of the order (Δx), i.e., a truncation error term proportional to Δx. The centered-difference formula approximates the slope of u at x, using points u(x - Δx) and u(x + Δx) and has a leading error term proportional to $(\Delta x)^2$:

$$\frac{\partial u}{\partial x} \cong \frac{u(x+\Delta x)-u(x-\Delta x)}{2\Delta x} \qquad (24)$$

Higher order derivatives can also be approximated as shown in Smith (1985), Aki and Richards (1980), and elsewhere.

2.3.1 Usage of the Finite Difference Method

Bond (1990) provides a review comparing several numerical techniques as they relate to practical ultrasonic NDT (non-destructive testing). One conclusion reached stresses the importance of matching the technique to the problem. The finite difference method is well suited for modeling wave propagation for ultrasonic NDE as noted in Bond (1978), Blake, Bond and Downie (1982), Bond, Saffari and Punjani (1987), Chang and Randall (1988), Bond, Punjani and Saffari (1988), Blake and Bond(1990) and (1991) and elsewhere. Wave propagation phenomena are important in other fields besides ultrasonic NDT/NDE, such as, geophysics and seismology, civil and mechanical engineering, electronics, and mathematics/applied mechanics as pointed out in Bond, et al (1988).

Boore (1972) and Alterman and Leowenthal (1972) used the finite difference method for the modeling of seismic waves. Virieux (1986) used a velocity-stress finite difference method to model P-SV (compression and shear) wave propagation. Dow, Jones and Harwood (1990) used the finite difference method to model a static problem in solid mechanics, as opposed to the transient type problems of the others above. The finite difference method was used to model three-dimensional viscous flow in a

channel by Rai and Moin (AIAA 89-0369) as reported in the December, 1991 NASA Tech Briefs. In the January, 1992, Aerospace America issue on computational fluid dynamics, finite difference numerical methods were identified as part of significant research on the "blunt-body problem" in atmosphere reentry aerophysics. Finally, Lawrence (1973) used the finite difference method as a tool to calculate the wave propagation in both viscoelastic materials and laminated composites.

2.3.2 Finite Difference Comparisons

Alford, Kelly, and Boore (1974) compared the finite difference method to solutions obtained from more "classical analytical approaches." Their conclusions reinforced the concern of grid spacing and number of grid points per wavelength while cautioning that "grid dispersion can distort the results to a point where serious errors may be made in interpretation of the events."

Roberts and Selim (1984) compared eight different finite difference methods for solving parabolic partial differential equations. They ranked the methods with respect to accuracy, execution time, and programming effort. In their words "it is clear that each of these schemes has its own advantages, and it is therefore difficult to make a selective judgment of the best scheme." Once again, match the method to the problem.

Frankel (1989) reviews applications of the finite-element and finite-difference methods in studies of seismic waves. He makes several observations which are repeated here:

- These techniques can produce synthetic seismograms for media where fluctuations are about the same size as the seismic wavelength, a regime where the scattering effects can be most severe.
- A minimum number of grid points per seismic wavelength is necessary to achieve acceptable accuracy.
- Almost all of the numerical studies published to date involved two-dimensional problems with material variations in two spatial dimensions.
- The explicit method is the most common finite-difference technique and updates the wave field one grid point at a time for each time step.
- The accuracy of the finite-difference method depends on how finely the grid samples the seismic wave in space and time.
- Because of numerical errors, the phase velocity of a propagating body wave becomes a function of frequency at short wavelengths, a phenomenon known as 'grid dispersion.' . . . at least 10 grid points per wavelength . . . S-wavelength [transverse] to grid spacing is the critical parameter.
- In conclusion, numerical experiments using the finite-difference and finite-element techniques have improved our understanding of wave propagation in media with complex velocity structures.

In his review of numerical techniques used to study scattering and wave propagation Bond (1990) provides, Table 2.2, which compares several techniques. One property of interest is the "ka restriction," where $k = \frac{2\pi}{\lambda}$ the wave number, and a is the flaw dimension. For ultrasonic NDE of SRM propellant segments for detecting voids, ka is approximately 2. Table 2.2 is shown on the next page.

Chang and D'Angelo (1990) compare finite difference predictions to actual experimental results with excellent agreement. Ayme-Bellagarda, Chang and Habashy (1990) use the finite difference method as an independent technique to compare results with the fractional derivative model. They found good agreement between the two methods.

2.3.3 Finite Difference Notes

Reali, Rangogni and Pennati (1984) provide another form for finite difference formula generation, which include general analytical compact expressions. Cerjan, D. Kosloff, R. Kosloff and Reshef (1985) provide a practical method for reducing the impact of false boundaries on the implementation of numerical methods in solving wave equations.

This section concludes the literature review. The viscoelastic model of the SRM propellant is presented in Chapter III.

Table 2.2 Comparison of Various Modeling Techniques Applied to Ultrasonic Wave Propagation and Scattering. (Bond, 1990, Table 1, p21)

Technique. Property.	Analytical methods	Finite differences	Elastic Kirchhoff	Born Approx.	Geometrical theory of diffraction	T-Matrix.	BIE or BEM.
ka restriction.	ka<< 1 ka>> 1	0.1< ka <20	ka>>1	ka <1	ka >>1	0<ka<15	0 <ka< 6
Field region	Far	Near or Far	Far	Far	Far	Either	Near or Far
Dimension	3-D	2-D (3-D)	3-D	3-D	2.5-D	3-D	Most 3-D
Shape of scatterer	circle, cylinder sphere.	limited (square.) *	small surface slope.	good range **	crack-like	ellipsoidal cavity.	Arbitrary.
Included material	restricted	most ***	**	weak	X	***	Strong or weak
Mode conversion	**	***	***	**	*	***	***
Incident wave.	plane or spherical	arbitrary 2-D	plane or spherical	**	**	**	Arbitrary
Short pulse.	**	***	*	+	*	X	FFT used.
Multiple scattering. (2 Body)	+	***	+	+	*	**	**.

Rating system: *** Very good, ** Good, * Copes, + poor, X Very Poor.

CHAPTER III

METHODOLOGY OF ULTRASONIC NDE

3.0 Overview

The previous background chapter discussed the different methods of modelling viscoelastic wave propagation, one of which, the Kelvin-Voigt model, will be used here. The engineering approach to using ultrasonics as a NDE technique, the form and substance of the numerical model, and the experimental analysis used to support the model are discussed in this chapter. This forms an unique methodology that is the foundation for the next several chapters, and the basis of a novel NDE safety program.

3.1 Engineering Approach

The strategy for investigating the problem and developing a solution will be a top down approach. Top down approach in this context means to break a problem into smaller and smaller tasks starting from a global view. The global view consists of a safety program that detects, locates, and sizes defects in SRM propellant segments. It was for this reason that ultrasonic NDE was first investigated, specifically for the investigation of internal volumetric voids produced in the SRM manufacturing process.

It was realized during this research, that any safety program that detects, locates, and sizes defects should operate more than once. Figure 3.1 depicts a simplified version of an ultrasonic NDE (labeled test) ongoing effort as part of a future safety program.

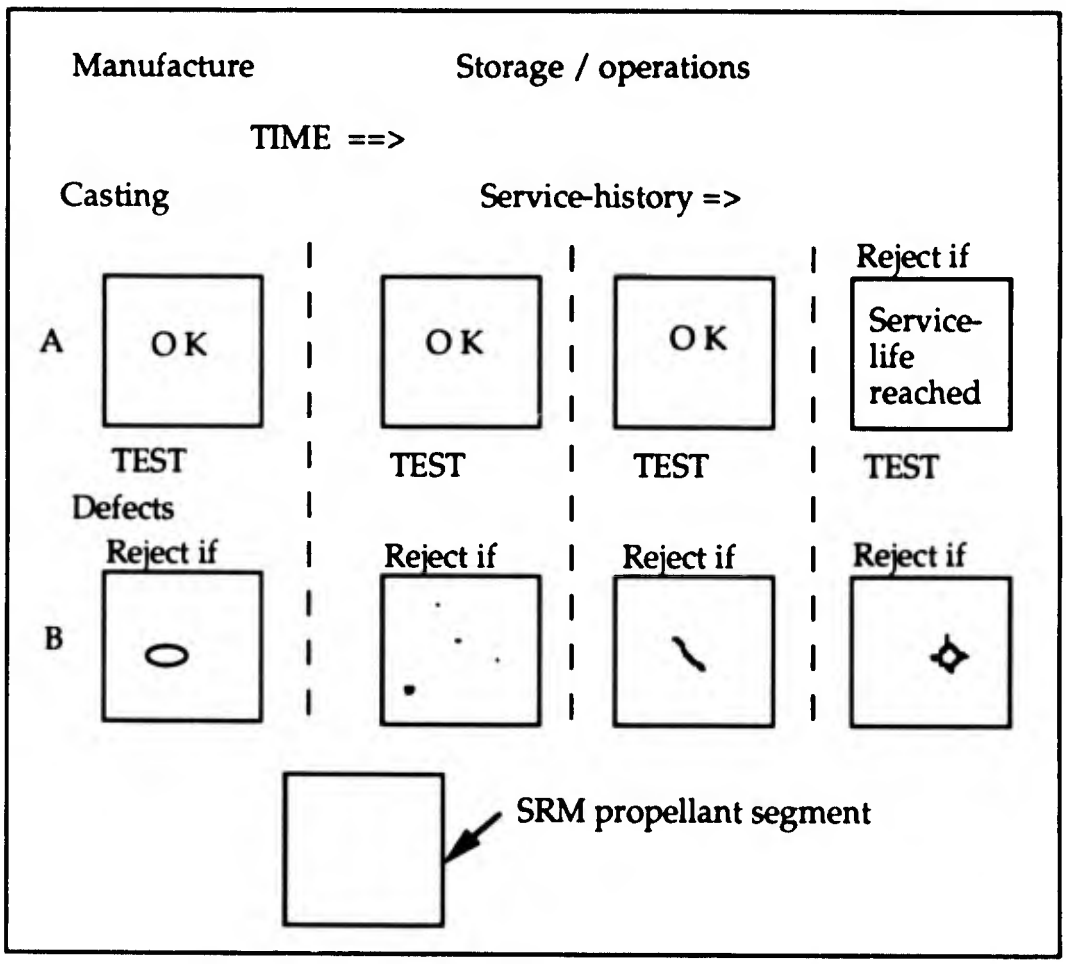

Figure 3.1. Ongoing Ultrasonic NDE as part of a Safety Program, Line A are the inclusion free SRM propellant segments, Line B are the defective SRM propellant segments.

Each square block represents an SRM propellant segment. Time increases as one moves from left to right. The dashed lines separate different test dates.

The first test, directly following the casting in the manufacturing process, checks for the flaws outlined in Section 1.5. Detecting the first rejected SRM propellant segment of line B, was the focus of this research effort at its onset. The Figure depicts an internal volumetric void. As time progresses, ultrasonic NDE occurs at regular intervals in the storage and operations phase of the SRM propellant segment's service-history. The service-history flaws portrayed in the rest of the tests in Figure 3.1 line B are microvoids and cracks, crazing, and dewetting (in the last frame). The specific requirements of ultrasonic NDE for each flaw will not be identified here, but each flaw must be detected, located, and sized nonetheless. Line A lists the SRM propellant segment, again tested over time, but the last frame depicts a rejected segment that does not have an internal flaw but has reached the end of its useful service-life. As mentioned in Chapter I, the service-life end is reached when the bulk viscoelastic properties, which change with time, are outside acceptable limits due to interactions with reactants in the atmosphere. Although it is depicted as a result of an ultrasonic NDE in Figure 3.1, currently the service-life is based just on time, without any considerations for the specific service-history of an SRM propellant segment.

With this picture of a safety program as part of the top down approach, the research effort was divided into six areas. The first was a methodology that ties together the other five areas. The next three consist of the experimental tests, numerical simulations, and the analytical bridge that connects numerical results to experimental data. The discussions, conclusions, and benefits are grouped together in one area as the pinnacle of this research effort. The last area gives a direction for future work

which narrows the many possible branches into, hopefully, the most productive regions.

3.2 Steps in Methodology of Ultrasonic NDE

The global view suggested a methodology, listed below, which appears useful for the investigation of ultrasonic NDE and ties in with Figure 3.1.

1- When casting an SRM, cast and set aside a test specimens;
2- Conduct ultrasonic NDE of the test specimens;
3- Analyze data, compute a Viscoelastic Damping Coefficient (VDC) by the method shown in this paper;
4- Use the VDC in a numerical simulation to validate the numerical model, specifically addressing SRM propellant characteristics;
5- Conduct a numerical parametric study and include critical flaws;
6- Use a model based inversion for the accept/reject criterion;
7- Conduct periodic ultrasonic NDE of the accepted SRM propellant segments and samples to monitor for defects and aging.

The uniqueness of this methodology is the fact that the aging test specimen will be used to tune the numerical model, for the subsequent SRM tests, not just to characterize the propellant at the time of manufacturing. Further, as noted in step 7, the test specimen should be monitored for defect formation and aging effects while it is maintained in a laboratory environment. Since there are differences in bulk material properties of SRM propellant segments with different compositions, as well as between different batches of the same composition, the test results from the ultrasonic NDE of the test specimen should provide quantitative information concerning service-life of the actual SRM propellant segment.

Steps 2 - 4 are interrelated but the order is important. The task is to characterize the bulk viscoelastic properties of the SRM propellant segment. This is done through the ultrasonic NDE of the test specimen, determining the VDC, and tuning the numerical simulations. The VDC (analytical bridge) will be explained shortly. Figure 3.2 depicts a block diagram outlining this process. One notes that the numerical model consists of modelling the propellant as a viscoelastic material and also using a finite difference method to model the partial differential equations, both together are considered the "numerical model."

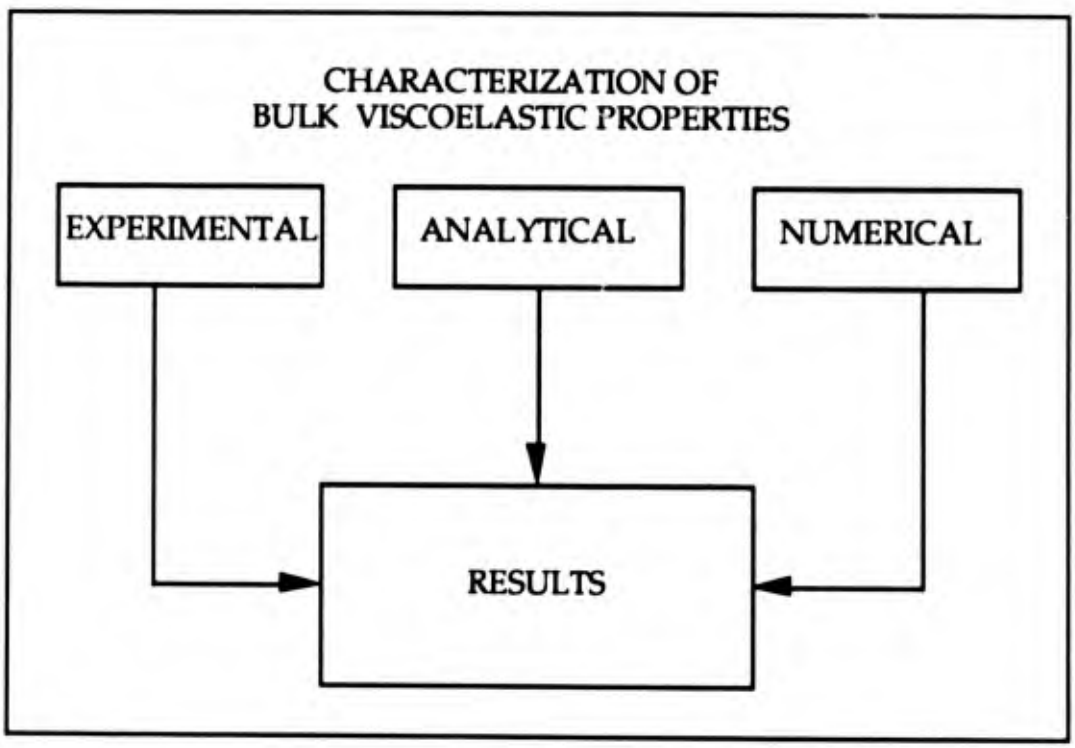

Figure 3.2. Characterization of Bulk Viscoelastic Properties of SRM propellant segments.

Each of the areas noted in Figure 3.2, Experimental, Analytical, and Numerical, are addressed in Sections 3.3 -3.5. The last three steps were just presented, but not incorporated in this research effort.

3.2.1 Use Experimental Data to Validate the Wave Propagation Model

The goal of utilizing ultrasonics to replace x-ray methods in search of void inclusion recognition for NDE of SRM propellant requires a technique to detect, locate and size voids by ultrasonic methods. This technique would require the known response of void inclusions to ultrasonic testing.

Specifically, the ultrasonic signal time series can be analyzed by means of a Discrete Fourier Transform (DFT). The information contained in the signal for various thicknesses of material can accurately characterize the response of the propellant in the numerical models. The exact information extracted by using the DFT and the signal time series are presented in the experimental analysis section, but the questions concerning the model and the inclusions in the model themselves are discussed next.

3.2.2 Model the SRM Propellant as a Viscoelastic Material

Before the response of void inclusions can be identified, the response without inclusions should be characterized as a reference. To this end, the Kelvin-Voigt model mechanical approximation to the stress-strain relationship, presented in Chapter II, was used to numerically represent the SRM propellant as a viscoelastic material. The numerical simulation includes this sub-model of the viscoelastic attenuation which mimics the attenuation that was prevalent in the experimental ultrasonic signals after they propagated through the inert propellant. Furthermore,

this ultrasonic NDE of the inert propellant was used to tune the viscoelastic models to these actual responses exhibited by the inert propellant through a Viscoelastic Damping Coefficient (VDC). The ongoing ultrasonic NDE would track the change of the VDC as the specimen aged. The changes would be compared to the reference values and empirical relationships between the various bulk material properties could be identified. It is in this vein that service-life could be quantified based on a range of values of the bulk material properties, without reference to service-history. This clearly falls within the range of future work and will be addressed in the last chapter of this work.

3.1.3 Model with Inclusions

Once the viscoelastic models are established as good representations of wave propagation through the SRM propellant, inclusions can be added to the numerical simulation. This will provide insight into use of ultrasonics as a means to find inclusions in SRM propellant. The location, number and orientation between voids can be varied relatively quickly. Trends of the responses can be used to show the relationship between void location and ultrasonic signal response. As stated previously this endeavor was not completely included here. More information is required than a single two transducer ultrasonic through-transmission test. The use of numerical simulations in a model based inversion system, using multiple receive locations in conjunction with an Artificial Intelligence system like a Neural Network, would be required to solve this ill posed problem and detect, locate, and size voids. If the numerical

model is tuned correctly, it would provide the means to teach the Neural Networks how void location and size affects the received ultrasonic signals.

3.3 Experimental Analysis

With the caveat that all experimental data has error, the following steps to obtain the bridge from SRM propellant to the numerical model are presented. The experimental error analysis will be addressed in Chapter V, Experimental Measurement. This section is divided into three parts:

- the information obtained from the time series signal;
- the information from the spectrum of the time domain signal (frequency domain);
- how the experimental data was used to tune the numerical model.

3.3.1 Signal Time Series

After the time signal is imparted into the SRM material, attenuation and the group velocity can be determined. The attenuation is the peak-to-peak amplitude ratio of the received signal to the transmitted signal. The group velocity is determined by taking the difference between the time of the start of the transmitted signal and the time of the first arrival of the received signal, and then dividing by the distance the signal

traveled. Both the attenuation and the group velocity are single data points associated with a specific test.

3.3.2 Spectrum of the Signal Time Series (Frequency Domain)

The spectrum of the signal time series (frequency domain) is obtained by a DFT algorithm directly from the waveform analyzer after the signal was recorded on the oscilloscope. However, for Test 3, the author calculated the DFT from the signal time series. Further details of the experimental setup are contained in Chapter V, Experimental Measurements.

The magnitude portion of the frequency domain provides the attenuation versus frequency information, as computed in Purnell (1986). As the attenuation is a bulk viscoelastic property, the diffraction and impedance mismatch, between the sample and elastomer coupler, must also be accounted for in the calculations. Atalar (1988) provides a method to address diffraction losses. Simpson and McClung (1991) provides alternate means to address the diffraction based on Seki, Granato, and Truell (1956) and Rogers and Van Buren (1974). The sample/elastomer interface is the only transformation between the transmitted reference signal data and the received signal data. This interface correction must be applied twice, since it occurs at both the transmit and receive transducers.

The phase portion of the frequency domain determines phase velocity versus frequency information, as in Sachse and Pao (1978) and Fortunko, et al (1992). The latter includes the diffraction corrections in the phase terms as identified in Rogers and Van Buren (1974).

3.3.3 Steps in using Experimental data to tune the Numerical model

Figure 3.3 depicts the specimen undergoing ultrasonic NDE in step 1. Then the VDC or η was used in a simulated ultrasonic NDE in steps 2 - 4. Step 2 uses a one-dimensional model to compare its attenuation to experimental data. Then in step 3, the tuning progresses to the two-dimensional simulations to again compare attenuation. Finally the VDC should be used with a simulated void, to obtain a comparison to the experimental data. This was not done completely here.

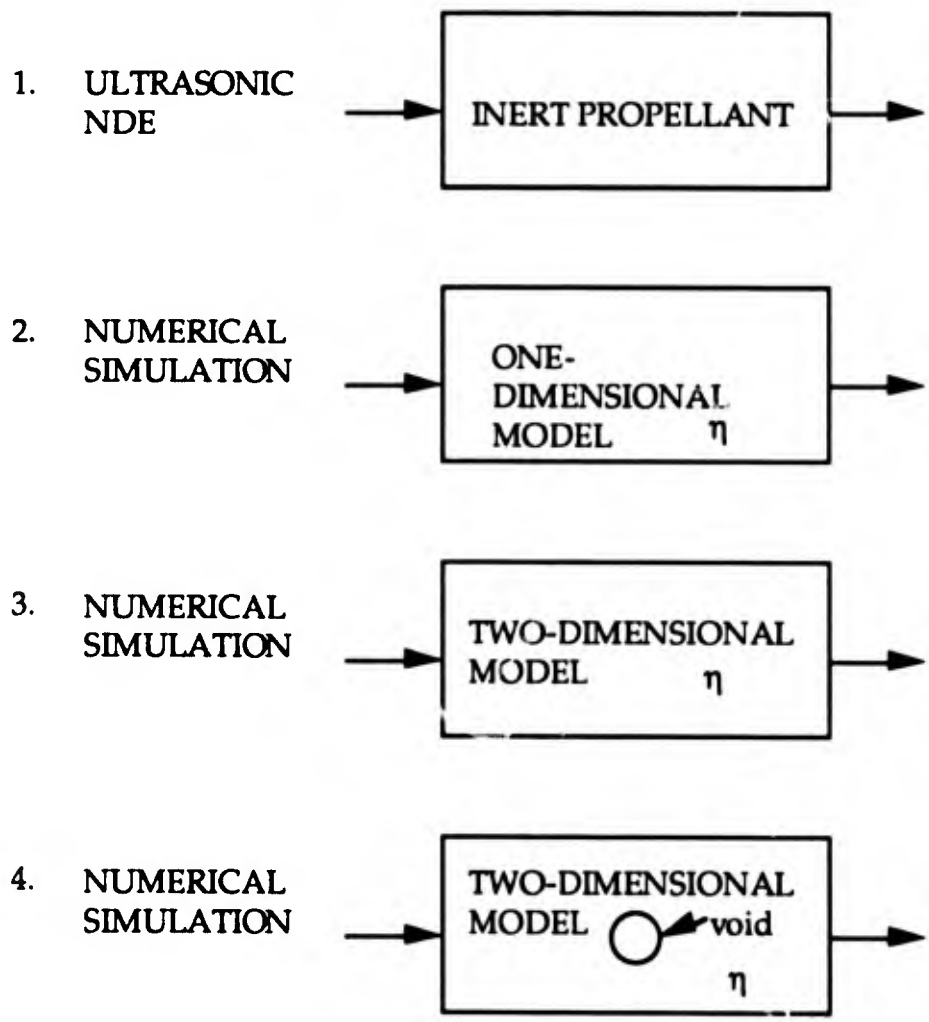

Figure 3.3. Steps in Tuning the Numerical model.

3.4 The Bridge between the Numerical Model and Experimental Data

The purpose of the numerical simulations was to develop a reference state corresponding to the SRM propellant segment during ultrasonic NDE. The bridge that connects the numerical model to the experimental data is the attenuation present in ultrasonic NDE signals, due to the viscoelastic nature of the SRM propellant.

Kino (1987), p8, shows an analytical method for determining the acoustic loss for a system that dissipates energy. This method is based on a one-dimensional equation. The attenuation, α, is a function of frequency ω, velocity V_c, density ρ, and the viscoelastic damping coefficient η, as shown in equation (25) and was corrected for diffraction effects and impedance mismatch.

$$\alpha = \frac{\omega^2 \eta}{2V_c^3 \rho} \quad \text{or} \quad \eta = \frac{\alpha 2V_c^3 \rho}{\omega^2} \tag{25}$$

Truell, Elbaum, and Chick (1969) referenced a "standard expression for sound attenuation," which is equal to 4 and 16/3 times the attenuation in equation (25) for transverse and longitudinal waves, respectively. For simplicity Kino (1987) was used to calculate VDC.

The attenuation and the phase velocity at each frequency were used in determining the VDC. Once the VDC was used in the numerical model, the numerical α_n was matched to the experimental α_e and refinement was made on the VDC for the next iteration. This was carried out for the one-dimensional and two-dimensional models which are described in section 3.5 below.

3.5 Numerical model of SRM propellant as a Viscoelastic Material

The numerical model consists of a modification to the elastic equations of motion accounting for the viscoelastic stress-strain relationship evident in SRM propellant. In Chapter II the elastic equations of motion (EOMs) based on Hooke's law, $\sigma = E\varepsilon$ in equation (1), were developed. The viscoelastic EOMs presented here are just modifications to the elastic EOMs.

The Kelvin-Voigt stress-strain relationship shown in equation (15), $\sigma = E\varepsilon + \eta\dot{\varepsilon}$, can be rewritten as a modified stress-strain relationship and is shown in equation (26) below.

$$\sigma = \left(1 + \eta / E\frac{\partial}{\partial t}\right)E\varepsilon \qquad (26)$$

This is now substituted for the stress σ in equation (8) and equation (3).

$$\nabla\cdot\sigma = \mu\nabla^2\mathbf{u} + (\lambda + \mu)\nabla\nabla\cdot\mathbf{u} \qquad (8)$$

$$(\lambda + \mu)\nabla\nabla\cdot\mathbf{u} + \mu\nabla^2\mathbf{u} + \rho\mathbf{f} = \rho\ddot{\mathbf{u}} \qquad (3)$$

Equations (3) and (8), without body forces, i.e. $\mathbf{f} = \mathbf{0}$, therefore reduces to the short algebraic form:

$$\nabla\cdot\sigma = \rho\ddot{\mathbf{u}} \qquad (27)$$

For the Kelvin-Voigt model, equation (26), instead of equation (1), is substituted into equation (27). When this is completed the elastic EOMs can be modified by $\left(1+\eta/E\frac{\partial}{\partial t}\right)$, the term in equation (26) that precedes the strain. Since the left hand side of equation (27) contains only spatial derivatives and the right hand side contains only time derivatives when the terms are rearranged, it is still easy to modify only the left hand side of equation (27) terms wherever they may be. The one-dimensional and two-dimensional models using the Kelvin-Voigt representation are presented below.

3.5.1 One-Dimensional Kelvin-Voigt Model

The one-dimensional model is the scalar equivalent of equation (27) which can be found in many texts covering wave propagation, specifically Kino (1987), page 4. When the elastic stress-strain relationship is used, equation (28) below is the model form. When equation (26) is used for the stress-strain relationship, the one-dimensional scalar equation takes the form of equation (29).

$$\frac{\partial^2 u}{\partial t^2} = V_x^{\,2}\frac{\partial^2 u}{\partial^2 x} \tag{28}$$

$$\frac{\partial^2 u}{\partial t^2} = \left(1+\eta/E\frac{\partial}{\partial t}\right)V_x^{\,2}\frac{\partial^2 u}{\partial^2 x} \tag{29}$$

Here, as before, u is the displacement, E is the elastic modulus, η is the viscoelastic damping coefficient (VDC), and V_x is either the compressional or shear velocity.

3.2.2 Two-Dimensional Kelvin-Voigt Model

The two-dimensional models used for the viscoelastic equations must reduce to the elastic equations (9) and (10) from Chapter II and repeated below when VDC is zero:

$$\frac{\partial^2 v}{\partial t^2} = V_s^2 \frac{\partial^2 v}{\partial x^2} + \left(V_c^2 - V_s^2\right)\frac{\partial^2 u}{\partial x \partial y} + V_c^2 \frac{\partial^2 v}{\partial y^2} \quad , \qquad (9)$$

$$\frac{\partial^2 u}{\partial t^2} = V_c^2 \frac{\partial^2 u}{\partial x^2} + \left(V_c^2 - V_s^2\right)\frac{\partial^2 v}{\partial x \partial y} + V_s^2 \frac{\partial^2 u}{\partial y^2} \quad . \qquad (10)$$

Once again, for the Kelvin-Voigt model the spatial derivative terms in the above EOMs can be modified by $\left(1 + \eta / E \frac{\partial}{\partial t}\right)$ to give the viscoelastic EOMs shown as equations (30) and (31) below. This is comparable to the viscoelastic term used in Blake (1982). You, et al (1991), mentions that the number of viscoelastic constants range from 2 to 21, depending on the degree of anisotropy in the material. You further states "modeling of viscoelastic phenomena is experimentally challenging since such data is not readily available." After some manipulation these equations can be made to agree with the basic viscoelastic models presented in Gaunaurd (1976). My simplifying assumption is that the two viscoelastic damping coefficients modifying the Lamé parameters are equal, while Gaunaurd

(1976) presents the more generalized equations. This simplifying assumption limits ones ability to alter the viscosity in the longitudinal and transverse directions separately.

$$\frac{\partial^2 u}{\partial t^2} = V_c^2 \frac{\partial^2 u}{\partial x^2} + \left(V_c^2 - V_s^2\right)\frac{\partial^2 v}{\partial x \partial y} + V_s^2 \frac{\partial^2 u}{\partial y^2}$$
$$+\eta \frac{\partial}{\partial t}\left\{V_c^2 \frac{\partial^2 u}{\partial x^2} + \left(V_c^2 - V_s^2\right)\frac{\partial^2 v}{\partial x \partial y} + V_s^2 \frac{\partial^2 u}{\partial y^2}\right\} \tag{30}$$

$$\frac{\partial^2 v}{\partial t^2} = V_s^2 \frac{\partial^2 v}{\partial x^2} + \left(V_c^2 - V_s^2\right)\frac{\partial^2 u}{\partial x \partial y} + V_c^2 \frac{\partial^2 v}{\partial y^2}$$
$$+\eta \frac{\partial}{\partial t}\left\{V_s^2 \frac{\partial^2 v}{\partial x^2} + \left(V_c^2 - V_s^2\right)\frac{\partial^2 u}{\partial x \partial y} + V_c^2 \frac{\partial^2 v}{\partial y^2}\right\} \tag{31}$$

In the Kelvin-Voigt EOMs, when the η viscoelastic damping coefficient is set to zero, the elastic EOMs are recovered. The full three-dimensional derivation of the Kelvin-Voigt EOMs can be found in Appendix A. The two-dimensional EOMs are a subset of the three-dimensional EOMs presented in the Appendix.

CHAPTER IV

NUMERICAL MODEL – FINITE DIFFERENCE APPROXIMATION TO THE PARTIAL DIFFERENTIAL EQUATIONS OF MOTION

4.0 Overview

The EOMs from Appendix A for the Kelvin-Voigt model are approximated and replaced by the finite difference formulas used in the numerical model. The boundary conditions will be addressed after the internal body node formulation of the finite difference formulas are presented.

4.1 Body Node Formulation

The EOMs, equation (A12) from Appendix A for the Kelvin-Voigt model were the basis of the body node formulation. However, since they were just a modification to the elastic EOMs, equation (A7) was used to develop the finite difference formulations and then modified again to include the viscoelastic damping coefficient.

The EOM can be represented by simple difference schemes of the appropriate order to ensure stability. The stability and accuracy considerations were addressed in Section 4.2.5. Before equation (A7) was developed into a finite difference formulation, several building blocks were developed to help in the understanding of the formulation. These

modularized building blocks also increased the readability. Even though the formulation was a little longer than those presented elsewhere, the modularized building blocks provide a means of error checking with just a glance. It must be understood that the displacements were functions of the spatial variables and time while they may be shown as functions of fewer variables for clarity in the finite difference formulations. In any of these cases the variables not shown do not change and therefore were not indexed.

Chapter II addressed the basic first derivative finite difference formulation. Section 2.3 presented centered, forward, and backward difference formulas which can easily be extended to the second derivatives (order). Equation (32) presents a second derivative, centered difference formula, where a displacement u can be in any direction and the partial derivative can be spatial or time referenced or both. The Δx must be selected judiciously to provide both stability and accuracy.

$$\frac{\partial^2 u}{\partial x^2} = \frac{u(x+\Delta x)+u(x-\Delta x)-2u(x)}{\Delta x^2} \qquad (32)$$

When one uses arrays or numerical grids to represent the displacement u above, the Δx is just the grid spacing and the $x + \Delta x$ and $x - \Delta x$ terms refer to the next or previous index. One can use different size grid spacing for the different displacements, but here all spatial grid sizes Δx are equal. Another variation of equation (32) shows a second partial derivative with respect to two variables, equation (33), with an incremental step of Δx and Δy. As before, Δx and Δy are equal, but they do not necessarily have to be.

$$\frac{\partial^2 u}{\partial x \partial y} = \frac{u(x+\Delta x, y+\Delta y)+u(x-\Delta x, y-\Delta y)-u(x+\Delta x, y-\Delta y)-u(x-\Delta x, y+\Delta y)}{4\Delta x \Delta y} \quad (33)$$

Unless noted otherwise, the above equations are standard. The terms are chosen in the numerator as being positive or negative based on the relationship between each point and the center reference point u(x,y) and the positive direction of the spatial variables, as shown in the Figure below.

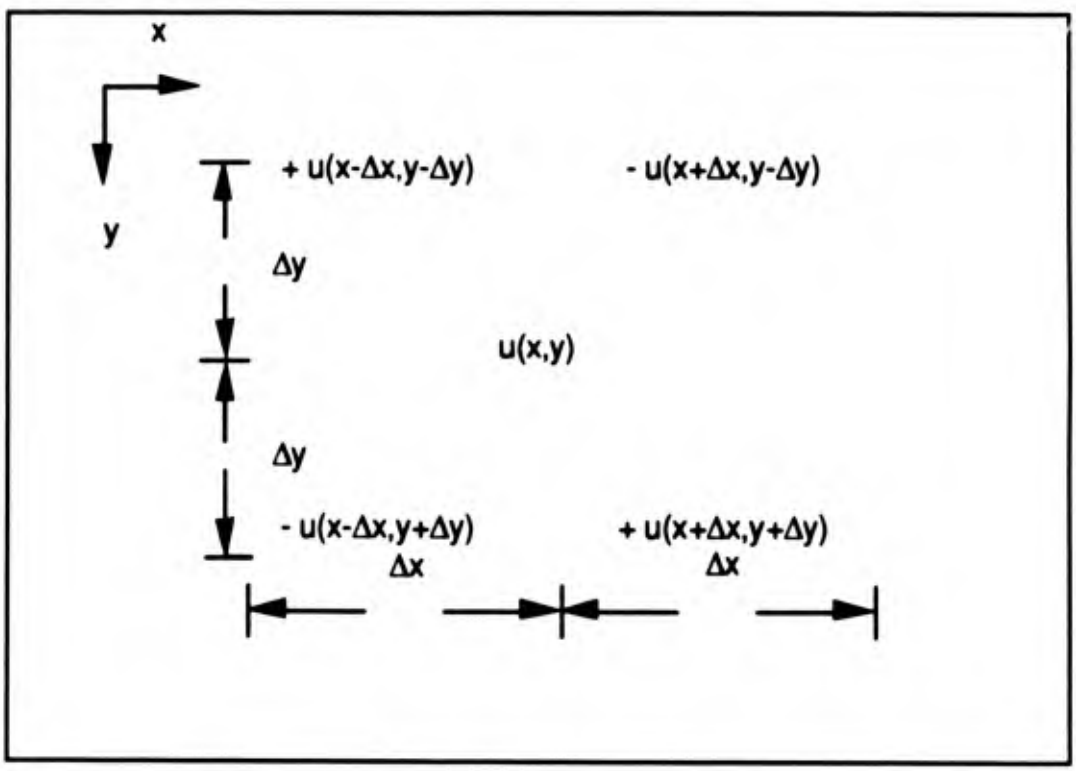

Figure 4.1. Sign Convention for Mixed Derivative Finite Difference Formulations.

The symbol d2x(u) stands for an expression such as the numerator of equation (32). The x and the u may be replaced by any partial derivative or displacement. As an example, the second partial derivative of the

displacement w with respect to the direction y would be d2y(w) and would be the numerator of equation (34). The usefulness of this function is evident when w varies in all spatial directions and time and the partial derivative, as in equation (34), only requires the changes in the y direction.

$$\frac{\partial^2 w}{\partial y^2} = \frac{w(y+\Delta y)+w(y-\Delta y)-2w(y)}{\Delta y^2} \qquad (34)$$

The term d2xy(u) relates to the numerator in equation (33) in the same manner as d2x(u) relates to the numerator of equation (32). Thus, equation (A7) repeated here as equation (35) can be transformed into a finite difference formulation such as equation (36) with Δx as the grid step and Δt as the time step.

$$\rho\frac{\partial^2 u}{\partial t^2} = (\lambda+2\mu)\frac{\partial^2 u}{\partial x^2} + \lambda\frac{\partial^2 v}{\partial x\partial y} + \lambda\frac{\partial^2 w}{\partial x\partial z} + \mu\left(\frac{\partial^2 u}{\partial y^2} + \frac{\partial^2 v}{\partial x\partial y}\right) + \mu\left(\frac{\partial^2 u}{\partial z^2} + \frac{\partial^2 w}{\partial x\partial z}\right) \qquad (35a)$$

$$\rho\frac{\partial^2 v}{\partial t^2} = (\lambda+2\mu)\frac{\partial^2 v}{\partial y^2} + \lambda\frac{\partial^2 u}{\partial x\partial y} + \lambda\frac{\partial^2 w}{\partial y\partial z} + \mu\left(\frac{\partial^2 v}{\partial x^2} + \frac{\partial^2 u}{\partial x\partial y}\right) + \mu\left(\frac{\partial^2 v}{\partial z^2} + \frac{\partial^2 w}{\partial y\partial z}\right) \qquad (35b)$$

$$\rho\frac{\partial^2 w}{\partial t^2} = (\lambda+2\mu)\frac{\partial^2 w}{\partial z^2} + \lambda\frac{\partial^2 v}{\partial y\partial z} + \lambda\frac{\partial^2 u}{\partial x\partial z} + \mu\left(\frac{\partial^2 w}{\partial y^2} + \frac{\partial^2 v}{\partial z\partial y}\right) + \mu\left(\frac{\partial^2 w}{\partial x^2} + \frac{\partial^2 u}{\partial x\partial z}\right) \qquad (35c)$$

$$\frac{\rho d2t(u)}{\Delta t^2} = \frac{1}{\Delta x^2}\left\{\begin{array}{l}(\lambda+2\mu)d2x(u)+\lambda[d2xz(w)+d2xy(v)]/4+\\ \mu[d2y(u)+d2xy(v)/4]+\mu[d2z(u)+d2xz(w)/4]\end{array}\right\} \quad (36a)$$

$$\frac{\rho d2t(v)}{\Delta t^2} = \frac{1}{\Delta x^2}\left\{\begin{array}{l}(\lambda+2\mu)d2y(v)+\lambda[d2xy(u)+d2yz(w)]/4+\\ \mu[d2x(v)+d2xy(u)/4]+\mu[d2z(v)+d2yz(w)/4]\end{array}\right\} \quad (36b)$$

$$\frac{\rho d2t(w)}{\Delta t^2} = \frac{1}{\Delta x^2}\left\{\begin{array}{l}(\lambda+2\mu)d2z(w)+\lambda[d2yz(v)+d2xz(u)]/4+\\ \mu[d2y(w)+d2yz(v)/4]+\mu[d2x(w)+d2xz(u)/4]\end{array}\right\} \quad (36c)$$

The longitudinal velocity (V_c) and the transverse velocity (V_s) are related to the Lamé constants in equations (11) and (12), rewritten below as equations (37) and (38):

$$V_c^2 = (\lambda + 2\mu)/\rho, \quad (37)$$

$$V_s^2 = \mu/\rho. \quad (38)$$

Two additional variables are defined to simplify the EOMs, i.e. rate and max. The rate, found in equation (39), is just the ratio of the transverse to longitudinal wave velocity in the material. The term max, found in equation (40), incorporates the time and space steps with the longitudinal velocity to nondimensionalize the EOMs.

$$\text{rate} = V_s / V_c \quad (39)$$

$$\max = V_c^2\left[\Delta t^2 / \Delta x^2\right] \tag{40}$$

The elastic three-dimensional EOMs (36) can be rewritten, substituting in equations (37)-(40), as equation (41a), (41b), (41c).

$$\begin{aligned} d2t(u) = {} & \max\ d2x(u) + \max\left(1 - rate^2\right)\left[d2xy(v) + d2xz(w)\right]/4 \\ & + \max\ rate^2\left[d2y(u) + d2z(u)\right] \end{aligned} \tag{41a}$$

$$\begin{aligned} d2t(v) = {} & \max\ d2y(v) + \max\left(1 - rate^2\right)\left[d2xy(u) + d2yz(w)\right]/4 \\ & + \max\ rate^2\left[d2x(v) + d2z(v)\right] \end{aligned} \tag{41b}$$

$$\begin{aligned} d2t(w) = {} & \max\ d2z(w) + \max\left(1 - rate^2\right)\left[d2xz(u) + d2yz(v)\right]/4 \\ & + \max\ rate^2\left[d2x(w) + d2y(w)\right] \end{aligned} \tag{41c}$$

In the right hand side of equation (41), the elastic EOMs can be modified by $\left(1 + \eta / E\frac{\partial}{\partial t}\right)$, as in Chapter III, to obtain the viscoelastic Kelvin-Voigt EOMs. Again, the ratio η /E is incorporated in η, the viscoelastic damping coefficient in equation (42a), (42b), (42c).

$$d2t(u) = \max d2x(u) + \max\left(1-\text{rate}^2\right)[d2xy(v)+d2xz(w)]/4$$
$$+\max \text{rate}^2[d2y(u)+d2z(u)]$$
$$+\eta\frac{\partial}{\partial t}\left\{\begin{matrix}\max d2x(u)+\max\left(1-\text{rate}^2\right)[d2xy(v)+d2xz(w)]/4\\ +\max \text{rate}^2[d2y(u)+d2z(u)]\end{matrix}\right\} \quad (42a)$$

$$d2t(v) = \max d2y(v) + \max\left(1-\text{rate}^2\right)[d2xy(u)+d2yz(w)]/4$$
$$+\max \text{rate}^2[d2x(v)+d2z(v)] \quad (42b)$$
$$+\eta\frac{\partial}{\partial t}\left\{\begin{matrix}\max d2y(v)+\max\left(1-\text{rate}^2\right)[d2xy(u)+d2yz(w)]/4\\ +\max \text{rate}^2[d2x(v)+d2z(v)]\end{matrix}\right\}$$

$$d2t(w) = \max d2z(w) + \max\left(1-\text{rate}^2\right)[d2xz(u)+d2yz(v)]/4$$
$$+\max \text{rate}^2[d2x(w)+d2y(w)] \quad (42c)$$
$$+\eta\frac{\partial}{\partial t}\left\{\begin{matrix}\max d2z(w)+\max\left(1-\text{rate}^2\right)[d2xz(u)+d2yz(v)]/4\\ +\max \text{rate}^2[d2x(w)+d2y(w)]\end{matrix}\right\}$$

The term d2t(u) has the next time step embedded in the function. The right hand side of equation (42) relies on the current time-step so the next time-step displacement term in d2t(u) is explicitly determined from the current and previous time step for every point on the grid.

The equations (42a), (42b), (42c) are the body node finite difference formulations which were used in the interior of the grid. The surface grid nodes are discussed in the next Section.

4.2 Free Surface Boundary Conditions

The elastic EOMs were formulated first then the viscoelastic damping coefficient was introduced. The free surface grid points were stress free by definition. The stress tensor components were calculated from equations (43), Mal and Singh (1991). Equation (7), is repeated here for convenience.

$$\sigma_{ij} = \lambda \varepsilon_{kk} + 2\mu \varepsilon_{ij} \tag{43}$$

$$2\varepsilon_{kl} = \frac{\partial u_k}{\partial x_l} + \frac{\partial u_l}{\partial x_k} \tag{7}$$

One free surface, x direction, will be formulated here with the other finite difference formulations found in Appendix B. This formulation follows the new composed method found in Bond (1978), except that it is a three-dimensional development instead of two-dimensional formulation. The grid free surface boundary consists of points on the y-z plane at a value of x, here the grid points surrounding the surface point R.

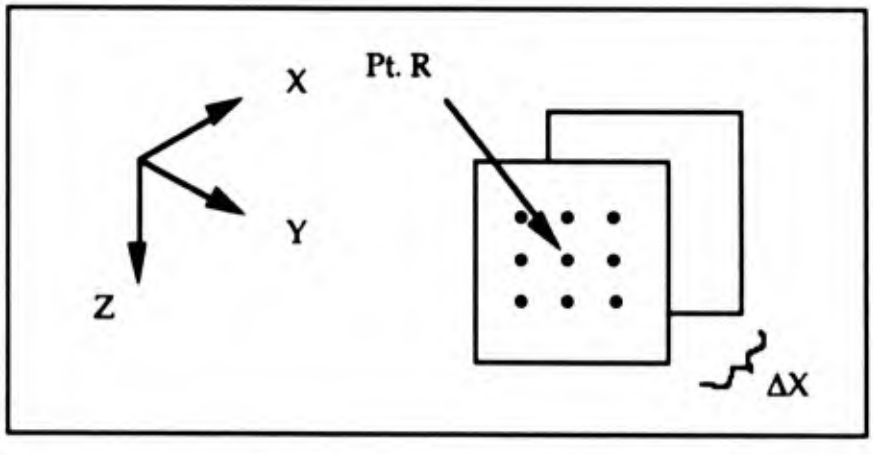

Figure 4.2. Point R on the Free Surface Grid Boundary in the X Direction.

The displacement in the x direction at point R is denoted by u(i,j,k,l), where i, j, k and l are indices of x, y, z and t (time). The current and previous time steps were required to explicitly determine u(i,j,k,l+1).

A Taylor series approximation was used to link the displacement at point R to one grid point below the surface. Note that since R was on the front of the grid, the next point was one Δx away in the positive x direction. The Taylor series approximation, from the Handbook of Engineering Fundamentals, was shown in equation (44).

$$u(i+1,j,k,l) = u(i,j,k,l) + h\frac{\partial u}{\partial x} + \frac{1}{2}h^2\frac{\partial^2 u}{\partial x^2} + O(h^3) \qquad (44)$$

Where third-order terms, $O(h^3)$, were neglected, h was equal to Δx, and the terms $\frac{\partial u}{\partial x}$ and $\frac{\partial^2 u}{\partial x^2}$ were to be replaced by the boundary conditions and EOMs respectively. The boundary condition σ_{xx} equal to zero was the free surface condition and is shown as equation (45). The EOM is equation (35a).

$$\sigma_{xx} = (\lambda + 2\mu)\frac{\partial u}{\partial x} + \lambda\left(\frac{\partial v}{\partial y} + \frac{\partial w}{\partial z}\right) = 0 \qquad (45)$$

$$\rho\frac{\partial^2 u}{\partial t^2} = (\lambda + 2\mu)\frac{\partial^2 u}{\partial x^2} + \lambda\frac{\partial^2 v}{\partial x \partial y} + \lambda\frac{\partial^2 w}{\partial x \partial z} + \mu\left(\frac{\partial^2 u}{\partial y^2} + \frac{\partial^2 v}{\partial x \partial y}\right) + \mu\left(\frac{\partial^2 u}{\partial z^2} + \frac{\partial^2 w}{\partial x \partial z}\right) \qquad (35a)$$

Equation (44) now becomes equation (46).

$$u(i+1,j,k,l) = u(i,j,k,l) + h\left[\frac{-\lambda}{(\lambda+2\mu)}\left(\frac{\partial v}{\partial y}+\frac{\partial w}{\partial z}\right)\right]$$
$$+\frac{1}{2}h^2\left[\frac{1}{(\lambda+2\mu)}\left\{\begin{array}{l}\rho\dfrac{\partial^2 u}{\partial t^2}-\lambda\left(\dfrac{\partial^2 v}{\partial x\partial y}+\dfrac{\partial^2 w}{\partial x\partial z}\right)\\ -\mu\left(\dfrac{\partial^2 u}{\partial^2 y}+\dfrac{\partial^2 v}{\partial x\partial y}+\dfrac{\partial^2 u}{\partial^2 z}+\dfrac{\partial^2 w}{\partial x\partial z}\right)\end{array}\right\}\right] \quad (46)$$

Before equations (24), (32), (33), (37)-(40) were substituted into equation (46), equation (33) was adjusted when applied to partials in the x direction. The adjustment changes the centered difference functions d2xy into quasi-centered difference functions, for the front, dxyf, shown as the numerator equation (47), since there was not a grid point at R - Δx. Thus a new sign convention must be established, for if point R was on the back then there would not be a point at R + Δx and in equation (47) the + Δx's would change to - Δx's, and this function was referred to as dxyb. Likewise, if the partial derivative was for the z direction instead of the y direction, the functions would be dxzf and dxzb, respectively. Further, the y free surface functions refer to left and right whereas the z directions refer to top and bottom.

$$\frac{\partial^2 u}{\partial x\partial y} = \frac{u(x+\Delta x,y+\Delta y)+u(x,y-\Delta y)-u(x+\Delta x,y-\Delta y)-u(x,y+\Delta y)}{2\Delta x\Delta y} \quad (47)$$

With this change equation, (46) can be used with equations (24), (32), (37)-(40), (47) to find the elastic three-dimensional EOMs for the free surface boundary conditions, similar to equation (41) presented as equation (49) with an intermediate result equation (48).

$$\rho\frac{\partial^2 u}{\partial t^2}=\frac{2(\lambda+2\mu)}{h^2}\left(u(i+1,j,k,l)-u(i,j,k,l)\right)+\frac{2\lambda}{h}\left(\frac{\partial v}{\partial y}+\frac{\partial w}{\partial z}\right)$$
$$+\lambda\left(\frac{\partial^2 v}{\partial x\partial y}+\frac{\partial^2 w}{\partial x\partial z}\right)+\mu\left(\frac{\partial^2 u}{\partial^2 y}+\frac{\partial^2 v}{\partial x\partial y}+\frac{\partial^2 u}{\partial^2 z}+\frac{\partial^2 w}{\partial x\partial z}\right) \quad (48)$$

$$\begin{aligned}
&d2t(u)=2\max\left(u(i+1,j,k,l)-u(i,j,k,l)\right)\\
&+\max\left(1-2rate^2\right)\left\{\begin{matrix}\left[v(i,j+1,k,l)-v(i,j-1,k,l)\right]\\+\left[w(i,j,k+1,l)-w(i,j,k-1,l)\right]\end{matrix}\right\}\\
&+\max rate^2\left[d2y(u)+d2z(u)\right]\\
&+\frac{\max}{2}\left(1-rate^2\right)\left[dxyf(v)+dxzf(w)\right]
\end{aligned} \quad (49)$$

The Kelvin-Voigt EOM for the x direction free surface is equation (50).

$$\begin{aligned}
&d2t(u)=2\max\left(u(i+1,j,k,l)-u(i,j,k,l)\right)\\
&+\max\left(1-2rate^2\right)\left\{\begin{matrix}\left[v(i,j+1,k,l)-v(i,j-1,k,l)\right]\\+\left[w(i,j,k+1,l)-w(i,j,k-1,l)\right]\end{matrix}\right\}\\
&+\max rate^2\left[d2y(u)+d2z(u)\right]\\
&+\frac{\max}{2}\left(1-rate^2\right)\left[dxyf(v)+dxzf(w)\right]\\
&+\eta\frac{\partial}{\partial t}\left\{\begin{matrix}2\max\left(u(i+1,j,k,l)-u(i,j,k,l)\right)\\+\max\left(1-2rate^2\right)\left\{\begin{matrix}\left[v(i,j+1,k,l)-v(i,j-1,k,l)\right]\\+\left[w(i,j,k+1,l)-w(i,j,k-1,l)\right]\end{matrix}\right\}\\+\max rate^2\left[d2y(u)+d2z(u)\right]\\+\frac{\max}{2}\left(1-rate^2\right)\left[dxyf(v)+dxzf(w)\right]\end{matrix}\right\}
\end{aligned} \quad (50)$$

The rest of the five free surfaces (back, left, right, top, and bottom) are developed in Appendix B in a similar fashion. The corner points are addressed next.

4.3 Corner Boundary Conditions

The corner node boundary conditions were developed for the two-dimensional case. One corner with two free surfaces follows with the other corners developed in Appendix B. As before, a Taylor series approximation was used in the finite difference formulation, however, this time it was a two variable formulation. In a two-dimensional plane strain formulation there are four corners, as depicted in Figure 4.3. The formulation for point A was developed here.

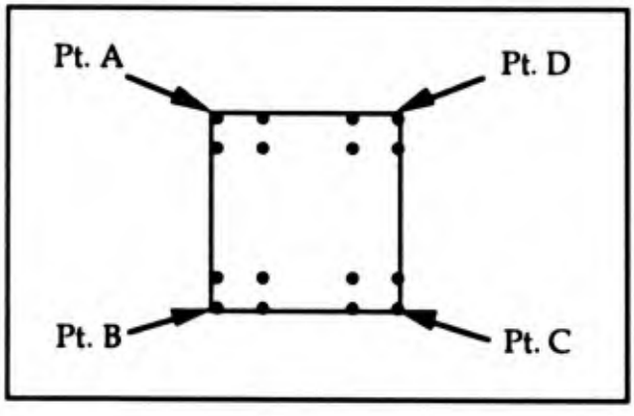

Figure 4.3. Four Corner Points for a Two-Dimensional Grid.

The Taylor series approximation for point A was shown as equation (51).

$$u(i+1,j+1,l)=u(i,j,l)+h\left(\frac{\partial}{\partial x}+\frac{\partial}{\partial y}\right)u(i,j,l)$$
$$+\frac{1}{2}h^2\left(\frac{\partial}{\partial x}+\frac{\partial}{\partial y}\right)^2 u(i,j,l)+O(h^3) \qquad (51)$$

As with the free surface formulation, the first partial derivatives were substituted with the zero normal stress and zero tangential stress equations. This rule was used to avoid ambiguity, when the u displacement was determined the σ_{xx}, equation (45), and σ_{xy} , two-dimensional equation (52) below, are set to zero. When the v displacement was determined, the σ_{yy} and σ_{xy} were set to zero.

$$\sigma_{xy}=\frac{\partial u}{\partial y}+\frac{\partial v}{\partial x}=0 \qquad (52)$$

The three-dimensional EOMs, with all w displacement and z derivative references deleted, were used to substitute for the second partial derivatives. The additional requirement was to use the partial derivative of σ_{xy} with respect to the y direction for the u displacement formulation and vice versa for the v displacement, to accommodate the second partial derivative with respect to y in the EOM and replace it by the cross derivative. Finally, the cross derivative in the last term of equation (51) requires the finite difference formulation in equation (33) to be modified again. This time the four points used for the cross derivative are just the corner point and the surrounding three points, as shown in Figure 4.3, the sign convention still holds for positive and negative terms inside the function. An interim result is shown in equation (53) with the finite difference formulation shown in equation (54).

$$\rho\frac{\partial^2 u}{\partial t^2} = 2(\lambda+\mu)\frac{\partial^2 v}{\partial x \partial y} - 2(\lambda+2\mu)\frac{\partial^2 u}{\partial x \partial y}$$
$$+\frac{2(\lambda+2\mu)}{h^2}\left(u(i+1,j+1,l) - u(i,j,l)\right) \qquad (53)$$
$$-\frac{2(\lambda+2\mu)}{h}\left(\frac{\partial u}{\partial x}+\frac{\partial u}{\partial y}\right)$$

$$d2t(u) = 2\max\left(1-\text{rate}^2\right)\begin{Bmatrix} v(i+1,j+1,l)+v(i,j,l) \\ -v(i+1,j,l)-v(i,j+1,l) \end{Bmatrix} \qquad (54)$$

Notice that all the spatial difference formulas for the u displacement canceled out in equation (54). Thus, the future u displacement was affected by the current v displacement in the points surrounding the corner. The Kelvin-Voigt finite difference formulas was shown as equations (55).

$$d2t(u) = 2\max\left(1-\text{rate}^2\right)\begin{Bmatrix} v(i+1,j+1,l)+v(i,j,l) \\ -v(i+1,j,l)-v(i,j+1,l) \end{Bmatrix}$$
$$+\eta\frac{\partial}{\partial t}\left[2\max\left(1-\text{rate}^2\right)\begin{Bmatrix} v(i+1,j+1,l)+v(i,j,l) \\ -v(i+1,j,l)-v(i,j+1,l) \end{Bmatrix}\right] \qquad (55)$$

Corner boundary conditions were also used with mirror conditions as well as free surface formulations in the numerical simulations. Instead of using equation (51), equations (56) and (57) were used in the body node formulation for point A. The grid starts at point A, (1,1) but if there was a grid point to the left of point A designated (0,1), the values of the displacements u and v would be determined from equations (56) and (57). The same equations could be used on the sides of the grid, defined as lines

AB, AD, DC, and CB from Figure 4.3. This allows the finite grid boundaries to represent a greater region than the free surface boundary condition. The problem of artificial boundary reflections must be taken into account, however this has not caused a problem in the numerical simulations.

$$u(0,1) = u(2,1) \tag{56}$$

$$v(0,1) = -v(2,1) \tag{57}$$

The points surrounding point A that are not in the grid, imaginary points, would be replaced with like relationships as at point (0,1). Instead of equation (55) the point A formulation for the u displacement was equation (58)

$$\begin{aligned} d2t(u) &= 2\max\left(u(i+1,j,l)-u(i,j,l)\right) \\ &+2\max\ rate^2\left(u(i,j+1,l)-u(i,j,l)\right) \\ &+\max\left(1-rate^2\right)\begin{Bmatrix} v(i+1,j+1,l)+v(i,j,l) \\ -v(i+1,j,l)-v(i,j+1,l) \end{Bmatrix} \\ &+\eta\frac{\partial}{\partial t}\begin{bmatrix} 2\max\left(u(i+1,j,l)-u(i,j,l)\right) \\ +2\max\ rate^2\left(u(i,j+1,l)-u(i,j,l)\right) \\ +\max\left(1-rate^2\right)\begin{Bmatrix} v(i+1,j+1,l)+v(i,j,l) \\ -v(i+1,j,l)-v(i,j+1,l) \end{Bmatrix} \end{bmatrix} \end{aligned} \tag{58}$$

As stated previously, the formulation for points A-D, v displacement and the rest of the u displacement finite difference equations were developed in Appendix B.

4.4 Voids

Void inclusions were modeled as internal free surfaces, i.e. the shape of the void was modeled by geometric configurations in the coordinate system and the finite difference formulas mimic those. Therefore the finite difference formulation in Section 4.2 applies here. When one uses Cartesian coordinates, squares can be used to build various shapes of voids. In the two-dimensional formulation, the corner boundary conditions of Section 4.3 apply, but the need arises for a 270 degree corner finite difference formulation which follows.

Figure 4.4 depicts a 270 degree corner, which was similar to the 90 degree corner except now there are seven points surrounding the center point instead of just three. All seven of these points were included in the cross derivative term in the equation of motion.

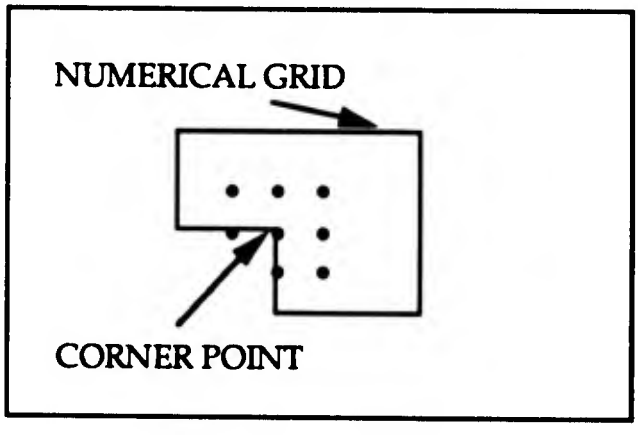

Figure 4.4 A 270 Degree Corner for a Two-Dimensional Grid.

The finite difference formulation starts out the same way as the previous section and equation (51) and (53) apply. Equation (53) was

repeated below, however as stated above, the cross derivative term has a form other than the one used in Section 4.3.

$$\rho\frac{\partial^2 u}{\partial t^2} = 2(\lambda+\mu)\frac{\partial^2 v}{\partial x\partial y} - 2(\lambda+2\mu)\frac{\partial^2 u}{\partial x\partial y}$$
$$+\frac{2(\lambda+2\mu)}{h^2}\left(u(i+1,j+1,l)-u(i,j,l)\right) \qquad (53)$$
$$-\frac{2(\lambda+2\mu)}{h}\left(\frac{\partial u}{\partial x}+\frac{\partial u}{\partial y}\right)$$

The cross derivative form used in this formulation was taken from Bond (1978) equation F.2.1, shown as equation (59).

$$\frac{\partial^2 u}{\partial x\partial y} = \frac{1}{4h^2}\begin{bmatrix} 2u(i+1,j+1,l)-u(i,j+1,l)-u(i+1,j-1,l) \\ +u(i,j-1,l)-u(i+1,j,l)-u(i-1,j+1,l)+u(i-1,j,l)\end{bmatrix} \qquad (59)$$

The elastic two-dimensional finite difference formulation for the 270 degree corner was presented as equation (61) with an interim result shown as equation (60). The Kelvin-Voigt formulations are presented as equations (62).

$$d2t(u) = 2\max\left(1-rate^2\right)\begin{Bmatrix} v(i+1,j+1,l)+v(i,j,l) \\ -v(i+1,j,l)-v(i,j+1,l)\end{Bmatrix}$$
$$-\frac{\max}{2}\begin{bmatrix} 2u(i+1,j+1,l)-u(i,j+1,l)-u(i+1,j-1,l) \\ +u(i,j-1,l)-u(i+1,j,l)-u(i-1,j+1,l)+u(i-1,j,l)\end{bmatrix} \qquad (60)$$
$$+2\max\left(u(i+1,j+1,l)-u(i,j,l)\right)$$
$$-2\max\left[u(i+1,j,l)-u(i,j,l)+u(i,j+1,l)-u(i,j,l)\right]$$

$$d2t(u) = 2\max\left(1-\text{rate}^2\right)\left\{\begin{matrix} v(i+1,j+1,l)+v(i,j,l) \\ -v(i+1,j,l)-v(i,j+1,l)\end{matrix}\right\}$$
$$-\frac{\max}{2}\left[\begin{matrix} -2u(i+1,j+1,l)-u(i,j+1,l)-u(i+1,j-1,l)-4u(i,j,l) \\ +u(i\ j-1,l)+3u(i+1,j,l)-u(i-1,j+1,l)+u(i-1,j,l)\end{matrix}\right] \quad (61)$$

$$d2t(u) = 2\max\left(1-\text{rate}^2\right)\left\{\begin{matrix} v(i+1,j+1,l)+v(i,j,l) \\ -v(i+1,j,l)-v(i,j+1,l)\end{matrix}\right\}$$
$$-\frac{\max}{2}\left[\begin{matrix} -2u(i+1,j+1,l)-u(i,j+1,l)-u(i+1,j-1,l)-4u(i,j,l) \\ +u(i,j-1,l)+3u(i+1,j,l)-u(i-1,j+1,l)+u(i-1,j,l)\end{matrix}\right]$$
$$+\eta\frac{\partial}{\partial t}\left\{\begin{matrix} 2\max\left(1-\text{rate}^2\right)\left\{\begin{matrix} v(i+1,j+1,l)+v(i,j,l) \\ -v(i+1,j,l)-v(i,j+1,l)\end{matrix}\right\} \\ -\frac{\max}{2}\left[\begin{matrix} -2u(i+1,j+1,l)-u(i,j+1,l)-u(i+1,j-1,l)-4u(i,j,l) \\ +u(i,j-1,l)+3u(i+1,j,l)-u(i-1,j+1,l)+u(i-1,j,l)\end{matrix}\right]\end{matrix}\right\} \quad (62)$$

The body node formulations, equations (44a) - (44c), were also used in place of equation (62) with stable results however any grid point that was inside the void must stay with zero displacement. This concludes the development of the finite difference formulations.

The next two Sections, 4.5 Stability and Accuracy, and 4.6 Input Sources for the Numerical Model, are directly related to the finite difference formulations. The numerical grid size affects the accuracy of the finite difference formulations. The discontinuities of the input source (off - on - off), as well as the grid size, contribute to the stability of the numerical model. Therefore, both discussion are included in Chapter IV, and are presented next.

4.5 Stability and Accuracy

Smith (1985) in the Section, HYPERBOLIC EQUATIONS AND CHARACTERISTICS, discusses the Courant-Friedrichs-Lewy (C.F.L.) condition and explicit methods of finite difference formulations on rectangular grids. He states "This C.F.L condition for convergence is usually expressed by saying that the numerical domain of dependence of the difference equation must include the domain of dependence of the differential equation." Bond (1978) states the same information in a slightly more understandable way, "a practical limit that must always be observed is that information must be able to propagate across the grid faster than the highest wave velocity." Both authors conclude that the change in the numerical grid, as referred to by the ratio of the time step to grid spacing, should be bounded by the speed of information transfer in the differential equation, referred to as the transverse and longitudinal wave speeds. Bond (1978) refers to a von Neumann stability limit shown as equation (63).

$$\frac{\Delta t}{\Delta x} \leq \frac{1}{\sqrt{V_c^2 + V_s^2}} \qquad (63)$$

Aki and Richards (1980) refer to equation (63) as a stability condition for the finite difference formulation, whereas Bond (1978) suggested that using up to 90% of this limit will still give accurate results. Ilan and Weight (1990), experimentally determined that a limit of 90% of the value from equation (63) would still give stability on a finite grid with cylindrical coordinates. Press, et al (1989) refers to equation (63) as "the famous

Courant-Friedrichs-Lewy stability criterion, often simply called the Courant condition." They further state that when using a method that was first-order accurate in time but second-order accurate in space, a value of no more than 20% of equation (63) may be used to obtain desired accuracy. The numerical model described in this chapter was second-order accurate in time, however Press, et al (1989) was referenced to show that the Courant condition may not always be the limiting value for stability and accuracy. Accuracy was also affected by the number of grid points that are equal to one wavelength. The wavelength was determined from the velocity of propagation and the frequency of the input source, or frequencies from a broad band source. Since this material acts in a dispersive manner, i.e., the higher frequencies travel at higher velocities, it was necessary that all frequencies have at least 10 nodes, or grid points, per wavelength to avoid aliasing, inaccuracies, and instability (Thomson, 1988). Craig (1981) also recommends 10 nodes per wavelength when he used the rule of thumb that Δt should satisfy $\Delta t \leq T/10$ where T was the smallest period in the excitation (highest frequency) and one considers equation (63). In the elastic case Bond (1978) determined that using 35 nodes per wavelength was necessary for the pulses to propagate without distortion. Alterman and Leowenthal (1972) concluded that, for the accuracy they required in their studies, waves close to the source required seven times more nodes per wavelength than those farther away from the source.

The variable vonN a multiplier to equation (63), was used to take into account when a fraction of the von Neumann limit was needed. Equation (63) was rearranged to show the dependence of the time step, Δt, on vonN, as shown in equation (64).

$$\Delta t \leq \frac{\text{vonN } \Delta x}{\sqrt{V_c^2 + V_s^2}} \qquad (64)$$

There was a requirement for a tradeoff between the time step and the grid spacing to maintain the stability and accuracy of the numerical model. The grid spacing, Δx, was determined by multiplying the wavelength associated with the longitudinal velocity, V_c, by the nodes per wavelength chosen for stability. Therefore the time step, Δt, can be held constant if the ratio between vonN and the nodes per wavelength was maintained. Stated differently, for a fixed number of grid points, the grid can equate to several arbitrary sample sizes based on the number of nodes per wavelength chosen, and the time step can remain the same for each sample size. Since the number of iterations used during a test of the numerical model depends on the duration necessary for the propagation of the waveforms and the time step, reducing the number of iterations and thereby limiting the numerical dispersion in the numerical model requires controlling either the duration of the test or the time step. Although the test specimen were chosen by the author based on several factors, they are of fixed dimensions and therefore waveforms require a fixed amount of time to propagate through them, thus dictating the test duration of any numerical simulation. The only factor available to reduce the iterations of the numerical simulations, and associated numerical dispersion, was therefore the time step. However, this assumed the grid spacing, Δx, did not cause any problems, which was not the case.

Once the grid spacing was determined and hence the time step was chosen to reduce the number of iterations, the problem of numerical

instability in the numerical simulation occurs due to the "nodes per wavelength" value chosen. The nodes per wavelength value chosen in the above relates the longitudinal velocity related wavelength λ_l and the grid spacing. During the numerical simulation, the highest frequencies propagating at the slowest velocities will have the smallest wavelength, denoted λ_s. Once the test was started and the grid size was fixed, the numerical stability of the numerical model was dependent on the nodes per wavelength for λ_s not λ_l, and this was where the problem rested. In order to have an appropriate nodes per wavelength for λ_s the value used for the nodes per wavelength for λ_l must be increased, which decreases the time step, and hence increases the number of iterations used in the test. Therein lies the tradeoff. As a side note, the computation time was very much affected by the time step and number of iterations, while the size of the memory required for the computations was dictated by the grid size; this in itself presents some more considerations for the tradeoff. A preliminary study of the elastic numerical model determined how the above were chosen.

4.6 Input Source for the Numerical Model

The original goal for modeling an input source was to mimic the actual transducer source used in the experiments. A smooth start and finish, narrow frequency band, and short duration were characteristics that were specified for the numerical model input pulse . This goal was tempered by the fidelity of the model to withstand high frequency inputs. A stable finite difference scheme was required if any results were to be

useful. Several source inputs were tried before the final choice was made. The sources presented below are a computer generated discrete inverse FFT source, a Gaussian inverse FFT and modified versions, and finally the chosen Ricker pulse.

4.6.1 Computer-Generated Discrete Inverse FFT Source

With the use of the transducer excitation pulse discarded as an input to the numerical simulation because of the requirements outlined in Section 4.6, the choice of a single cycle of the excitation frequency was used. This single cycle of the drive frequency is the multiplication of the continuous sine or cosine wave with a gating function. The information concerning the Fourier Transform, its applications, and properties are taken from Stremler (1982). The Fourier transform of this modulation is the convolution of the two signals and results in the frequency spectrum of the gated signal displaced on the frequency axis by plus and minus the drive frequency. It also results in some component of all frequencies being introduced as part of the source. Therefore, the high frequencies causing instability in the numerical grid are included in the source and cause accuracy problems. To counteract the introduction of unwanted frequencies, the author used an algorithm for the inverse FFT from Press, et al (1989), with the desired frequencies chosen, and obtained a discrete time series signal as an input source for the numerical model. This method exhibited varying degrees of success. Figure 4.5 is an example of a signal time series that was the result of using a mixed frequency signal, centered around 50 kHz, used as input for an inverse FFT. The time steps

are a function of the frequency steps and the number of points used in the inverse FFT. In this case, 512 points were used at frequency intervals of 500 Hz.

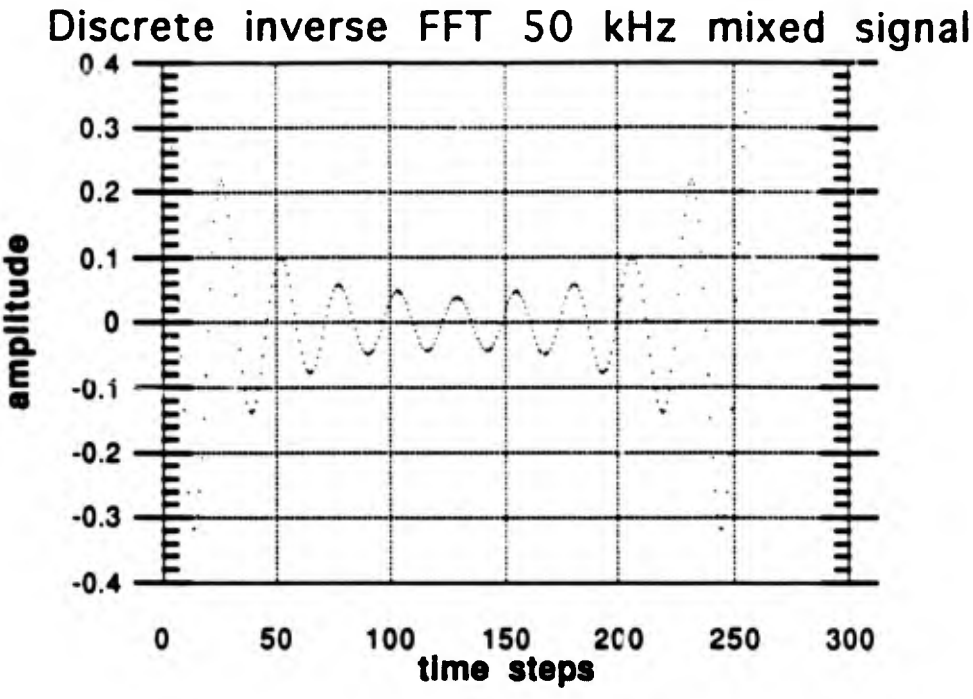

Figure 4.5. Computer-Generated Signal Time Series from Inverse FFT with Discrete Frequency Inputs.

This signal was rejected because of its sharp start and stop. The next signal tried was a Gaussian, because it is its own Fourier transform.

4.6.2 Gaussian Inverse FFT Source

A large portion of the frequency content of the Gaussian signal could be limited to a small area. The numbers in parenthesis after

Gaussian are the mean and standard deviation used to construct a time series signal. A 90 degree phase shift was used to obtain a signal that started from zero. The +/- mean on the frequency axis was used to produce a pure real time signal. Figure 4.6 is a typical signal used, again without much success. The numerical distortion caused by the lack of a smooth beginning led to the use of an exponential rise blending to the Gaussian shown in Figure 4.7

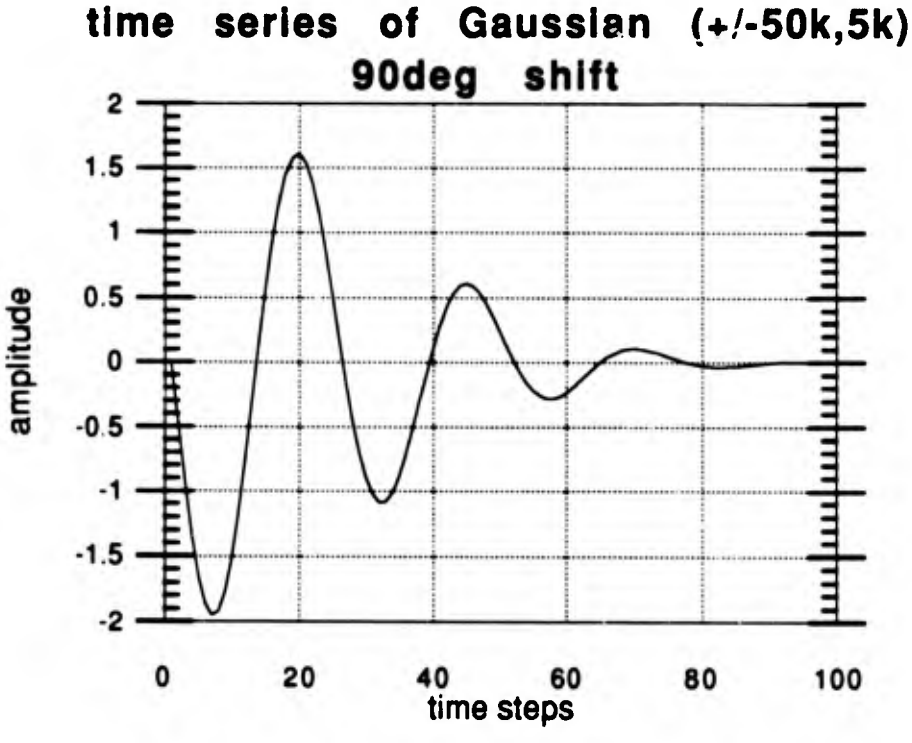

Figure 4.6. Computer-Generated Signal Time Series from Inverse FFT with Discrete Gaussian Frequency Inputs.

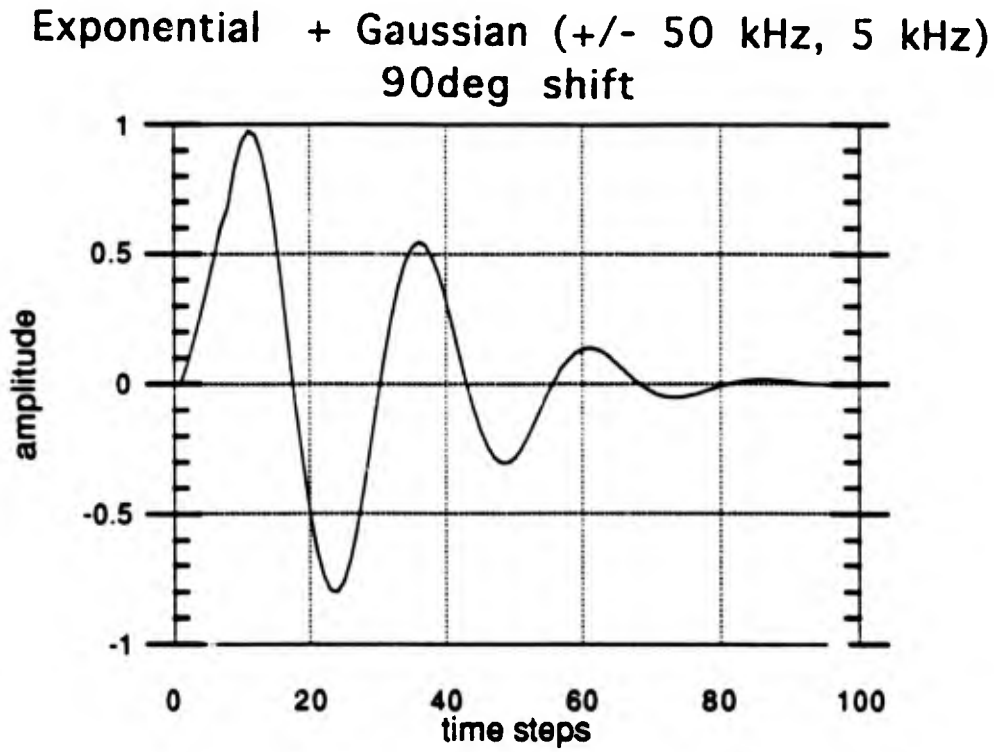

Figure 4.7 Exponential Blended with a Computer-Generated Signal Time Series from Inverse FFT with Discrete Gaussian Frequency Inputs.

This last signal was similar to the one shown in Cavicchi (1990), however, it did not meet with success here. The next and current signal used as a source input for the numerical model is the Ricker pulse.

4.6.3 Ricker Pulse

Boore (1972) used the Ricker pulse with much success. The Ricker pulse, shown in Figure 4.8 below, is explained in Ricker (1977) and his previous works. This analytic expression, represented as R in equation (65), has almost all of the frequency spectrum content within three times the peak frequency, f in equation (67), as shown in Figure 4.9. The term b

in equation (66) is the peak-to-peak displacement in seconds of the two humps in the Ricker pulse, with t as time.

$$R = \left(\frac{u^2}{4} - \frac{1}{2}\right)\frac{\sqrt{\pi}}{2}\exp\left(-\frac{u^2}{4}\right) \tag{65}$$

$$u = \frac{2\sqrt{6}}{b}t \tag{66}$$

$$f = \frac{\sqrt{6}}{\pi}\frac{1}{b} \tag{67}$$

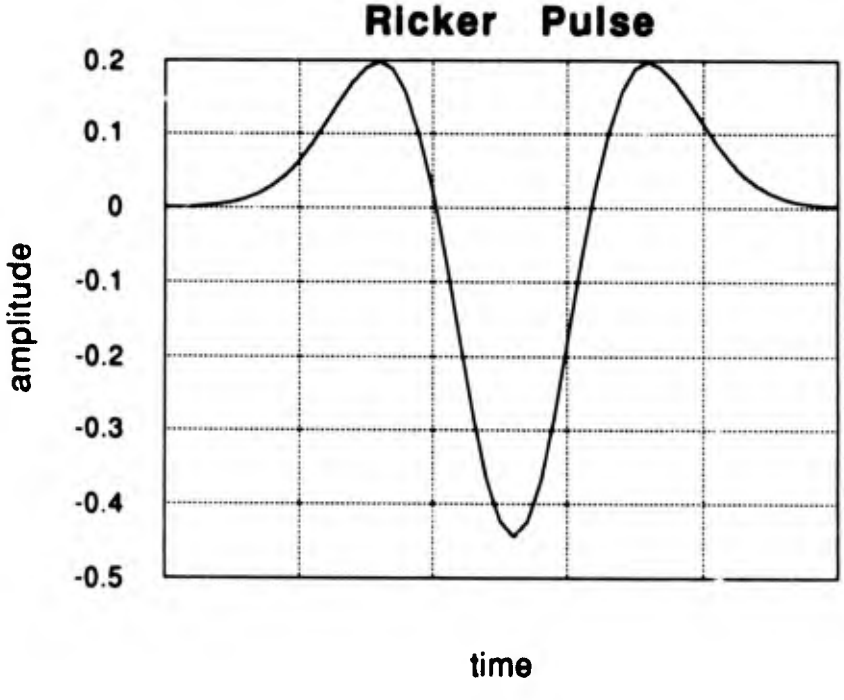

Figure 4.8. Ricker Pulse. (Zero time starts at the bottom of the pulse.)

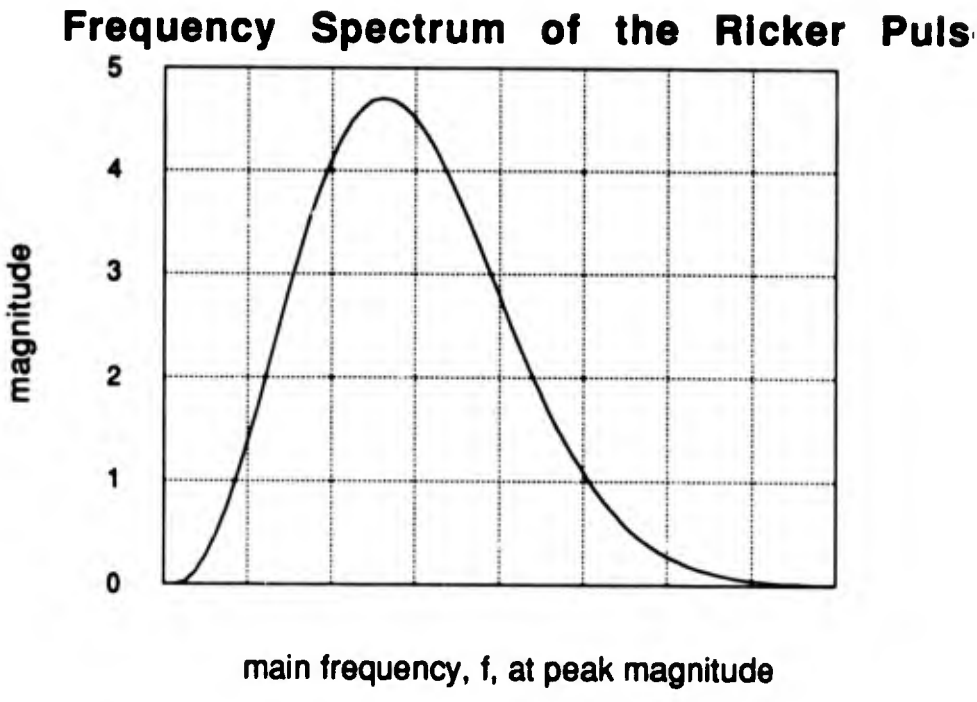

Figure 4.9. Spectrum of Signal Time Series Ricker Pulse.

The Ricker pulse provides a nearly distortionless numerical wave for use as a source input. The viscoelastic effects of the solid rocket motor propellant can now be observed in the model. The experimental data that the model simulates follows in Chapter V

CHAPTER V

EXPERIMENT MEASUREMENTS

5.0 Overview

The previous chapter developed the finite difference formulation, including the estimation method for the viscoelastic damping coefficient. Numerical calculations using this formulation will be compared in the next chapter with the experimental results herein. In this chapter the experimental tests are explained and results presented. First the limitations on experimentation are discussed, resulting in the goal to fully characterize the SRM propellant at 50 kHz without considering temperature effects. A schematic of the test setup as well as a Table with a typical equipment list follows. The data on the attenuation versus frequency, and the phase velocity versus frequency, in the parent material without inclusions in the SRM propellant are discussed next. The resultant viscoelastic damping coefficient, which will be used to tune the numerical simulations, and the uncertainty in the data are followed by experimental results with inclusions (a spongy paddle ball and a ping pong ball) in the SRM propellant.

5.1 Limitations on Experimentation

The tradeoff between resolution and penetration, as it influences frequency selection, was critical when the experiments were designed. As mentioned in Chapter I, Djordjevic (1990) reported a received signal with a 60 db signal to noise ratio when using a 50 kHz transducer during ultrasonic testing on a SRM segment. Higher frequencies have an even higher attenuation in SRM propellant and therefore would have less, if any, signal at the receive transducer. Deeper signal penetration in SRM propellant can be achieved with lower frequencies. However, the 50 kHz frequency has a wavelength, λ, of 3.2 cm in the SRM propellant . Resolution of inclusions in the SRM propellant was the reason for using the ultrasonic NDE. The critical flaw size, d, of a single void, 2.5 cm, is smaller than this wavelength resulting in a ratio d/λ of 80%. Any lower frequency would have a larger wavelength and a corresponding lower ratio. The higher the ratio, the easier it is to detect scattering and hence flaws. These conflicting influences, i.e., lower frequency giving more penetration, higher frequency giving more resolution were reconciled with a choice of 50 kHz as the investigating frequency.

Further, the ultrasonic NDE can measure only velocity and amplitude attenuation of a signal time series using a through-transmission technique. The first arrival of excitation in the received signal when compared to the transmitted signal is called the time-of-flight, and when divided into the distance traveled gives the group velocity. The maximum amplitude difference of the signal time series, positive minus negative, gives a peak-to-peak range, which, when compared to the transmitted signal, gives amplitude attenuation. This can be normalized

by the distance traveled to give db/cm. The same signal time series can provide additional information by means of spectrum analysis in the frequency domain with the use of a Discrete Fourier Transform (DFT). In the frequency domain information, the phase versus frequency plot can provide a velocity profile when the phase of the transmitted signal is known. The magnitude versus frequency, when compared to the transmitted wave's magnitude versus frequency, provides an attenuation versus frequency profile. The goal of the experimentation was to fully characterize the SRM propellant at 50 kHz. However, since the ultrasonic NDE method will be used as a flaw detector and will be applied immediately after casting at room temperature, this investigation does not consider temperature effects, although it is known that material properties change with temperature. All the data are presented in Appendix C.

5.2 Experiment Test Setup

For this research effort four samples were tested. Three samples were from the same casting, number 3323-2, and were identified as no inclusion, Paddle Ball, and Ping Pong Ball. A Paddle ball is slightly larger than a Ping Pong Ball, but is rubbery and smooth in texture. The last sample was from casting number 3323-1, and it also had no inclusion. The Ping Pong Ball was used because it is the same as the critical flaw size. The Paddle Ball was used, even though it was slightly larger then the Ping Pong Ball, because it was made of a more compliant material than the Ping Pong Ball and closer resembled a void in the SRM propellant.

The samples were cast in May, 1992, by Atlantic Research Corporation, in Gainesville, Va., under a NASA Marshall Space Flight Center program called Solid Propulsion Integrity Program, Bondlines Work Package (Contract # NAS 8-37802). Three sets of tests were conducted. The first, Test 1, was performed during the author's visit to Martin Marietta Laboratories, Baltimore MD (MMLB) in October, 1992. Test 2 occurred in November, 1992, and Test 3 in April, 1993. Each test session had specific goals. The experiments were conducted at MMLB by Mr. William Ferrell, but with the author's guidelines, under the direction of Dr. B. Boro Djordjevic Sensor/NDE Department Head and Mr. Michael Rooney, Program Technical Director.

In Test 1, 78 tests were conducted, one test through each dimension of the four samples (12) and a transducer-transducer test, at five different frequencies (drive signal of 30, 40, 50, 65 kHz, using a 50 kHz transducer, and a 100 kHz drive signal for the 100 kHz transducer). The drive signal frequency was a gated tone burst of three cycles. The last set of 13 tests was conducted with a single cycle 50 kHz drive signal using the 50 kHz transducer. A DFT was taken on each test signal time series providing a magnitude and phase versus frequency plot.

Test 2, taken in November 1992, tested sample 3323-2 no inclusion, at four additional frequencies 150, 200, 300, and 500 kHz. The final test, Test 3, again focused on sample 3323-2 no inclusion, but repeatability was investigated. Six and ten cycle tone bursts at two different drive signal frequencies (30 and 65 kHz), with a 50 kHz transducer, were used in 80 tests. A generic schematic of the test setup is provided in the Figure 5.1. Table 5.1 shows the equipment used in a typical ultrasonic NDE on the SRM propellant specimen.

A robot positioned two 50 kHz transducers on opposite sides of the sample. Sonotrace 40 ultrasonic couplant was used between the transducer and the elastomer, keeping the sample in dry contact with the elastomer. The pulse generator sent a gated signal to the sweep generator, the ultrasonic flaw detector system (UFDS), and the waveform analyzer. The sweep generator sent the tone burst signal to the waveform analyzer and to the transmit transducer (excitation), which propagated through the sample and was recorded by the receive transducer (time series signal). The received transducer signal was amplified 30 db by the linear amplifier, sent to the UFDS and then to the waveform analyzer (time series signal captured and analyzed). Input maximum voltage was 30 volts.

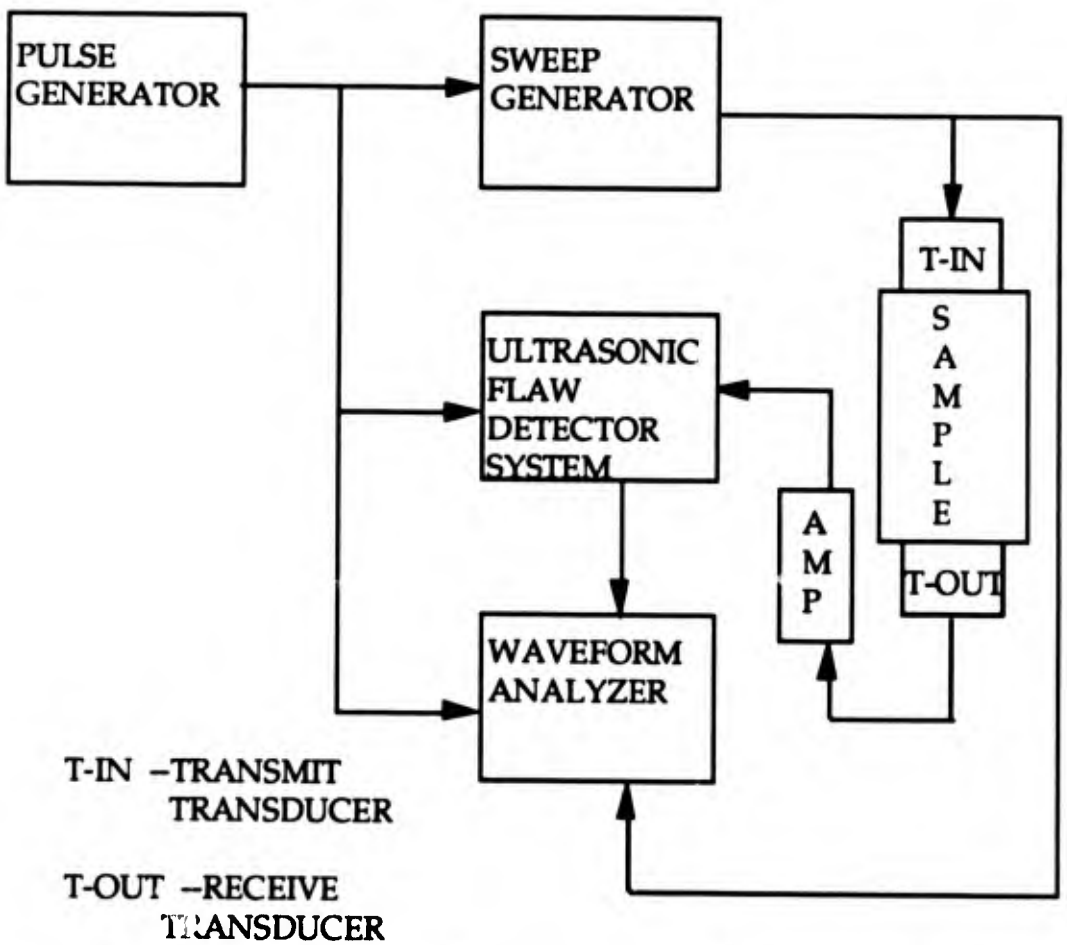

Figure 5.1. Schematic of Ultrasonic NDE on SRM Setup at Martin Marietta Laboratories, Baltimore.

Table 5.1. Equipment used in a Typical Test Setup, with Output Identified.

Box identifier	Equipment	Output
Pulse Generator	HP 8111A	Gated Pulse to Sweep Generator
Sweep Generator	Wavetek 164	3 cycle 50 kHz drive signal
T-In	Matched pair - 50 kHz	Excitation
Sample	3323-2 no inclusion	propagated ultrasonic wave
T-Out	Matched pair - 50 kHz	signal time series
Amp	Pacific 2A35 linear amplifier	combined with UFDS
Ultrasonic Flaw Detection System (UFDS)	Sonotest Master Scan 320	used to increase signal voltage by 30 db
Waveform Analyzer	Data Precision 6100	8 bit digitizer signal time series and DFT

The robot was programmed to apply a constant force between 57 +/- 1 N to the inert propellant. This was to ensure that the transducer/sample contact was the same for each test. It also ensured that the couplant layer thickness was similar for each test. The sweep generator was gated to transmit a burst of between one and ten wavelengths at the frequencies of interest. The received signal was recorded and then analyzed by means of a DFT.

5.3 Experiment Data

As stated in Section 5.2, Test 1 consisted of 78 tests which used both a 50 kHz transducer matched pair and a 100 kHz transducer matched pair to record through-transmission signals on four inert propellant samples: identified as 3323-2 no inclusion, 3323-2 with Paddle Ball, 3323-2 with Ping Pong Ball, and 3323-1 no inclusion. Figure 5.2 shows the dimensions through which the tests were conducted for sample 3323-2 no inclusion. The dimensions of the samples, as well as the labels used to identify the dimensions in all tests, are found in the Table 5.2.

Each individual test was referred to by the letter label corresponding to the sample dimension found in Table 5.2, which was the through-transmission dimension, and the frequency of the drive signal used for the tone burst, see Table 5.3.

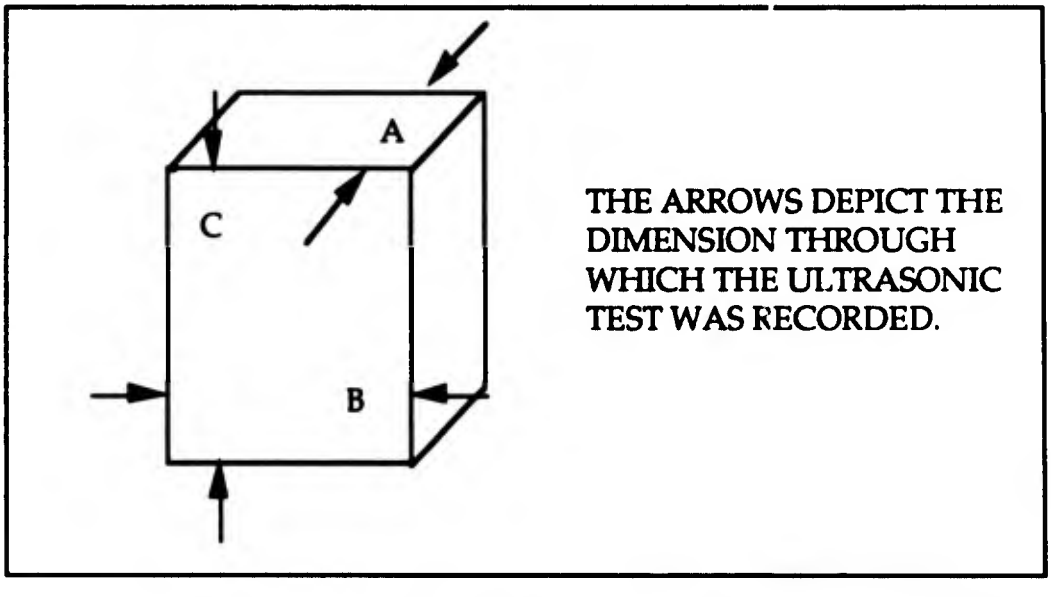

Figure 5.2. Graphic Representation of the Labels and Dimensions of Sample 3323-2 No Inclusion During Ultrasonic NDE.

Table 5.2. Sample Dimensions and Labels that Coincide with each Tests.

Test Sample	Label	Thickness cm +/- 0.01	Label	Width cm +/- 0.01	Label	Length cm +/- 0.01
3323-2 no inclusion	A	8.50	B	11.35	C	13.10
3323-1 no inclusion	D	7.33	E	7.39	F	11.10
3323-2 Paddle Ball	G	8.26	H	11.24	IC*	12.11
					IF*	
3323-2 Ping Pong Ball	J	8.38	K	11.68	LC*	13.21
					LF*	

* Refers to whether the off-center inclusion is Closer to the transmit transducer than the receive transducer or Farther from the transmit transducer than the receive transducer.

Table 5.3. Test 1 Key, Identifiers used in Tables and Figures.

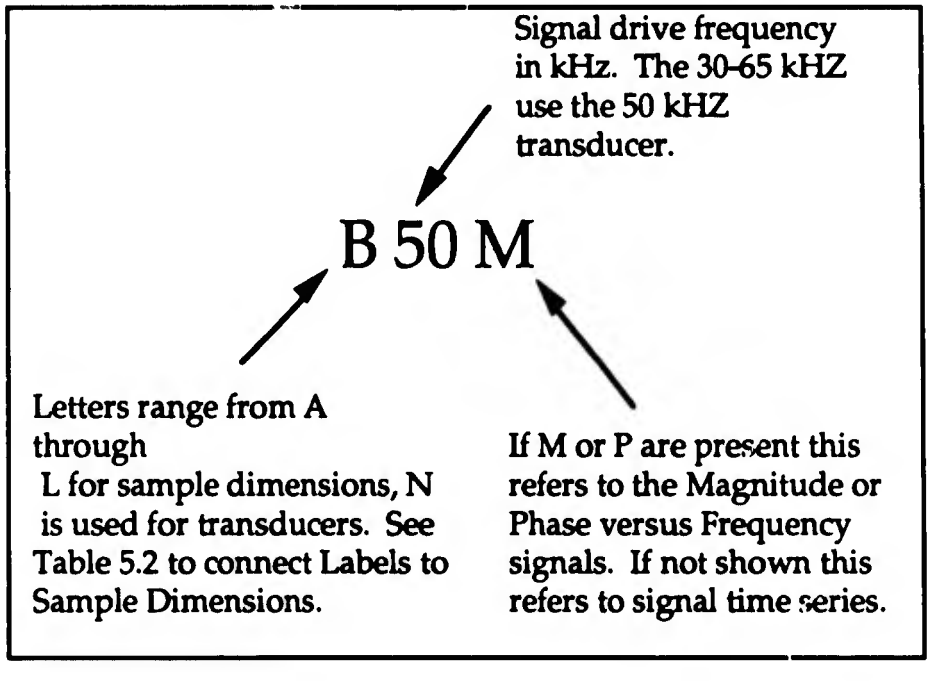

The Paddle Ball, in the IC test, is located roughly 4 cm down the G dimension, 5 cm down the H dimension, and 4.3 cm down the I dimension. The Ping Pong Ball in the LC test, is located roughly 4.2 cm down the J dimension, 6 cm down the K dimension, and 5 cm down the L dimension.

For example, the A50 test was a three cycle tone burst gating a 50 kHz drive signal through the smallest dimension of the inert sample 3323-2, no inclusion. When the time signal A50 was analyzed by the DFT, a magnitude versus frequency, A50M, and a phase versus frequency, A50P, signal were produced and referred to as such. The transducer-transducer signals without a sample between the transducers are identified with the label N. The last dimension in the sample with the paddle ball and the ping pong ball both have two labels due to the fact that the inclusion was offset from the centroid in this axis allowing the inclusion to be measured C, close to the transmit transducer, and measured F, far from the transmit transducer and labeled as such.

The time series signals of a few of the tests are shown in Section 5.3.1 with the remainder presented in Appendix C. The peak-to-peak amplitudes are compared to determine attenuation. The DFT magnitude and phase plots are presented in Section 5.3.2, with the bulk of the data found in Appendix C. The phase velocity and attenuation, both as a function of frequency, provide the means for determining the viscoelastic damping coefficient. The results follow the process outlined in Figure 5.3 Steps in Data Processing (shown on next page) with corresponding steps identified in Table 5.4.

Steps in Data Processing

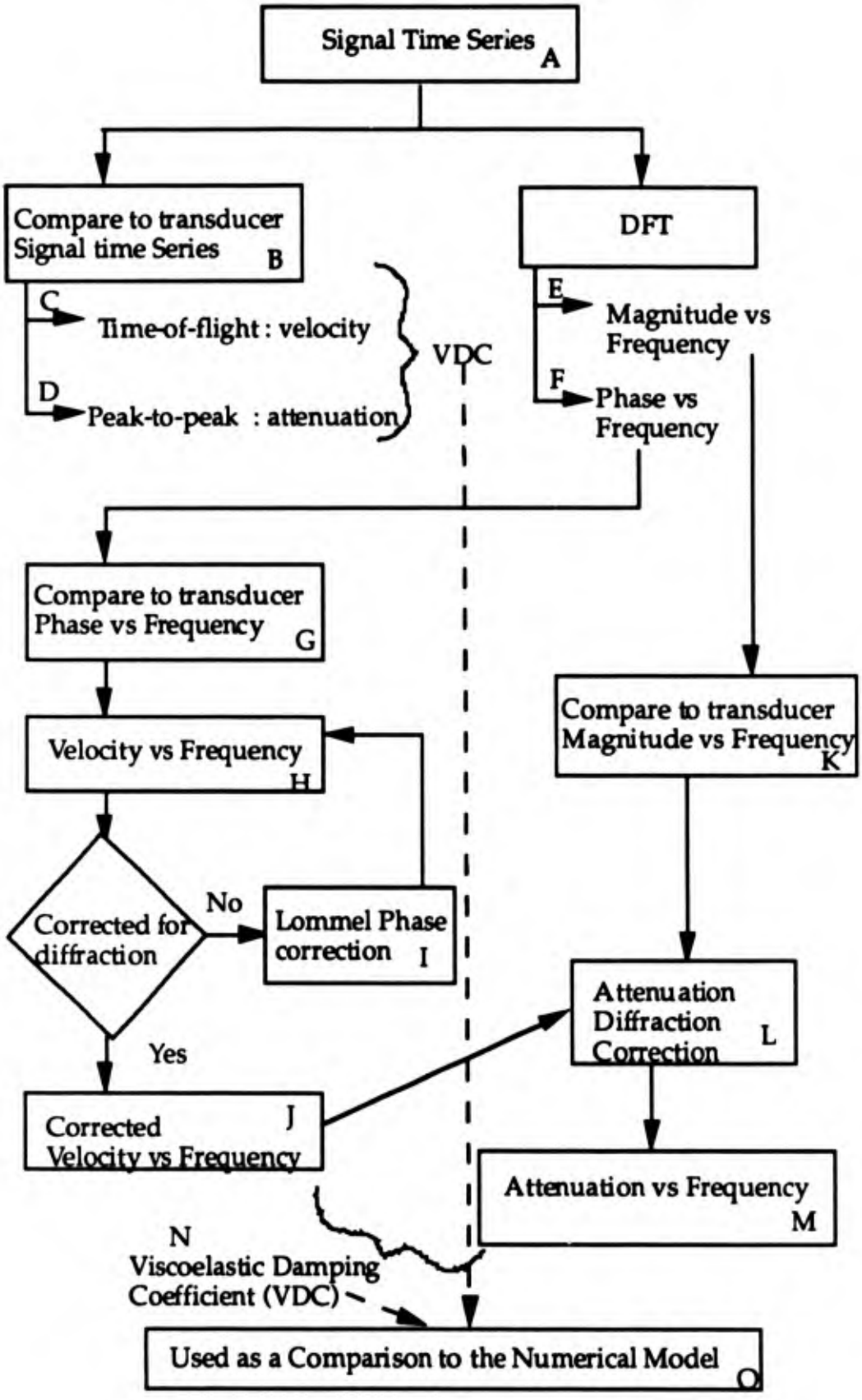

Table 5.4. Figures, Tables, and Equations Identified in Figure 5.3, Steps in Data Processing.

Step	Figure, Table, or Equation	Page
A	Figure 5.5	99
B	Figure 5.4	99
C	Table 5.5	101
D	Table 5.7	103
E	Figure 5.10	108
F	Figure 5.11	108
G	Figure 5.9	107
H	Figure 5.16	112
I	Equation (70)	109
J	Figure 5.19 a, and b	114
K	Figure 5.8	107
L	Table 5.6	102
M	Figure 5.22	117
N	Equation (25)	55
O	Table 5.11 A, B, and C,	121

5.3.1 Signal Time Series

The A50, B50, C50, and N50 are shown below with the other test results presented in Appendix C.

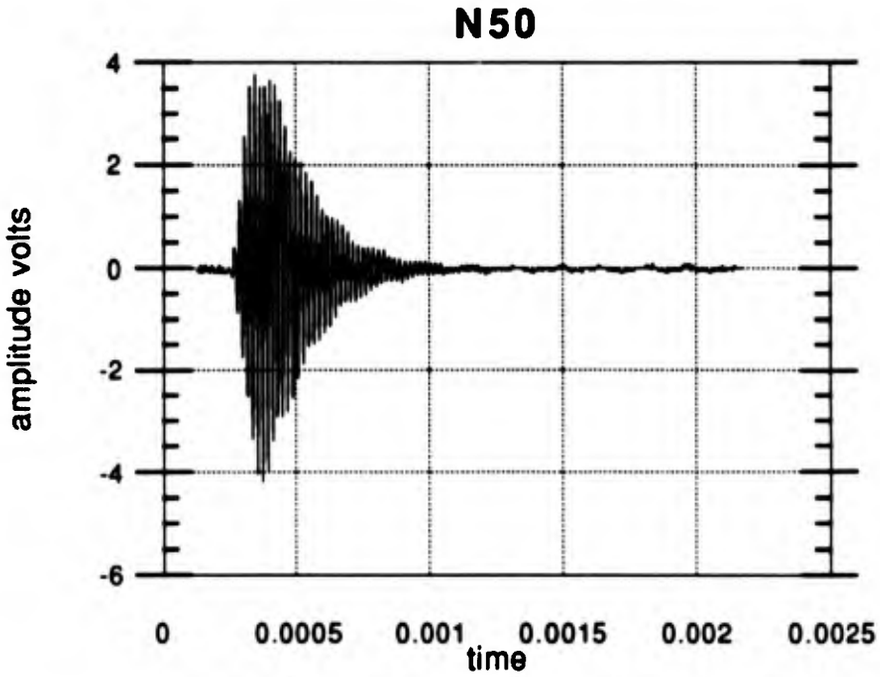

Figure 5.4. Transducer Signal Time Series (Input Equivalent).

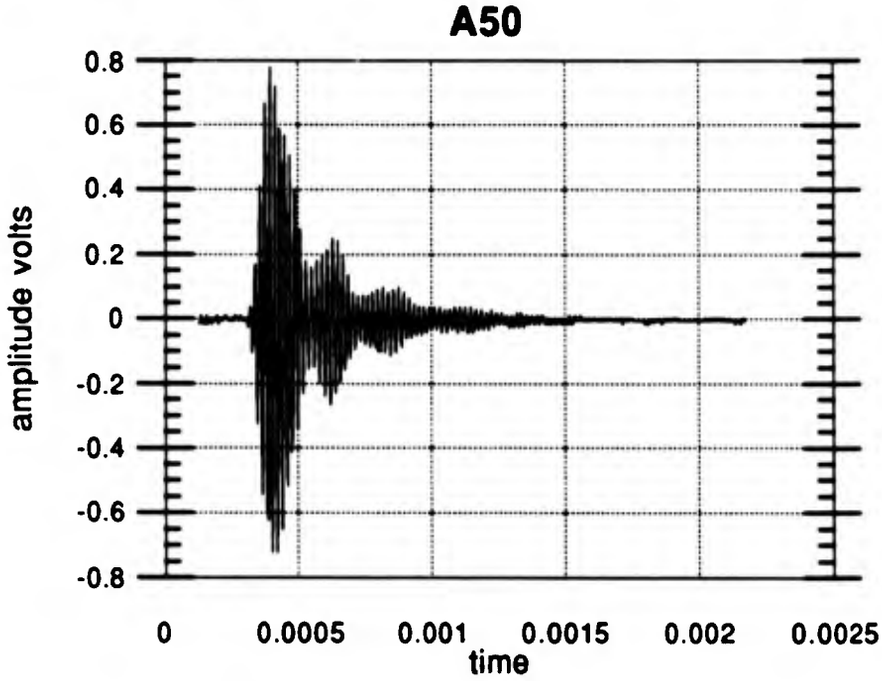

Figure 5.5. Sample A50 Signal Time Series (Output).

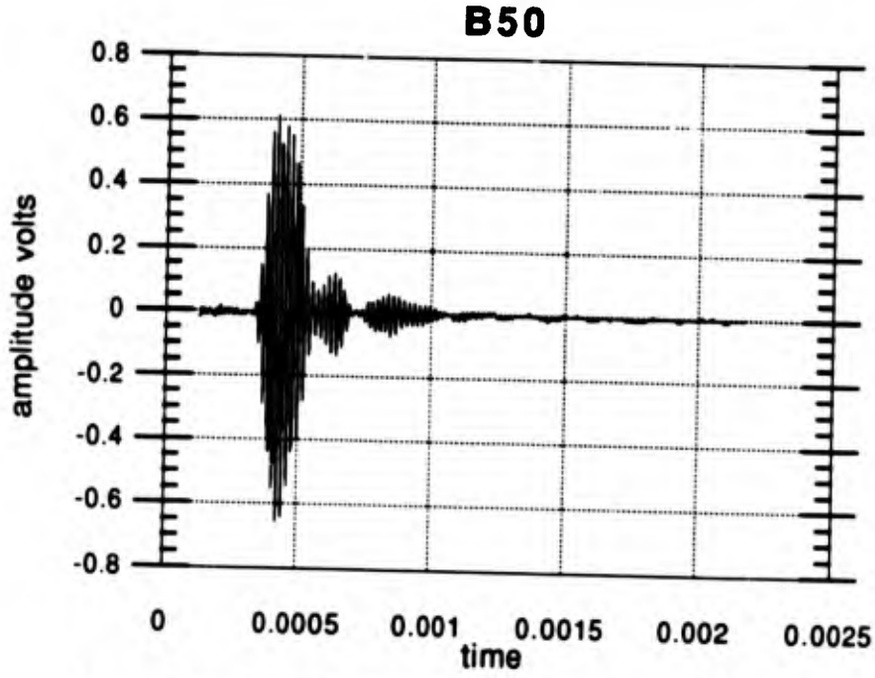

Figure 5.6. Sample B50 Signal Time Series (Output).

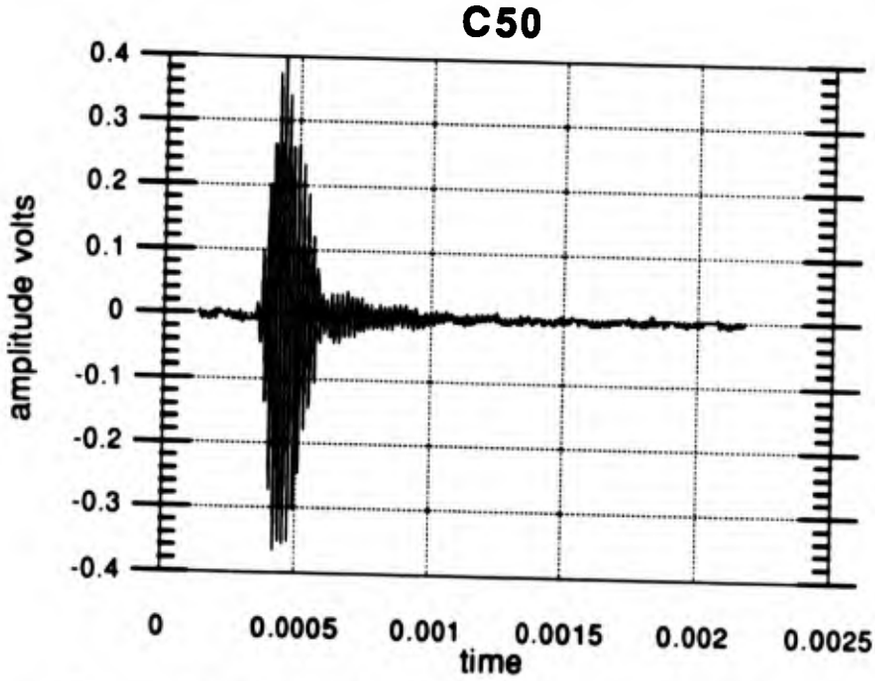

Figure 5.7. Sample C50 Signal Time Series (Output).

The group velocity can be determined by comparing the time signal series time-of-flight from an ultrasonic NDE through a dimension of the sample and the time signal series time-of-flight from the transducer reference signal. A comparison between the time signal series time-of-flight from an ultrasonic NDE through two different dimensions of the same sample could also be used. Table 5.5 below, shows the six estimates of group velocity determined from comparing the zero-point crossing of N50 with A50 (N&A), N50 with B50 (N&B), and N50 with C50 (N&C) and then between A50 and C50 (A&C), B50 and C50 (B&C), and A50 and B50 (A&B).

Table 5.5. Resultant Group Velocity from Time-of-Flight Pairings (Using the 50 kHz Drive Signal Tests).

Pairs	N&A	N&B	N&C	A&B	A&C	B&C
Velocity m/sec	1710	1656	1643	1533	1514	1564
	+/-18	+/-13	+/-11	+/-28	+/-34	+/-60

Not only is this method very much dependent on the judgment of the individual looking at the signal time series for the zero-point crossing, but with a tone burst of three cycles the question of which frequency the velocity is associated with carries a great deal of uncertainty. The convention followed was to associate the velocity with the frequency of the peak magnitude of the DFT.

In Figure 5.8, the frequency on the transducer spectrum of the signal time series (input equivalent), magnitude versus frequency (N50M) at peak magnitude was 51,758 Hz. The velocities in Table 5.5 were associated with this frequency and used in Table 5.7, where appropriate.

The above signal's peak-to-peak amplitude, in Figures 5.4 - 5.7, can be used to determine the attenuation. This attenuation must be corrected for diffraction loss. Both the Atalar (1988) and the Rogers and Van Buren (1974) methods were used for comparison. Atalar (1988) is based on a diffraction loss of 2.5 db for the first a^2/λ distance (a is the radius of the transducer, λ is the signal wavelength) with a 6 db loss for each doubling of distance thereafter, see Table 5.6.

Table 5.6. Atalar Diffraction Loss db.

Sample dimension (r) $< a^2/\lambda$	Diffraction loss = -2.5 db
$a^2/\lambda < r < 2a^2/\lambda$	Diffraction loss = $-2.5 + \frac{6(r - a^2/\lambda)}{a^2/\lambda}$ db
$2a^2/\lambda < r < 3a^2/\lambda$	Diffraction loss = $-8.5 + \frac{6(r - 2a^2/\lambda)}{2a^2/\lambda}$ db

Rogers and Van Buren (1974) base the diffraction on an expression for the Lommel diffraction integral, as shown in equation (68)

$$|D_L| = \left\{\left[\cos(2\pi/s) - J_0(2\pi/s)\right]^2 + \left[\sin(2\pi/s) - J_1(2\pi/s)\right]^2\right\}^{1/2}. \qquad (68)$$

Here $|D_L|$ is the magnitude of the diffraction correction, J_0 and J_1 are Bessel functions of the first kind of order 0 and 1, respectively. The argument $(2\pi/s)$ is a composite variable equal to ka^2/z, with z being the distance traveled, k the wave number, and a defined above.

The attenuation results are presented in Table 5.7. The data from the 50 κHz drive signal ultrasonic tests were used as an example. In

addition, the impedance mismatch was estimated to be -0.5 db, which corresponds to a 97% transmission coefficient for the elastomer/sample and sample/elastomer interfaces. The entries that use this estimate are sensitive to small changes in this value. The impedance mismatch at other interfaces was not needed because this was the only experimental difference between tests. The elastomer density and longitudinal velocity were 1270 kg/m^3 and 1778 m/s, respectively.

Table 5.7. Signal Pairing and Resultant Attenuation. (Using N50, A50, B50, and C50).

Pairings	N&A	N&B	N&C	A&B	A&C	B&C
Attenuation Peak-to-Peak (db)	-14.7	-16.2	-20.5	-1.5	-4.4	-5.9
Diffraction-(db) Atalar (1988)**	-7.1	-9.4	-10.4	-3.1	-4.0	-0.9
Attenuation (db/cm)**	-0.84*	-0.56*	-0.73*	NA	-0.41	-1.97
Diffraction- (db) Rogers and Van Buren (1974)**	-11.2	-13.4	-14.5	-2.5	-3.7	-1.2
Attenuation (db/cm)**	-0.35*	-0.20*	-0.42*	NA	-0.48	-1.83

Notes: * -0.5 db impedance mismatch estimate. NA -- Not applicable.
** -- Frequency dependent entries based on 51,758 Hz.

From the above Table 5.7, the attenuation in the inert propellant is estimated to be -0.63 db/cm at 51,758 Hz. For comparison, at 150 kHz and 500 kHz the attenuation was reported to be -2.1 db/cm and -6.8 db/cm, not corrected for diffraction and impedance mismatch (Martin Marietta IRAD R-619R). The viscoelastic damping coefficient, determined by using equation (25), with a frequency of 51,758 Hz, density of 1910 kg/m^3, and

velocity of 1603 +/- 32 m/s, is -9370 +/- 550 db Ns/m^2 or -0.10 +/- 0.01 db when nondimensionalized by multiplying by 1/(density*velocity*wavelength). For comparison, You et al (1991) used values of the damping parameter ranging from -25.07 to -1114.5 Ns/m^2 when modeling the energy absorption in a simulated aluminum block.

Data from Test 2, conducted in November 1992, was presented in Table 5.8 and 5.9 as a comparison to data from Test 1. The results show general increases in group velocity and attenuation with frequency. However further experimental data would be necessary to fully characterize the SRM propellant at the higher frequencies. These tests were taken to show trend information only.

Table 5.8. Resultant Group Velocity from Time-of-Flight Pairings for the Frequency at Peak Magnitude shown for Each Drive Signal Test.

Drive Signal	Frequency at Peak Magnitude	Resultant Group Velocity from Time-of-Flight Pairings m/s					
kHz	Hz	N&A	N&B	N&C	A&B	A&C	B&C
30	52246	1663	1677	1697	1717	1762	1842
40	51270	1613	1652	1627	1781	1655	1483
50	51758	1710	1656	1643	1533	1514	1564
65	51758	1635	1576	1638	1425	1643	2188
100	58594	1657	1621	1638	1524	1603	1750
150	146480	4025	2919	2650	1605	1625	1657
200	199380	4118	2955	2650	1605	1597	1585
300	313310	1640	1631	1625	1605	1597	1585
500	524900	4464	3111	2624	1634	1490	1302

Table 5.9. Attenuation (db/cm), Based on Atalar (1988), Using the Group Velocity and Frequency from Table 5.8.

Drive Signal	Frequency at Peak Magnitude	Attenuation (db/cm), Atalar (1988), using Group Velocity from Table 5.4					
kHz	Hz	N&A*	N&B*	N&C*	A&B	A&C	B&C
30	52246	-0.76	-0.90	-0.38	-1.16	-0.42	NA
40	51270	-0.50	-0.35	-0.62	-0.17	-1.72	-2.59
50	51758	-0.82	-0.55	-0.73	NA	-0.41	-1.97
65	51758	-0.67	-0.62	-0.62	NA	-0.99	-0.19
100	58594	-1.36	-0.86	-0.86	NA	-0.48	-0.70
150	146480	-0.92	-0.99	-1.11	-1.07	-1.49	-2.16
200	199380	-1.76	-1.52	-1.56	-0.71	-1.17	-1.92
300	313310	-2.53	-2.43	-2.33	-2.11	-1.96	-1.72
500	524900	-2.89	-2.77	-2.72	-2.39	-2.40	-2.42

Notes: * -0.5 db impedance mismatch estimate. NA -- Not applicable.

From the data in Tables 5.7 and 5.9, it is clear that the attenuation is very dependent on velocity. Rogers and Van Buren (1974) relies on the fulfillment of the inequality in equation (69) below, to decide the goodness of the approximation of D_L, the diffraction correction.

$$(ka)^{1/2} >> 1 \qquad (69)$$

The range of values for $(ka)^{1/2}$ for the 30-100 kHz Drive signals, are 1.74 -1.89, whereas the 150-500 kHz Drive signals range from 2.46 to 4.64. Therefore the attenuation will be based on Atalar (1988) for the next Section. DFTs were obtained on all the recorded signals using either the waveform analyzer or a computer.

5.3.2 Frequency Domain Information

There were not any units on the magnitude axis of the magnitude versus frequency figures because the magnitude was always used in a ratio to determine attenuation and any associated unit would cancel out.

Due to the inability to determine velocity versus frequency at frequencies higher than 50 kHz from the test data, the only velocity and attenuation information determined was as depicted. This will be addressed in Section 5.5 Experimental Uncertainty.

Only the 50 kHz signals will be presented here with the balance of the signals presented in Appendix C. The following eight figures are the magnitude and phase plots of the frequency domain of the signal time series presented in the previous Section. Please refer to Figure 5.2 for orientation of sample during the ultrasonic testing (Letter designation in Figures). The number refers to the drive signal, while the "M" or "P" identifies the Figure containing either Magnitude or Phase information. Please refer to Tables 5.2 and 5.3.

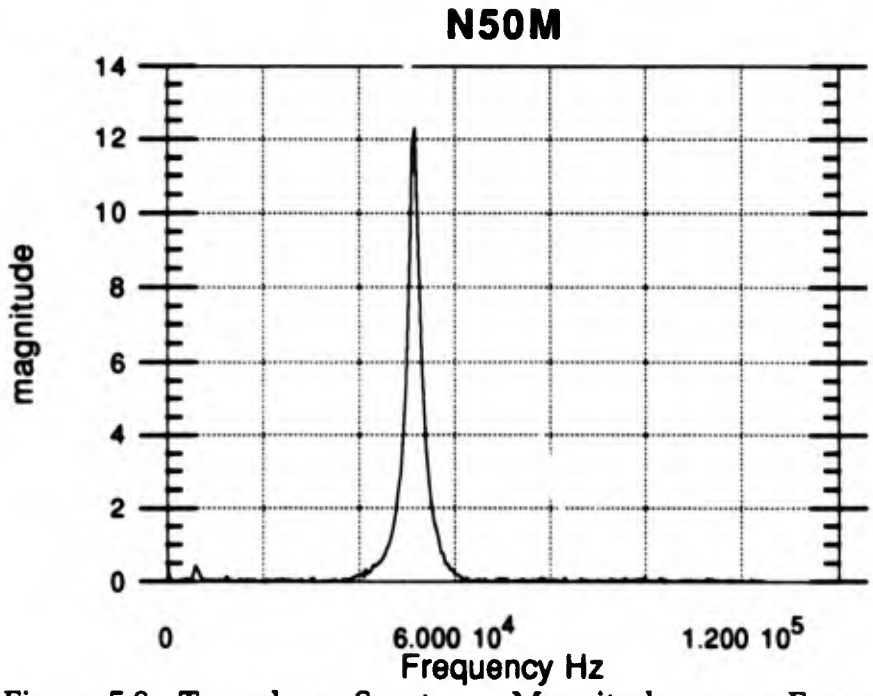

Figure 5.8. Transducer Spectrum, Magnitude versus Frequency (3 cycle 50 kHz drive signal, Input equivalent).

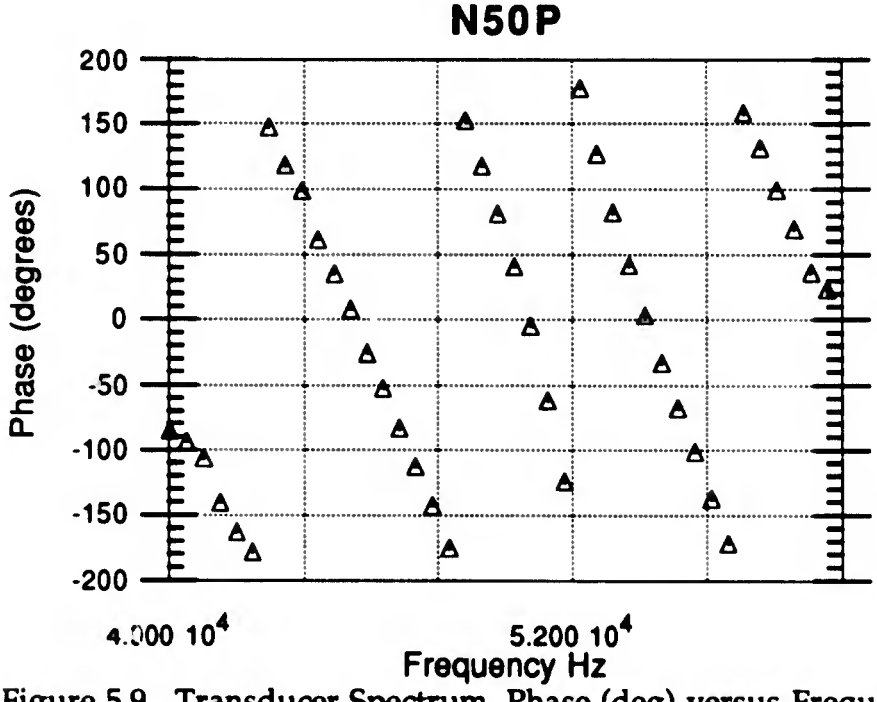

Figure 5.9. Transducer Spectrum, Phase (deg) versus Frequency (3 cycle 50 kHz drive signal, Input equivalent).

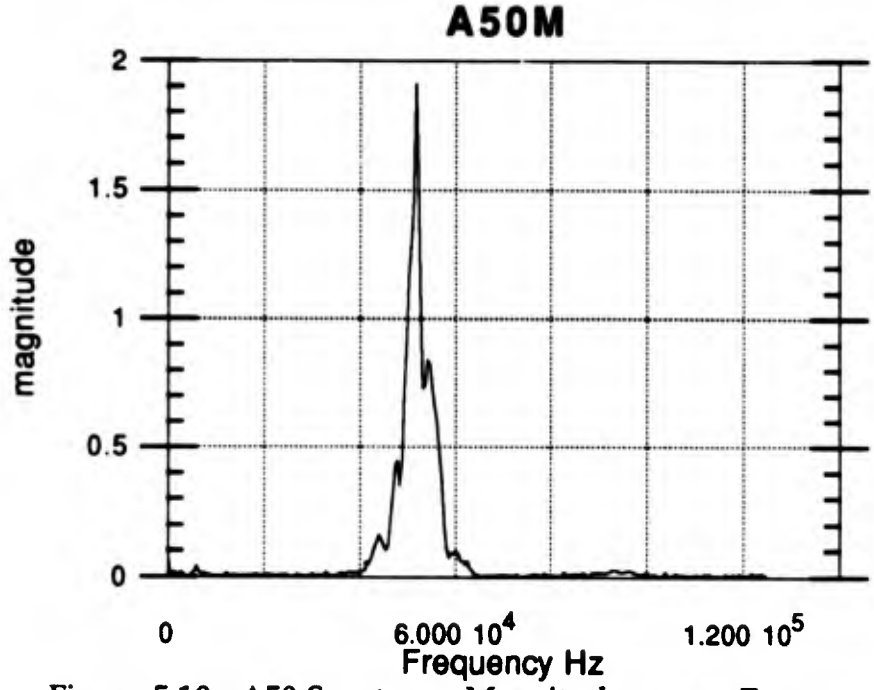

Figure 5.10. A50 Spectrum, Magnitude versus Frequency (3 cycle 50 kHz drive signal).

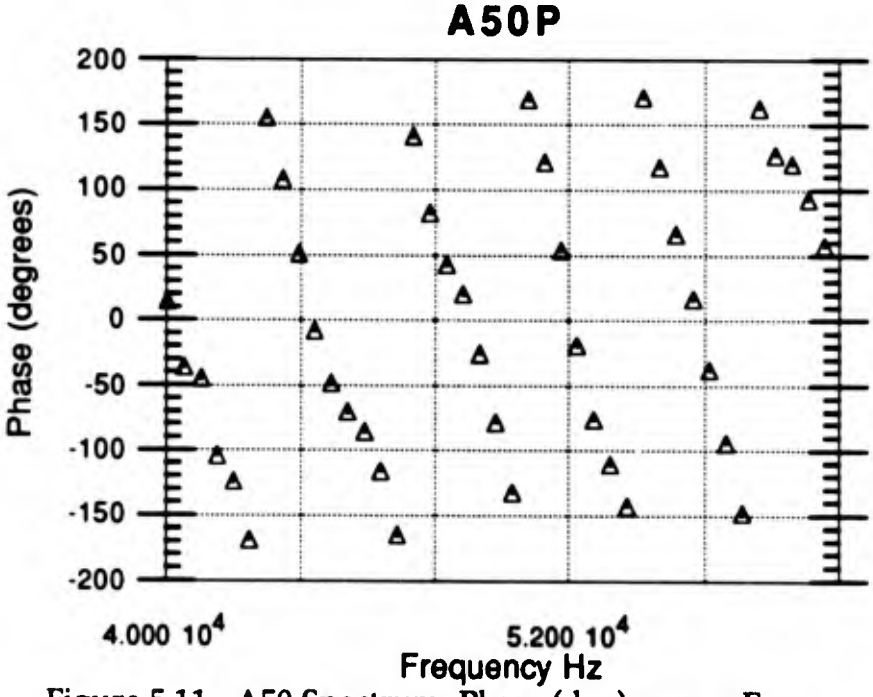

Figure 5.11. A50 Spectrum, Phase (deg) versus Frequency (3 cycle 50 kHz drive signal).

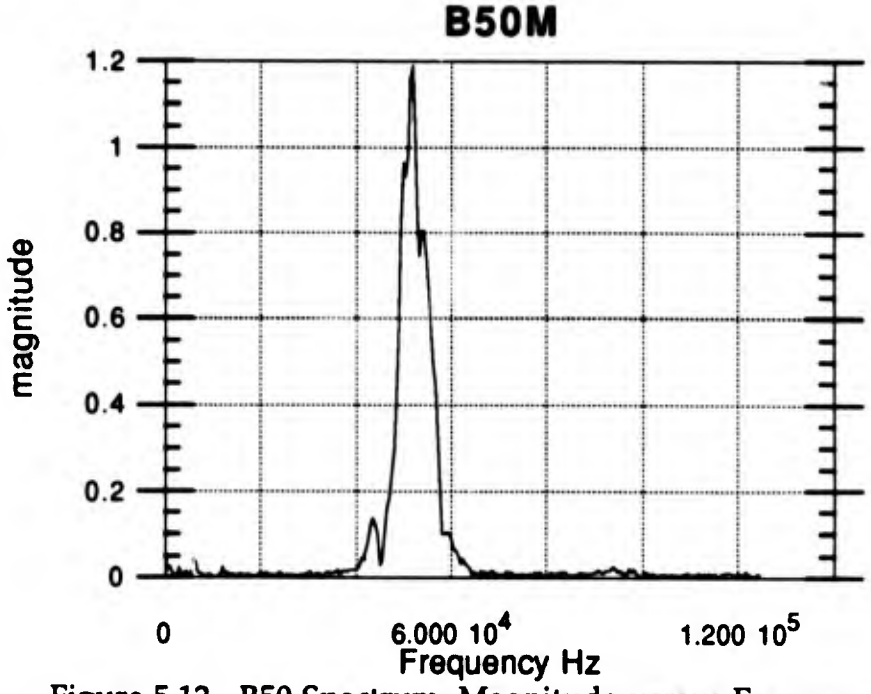

Figure 5.12. B50 Spectrum, Magnitude versus Frequency (3 cycle 50 kHz drive signal).

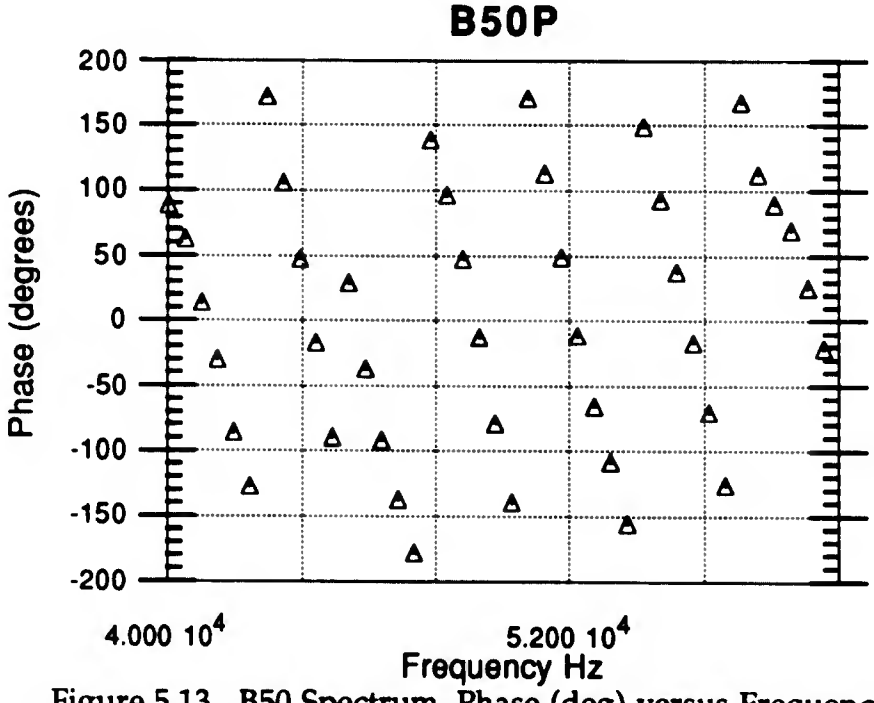

Figure 5.13. B50 Spectrum, Phase (deg) versus Frequency (3 cycle 50 kHz drive signal).

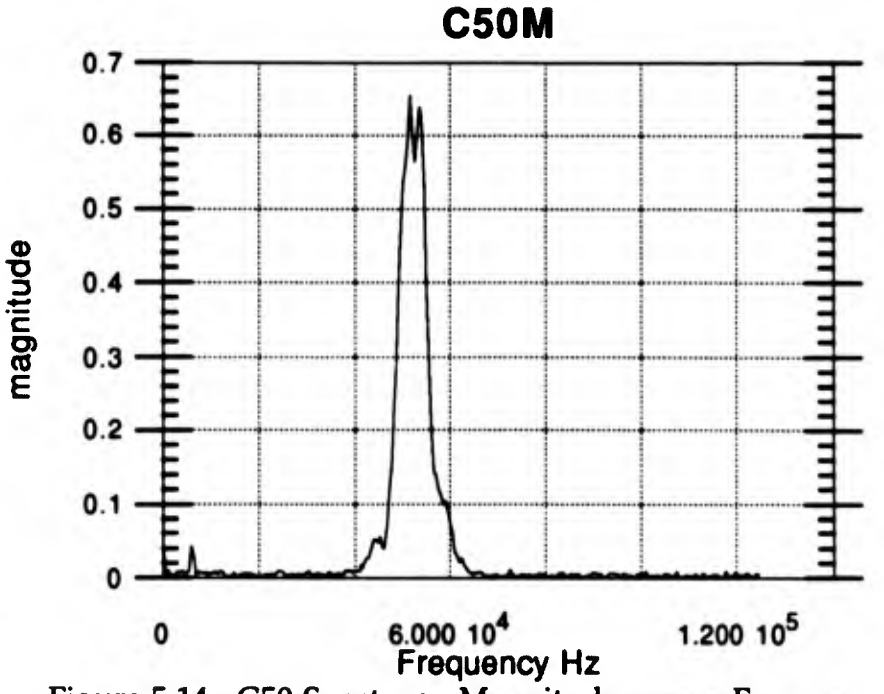

Figure 5.14. C50 Spectrum, Magnitude versus Frequency (3 cycle 50 kHz drive signal).

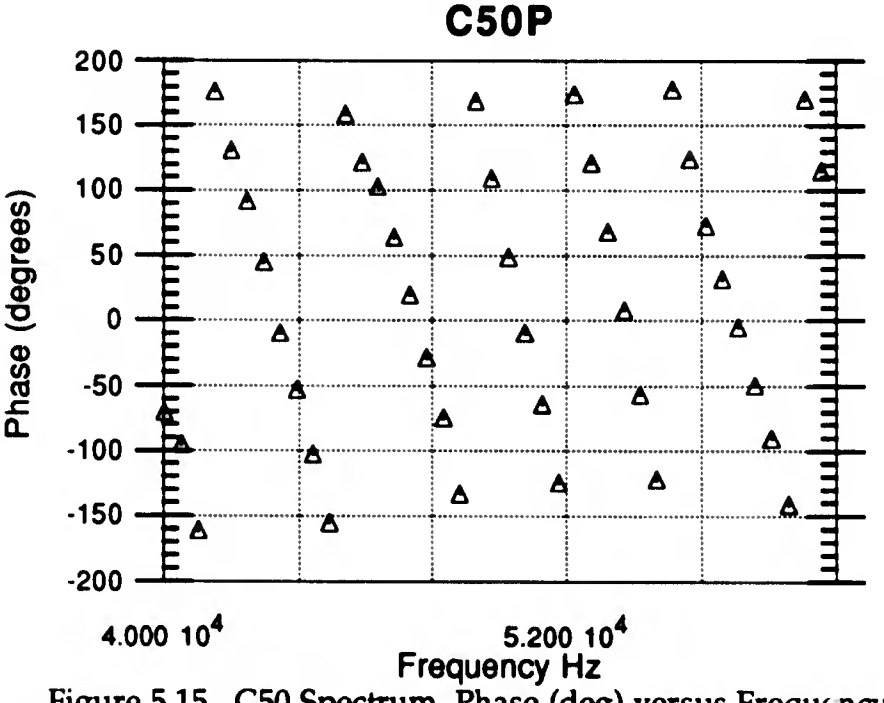

Figure 5.15. C50 Spectrum, Phase (deg) versus Frequency (3 cycle 50 kHz drive signal).

The attenuation information, as determined using the ultrasonic signal time series frequency domain magnitude information, follows the phase information because the diffraction loss corrections are based on phase velocity, which in turn is determined from the phase information obtained from the ultrasonic signal time series spectrum.

The phase velocity was determined following the method presented in Sachse and Pao (1978). The noise present in the phase signals were smoothed in the data in Figures 5.16, 5.17 and 5.18 as indicated. Fortunko et al (1992), suggested that the phase of the ultrasonic signal time series frequency domain should also be corrected for diffraction using the method of Rogers and Van Buren (1974). The phase correction using Rogers and Van Buren (1974) is presented in equation (70) and requires an estimate for velocity which is based on the phase. Therefore, the velocity must be determined twice, and Figures 5.16 - 5.18 are the first iteration. The phase correction formula is

$$\mathrm{TAN}(D_L) = \left\{ \frac{\left[\sin(2\pi/s) - J_1(2\pi/s)\right]}{\left[\cos(2\pi/s) - J_0(2\pi/s)\right]} \right\}, \qquad (70)$$

where $\mathrm{TAN}(D_L)$ is the tangent of the phase diffraction correction, and J_0 and J_1 are Bessel functions of the first kind of order 0 and 1, respectively. The argument $(2\pi/s)$ is a composite variable equal to ka^2/z, with z being the distance traveled, k the wave number, and a is the transducer radius.

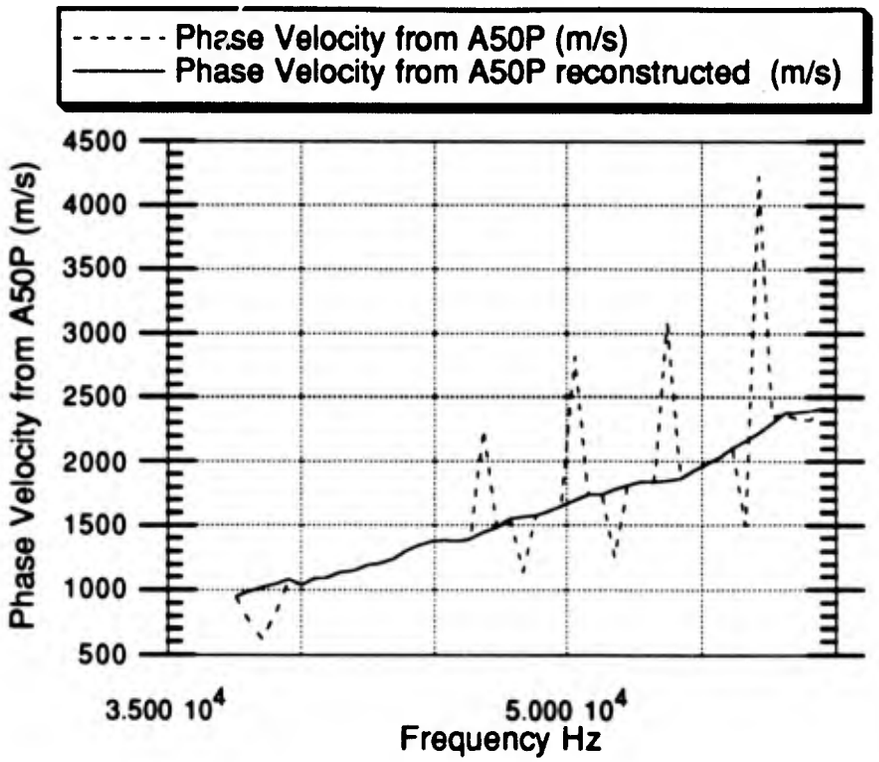

Figure 5.16. Original and Smoothed Phase Velocity using A50P.

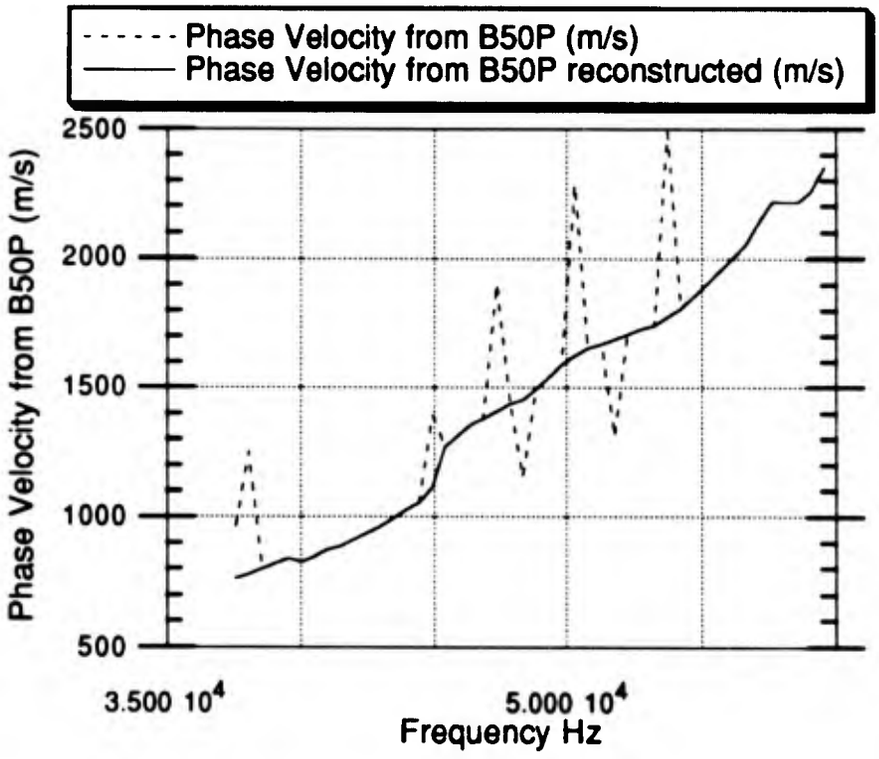

Figure 5.17. Original and Smoothed Phase Velocity using B50P.

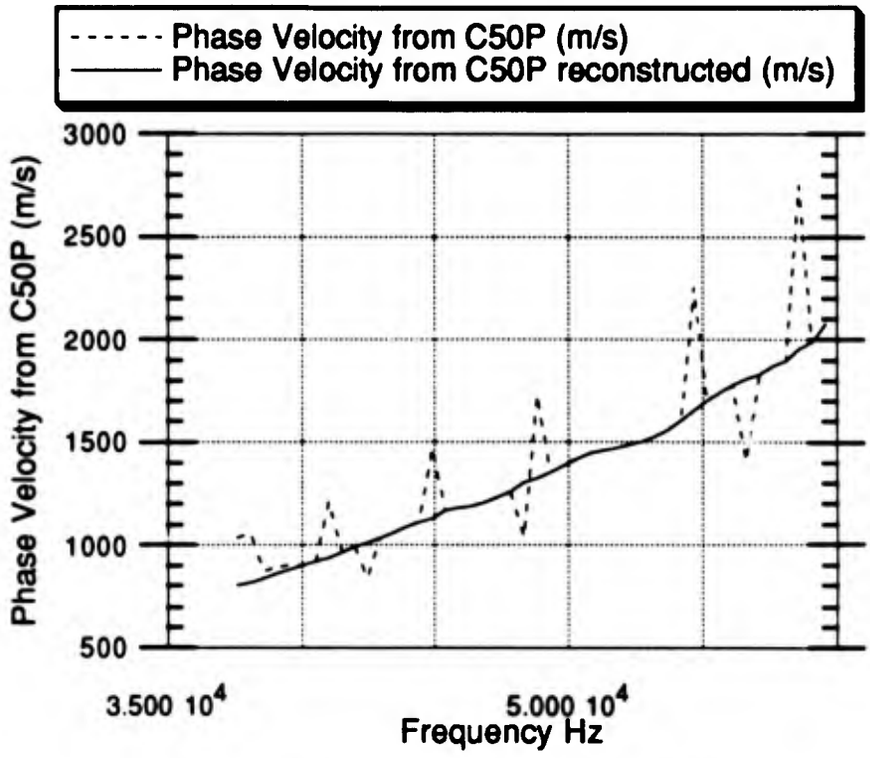

Figure 5.18. Original and Smoothed Phase Velocity using C50P.

Figure 5.19 a, and b, compare the reconstructed phase velocities from A50P, B50P, and C50P shown as Figure 5.16 - 18. For clarity the Figures 5.19 b and 5.20 b depict a smaller frequency band. Figure 5.20 a, and b, compares the corrected phase velocities from A50P, B50P, and C50P.

Figure 5.21 shows the five previous Figures on one plot to show the dramatic effect of reconstruction and phase diffraction correction. From Figure 5.21, the diffraction correction for phase information seems to draw the phase velocity determined from each test closer together at each frequency point. C50P was corrected for ambiguity in the DFT before the phase velocity was determined, as suggested in Fortunko et al (1992).

The agreement among phase velocity determined from A50P, B50P, and C50P information was quite good.

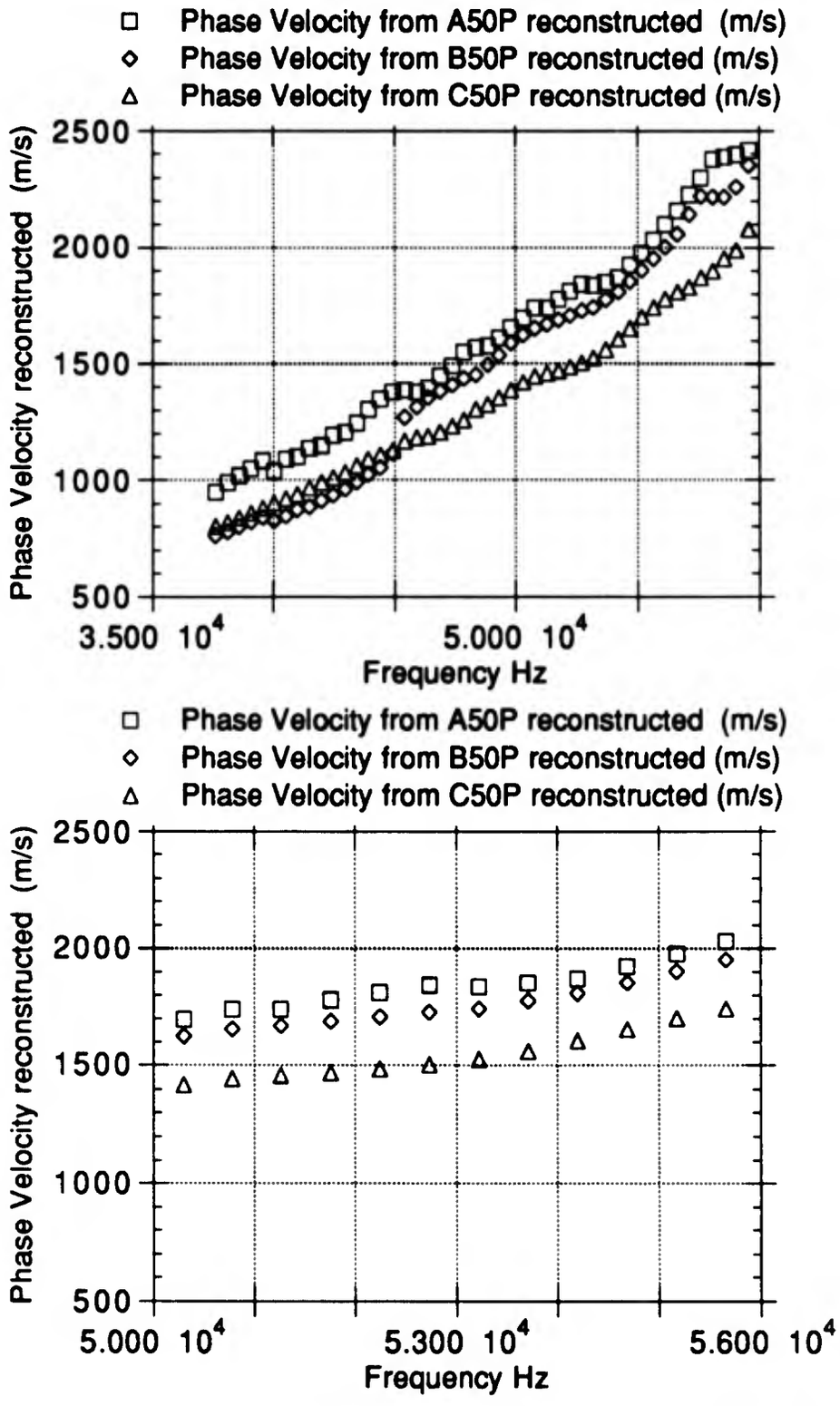

Figure 5.19 a, and b. Comparison of Phase Velocity from A50P, B50P, and C50P (Without Diffraction Correction).

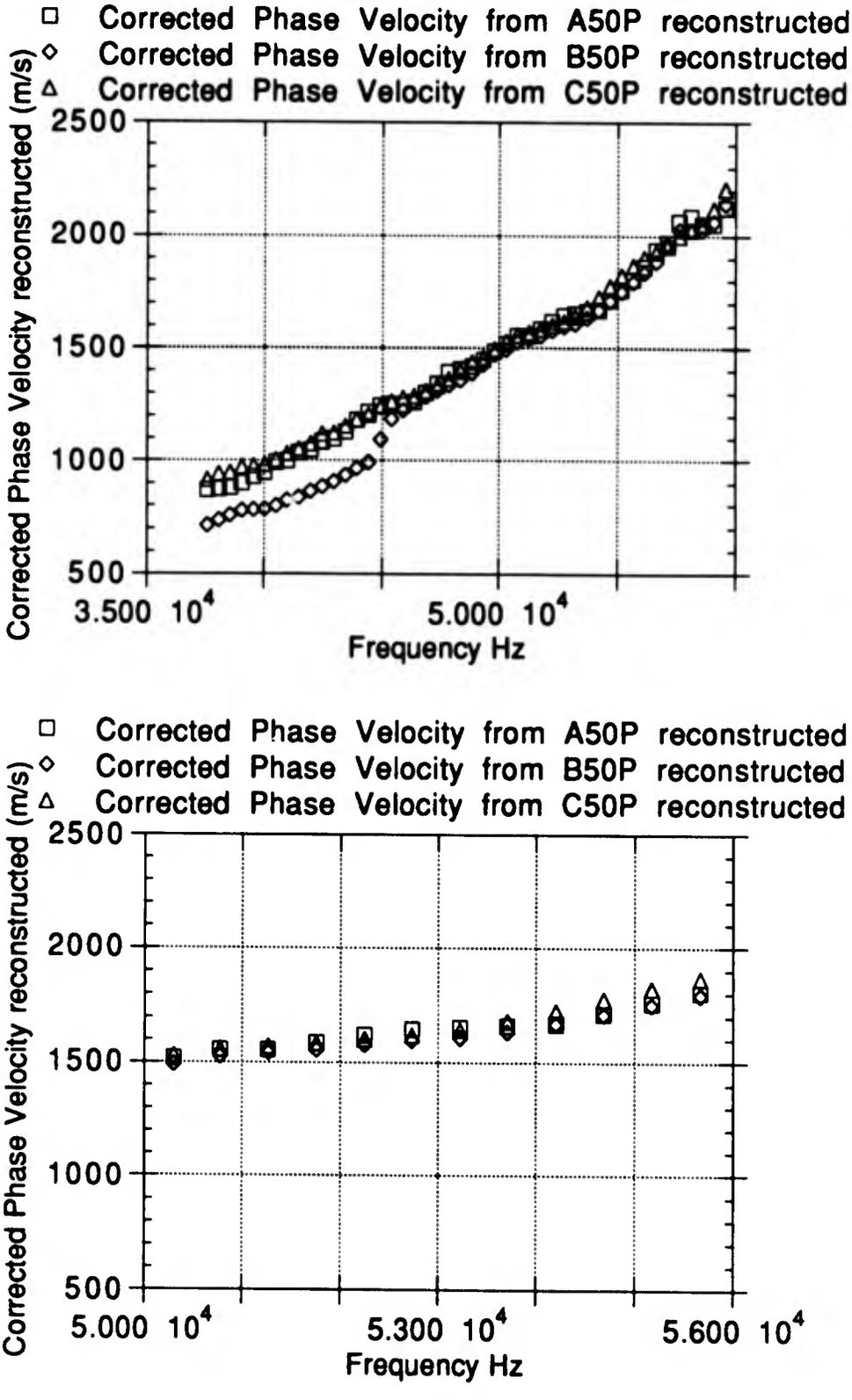

Figure 5.20 a, and b. Comparison of Phase Velocity from A50P, B50P, and C50P (Reconstructed and With Diffraction Correction).

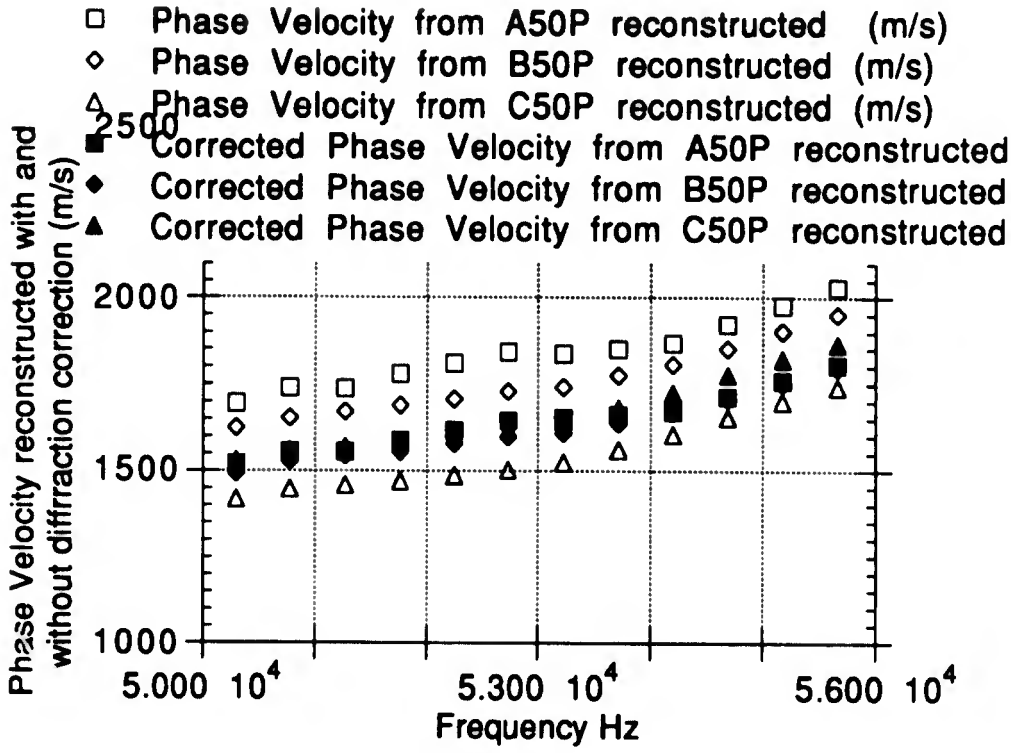

Figure 5.21. Comparison of Phase Velocity, from A50P, B50P, and C50P Reconstructed, With and Without the Diffraction Correction.

This phase velocity versus frequency profile, especially for 50 to 53 kHz, was used as the input in determining attenuation for all other tests when the 50 kHz transducer was used in Test 1, regardless of the drive signal of the test, i.e. it was used for A30 through C65, and to provide an equivalent attenuation for propellant without an inclusion in tests with the Paddle Ball and the Ping Pong Ball.

Using the Magnitude versus Frequency information from Figures 5.7 - 5.14, and the information from Figure 5.20 for diffraction correction, the Attenuation versus Frequency curves were developed in the Figures 5.22 - 5.26.

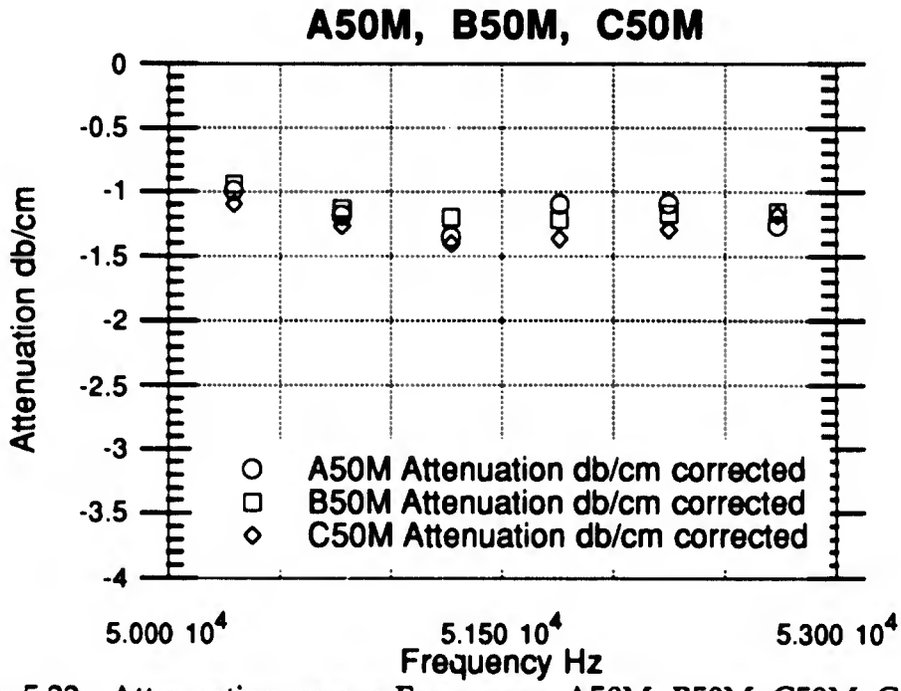

Figure 5.22. Attenuation versus Frequency, A50M, B50M, C50M, Corrected for Diffraction Losses Using Atalar (1988), and for Impedance Mismatch.

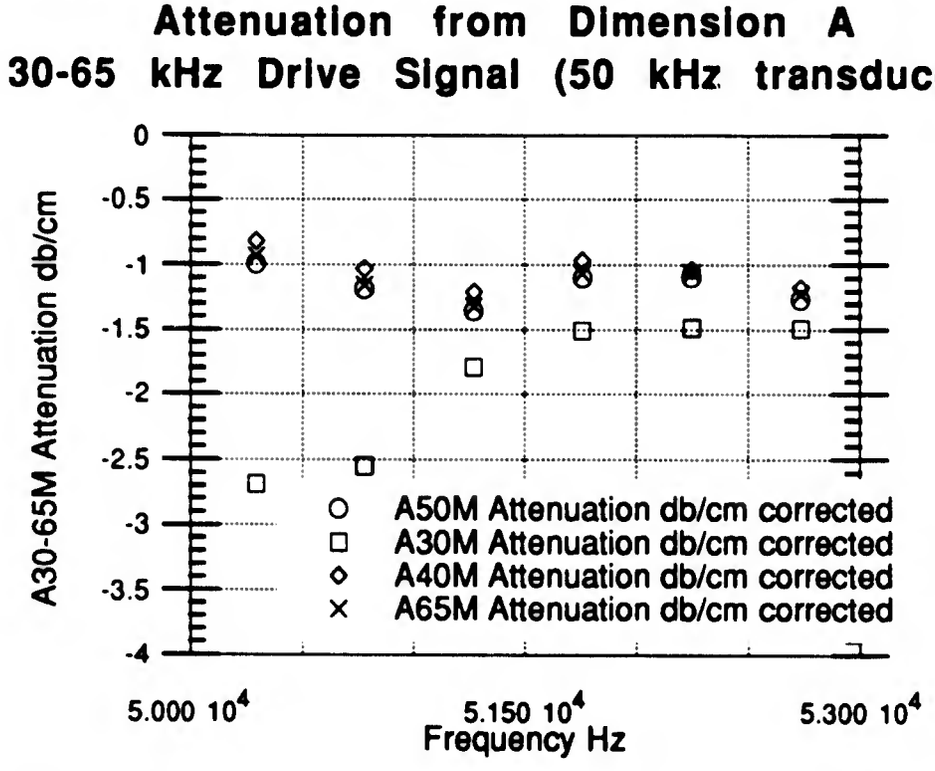

Figure 5.23. Attenuation versus Frequency, A30M, A40M, A50M, A65M, Corrected for Diffraction Losses Using Atalar (1988), and for Impedance Mismatch.

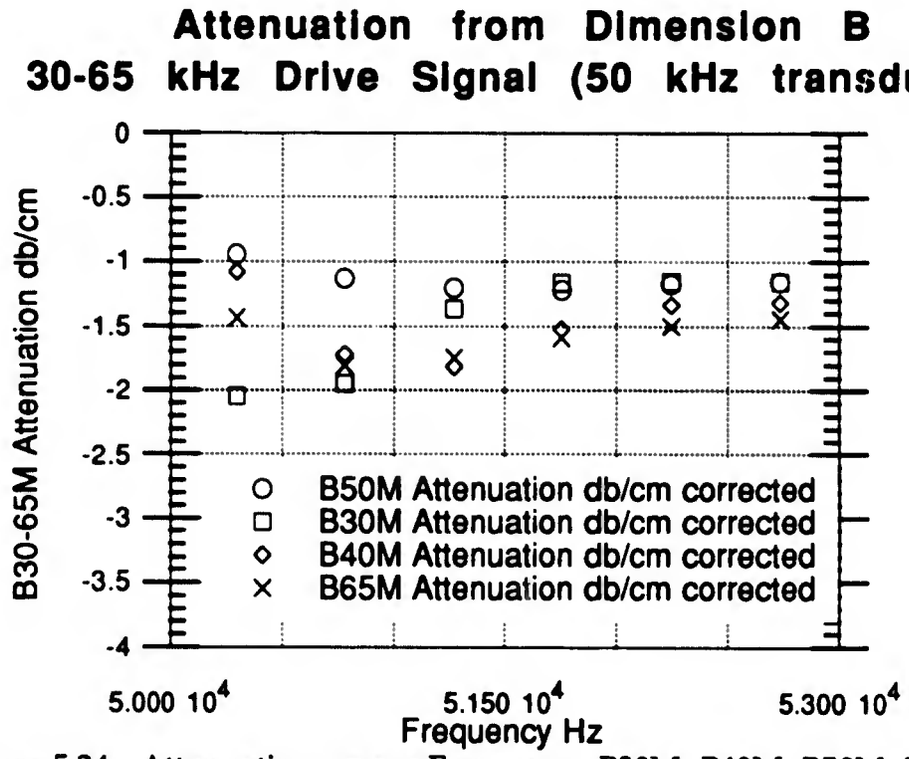

Figure 5.24. Attenuation versus Frequency, B30M, B40M, B50M, B65M, Corrected for Diffraction Losses Using Atalar (1988), and for Impedance Mismatch.

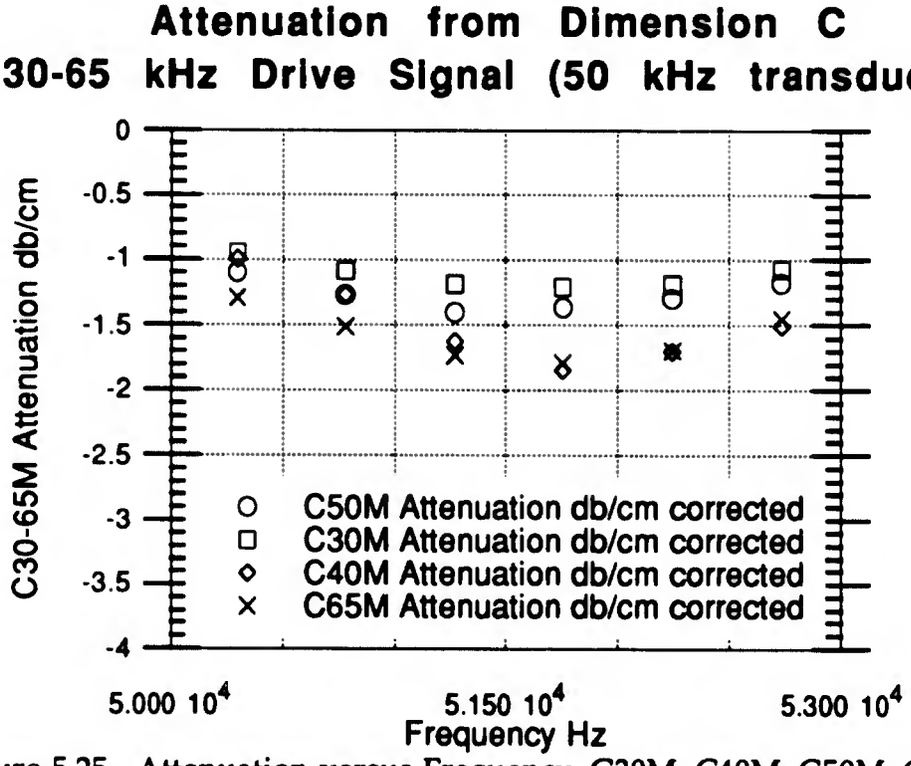

Figure 5.25. Attenuation versus Frequency, C30M, C40M, C50M, C65M, Corrected for Diffraction Losses Using Atalar (1988), and for Impedance Mismatch.

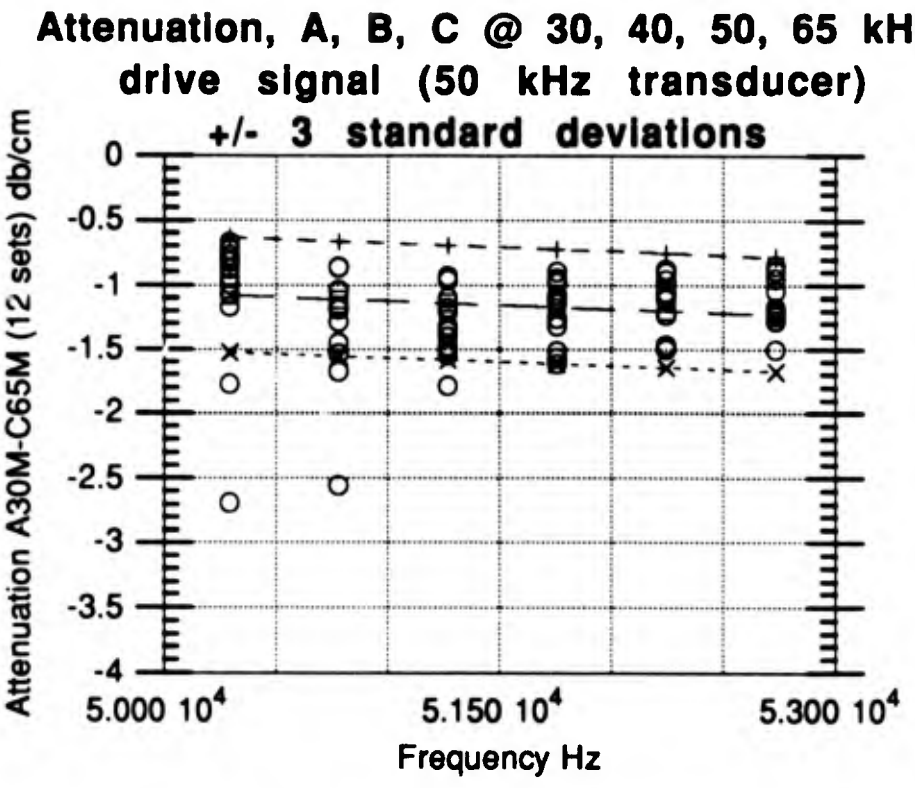

Figure 5.26. Summary of Attenuation versus Frequency, A30M-C65M, Corrected for Diffraction Losses Using Atalar (1988), and for Impedance Mismatch.

From Figure 5.26, one can notice a large scatter in the attenuation data while the phase velocity data shows quite a bit more agreement. Section 5.5 determined a standard deviation of 0.149 db/cm. Figure 5.26 shows +/- 3 standard deviations (outer dashed lines) around a linear regression curve (mean attenuation, identified by the inner dashed line). Most of the Test 1, experimental values, at each frequency fall within this +/- 3 standard deviation band. Therefore, the mean attenuation and standard deviation was assumed to be a good approximation of the attenuation for the sample 3323-2 no inclusion, at these frequencies. Table 5.10 depicts the values for A50M, B50M, and C50M, which are shown in Figure 5.22, the combined attenuation, and the mean attenuation in

Figure 5.26 (inner dashed line at each frequency). The mean attenuation was used as a comparison to the experimental tests with inclusions.

Table 5.10. A50M, B50M, C50M, Combined and Mean Attenuation.

Frequency Hz	A50M Atten db/cm	B50M Atten db/cm	C50M Atten db/cm	Combined Atten db/cm	Mean Atten db/cm
50293	-0.99	-0.67	-0.87	-0.80	-1.08
50781	-1.19	-0.86	-1.04	-1.18	-1.11
51270	-1.35	-0.94	-1.18	-1.39	-1.14
51758	-1.11	-0.95	-1.14	-1.28	-1.17
52246	-1.11	-0.90	-1.07	-1.20	-1.20
52734	-1.28	-0.88	-0.95	-1.17	-1.23

Table 5.10 lists only the frequency data that encompasses magnitudes that are half or more of the peak value of the magnitude in the transducer spectrum. Table 5.10 and Figure 5.20 characterizes the SRM inert propellant and provides a baseline for comparison with future testing. With the addition of the Viscoelastic Damping Coefficient, the material bulk viscoelastic properties can be characterized and tracked over time.

5.4. Determination of the Viscoelastic Damping Coefficient

The attenuation versus frequency and the phase velocity versus frequency information can now be combined to give the Viscoelastic Damping Coefficient using equation (25) from Kino (1987). The density r, for the inert sample 3323-2 was reported to be 1910 kg/m^3.

$$\alpha = \frac{\omega^2 \eta}{2 V_c^3 \rho} \qquad \text{Kino (1987)} \qquad (25)$$

Table 5.11 A, B, C. Viscoelastic Damping Coefficient A50M, B50M, C50M.

Frequency Hz	A50 Velocity m/s	A50 Attenuation db/cm	db Visco Damping Coefficient	**Visco Damping Coefficient
50293	1519.7	-0.99	-0.1521	-4.8E-07
50781	1554.7	-1.19	-0.1841	-5.8E-07
51270	1555.1	-1.35	-0.2081	-6.5E-07
51758	1585.7	-1.11	-0.1715	-5.3E-07
52246	1617.5	-1.11	-0.1738	-5.3E-07
52734	1644.2	-1.28	-0.2022	-6.1E-07

Frequency Hz	B50 Velocity m/s	B50 Attenuation db/cm	db Visco Damping Coefficient	**Visco Damping Coefficient
50293	1492.3	-0.67	-0.1007	-3.2E-07
50781	1527.6	-0.86	-0.1309	-4.1E-07
51270	1543.7	-0.94	-0.1427	-4.4E-07
51758	1555.0	-0.95	-0.1444	-4.4E-07
52246	1578.4	-0.90	-0.1377	-4.2E-07
52734	1597.3	-0.88	-0.1358	-4.1E-07

Frequency Hz	C50 Velocity m/s	C50 Attenuation db/cm	db Visco Damping Coefficient	**Visco Damping Coefficient
50293	1530.1	-0.87	-0.1345	-4.3E-07
50781	1557.7	-1.04	-0.1621	-5.1E-07
51270	1570.3	-1.18	-0.1831	-5.7E-07
51758	1583.5	-1.14	-0.1767	-5.4E-07
52246	1601.4	-1.07	-0.1662	-5.1E-07
52734	1619.4	-0.95	-0.1480	-4.5E-07

The Viscoelastic Damping Coefficient values are shown in Table 5.11 A, B, and C. The values from equation (25) are normalized per $\frac{1}{\rho V_c \lambda}$ (1/(density*velocity*wavelength)) or $\frac{f}{\rho V_c^2}$ (frequency/(density*velocity*velocity)). The last column of Table 5.11 shows the value of the Viscoelastic Damping Coefficient that would be input in the numerical simulation.

Table 5.12. Combined Viscoelastic Damping Coefficient Data.

Frequency Hz	Combined Velocity m/s	Combined Attenuation db/cm	db Visco Damping Coefficient	**Visco Damping Ccefficient
50293	1514 +/-16	-0.80	-0.1220	-3.9E-07
50781	1547 +/-14	-1.18	-0.1816	-5.7E-07
51270	1556 +/-11	-1.39	-0.2131	-6.6E-07
51758	1575 +/-14	-1.28	-0.1980	-6.1E-07
52246	1599 +/-16	-1.20	-0.1853	-5.7E-07
52734	1620 +/-19	-1.17	-0.1825	-5.5E-07

** VDC divided by frequency (radians/sec), used in this fashion for the numerical simulation.

Table 5.12 characterizes the SRM propellant at 50 kHz in regards to velocity, attenuation, and Viscoelastic Damping Coefficient. These were used as a comparison to the numerical simulations. Once the numerical simulation was tuned, a few numerical simulations with inclusions were investigated. However, it is important to note that the numerical model could also be used to characterize the viscoelastic changes that occur in the SRM propellant during its service history. Test 3 allows a look at the laboratory process used in the experimental ultrasonic NDE of the specimen with the focus on experimental uncertainty. In addition, since Test 3 was performed five months after Test 1, it also allows one to compare the changes in viscoelastic properties.

5.5 Experiment Uncertainty

Several steps were taken to ensure that differences between tests were not introduced by the experiment methodology. The experiments were conducted in similar temperature and humidity ranges every time.

The robot was used to ensure repeatability of the transducer pressure and positioning on the sample. The same individual positioned the sample on the robot and changed the test setup each time.

Three sets of data (A, B, C), at two different drive signal frequencies (30, 65 kHz), with tone bursts of two lengths (6, 10 cycles), were replicated five times (A-E). Test 3 was conducted on sample 3323-2 no inclusion, using the 50 kHz transducer at both 30 kHz and 65 kHz signal drive frequencies, gated with a tone burst of 6 and 10 cycles, through three different linear dimensions. However, since the SRM propellant ages, one must consider that the material characteristics change with time when comparing Test 1 with Test 3.

Figures 5.28 - 5.31 are a summary of the Test 3 transducer spectrum, magnitude and phase versus frequency. Each Figure has an average curve (identified by s) which was used as an input equivalent for the rest of the 60 tests.

Figures 5.32 and 5.33 show the differences in the phase of the transducer spectrum for each repetition of the transducer-transducer test. It also highlights the problem of determining the velocity profile for the subsequent ultrasonic NDE of the samples. A slight phase shift causes a large error in the velocity.

Figures 5.34 - 5.45 are the 60 tests grouped in sets of five, identified A-E, relating to the repetition of each dimension tested at a particular frequency (i.e. CT30D was the C dimension, with Ten cycle, 30 kHz drive signal, D for fourth repetition). In all these Figures, "a" was the magnitude vs frequency, and "b" was the attenuation vs frequency.

One possible explanation of scatter was due to the cycling of the pressure applied by the robot on the samples during each test. Although

the pressure doesn't change rapidly enough to influence the results during data acquisition, the change of pressure between tests could influence the coupling efficiency between the elastomer and transducer (Martin Marietta, 1993b). Even the transducer-transducer tests use the elastomer and ultrasonic couplant on each transducer. The amount and thickness of ultrasonic couplant was not monitored during testing. As shown in Appendix C, the minor differences between the signal time series of the same test group (5 in each set, A-E) translates into major variations in the magnitude at the peak frequencies. Spot checks revealed a strong correlation between the higher amplitude signal time series and the higher magnitude versus frequency data points. As an example, the group CT30 A-E (where A is the first test on CT30 and so on), in Figure 5.27, depicts an order, high to low of A, B, D, C, E. .This can be compared to Figure 5.39 b, which shows an order at peak frequencies of A, B, E, D, C. It seems that the more excitation in the signal time series, the greater the DFT magnitude at each individual frequency.

Two other considerations on experimental methods may contribute to the scatter, namely, input voltage control and full scale voltage settings. The scatter present in these tests strongly emphasizes the need for rigorous experimental techniques to be followed during ultrasonic NDE on flight hardware. Any variation of input voltage during a test will cause a corresponding variation in the signal time series output. The contribution to uncertainty by the full scale voltage setting involves the recording of the ultrasonic NDE signal. In the capturing of signal time series, in order to take advantage of the 8-bit digitizer, one must try to have the full scale reading and the signal amplitude equal or there will be less than 256 digitized levels. In the Signal Time Series CT30A, an extract

shown in Figure 5.27, there appears to be approximately 120 digitized levels or the equivalent of a 7-bit digitizer. However, there is equipment currently available with more digitized levels which should be used on production ultrasonic NDE.

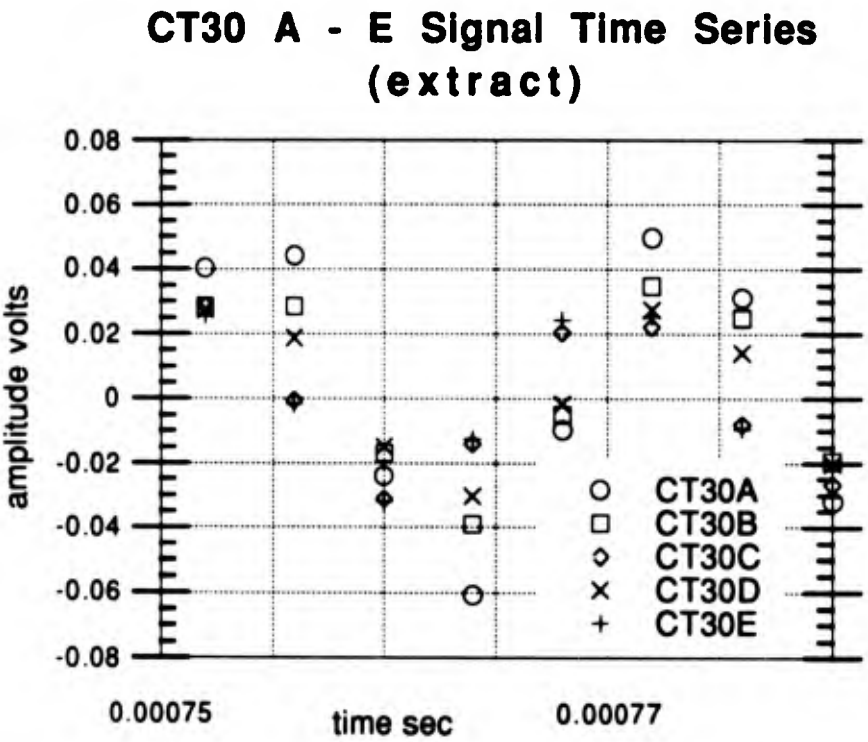

Figure 5.27. Extract of Signal Time Series of CT30 A-E (Shows order high to low, A, B, D, C, E).

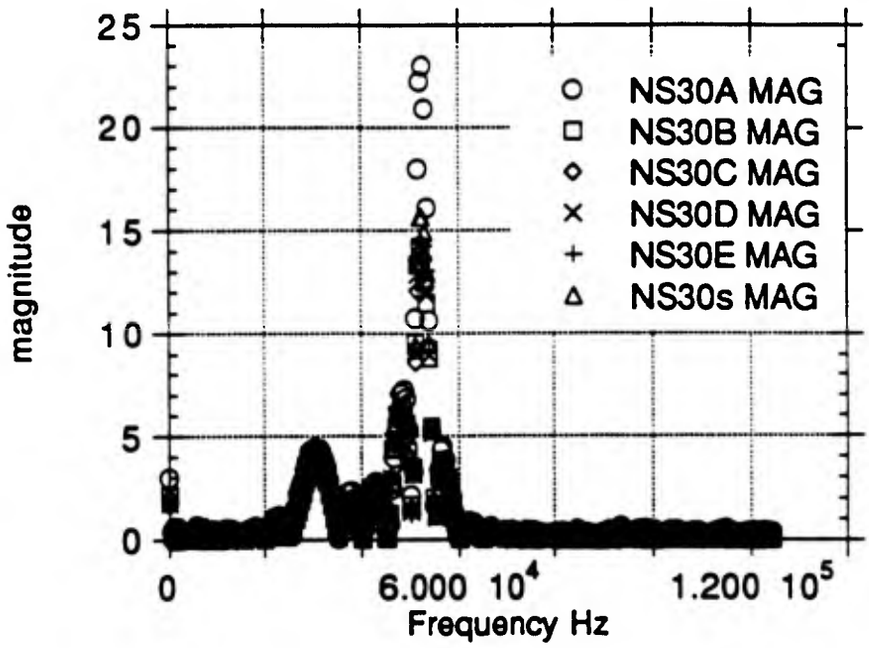

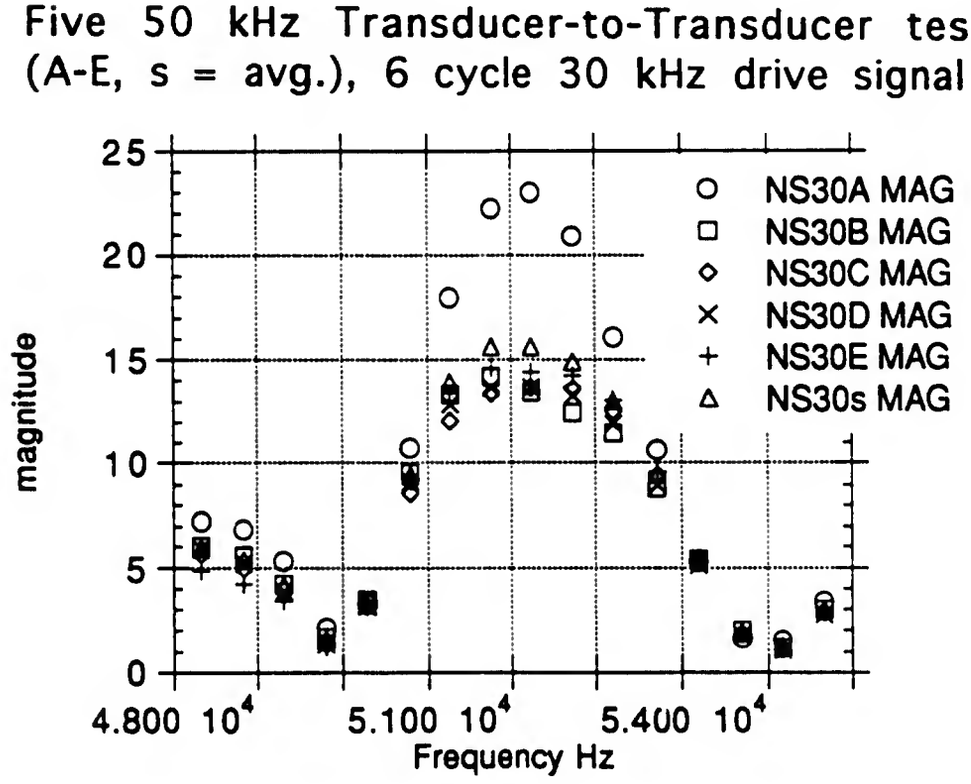

Figure 5.28 a, and b. Transducer Spectrum, Magnitude versus Frequency (6 cycle 30 kHz drive signal, Input Equivalent).

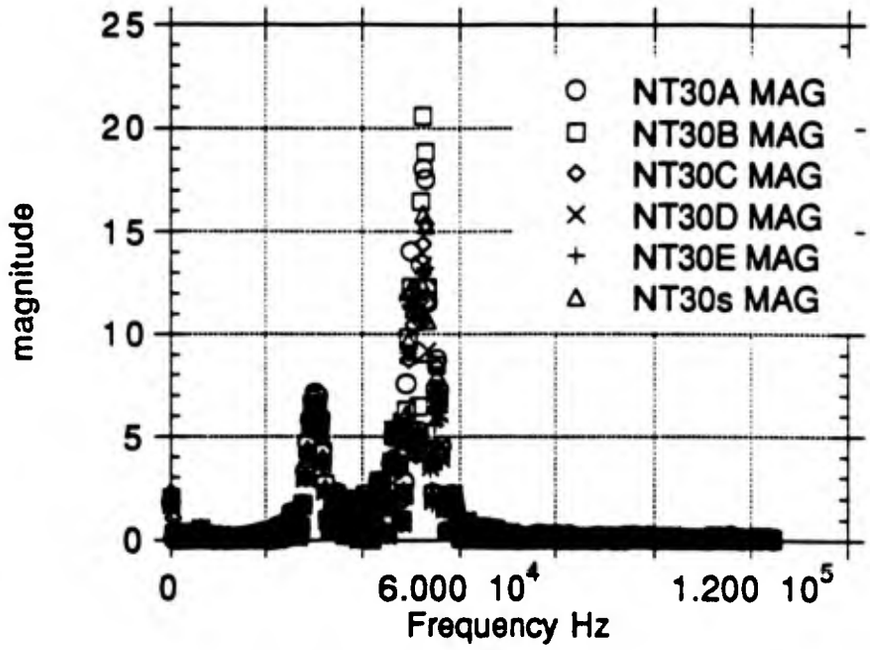

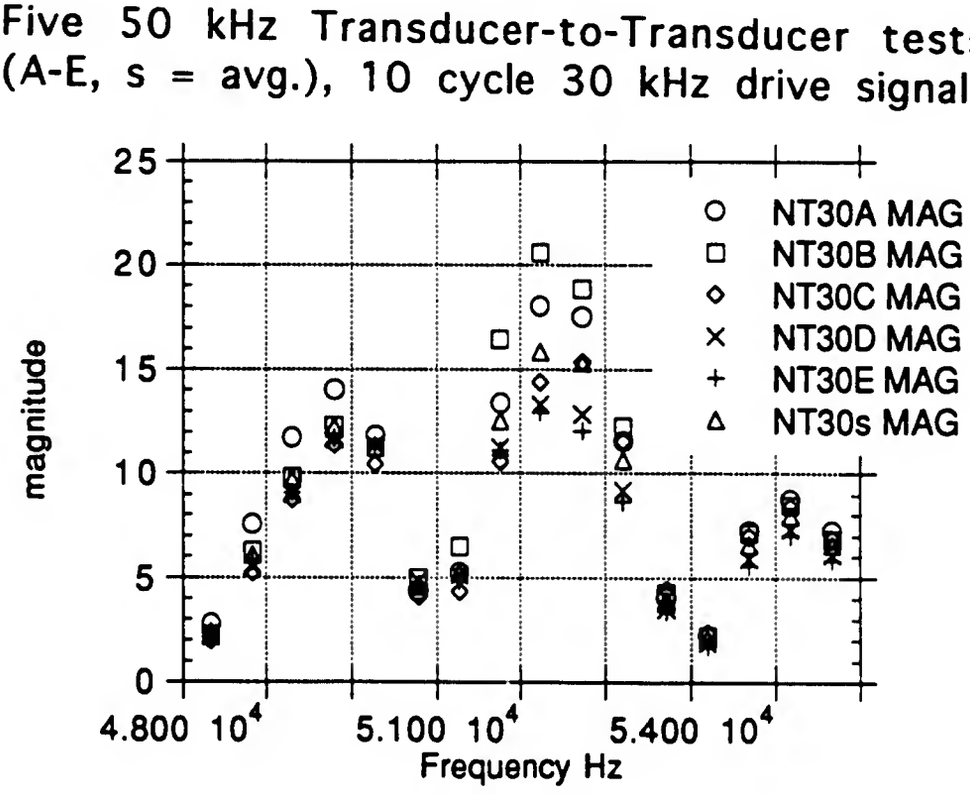

Figure 5.29 a, and b. Transducer Spectrum, Magnitude versus Frequency (10 cycle 30 kHz drive signal, Input Equivalent).

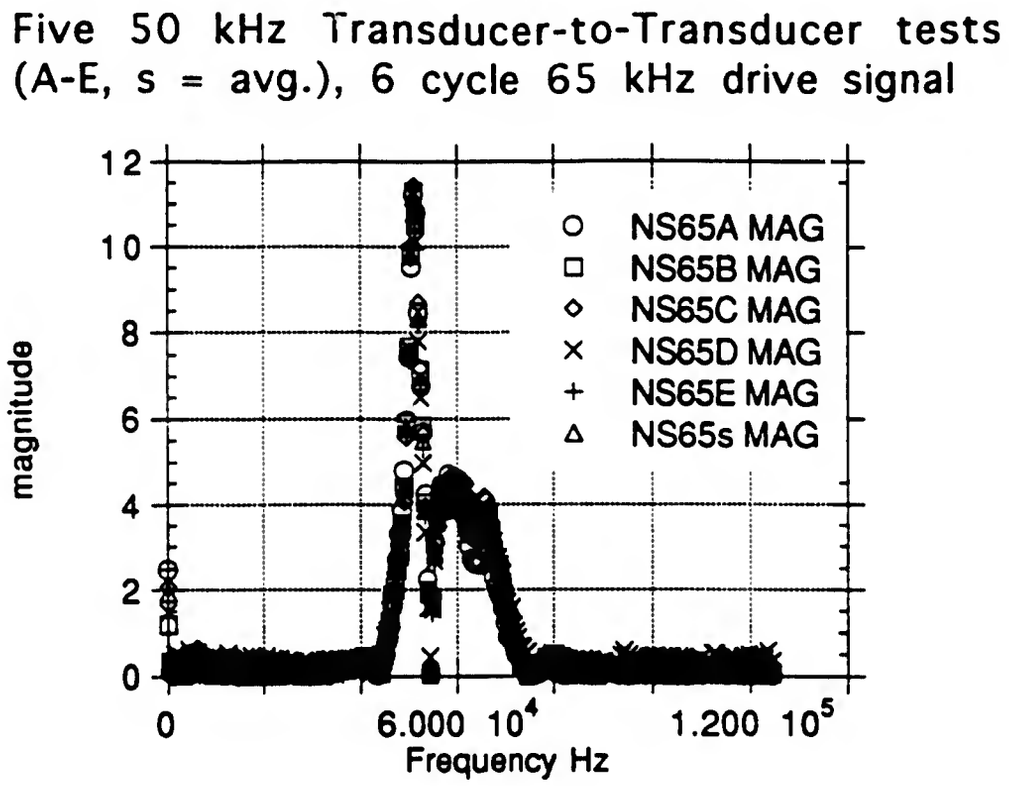

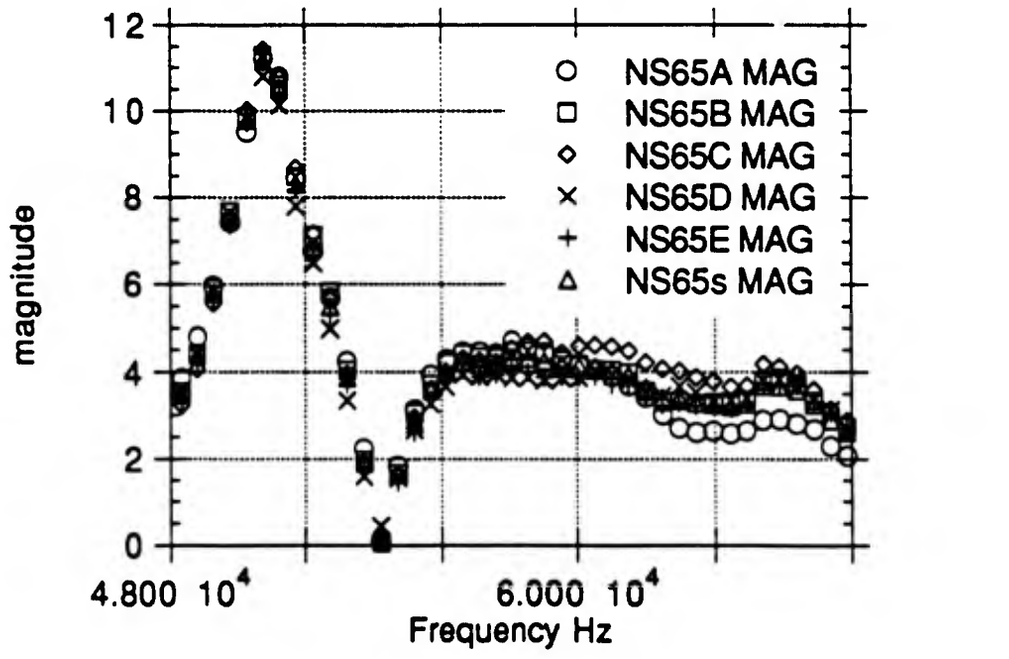

Figure 5.30 a, and b. Transducer Spectrum, Magnitude versus Frequency (6 cycle 65 kHz drive signal, Input Equivalent).

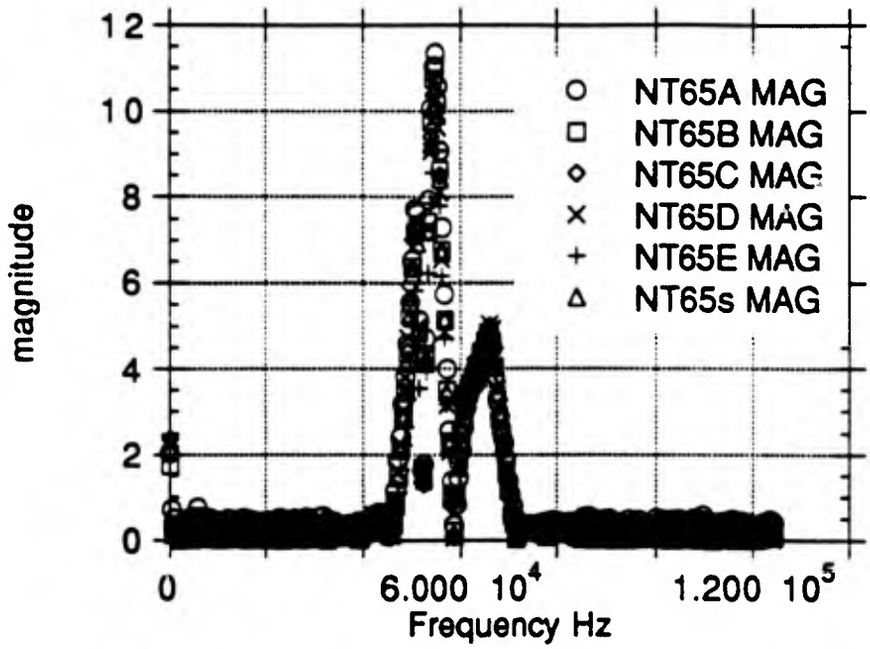

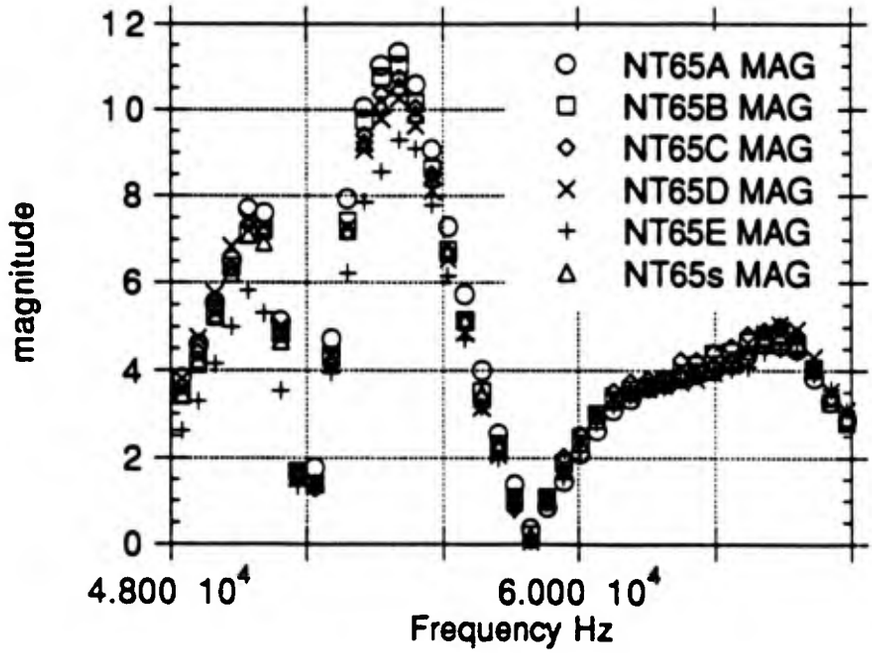

Figure 5.31 a, and b. Transducer Spectrum, Magnitude versus Frequency (10 cycle 65 kHz drive signal, Input Equivalent).

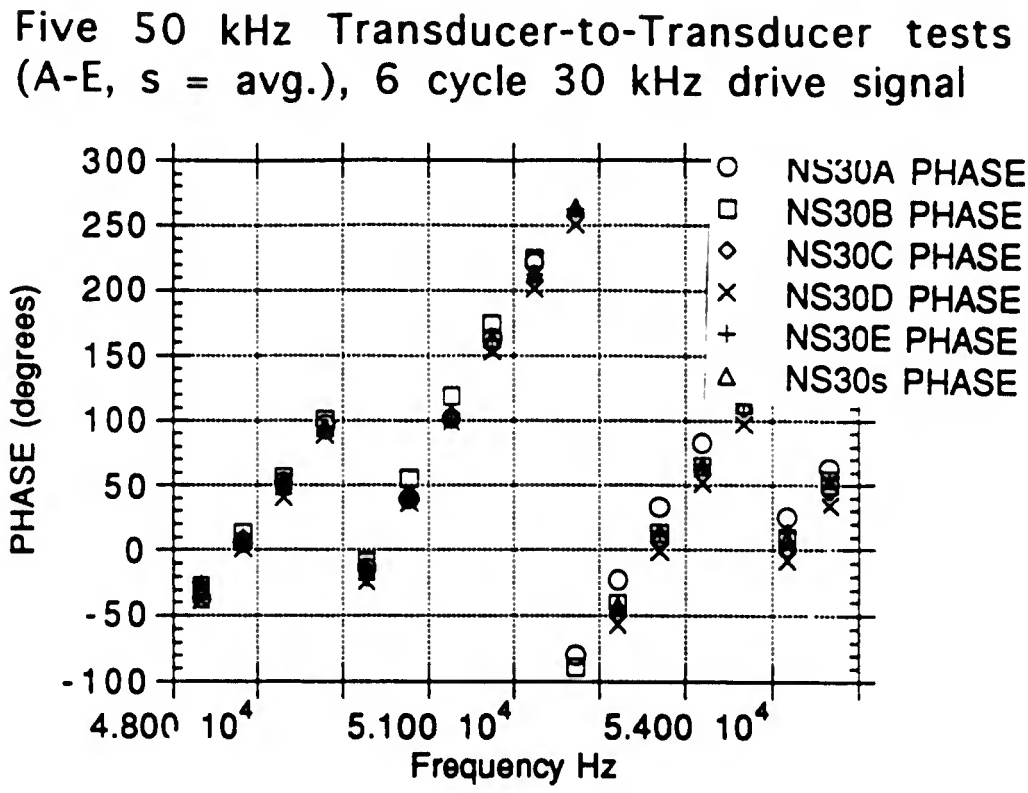

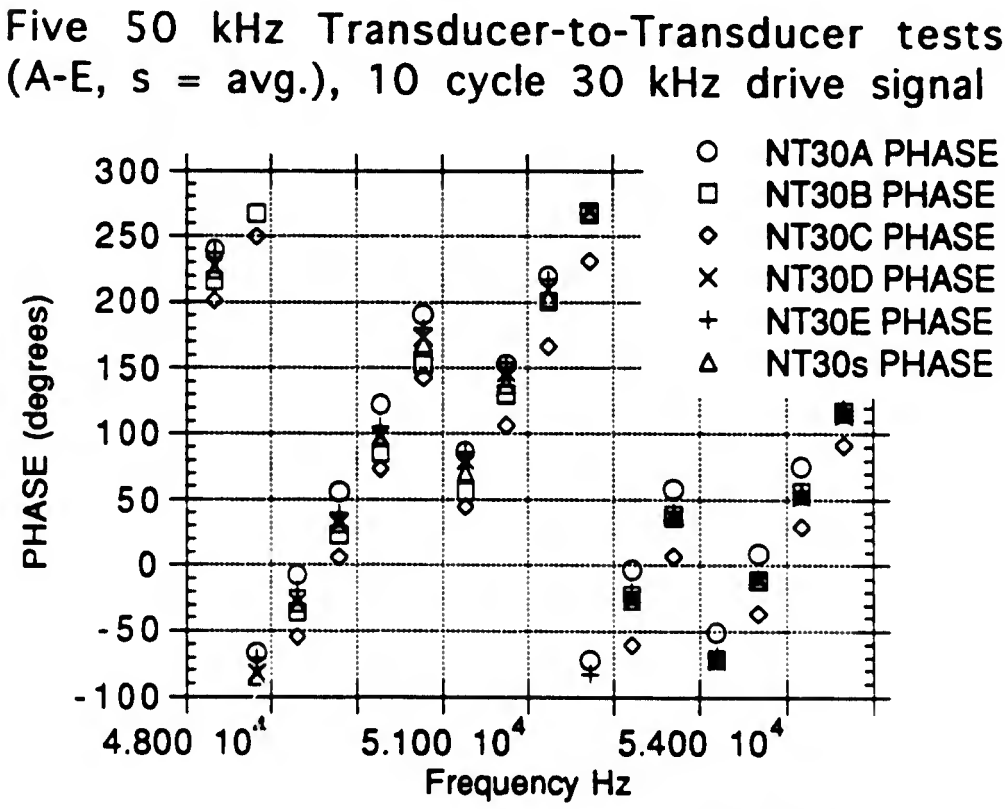

Figure 5.32 a, and b. Transducer Spectrum, Phase versus Frequency (6 and 10 cycle 30 kHz drive signal, Input Equivalent).

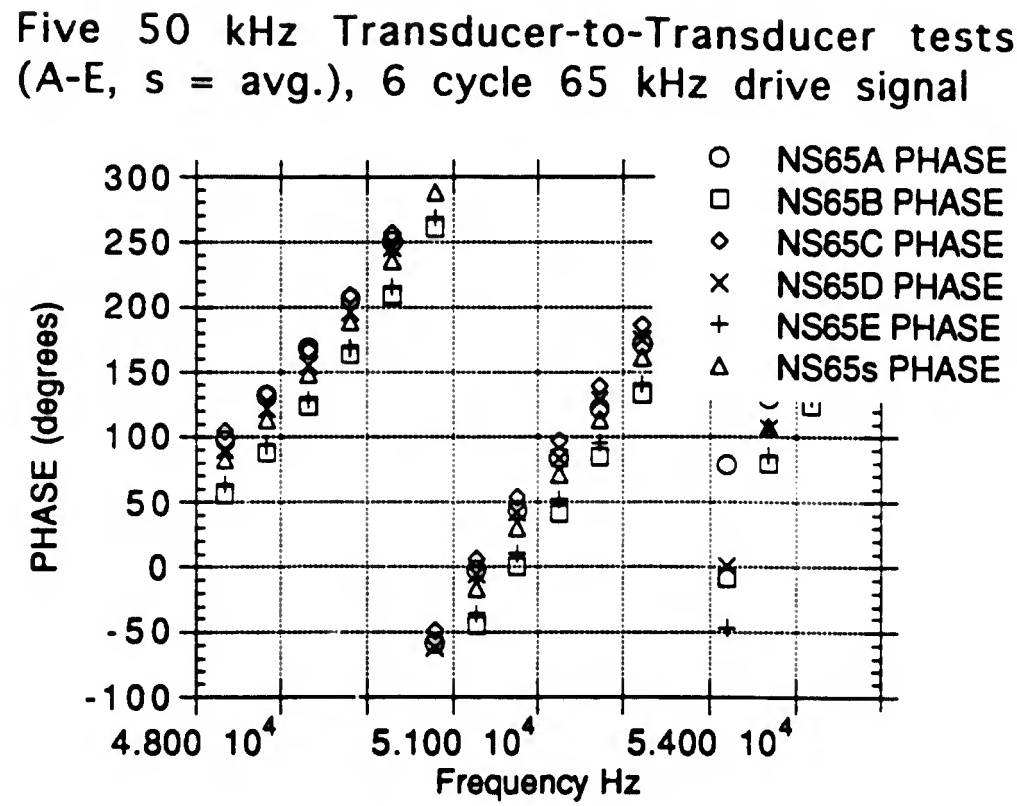

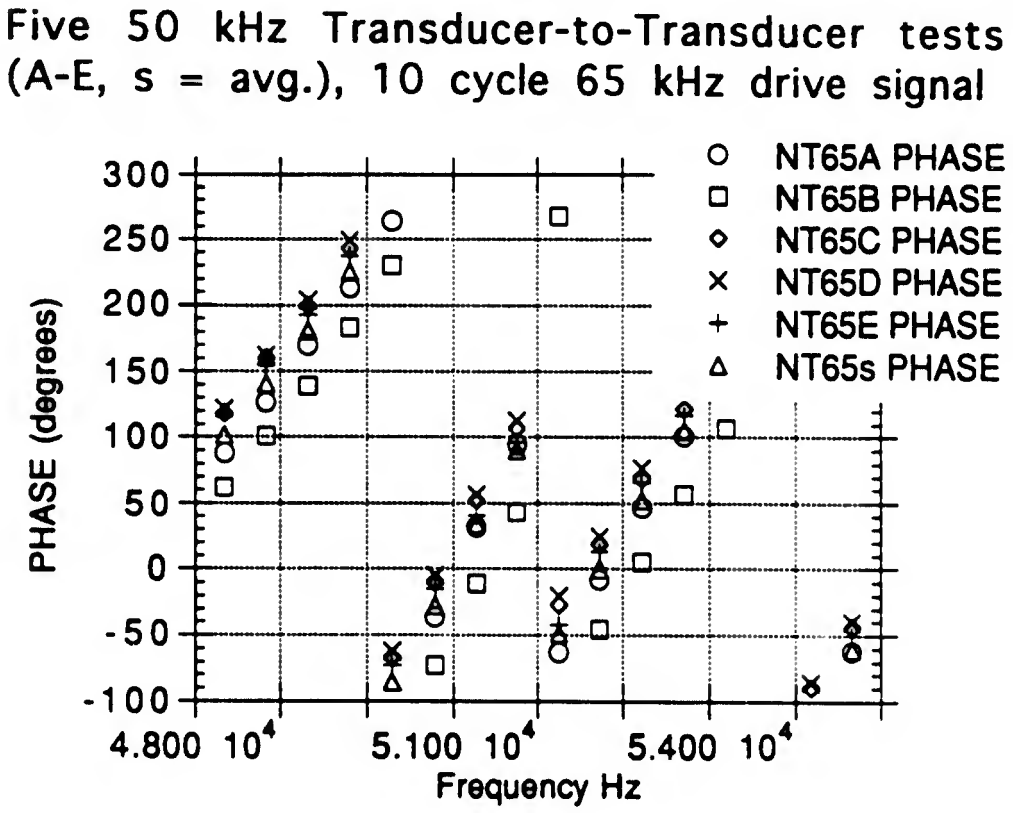

Figure 5.33 a, and b. Transducer Spectrum, Phase versus Frequency (6 and 10 cycle 65 kHz drive signal, Input Equivalent).

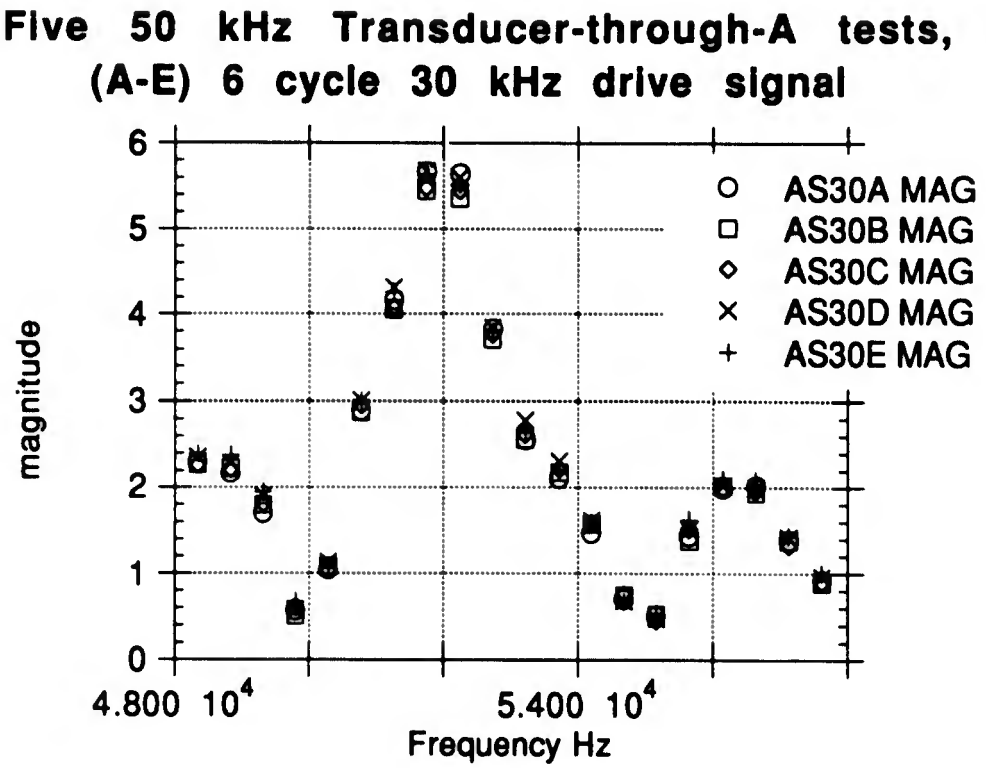

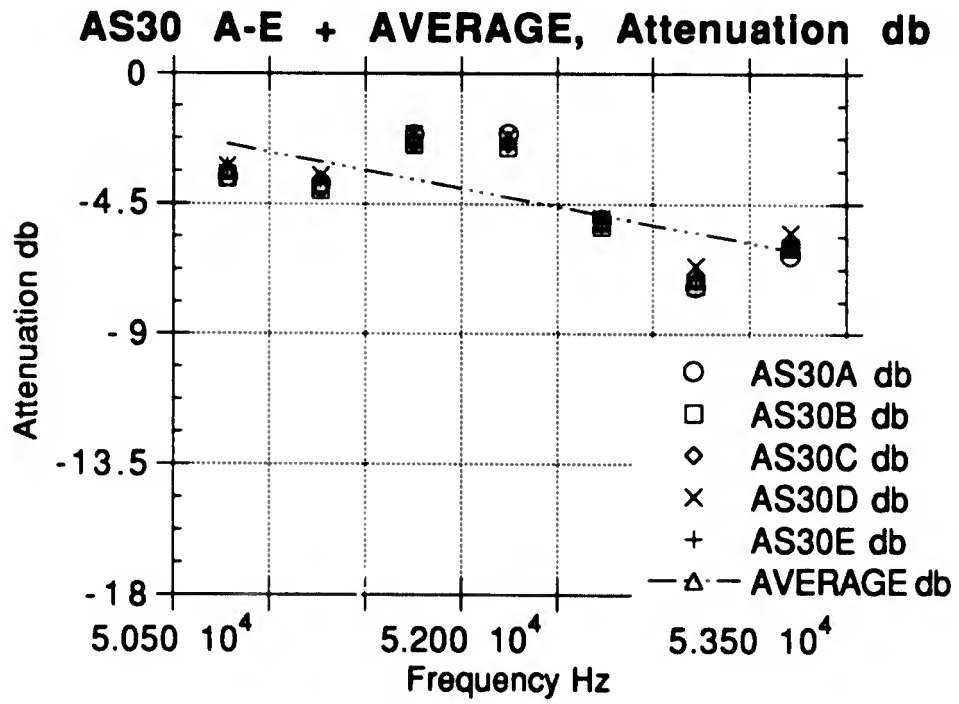

Figure 5.34 a, and b. Magnitude vs Frequency, and Attenuation vs Frequency (A-E 6 cycle 30 kHz drive signal).

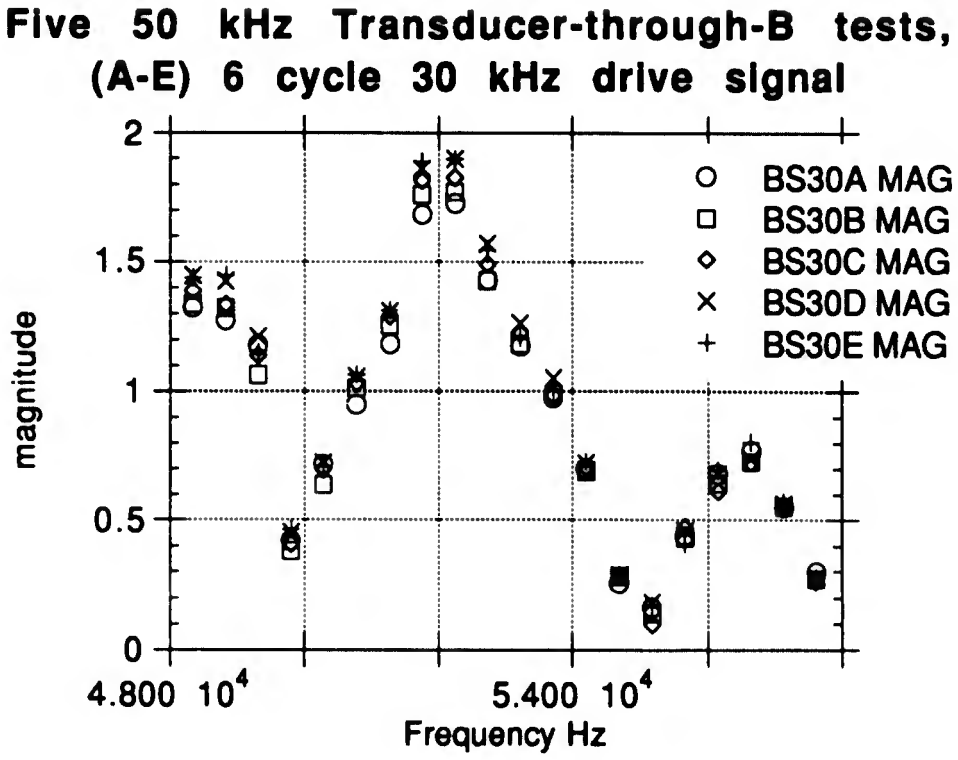

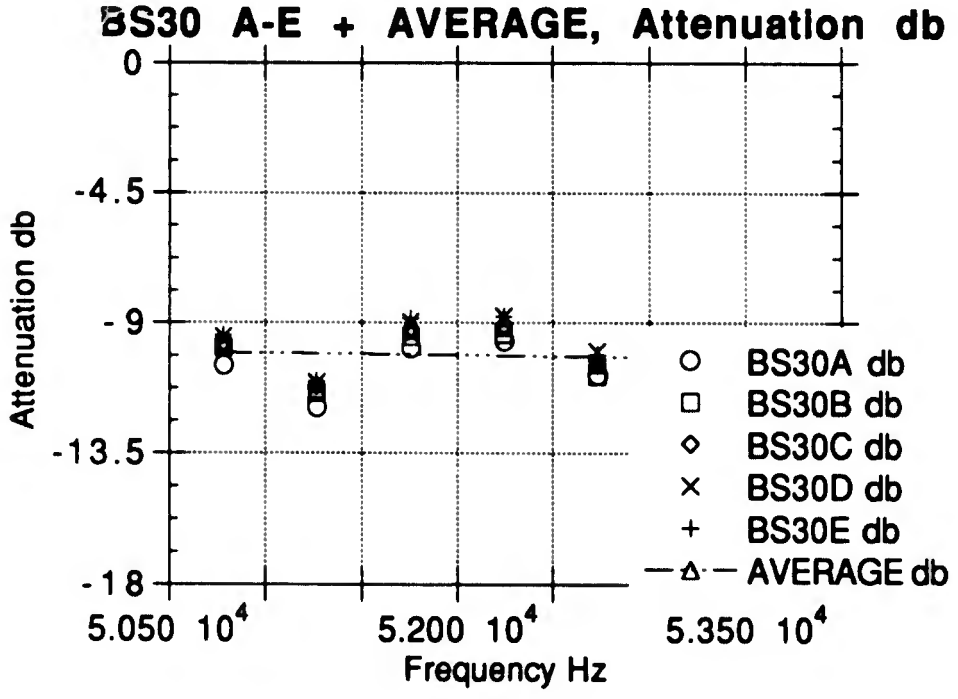

Figure 5.35 a, and b. Magnitude vs Frequency, and Attenuation vs Frequency (A-E 6 cycle 30 kHz drive signal).

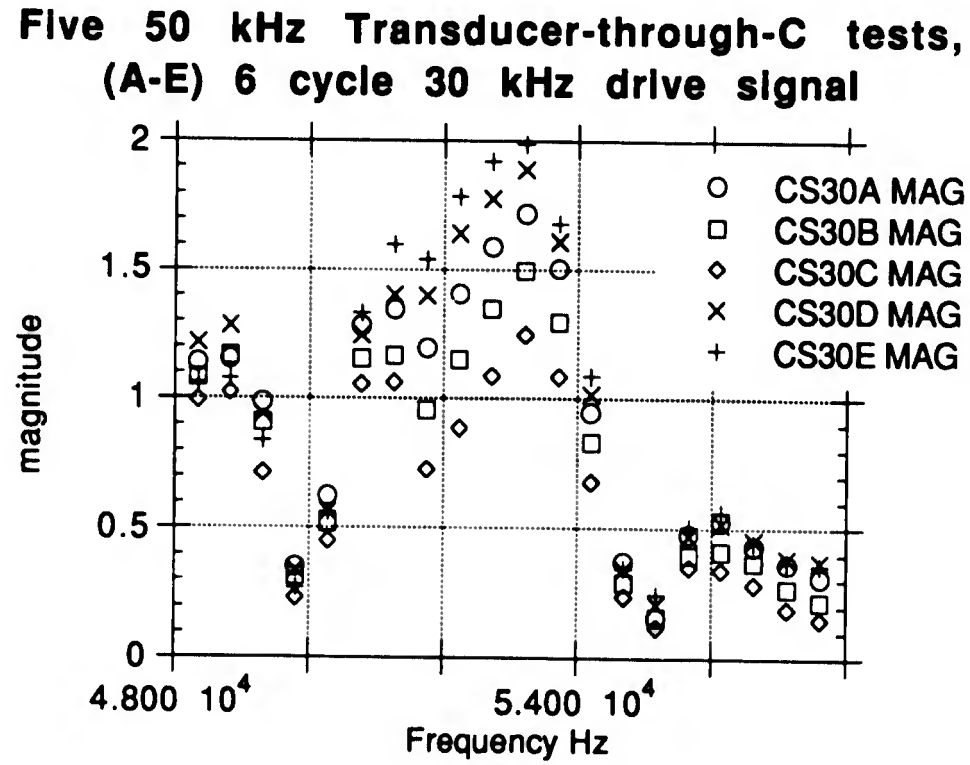

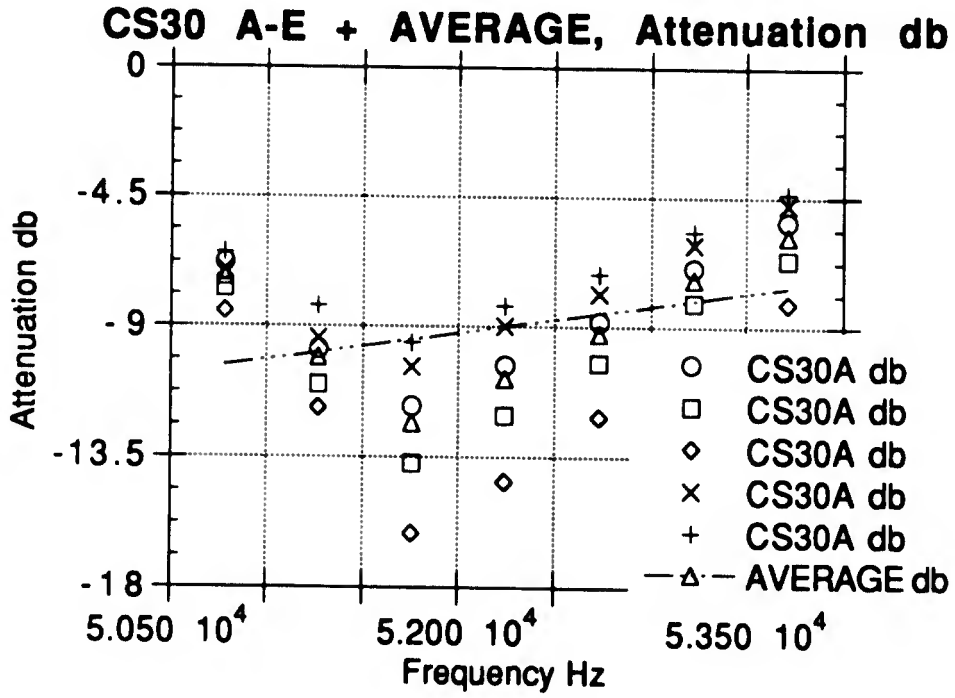

Figure 5.36 a, and b. Magnitude vs Frequency, and Attenuation vs Frequency (A-E 6 cycle 30 kHz drive signal).

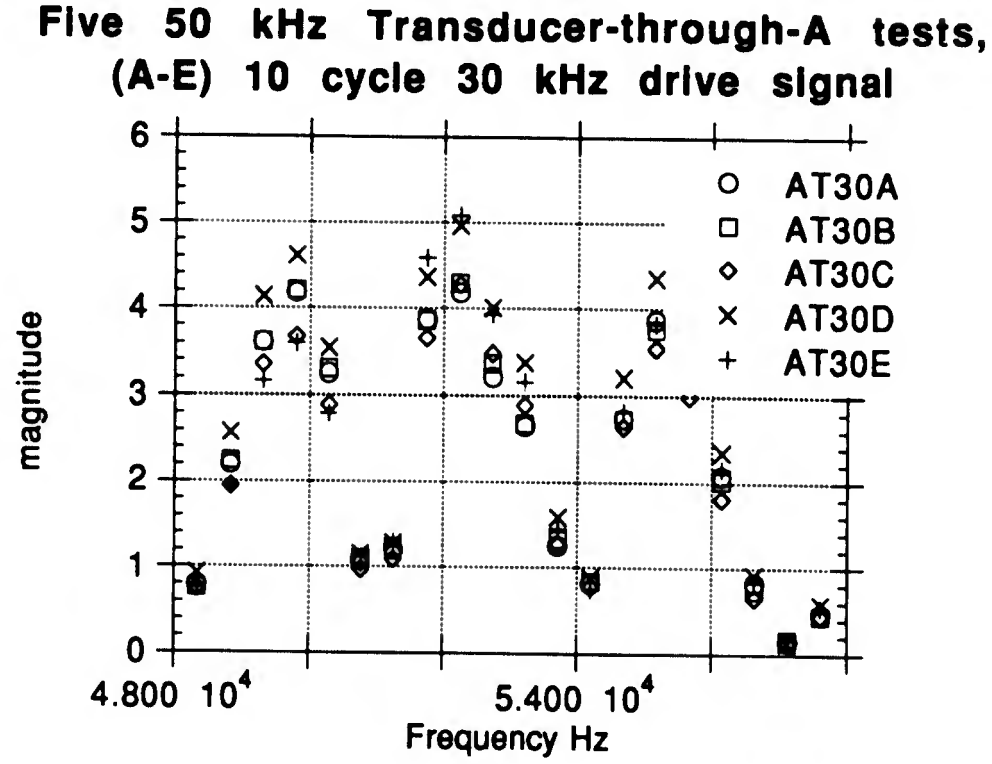

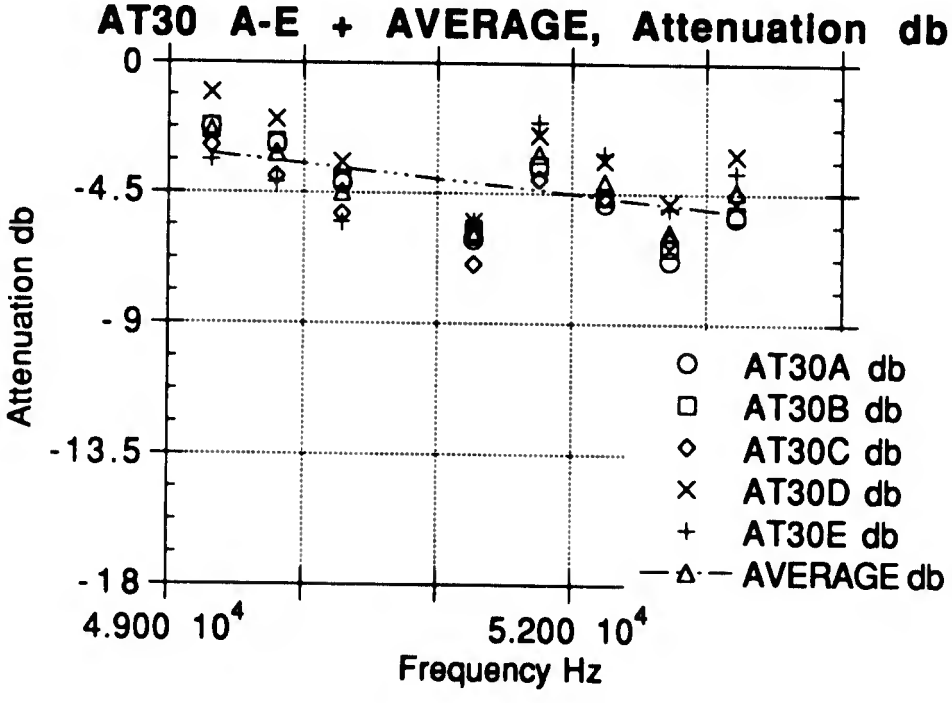

Figure 5.37 a, and b. Magnitude vs Frequency, and Attenuation vs Frequency (A-E 10 cycle 30 kHz drive signal).

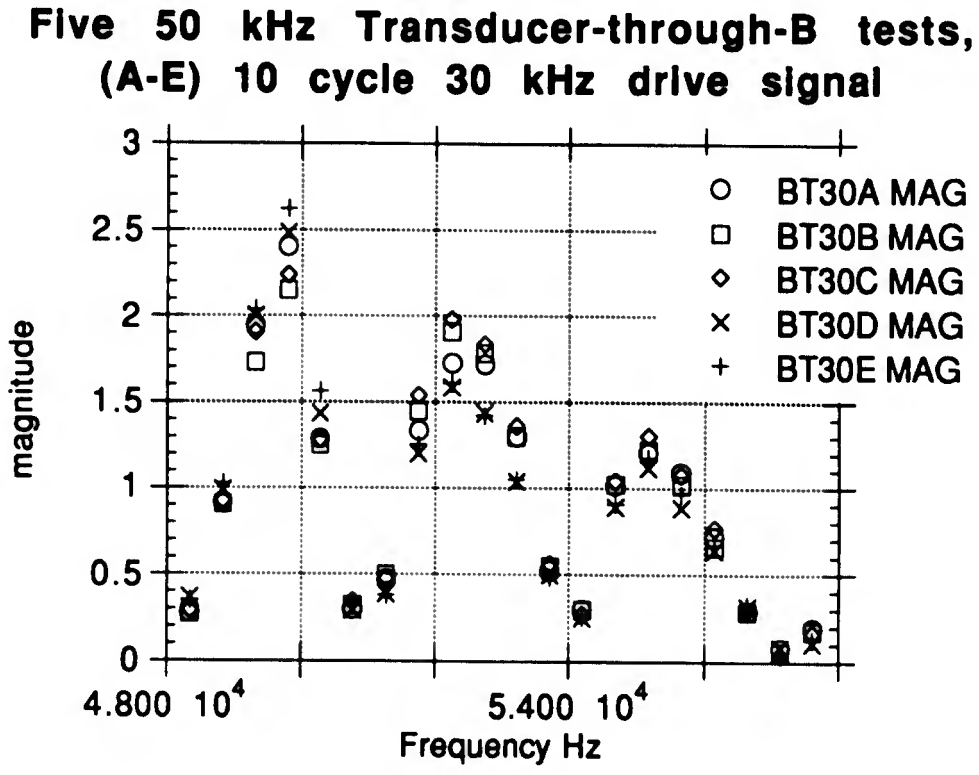

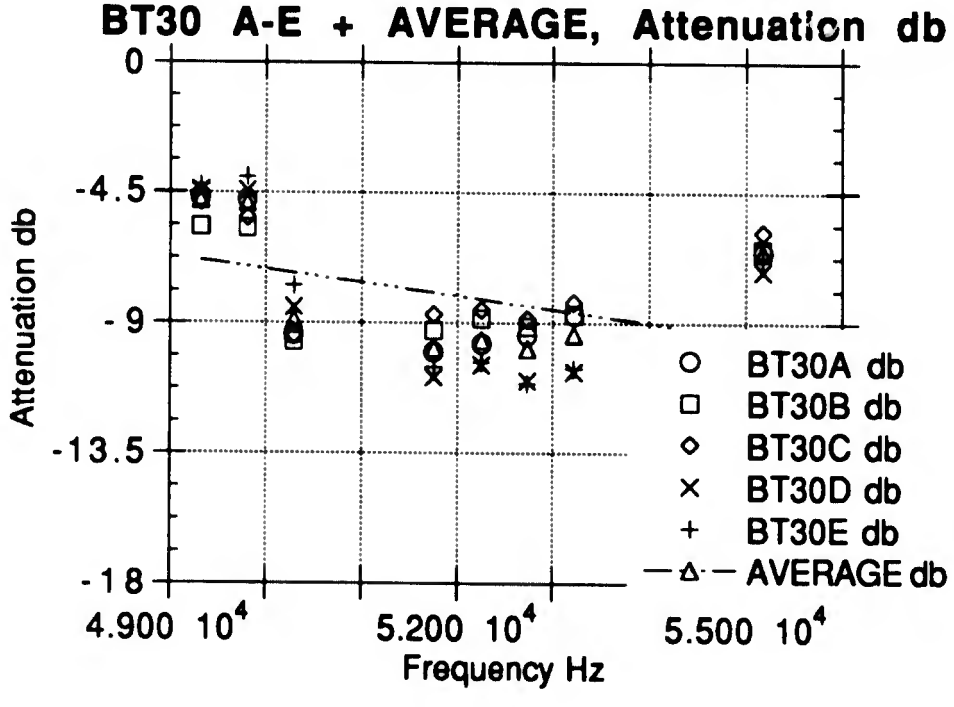

Figure 5.38 a, and b. Magnitude vs Frequency, and Attenuation vs Frequency (A-E 10 cycle 30 kHz drive signal).

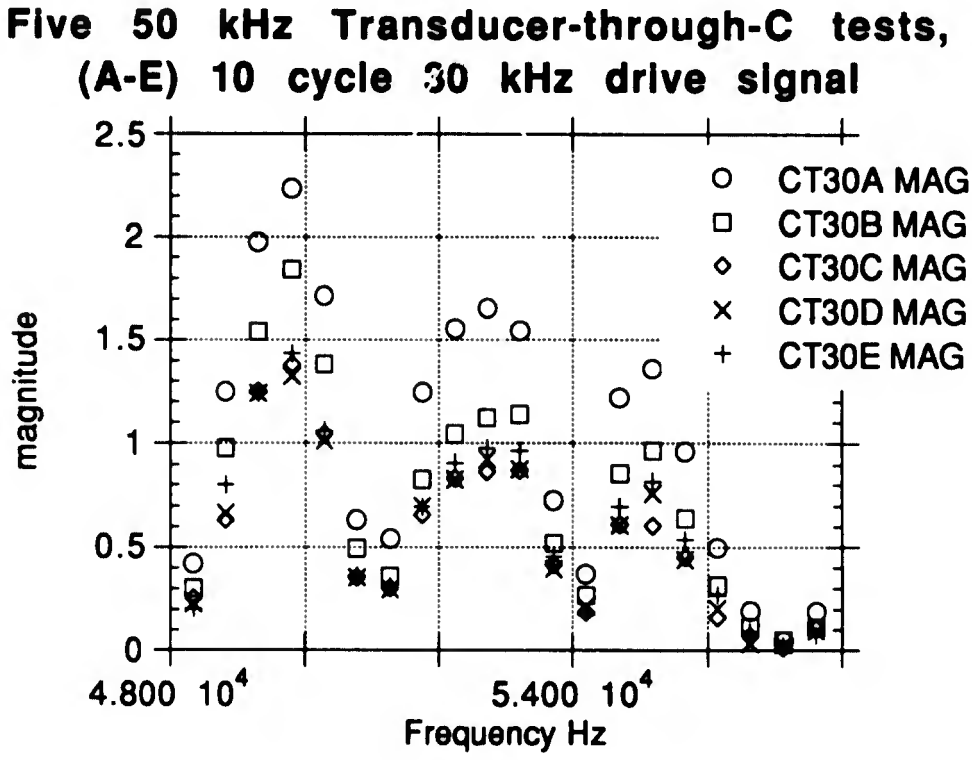

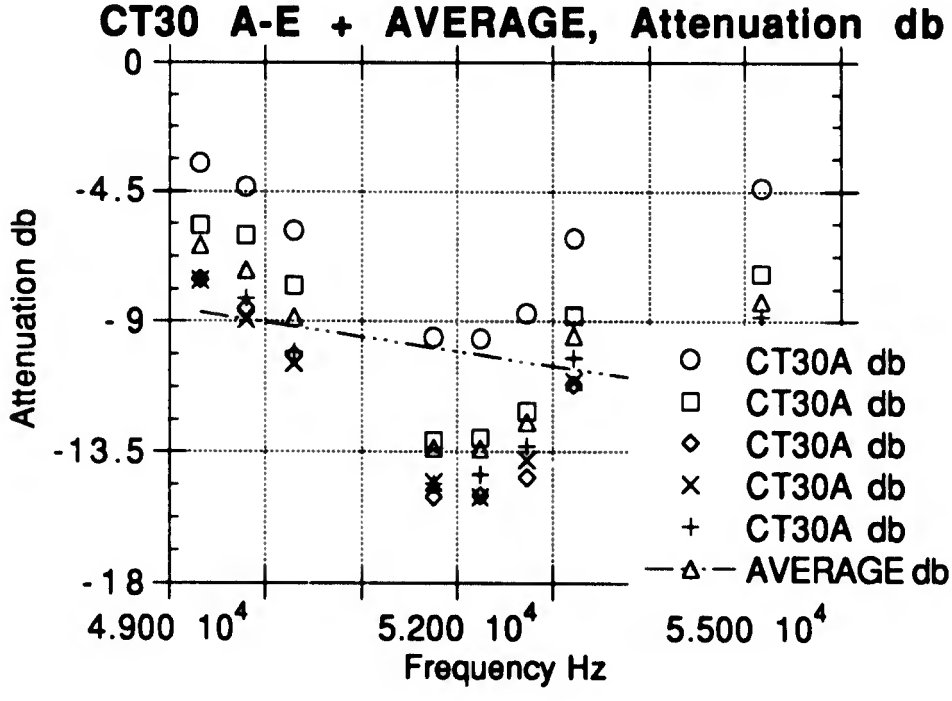

Figure 5.39 a, and b. Magnitude vs Frequency, and Attenuation vs Frequency (A-E 10 cycle 30 kHz drive signal).

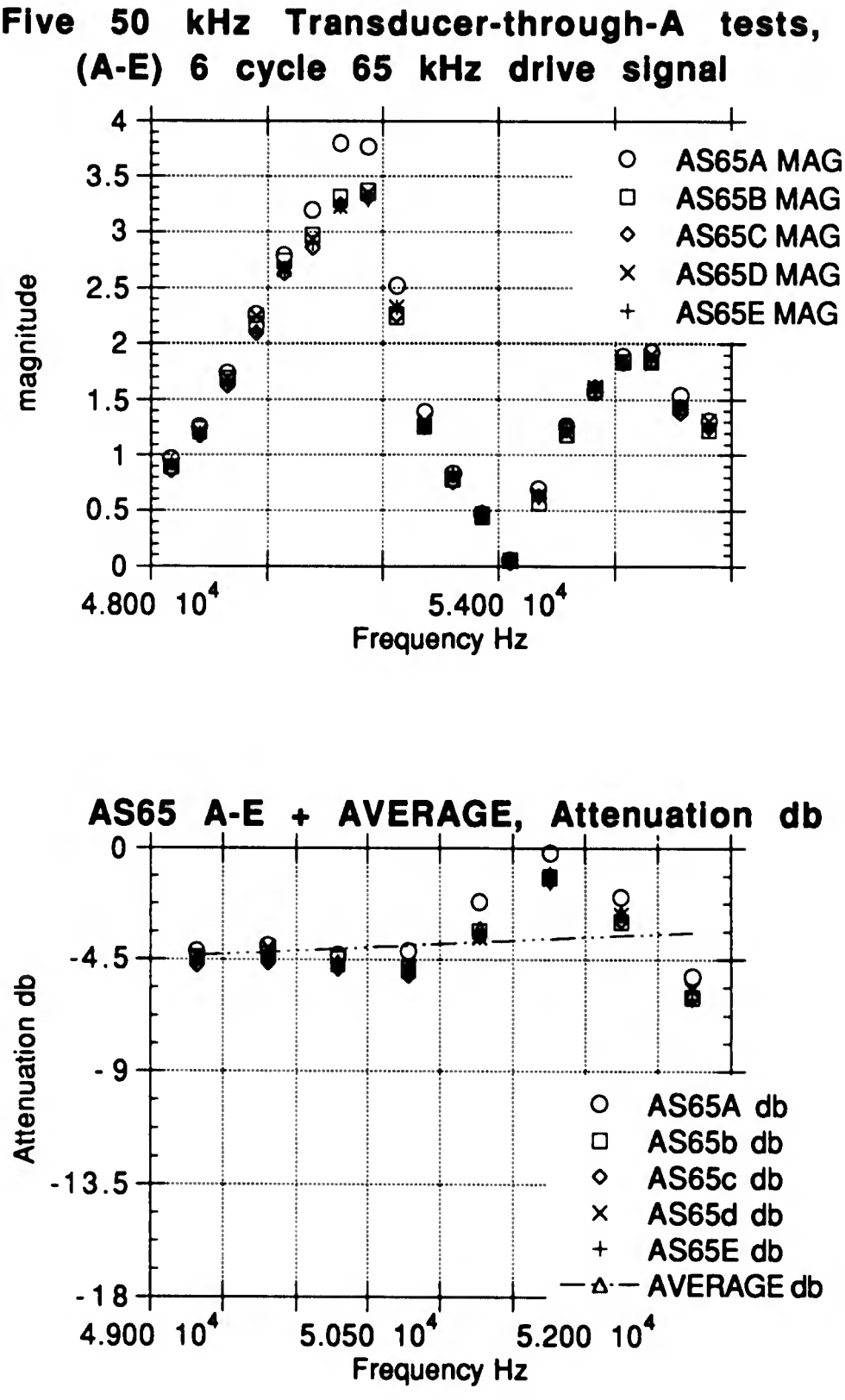

Figure 5.40 a, and b. Magnitude vs Frequency, and Attenuation vs Frequency (A-E 6 cycle 65 kHz drive signal).

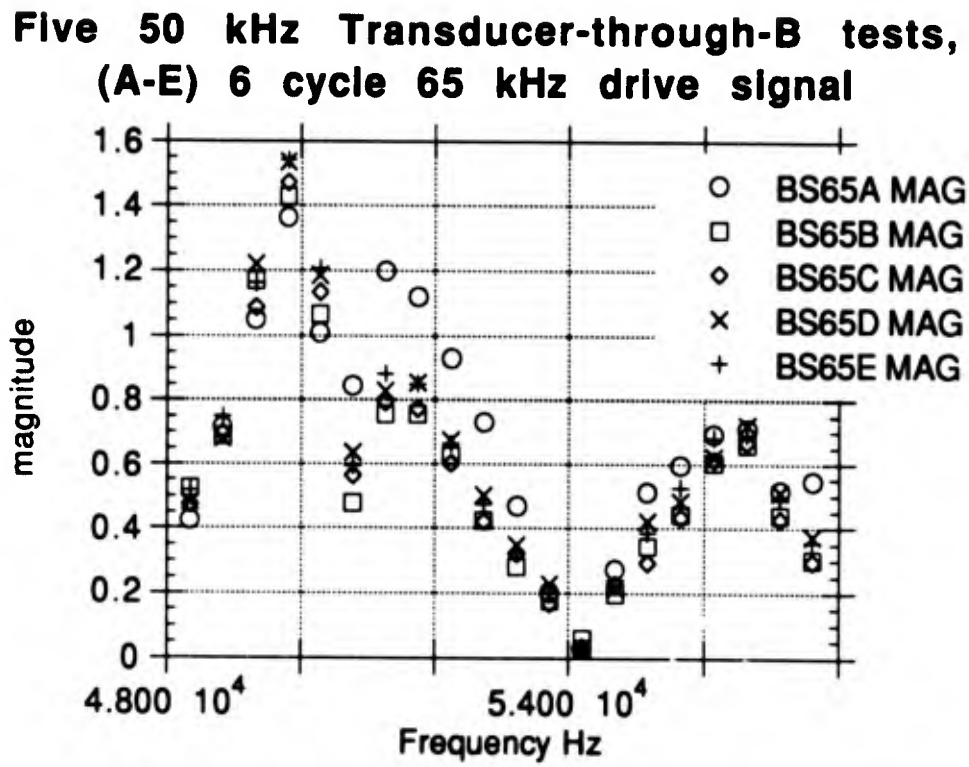

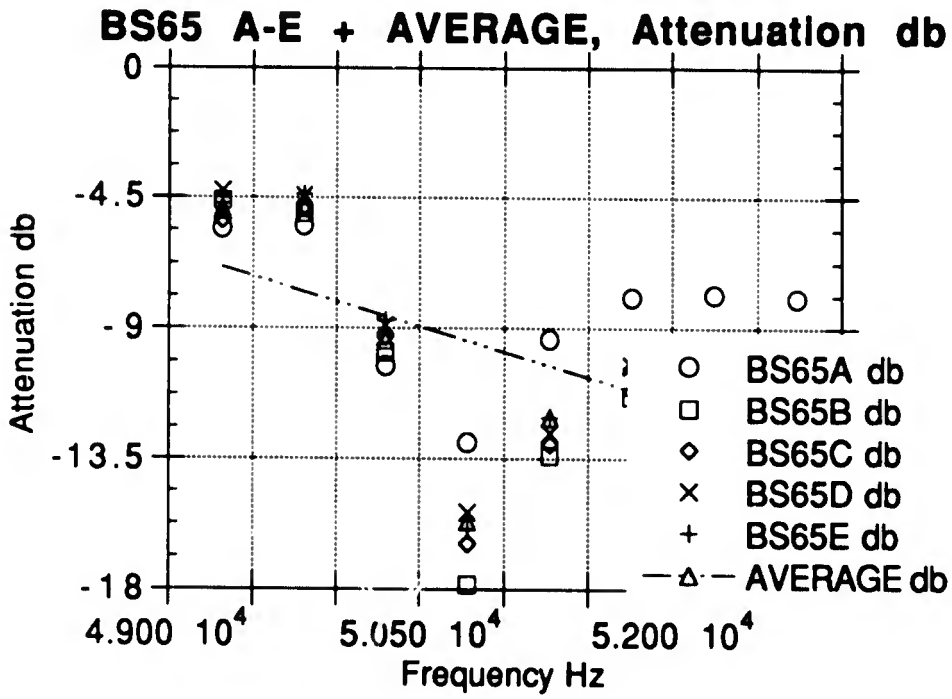

Figure 5.41 a, and b. Magnitude vs Frequency, and Attenuation vs Frequency (A-E 6 cycle 65 kHz drive signal).

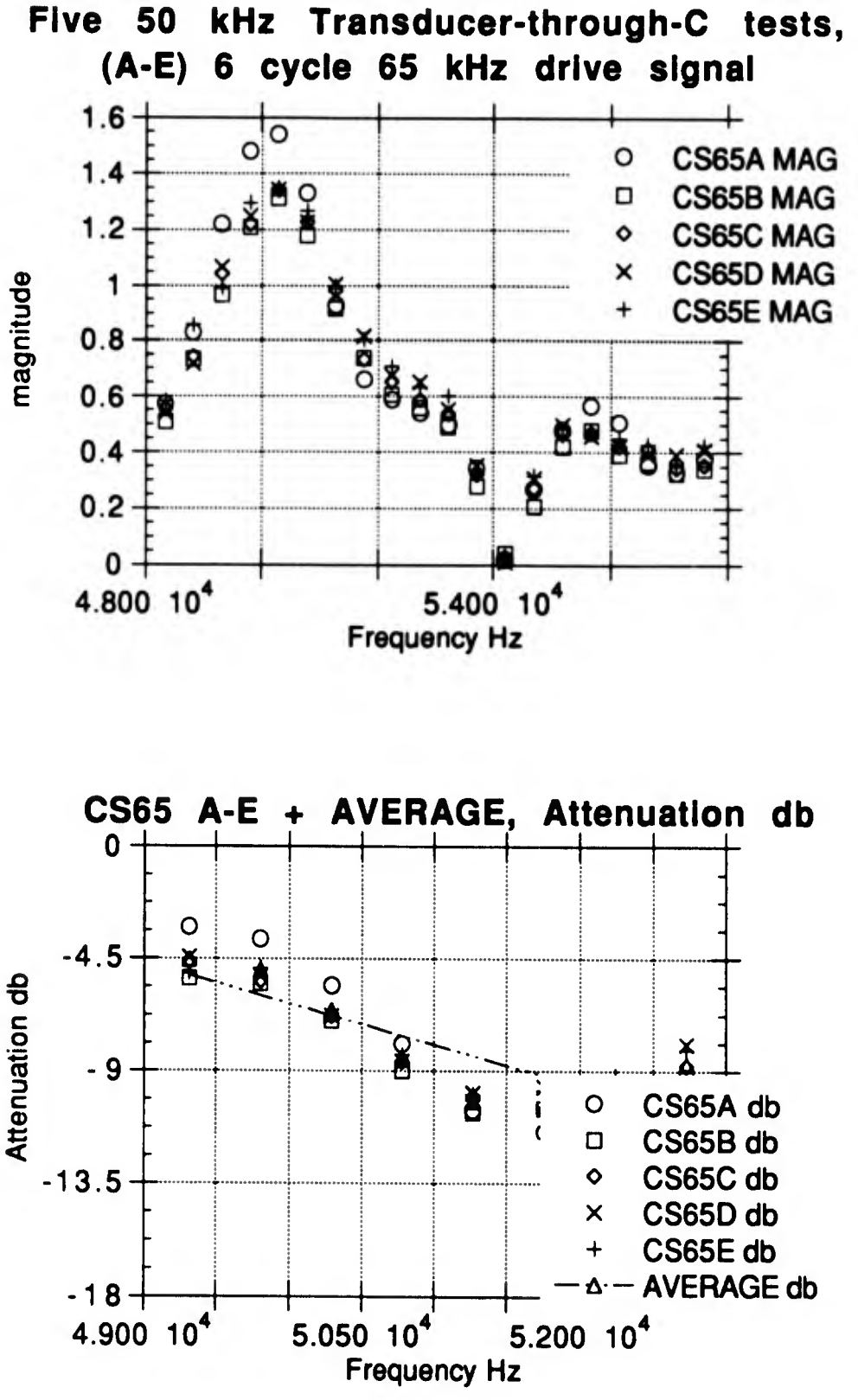

Figure 5.42 a, and b. Magnitude vs Frequency, and Attenuation vs Frequency (A-E 6 cycle 65 kHz drive signal).

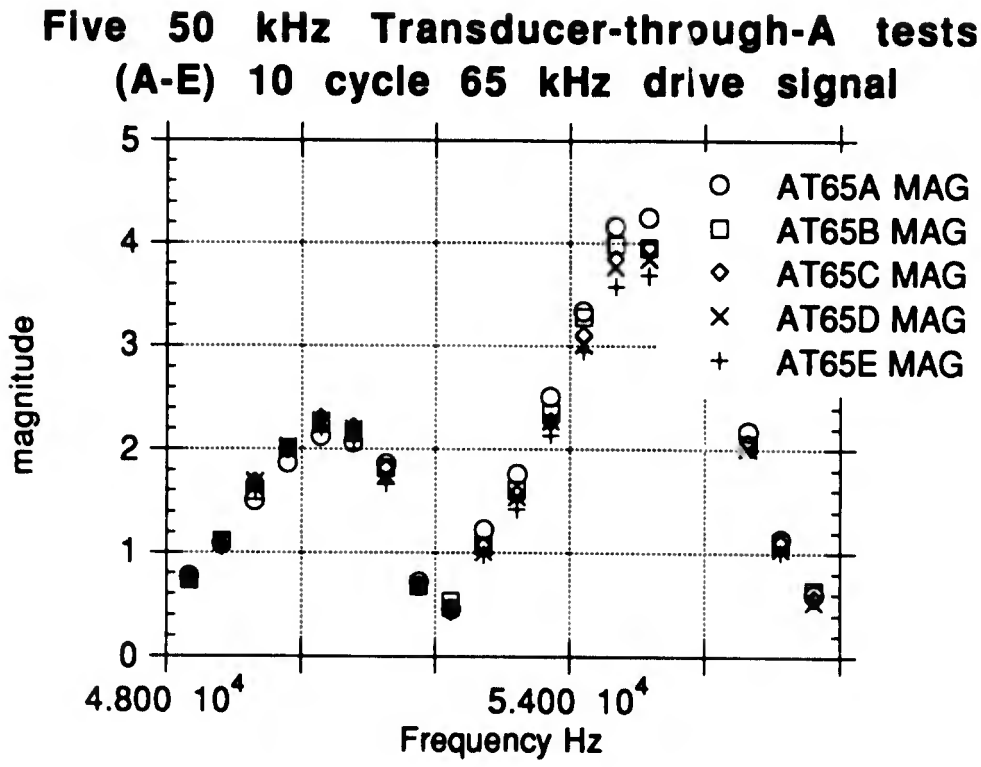

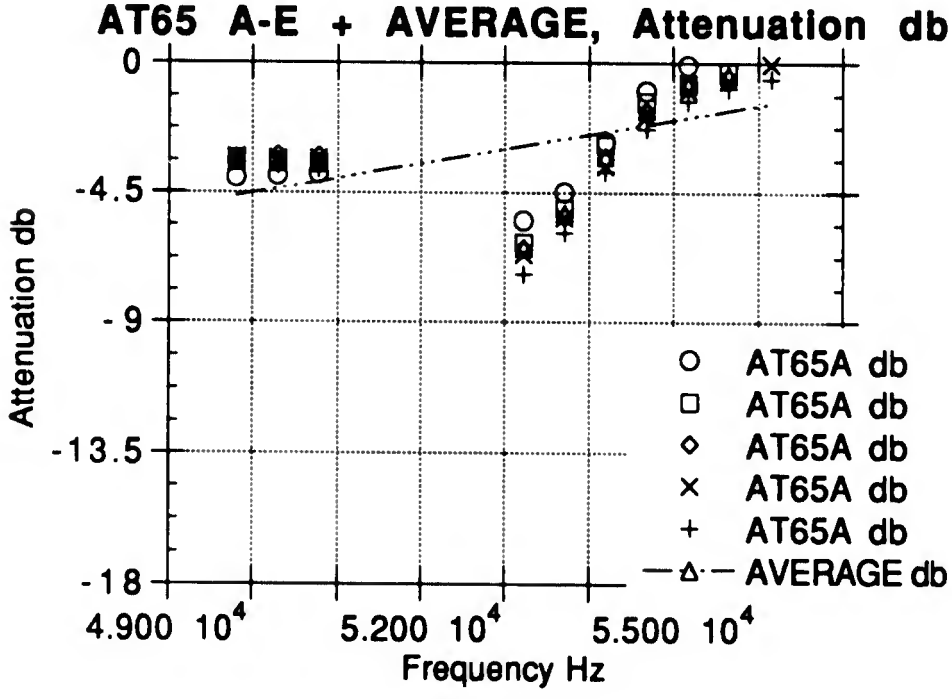

Figure 5.43 a, and b. Magnitude vs Frequency, and Attenuation vs Frequency (A-E 10 cycle 65 kHz drive signal).

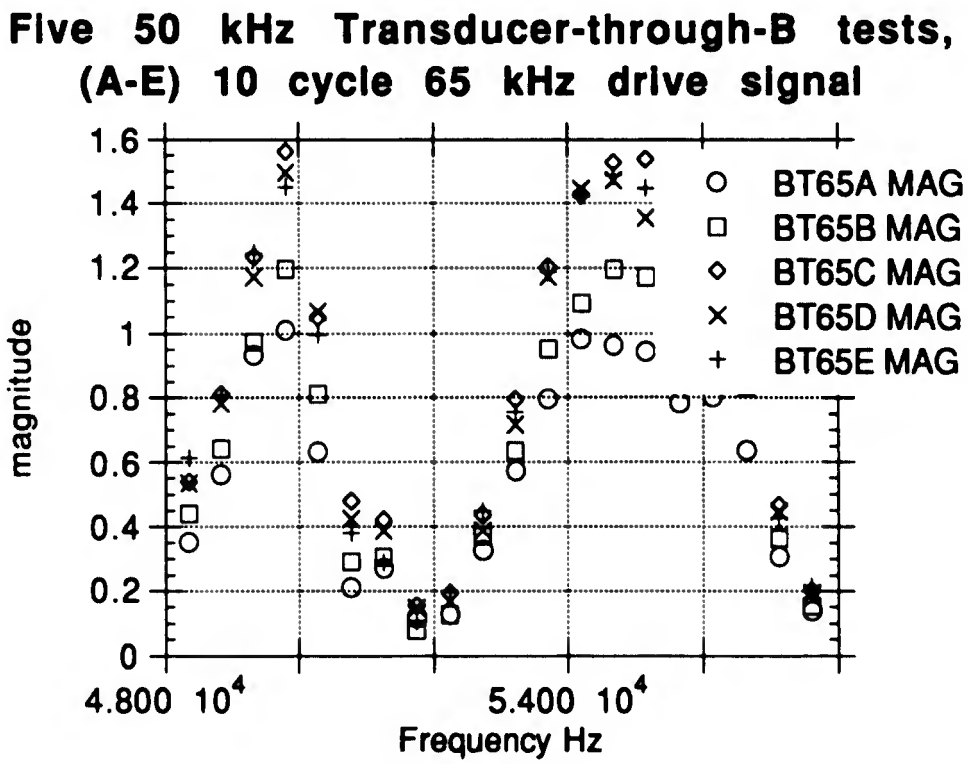

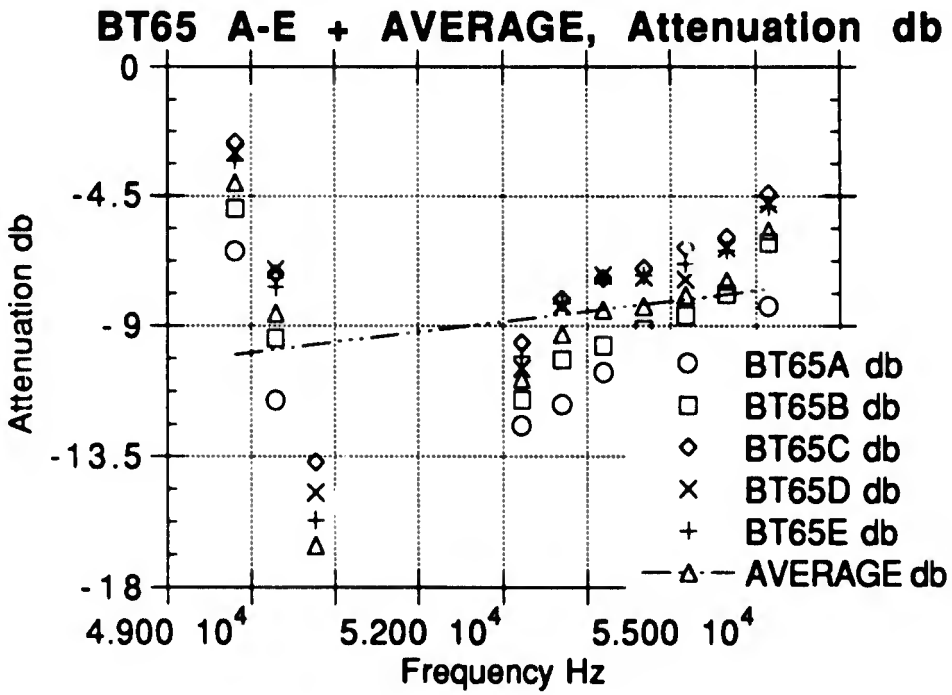

Figure 5.44 a, and b. Magnitude vs Frequency, and Attenuation vs Frequency (A-E 10 cycle 65 kHz drive signal).

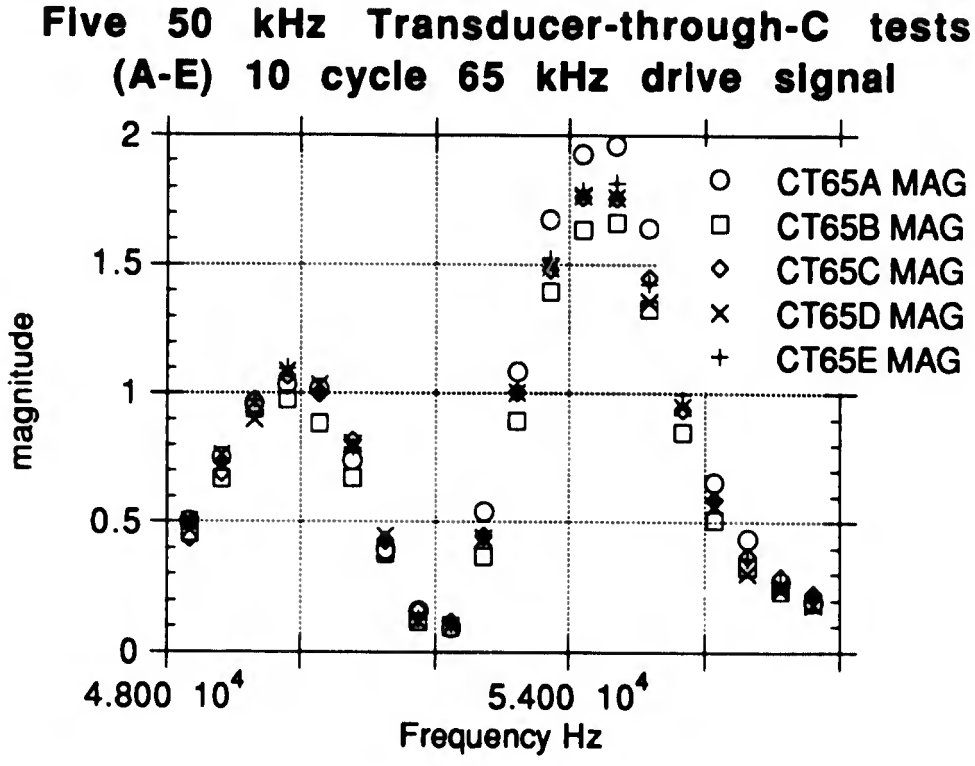

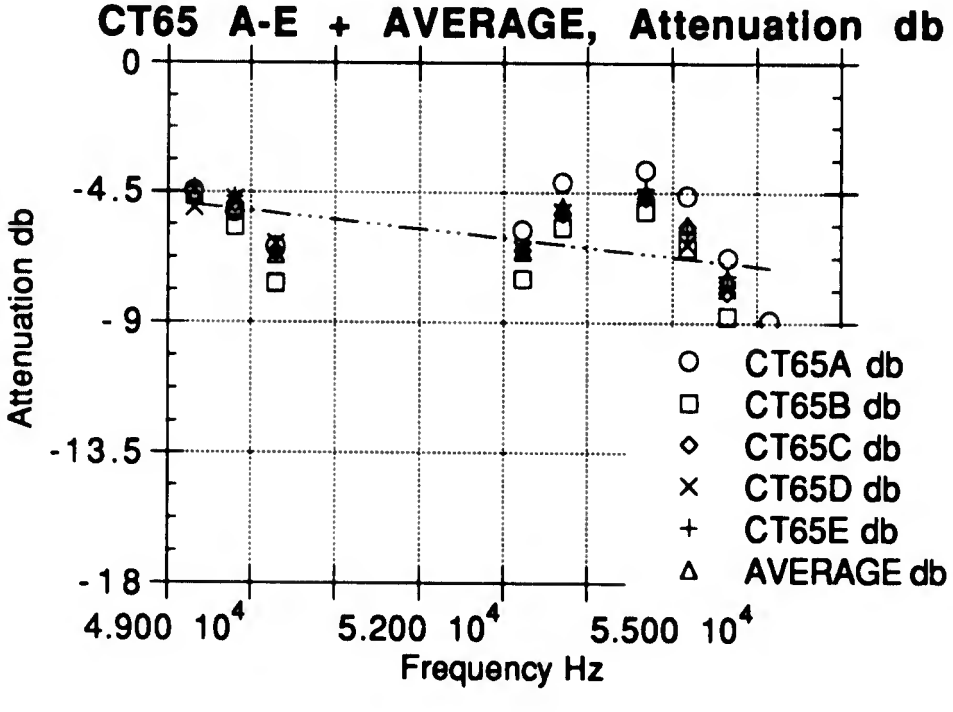

Figure 5.45 a, and b. Magnitude vs Frequency, and Attenuation vs Frequency (A-E 10 cycle 65 kHz drive signal).

The lower part of Figures 5.28 - 5.31, part b, emphasizes the differences among the five transducer-transducer tests. The attenuation curves, part b in Figures 5.34 - 5.45, used the average values in Figures 5.28 - 5.31, for the input equivalent. The spread in the magnitude versus frequency plots seems to be greatest in the transducer-through-C test in each of the four groupings. The attenuation, over the limited frequency range presented, shows a downward trend with increasing frequency in eight of twelve groups in the Figures.

The frequencies shown in the above Figures were selected on the basis of the normalized transducer magnitude . In order to obtain reliable information, only frequencies with a normalized magnitude greater than half the peak magnitude were used. Table 5.13 lists the normalized magnitudes for each transducer-transducer test. The normalized peak magnitude, value of 1.0, was found at several frequencies.

Table 5.13. Normalized Transducer Magnitude versus Frequency.

Frequency Hz	N30S norm	N30T norm	N65S norm	N65T norm
48340	0.38	0.15	0.31	0.33
48828	0.34	0.38	0.39	0.40
49316	0.27	0.61	0.52	0.50
49805	0.10	0.77	0.67	0.59
50293	0.21	0.71	0.88	0.67
50781	0.60	0.29	1.0	0.66
51270	0.89	0.33	0.94	0.44
51758	1.0	0.79	0.75	0.15
52246	1.0	1.0	0.62	0.14
52734	0.95	0.97	0.49	0.41
53223	0.83	0.67	0.35	0.68
53711	0.61	0.25	0.17	0.88
54199	0.34	0.13	0.013	0.96
54687	0.12	0.41	0.15	1.0
55176	0.079	0.50	0.26	0.94
55664	0.19	0.42	0.32	0.80
56152	0.24	0.26	0.36	0.64

Since the experiments were performed on sample dimensions ranging from 8.5 to 13 cm the attenuation and standard deviation were reported in terms of db/cm. Table 5.14 depicts the average attenuation (db/cm) and associated standard deviation for the 12 groups of 5 tests each, associated with Figures 5.34 - 5.45. The resultant standard deviation was +/- 0.149 db/cm, and is shown as high and low bars in subsequent Figures, especially in Chapter VI. The standard deviation for Test 3 of 0.149 db/cm is a conservative value because in its calculation the trend of increasing attenuation with increasing frequency was ignored, thus adding to the scatter of the attenuation.

Table 5.14. Average Attenuation and Standard Deviation of 12 Test groups of 5 tests each, using Frequencies with Transducer Magnitudes 49% of Peak values and higher.

Test group	Average Attenuation db/cm	standard deviation
AS30	-0.508	+/-0.0296
AS65	-0.461	+/-0.0579
AT30	-0.467	+/-0.112
AT65	-0.357	+/-0.077
BS30	-0.896	+/-0.035
BS65	-0.872	+/-0.149
BT30	-0.724	+/-0.088
BT65	-0.790	+/-0.206
CS30	-0.684	+/-0.168
CS65	-0.608	+/-0.056
CT30	-0.632	+/-0.175
CT65	-0.519	+/-0.072
Total	-0.627	+/-0.149

Table 5.15 lists the average attenuation and corresponding variance of the results of all 60 tests at a frequency of 52,734 Hz. This frequency was

chosen since it had the highest composite (add up all four values) value listed in Table 5.13. This was used as a comparison to Table 5.14.

Table 5.15. Average Attenuation and Standard Deviation using all data for 52,734 Hz.

Test group	Average Attenuation db/cm	Standard Deviation
AS30	-0.61	+/-0.014
AS65	-0.69	+/-0.045
AT30	-0.70	+/-0.102
AT65	-0.63	+/-0.090
BS30	-0.89	+/-0.033
BS65	-0.96	+/-0.167
BT30	-0.85	+/-0.091
BT65	-0.96	+/-0.095
CS30	-0.70	+/-0.150
CS65	-0.66	+/-0.051
CT30	-0.94	+/-0.171
CT65	-0.68	+/-0.090
Total	-0.77	+/-0.161

The total sample standard deviation of 0.161 db/cm for the single frequency data is larger than the total sample standard deviation of 0.149 db/cm of the grouped data because it included the magnitude information from NT65, which had a normalized value of 41% at 52,734 Hz. When NT65 was not included, the standard deviation was 0.144 db/cm, which was much closer to the grouped data result. The total sample standard deviation of 0.149 db/cm will be used on all subsequent figures containing error bounds.

A mean attenuation was determined from the twelve groups of Test 3, AS30 - CT65. Each group is the average, at each frequency, of five tests conducted at a particular setting: drive signal and number of cycles in the tone burst. Table 5.16 compares the Test 1 and Test 3 mean

attenuation. Figure 5.46 compares the Test 3 twelve groups over a frequency bandwidth of 50 to 53 kHz with a +/- three standard deviation band surrounding the Test 3 mean attenuation.

Table 5.16. Mean Attenuation db/cm for Test 1 and Test 3.

	Mean Attenuation db/cm	
Frequency Hz	Test 1	Test 3
50293	-1.08	-0.62
50781	-1.11	-0.64
51270	-1.14	-0.67
51758	-1.17	-0.69
52246	-1.20	-0.71
52734	-1.23	-0.73

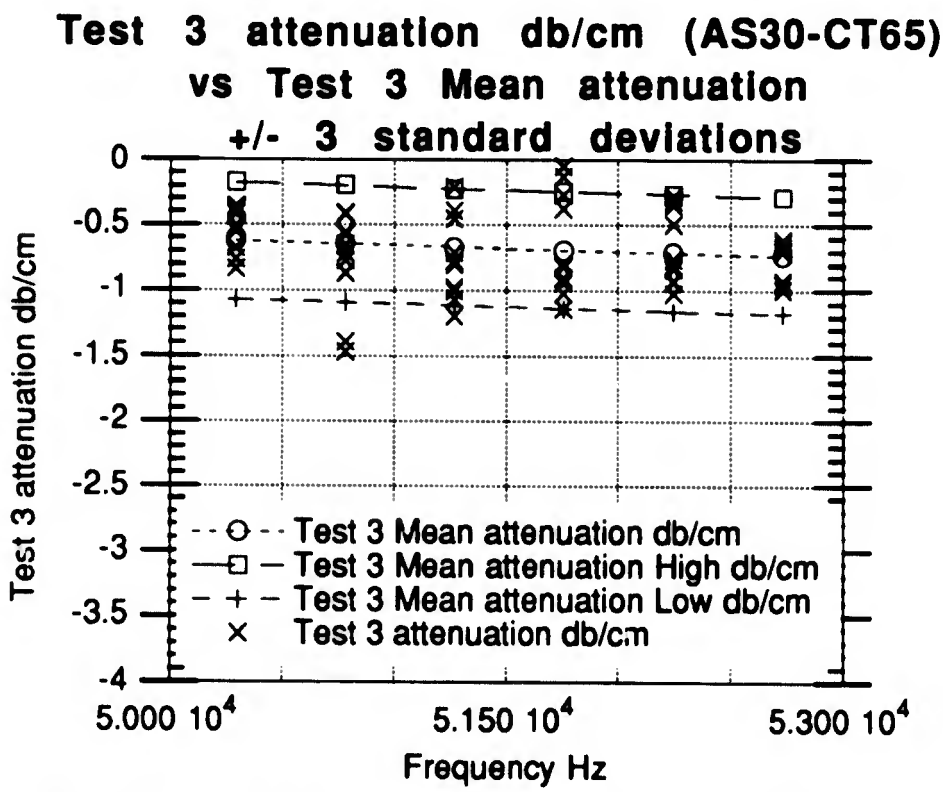

Figure 5.46. Test 3 Attenuation db/cm (AS30 - CT65, 12 data points at each frequency) versus Test 3 Mean Attenuation +/- 3 standard deviations.

The three standard deviation band in Figure 5.46 characterizes the Test 3 attenuation data quite good. The reason all the points do not fall into the +/- 3 standard deviation band is as follows. Each point on Figure 5.46 from the Test 3 attenuation, groups AS30 - CT65, are the average of five tests at a particular frequency. As can be seen in Table 5.13, in the frequency bandwidth shown in Figure 5.46, some normalized transducer magnitudes are far below 49%. The 49% normalized magnitude values were used in Table 5.14 to determine the standard deviation of the Test 3 data. Therefore it is understandable that not all the values of the Test 3 attenuation at the frequency bandwidth shown in Figure 5.46 would fall within the +/- 3 standard deviation band surrounding the Test 3 mean attenuation. However, one can notice the Test 3 attenuation, groups AS30 - CT65, values at 52,734 Hz, which are the far right points in Figure 5.46, are tightly grouped around the mean attenuation and well within the +/- 3 standard deviation band. The normalized magnitude values at 52,734 Hz in Table 5.13 are all above 41%, and are as a sum, the greatest for any frequency. Figure 5.47 compares The Test 3 mean attenuation with +/- 3 standard deviation band to the Test 3 attenuation for the groups AS30-CT65 of five tests each, like Figure 5.46, except all sixty data points for each frequency are shown. The same reasons why not all the data points are contained within the +/- 3 standard deviation band around the mean attenuation apply to Figure 5.47 as in Figure 5.46.

Figure 5.26 compares the Test 1 attenuation A30M- C65M twelve tests, with a +/- 3 standard deviation band surrounding the Test 1 mean attenuation in a similar fashion as Test 3 in Figure 5.46.

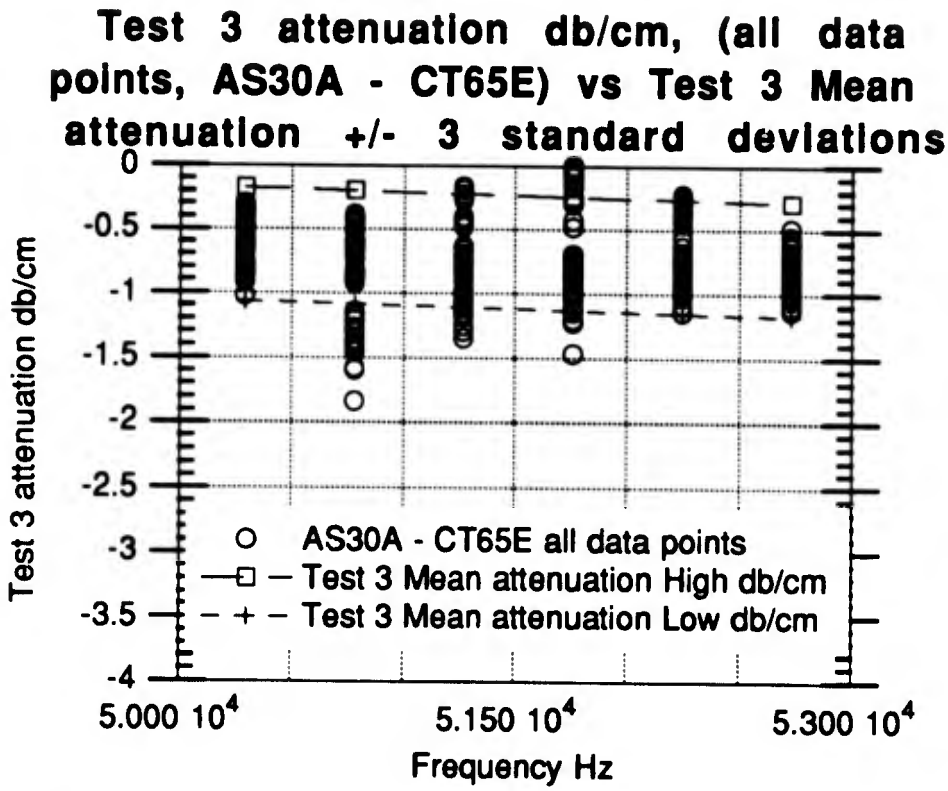

Figure 5.47. Test 3 Attenuation db/cm (AS30 - CT65 sixty points at each frequency) versus Test 3 Mean Attenuation +/- 3 standard deviations.

5.6 Effects of Aging

Figures 5.48 - 5.49 compare the Test 1 data taken in October, 1992 with the Test 3 data taken in April, 1993. Each Figure compares the ultrasonic NDE on a specific dimension A, B or C of sample 3323-2 no inclusion. Even taking into account the error bounds on each test datum, the change in the bulk viscoelastic properties are exhibited a smaller attenuation at each frequency in Test 3 compared to Test 1. Further, the characteristic snake in the A data, were consistent over both test periods, and may be due to an anisotropy in the inert propellant sample.

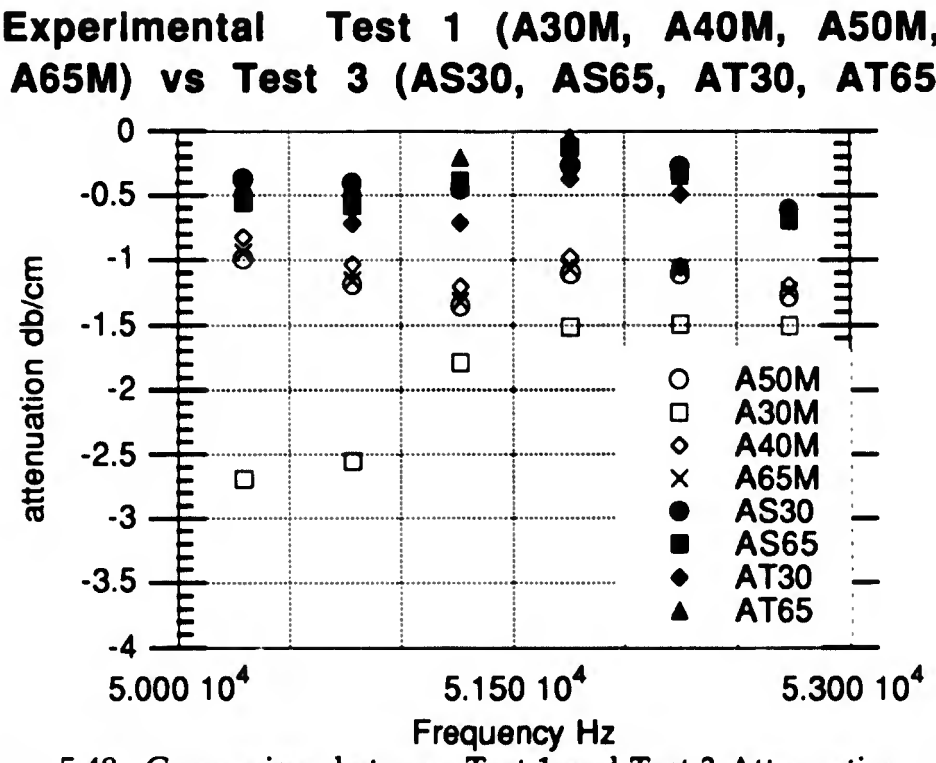

Figure 5.48. Comparison between Test 1 and Test 3 Attenuation versus Frequency, Transducer-through-A ultrasonic NDE.

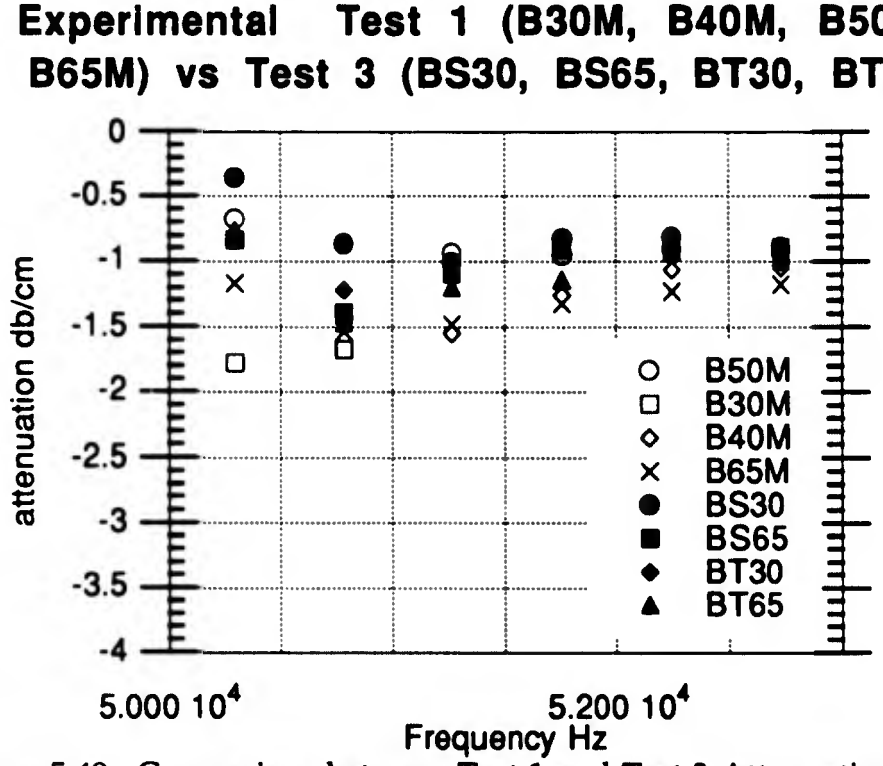

Figure 5.49. Comparison between Test 1 and Test 3 Attenuation versus Frequency, Transducer-through-B ultrasonic NDE.

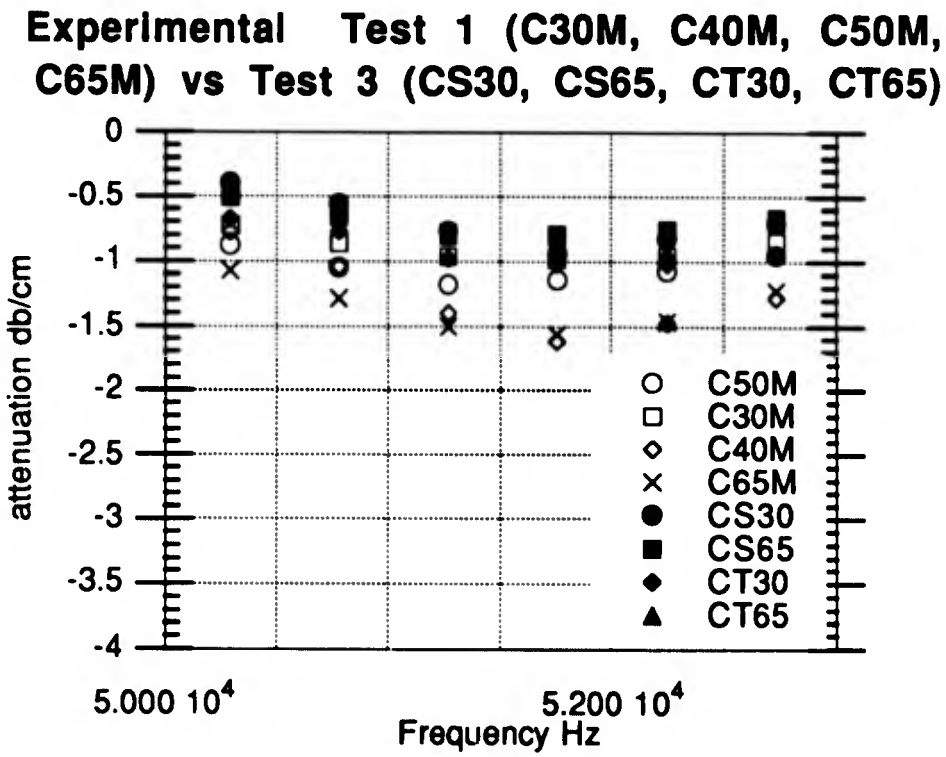

Figure 5.50. Comparison between Test 1 and Test 3 Attenuation versus Frequency, Transducer-through-C ultrasonic NDE.

In each of the Figures 5.48 - 5.50, the Test 3 data was above the Test 1 data. Figure 5.51 depicts Test 1 attenuation data with Test 3 data's mean attenuation and surrounding +/- 3 standard deviation band. It shows that Test 1 data and Test 3 data were statistically different. Figure 5.52 contains Test 3 data and Test 1 mean attenuation with error bounds and supports this conclusion. This significantly different sample attenuation between Test 1, performed at five months after sample 3323-2 no inclusion was cast, and Test 3 performed at eleven months after casting, can only be due to the effect of aging of the sample.

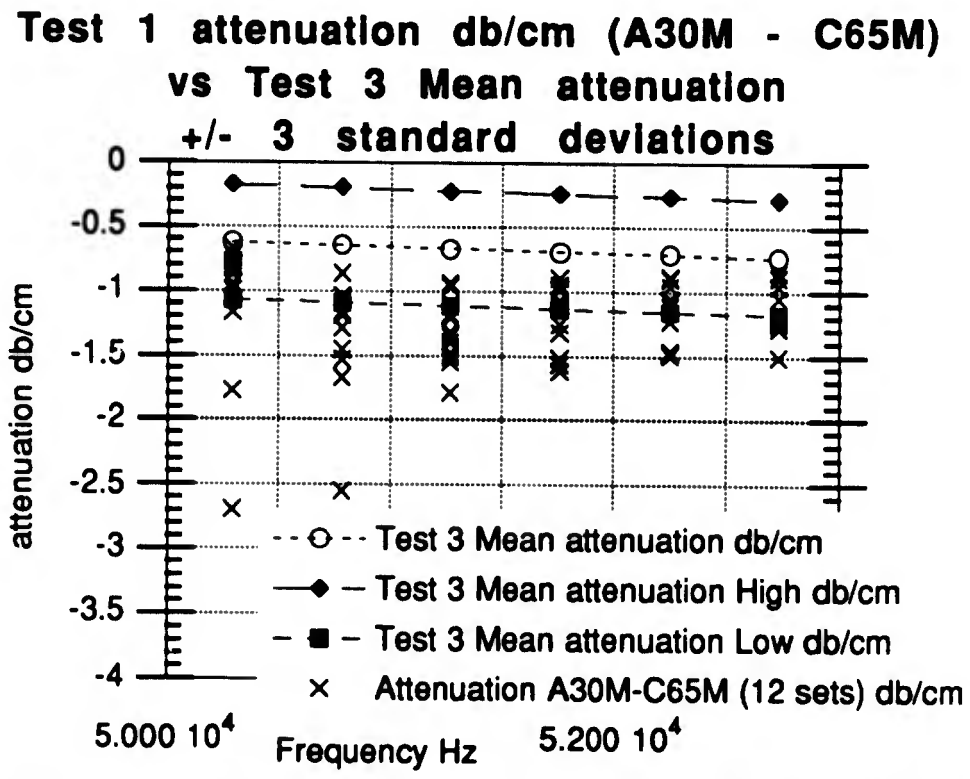

Figure 5.51. Comparison between Test 1 Attenuation (A30M - C65M) and Test 3 Mean Attenuation db/cm +/- 3 standard deviation.

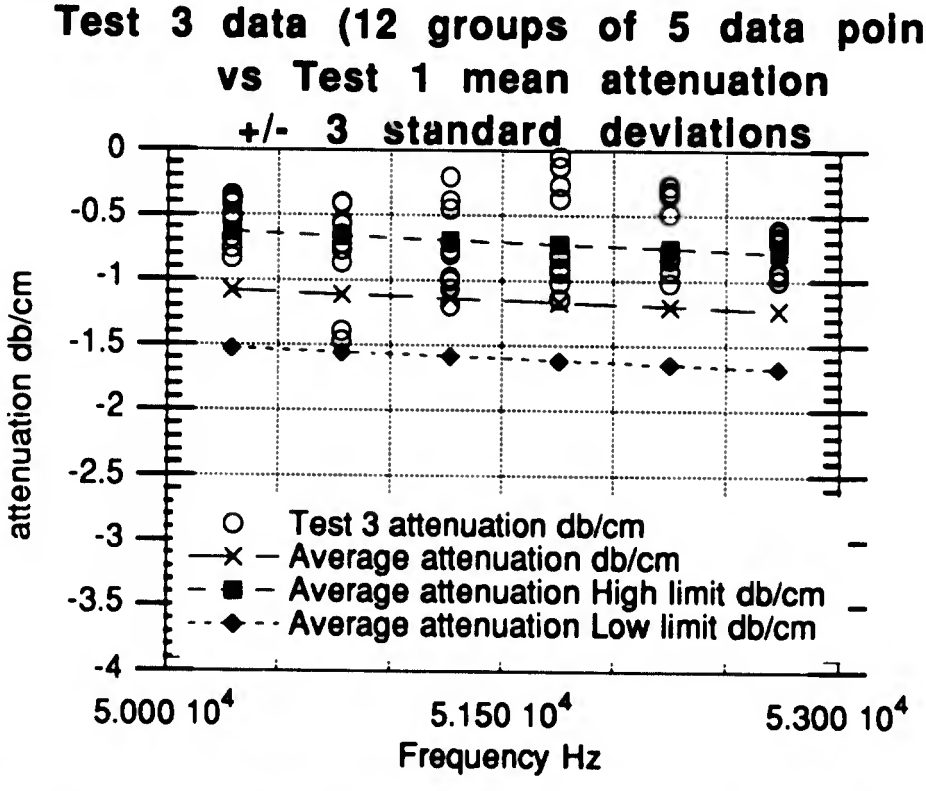

Figure 5.52. Comparison between Test 3 Attenuation (AS30 - CT65) and Test 1 Mean Attenuation db/cm +/- 3 standard deviation.

5.7 Experiment Data with Inclusion

In Test 1, the sample 3323-2 Paddle Ball (G, H, IC and IF), and the sample 3323-2 Ping Pong Ball (J, K, LC and LF), were tested with a 3 cycle 30-65 kHz drive signal using a 50 kHz transducer. Figures 5.53 - 5.58 present the effect of these inclusions on attenuation for each individual dimension compared in a bar type graph with an equivalent attenuation for no inclusion.

In each Figure there is an appreciable difference between the equivalent "no inclusion" attenuation one would expect and the attenuation actually recorded. This excess attenuation, bigger than the -1 to -2 db error bound (one standard deviation), holds the information which can be used to detect inclusions in the SRM propellant. The error bound was calculated from the standard deviation, +/- 0.149 db/cm, and the dimension of the side, i.e. G 8.26 cm, IC 12.1 cm, and LC 13.2 cm. The simple multiplication bounds the error for one standard deviation as +/- 1.23 db for G, +/- 1.8 db for IC, and +/- 1.97 db for side LC. At certain frequencies there was a difference greater than three standard deviations between the attenuation from the inclusion and the mean attenuation with no inclusion. Figures 5.59 - 5.64 present the +/- 3 standard deviation band surrounding an equivalent mean attenuation with no inclusion for each dimension. In every Figure there were at least four of the six frequencies with data points outside the +/- 3 standard deviation band surrounding an equivalent mean attenuation with no inclusion. This shows a statistical significant difference between the sample with and without inclusions. The ultrasonic NDE did detect the Paddle Ball and the Ping Pong Ball.

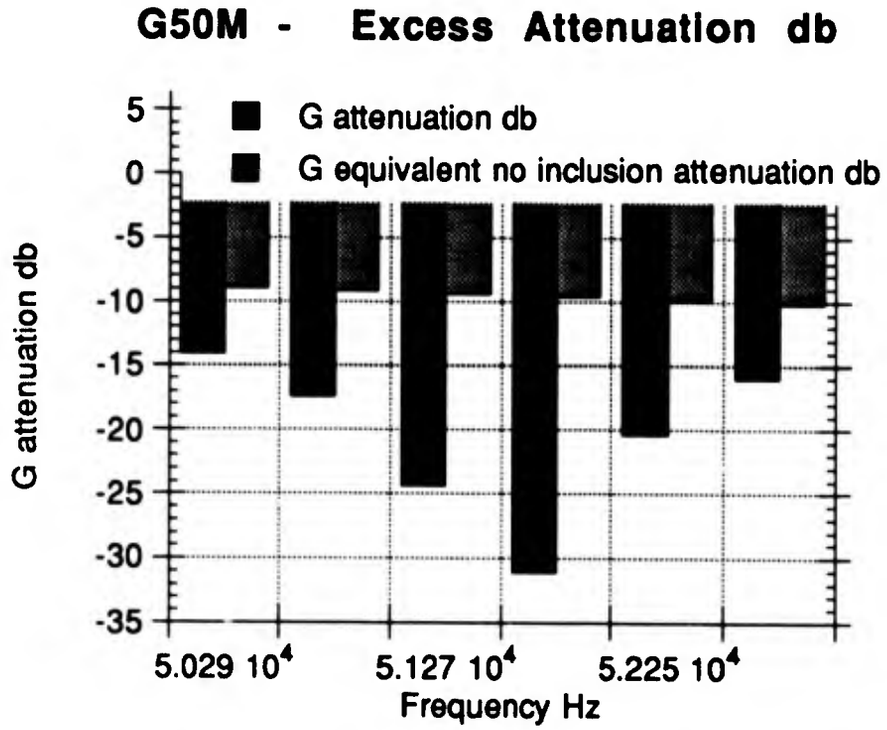

Figure 5.53. Comparison between Paddle Ball Attenuation (G50M) and Equivalent "no inclusion" Attenuation, db.

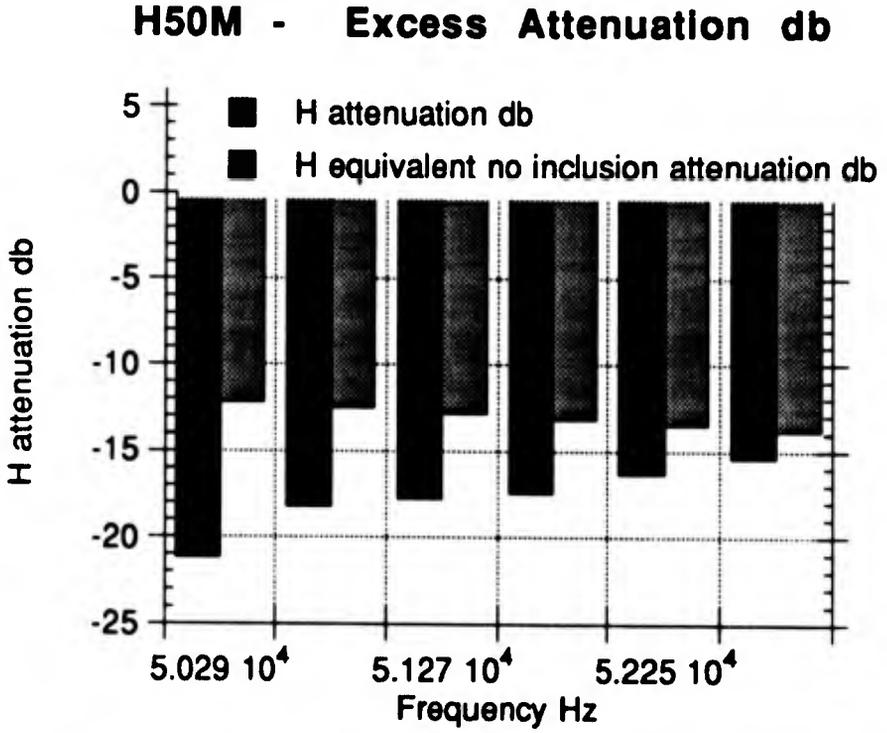

Figure 5.54. Comparison between Paddle Ball Attenuation (H50M) and Equivalent "no inclusion" Attenuation, db.

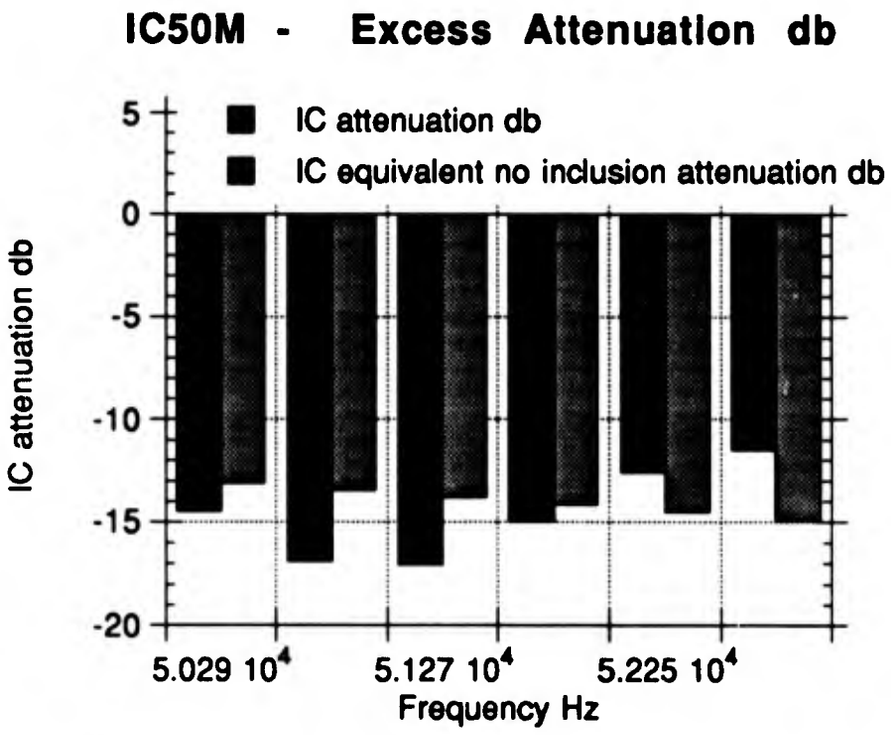

Figure 5.55. Comparison between Paddle Ball Attenuation (H50M) and Equivalent "no inclusion" Attenuation, db.

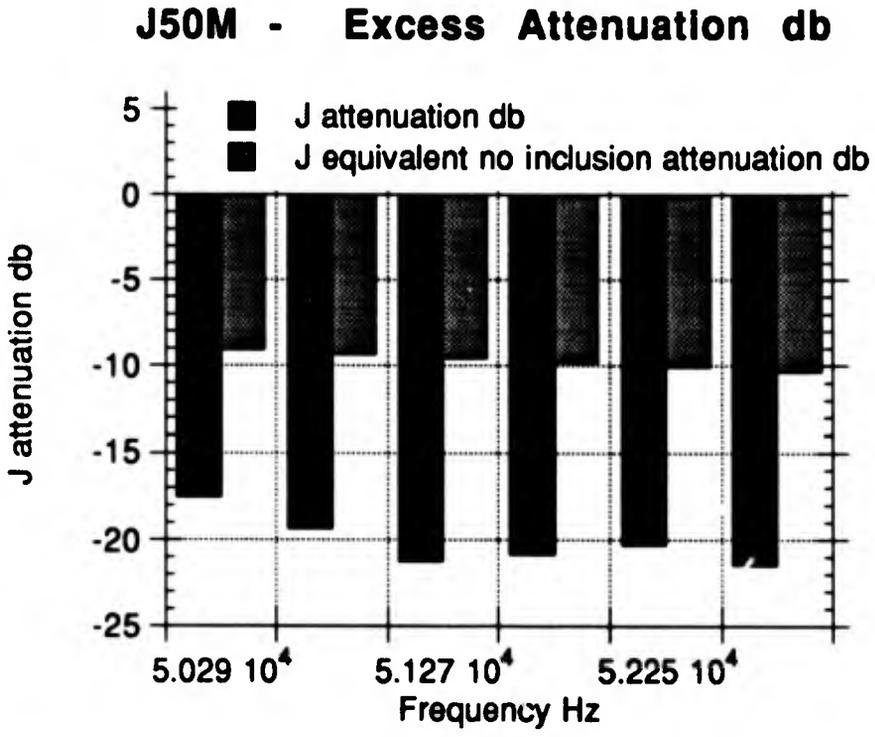

Figure 5.56. Comparison between Ping Pong Ball Attenuation (J50M) and Equivalent "no inclusion" Attenuation, db.

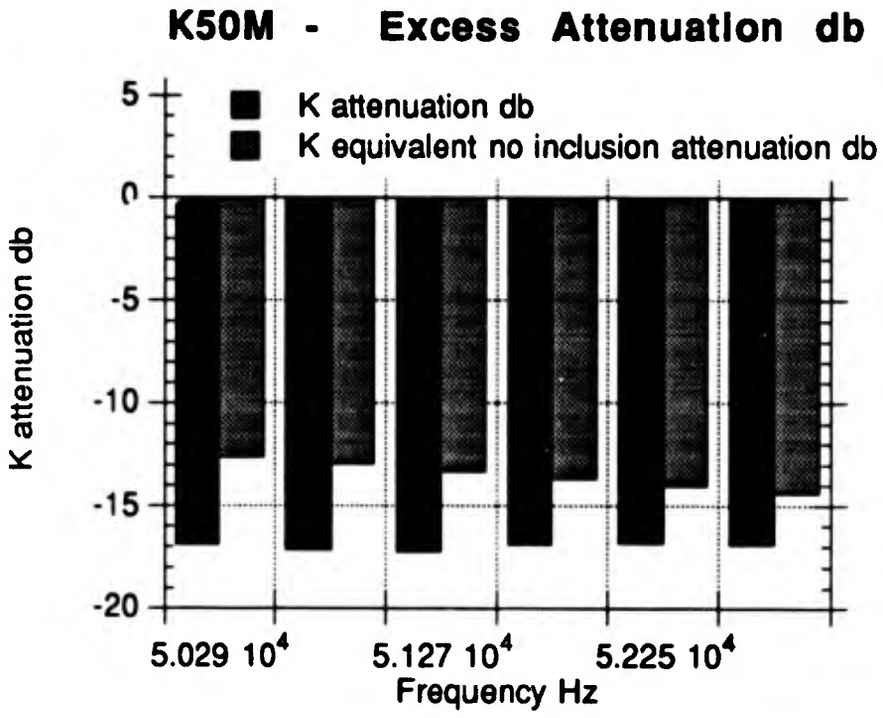

Figure 5.57. Comparison between Ping Pong Ball Attenuation (K50M) and Equivalent "no inclusion" Attenuation, db.

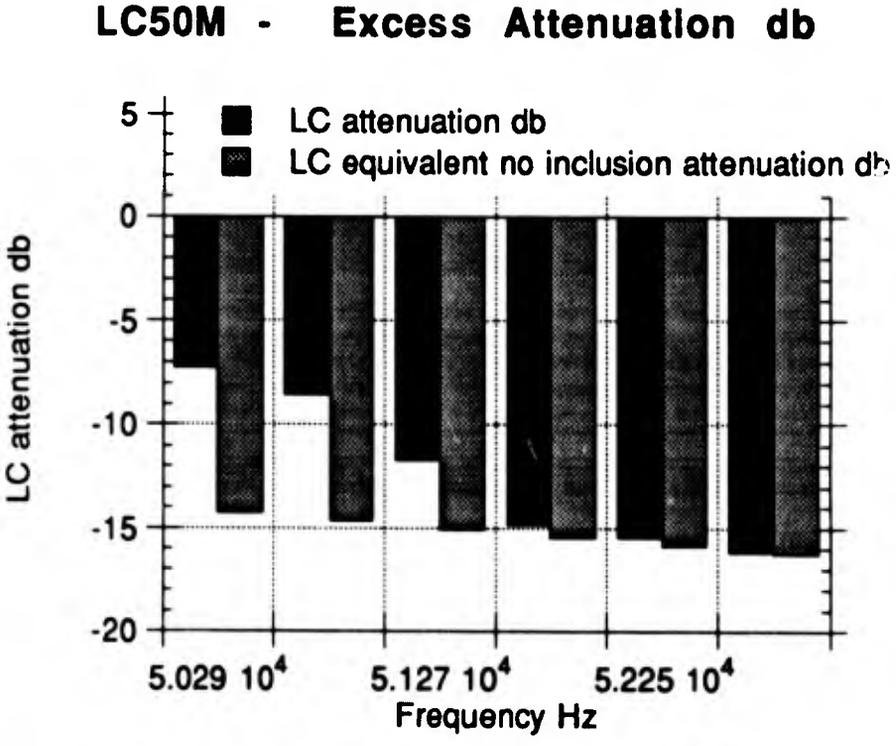

Figure 5.58. Comparison between Ping Pong Ball Attenuation (LC50M) and Equivalent "no inclusion" Attenuation, db.

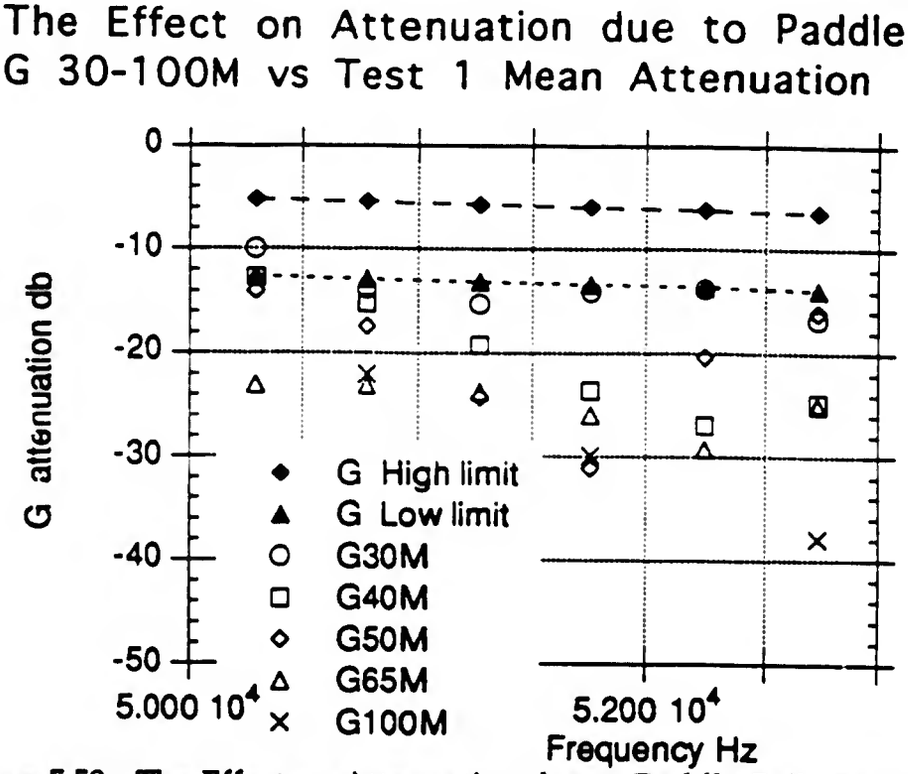

Figure 5.59. The Effect on Attenuation due to Paddle Ball, G30M - G100M vs Test 1 G equivalent Mean Attenuation db.

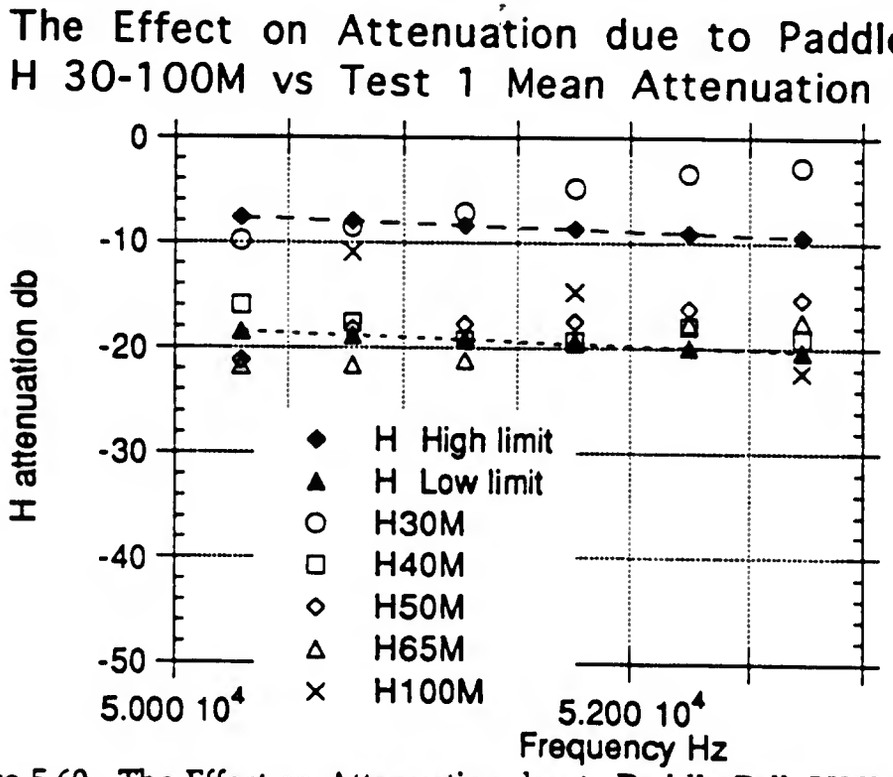

Figure 5.60. The Effect on Attenuation due to Paddle Ball, H30M - H100M vs Test 1 H equivalent Mean Attenuation db.

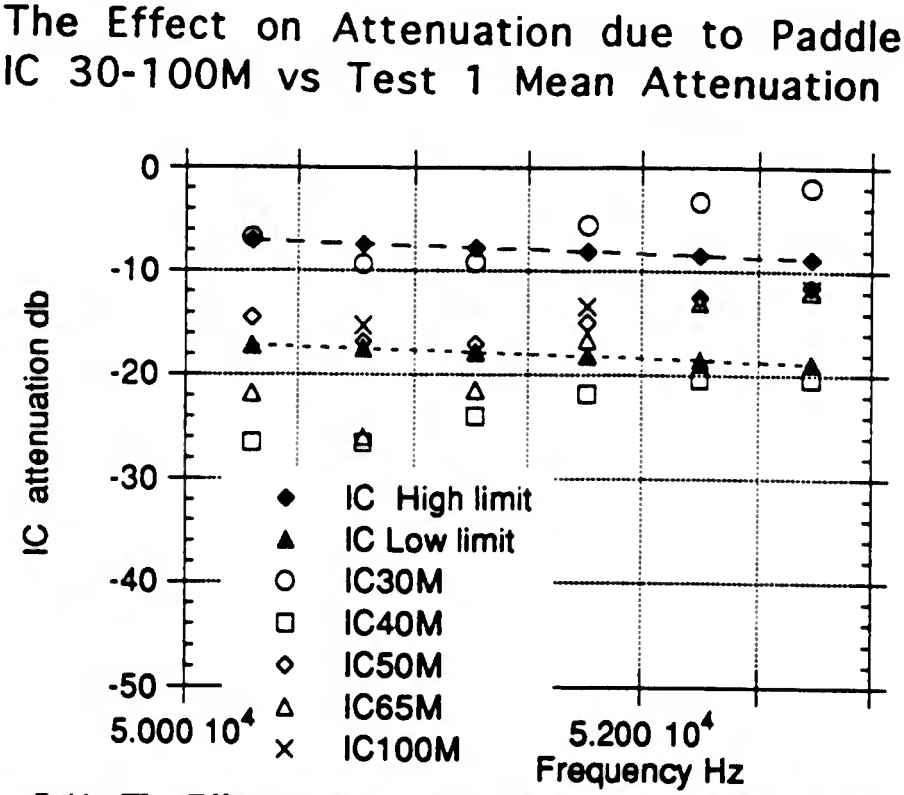

Figure 5.61. The Effect on Attenuation due to Paddle Ball, IC30M - IC100M vs Test 1 IC equivalent Mean Attenuation db.

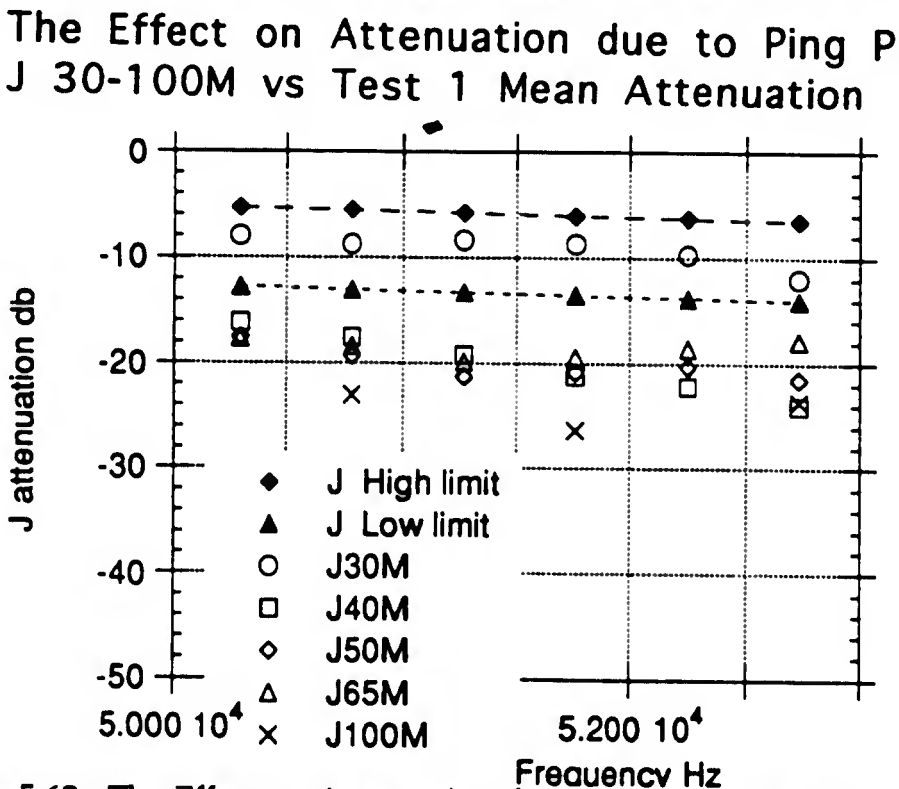

Figure 5.62. The Effect on Attenuation due to Ping Pong Ball, J30M - J100M vs Test 1 J equivalent Mean Attenuation db.

The Effect on Attenuation due to Ping Pong Ball, K 30-100M vs Test 1 Mean Attenuation

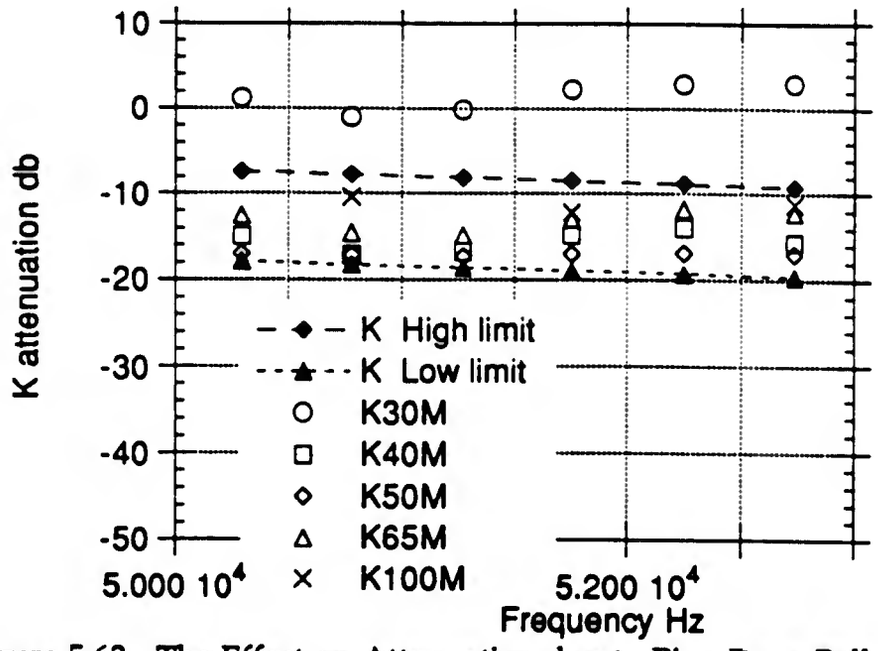

Figure 5.63. The Effect on Attenuation due to Ping Pong Ball, K30M - K100M vs Test 1 K equivalent Mean Attenuation db.

The Effect on Attenuation due to Ping Pong Ball, LC 30-100M vs Test 1 Mean Attenuation

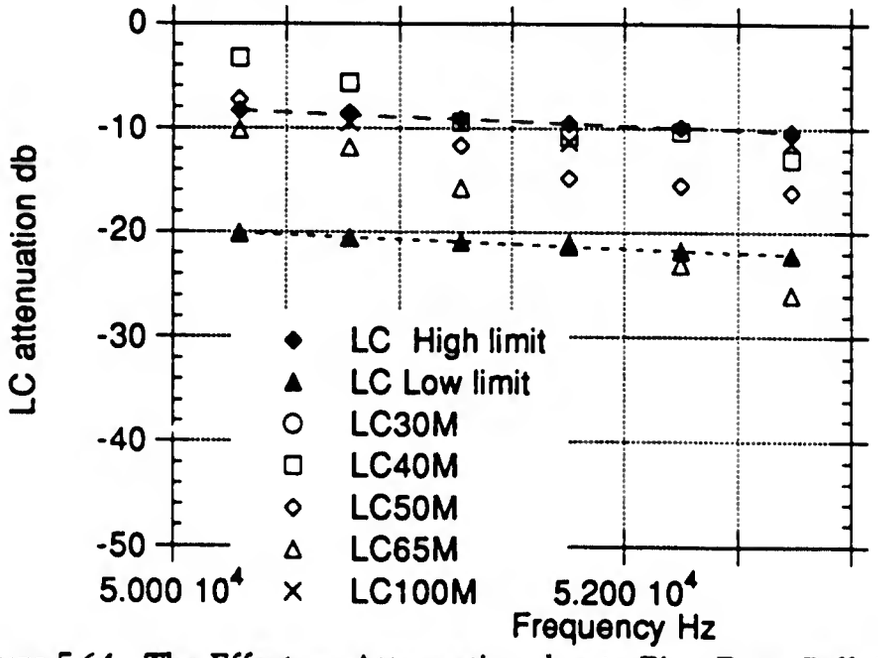

Figure 5.64. The Effect on Attenuation due to Ping Pong Ball, LC30M - LC100M vs Test 1 LC equivalent Mean Attenuation db.

CHAPTER VI

NUMERICAL RESULTS

6.0 Overview

The results of the numerical simulation of the ultrasonic wave propagation in the inert SRM propellant are presented herein. The research methodology steps from Chapter III, Figure 3.3, are followed in the next Sections.

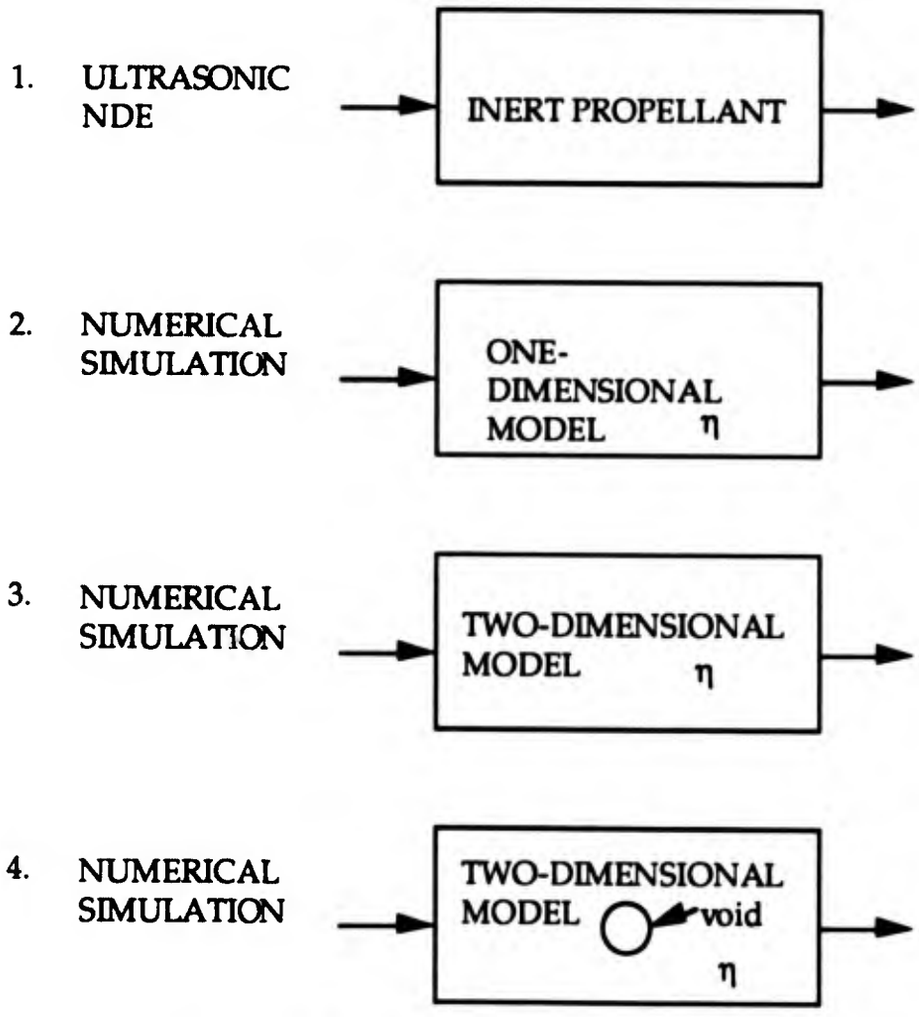

Figure 3.3. Steps in Tuning the Numerical model.

6.1 One-dimensional Numerical Simulation

The preliminary viscoelastic damping coefficient determined in Chapter V is incorporated in the numerical model. Figure 6.1 depicts the methodology to validate the one-dimensional model.

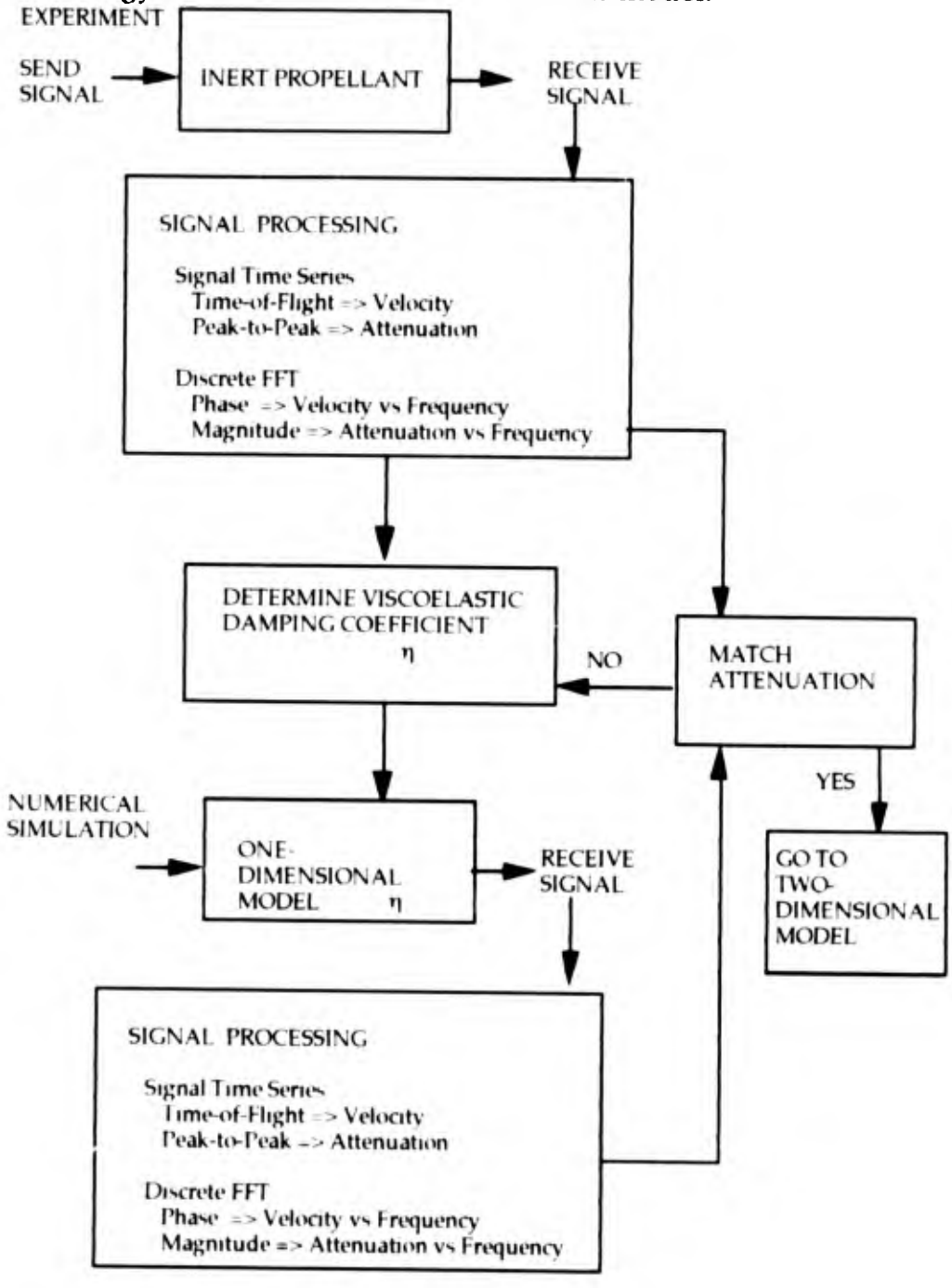

Figure 6.1. Methodology to Validate the One-dimensional Model.

Once the simulated source function propagates through the numerical grid, both the frequency domain magnitude and phase information are obtained from the source and from the received signal time series. The attenuation versus frequency plot is determined from magnitude information. However, there is not a need to correct the information for diffraction or impedance mismatch as before because the simulated source function used is a plane wave Ricker Pulse.

Kino (1987) use a slightly different equation than Truell et al (1969) which appears to be a closer approximation to the values determined from the experimental data, presented in Chapter V and repeated below.

$$\alpha = \frac{\omega^2 \eta}{2V_c^3 \rho} \qquad \text{Attenuation} \qquad (25)$$

Table 6.1 uses the frequency data with peak magnitude greater than half the peak value of the spectrum of the transducer. The Viscoelastic Damping Coefficient values are shown in the right two columns. The values from equation (25) are normalized per $\frac{1}{\rho V_c \lambda}$ or $\frac{f}{\rho V_c^2}$. The last column shows the value of the Viscoelastic Damping Coefficient that would be input into the numerical simulation.

Experimental data from tests A50, B50 and C50, using frequency domain information are input into equation (25) from Kino (1987). The three tests are combined into one mean phase velocity and one combined attenuation to derive a set of Viscoelastic Damping Coefficients presented in the Table 6.1. The Test 3 values indicate that the standard deviation was greater than these and was plotted in Tables and Figures as +/- 0.149 db/cm.

Table 6.1. Combined Phase and Mean Attenuation from A50, B50, C50 Combined with Viscoelastic Damping Coefficients (VDC) determined from equation (25).

Frequency Hz	Mean Phase Velocity m/s	Combined Attenuation db/cm	VDC db	Simulation Equivalent VDC**
50293	1514 +/-16	-0.80	-0.1220	-3.9E-07
50781	1547 +/-14	-1.18	-0.1816	-5.7E-07
51270	1556 +/-11	-1.39	-0.2131	-6.6E-07
51758*	1575 +/-14	-1.28	-0.1980	-6.1E-07
52246	1599 +/-16	-1.20	-0.1853	-5.7E-07
52734	1620 +/-19	-1.17	-0.1825	-5.5E-07

* Frequency at maximum magnitude
** VDC divided by frequency (radians/sec), used in this fashion for the numerical simulation.

Using the above as a guide, the one-dimensional numerical model with the Kelvin-Voigt formulations were tested over the range of Viscoelastic Damping Coefficients shown below in Table 6.2. A longitudinal velocity of the sample was required as an input to the numerical model, and the experimentally determined group velocity was used as an estimate. The attenuation at the equivalent distance to the experimental test samples are also presented. The combined attenuation, based on signal time series peak-to-peak attenuation, indicates that a Viscoelastic Damping Coefficient of approximately -5 e -7 should emulate the no inclusion, inert propellant responses. Both show an average value of approximately -1.2 db/cm. A VDC of -4 e -7 was also used as a comparison. One should notice in Table 6.2 that as the VDC gets more negative the attenuation increases.

Table 6.2 .Based on Signal Time Series, Peak-to-Peak Attenuation.

VDC (input value)	Attenuation A equivalent db/cm	Attenuation B equivalent db/cm	Attenuation C equivalent db/cm	Mean Attenuation db/cm
0.0 (elastic)	-0.0007	-0.0009	-0.0023	-0.0013 +/- 0.0007
-1 e -10	-0.0007	-0.0008	-0.0001	-0.0005 +/- 0.0003
-1 e -8	-0.042	-0.042	-0.042	-0.042 +/- 0
-1 e -7	-0.374	-0.361	-0.353	-0.363 +/- 0.009
-3 e -7	-0.916	-0.848	-0.813	-0.859 +/- 0.043
-4 e -7	-1.123	-1.027	-0.979	-1.043 +/- 0.06
-5 e -7	-1.303	-1.181	-1.119	-1.201 +/- 0.076
-6 e -7	-1.461	-1.314	-1.241	-1.339 +/- 0.091
-7 e -7	-1.603	-1.432	-1.348	-1.461 +/- 0.11
-1.5 e -6	-2.385	-2.073	-1.925	-2.128 +/- 0.19

One can notice there is a difference in Table 6.2 in the attenuation from each of the equivalent dimensions, A, B, and C. The reason for this is due to the fact that it is a peak-to-peak attenuation measurement. Thus, the deeper the wave propagates in the viscoelastic material during the simulation, the more the higher frequencies are attenuated. Therefore, the frequency at peak magnitude in the DFT for the spectrum of the signal time series was always highest for the shortest dimension in each test. Since the attenuation increases as a function of frequency, the shortest dimension which has the highest frequency, had the highest attenuation. This phenomenon increased as an absolute difference, and as a percentage change as the viscoelastic damping coefficient increased. This is because

the shape of the signal time series is determined by its frequency content. And the attenuation determined from a peak-to-peak measurement may be the average of the attenuation for each frequency present in the signal. The conclusion one can draw is that in a material that exhibits nominal viscoelastic behavior, determining the attenuation by means of a peak-to-peak measurement can be misleading. Further, as shown in Table 6.3, when one determines the attenuation at discrete frequencies the difference between dimensions vanish.

The numerical signal time series were used to obtain the DFT, Magnitude versus Frequency. Table 6.3 and Figure 6.2 depict the associated attenuation for each equivalent dimension of sample 3323-2 no inclusion, over a frequency range 40 - 60 kHz, using a VDC of -5 e -7.

Table 6.3. Attenuation versus Frequency, Using Viscoelastic Damping Coefficient -5 e -7, one-dimensional model.

Frequency Hz	Attenuation A equivalent db/cm	Attenuation B equivalent db/cm	Attenuation C equivalent db/cm
40140	-0.85	-0.85	-0.85
44600	-1.05	-1.05	-1.05
49060	-1.26	-1.26	-1.26
53520	-1.50	-1.50	-1.50
57980	-1.75	-1.75	-1.76
62440	-2.03	-2.03	-2.03

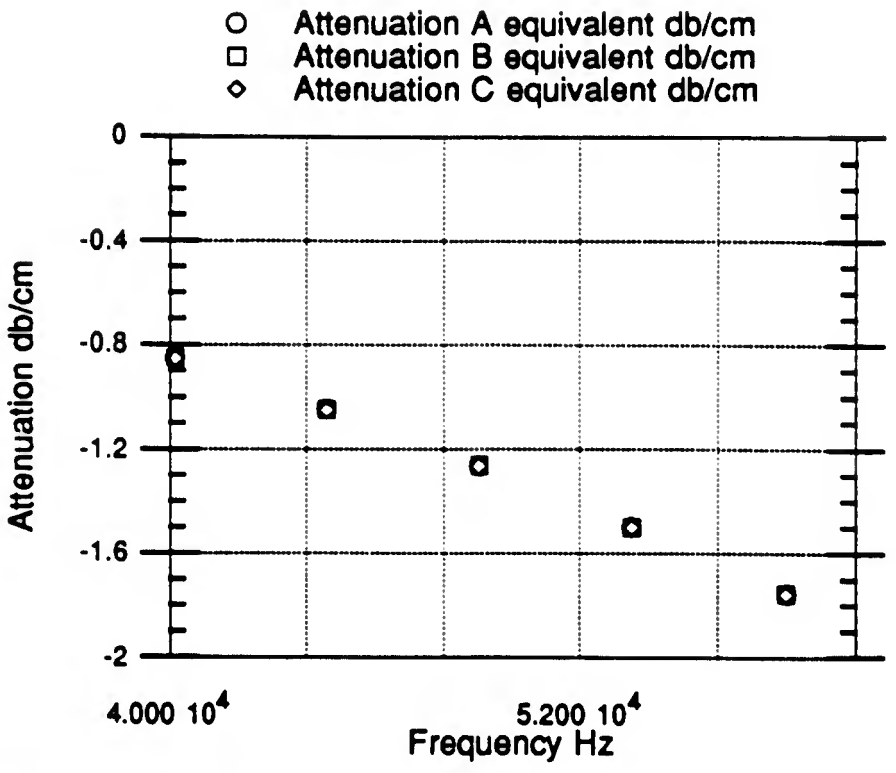

Figure 6.2. Attenuation versus Frequency, Numerical data, Viscoelastic Damping Coefficient (VDC) -5e -7.

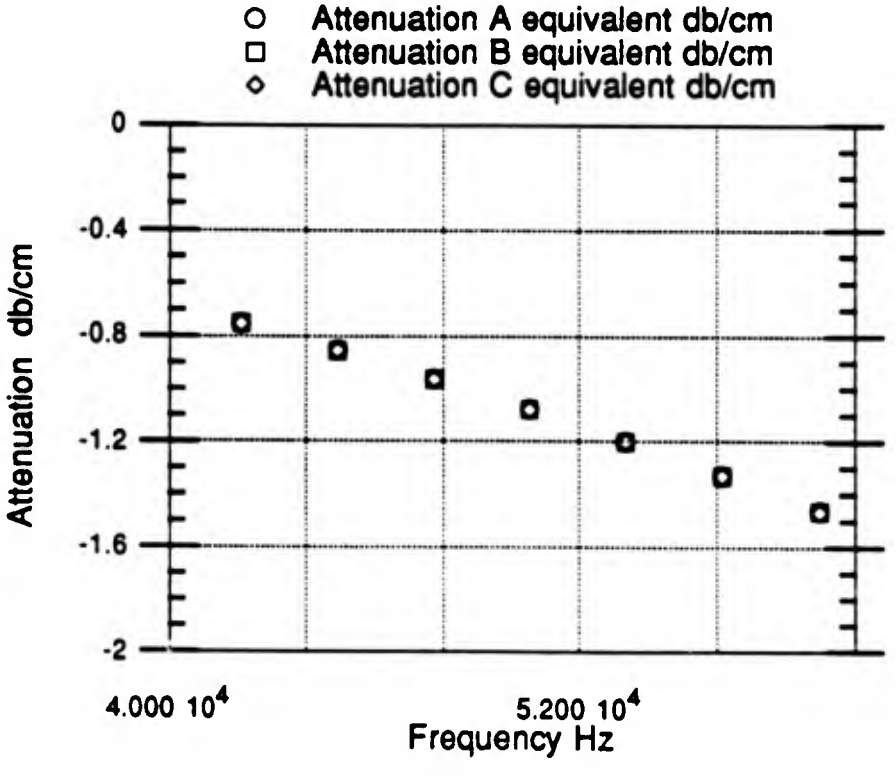

Figure 6.3. Attenuation versus Frequency, Numerical data, Viscoelastic Damping Coefficient (VDC) -4e -7.

Table 6.4 and Figure 6.3 are used to compare VDC -4 e -7 to Table 6.3 and Figure 6.2 VDC -5 e -7 in Table 6.5.

Table 6.4. Attenuation versus Frequency, Using Viscoelastic Damping Coefficient -4 e -7, one-dimensional model.

Frequency Hz	Attenuation A equivalent db/cm	Attenuation B equivalent db/cm	Attenuation C equivalent db/cm
42121	-0.75	-0.75	-0.75
44929	-0.85	-0.85	-0.85
47737	-0.96	-0.96	-0.96
50545	-1.08	-1.08	-1.08
53353	-1.20	-1.20	-1.20
56161	-1.33	-1.33	-1.33
58969	-1.46	-1.46	-1.46
61777	-1.60	-1.60	-1.60

Table 6.5. Attenuation versus Frequency Comparison between Experimental and Numerical data, Viscoelastic Damping Coefficient (VDC) -4 e -7 and -5 e -7, one-dimensional model.

Frequency Hz	Combined Attenuation db/cm	Interpolated Attenuation db/cm VDC -4 e -7	Interpolated Attenuation db/cm VDC -5 e -7
50293	-0.80	-1.08	-1.35
50781	-1.18	-1.10	-1.38
51270	-1.39	-1.12	-1.41
51758	-1.28	-1.15	-1.43
52246	-1.20	-1.17	-1.46
52734	-1.17	-1.19	-1.48

From the comparison between the experimental tests and numerical simulations, the one-dimensional simulations indicate a VDC closer to -4 e -7 than -5 e -7. Two contributing factors were identified for the discrepancy between Experimental and Numerical VDC; free surface boundary conditions and longitudinal velocity. Both were addressed in the two-dimensional model.

6.2 Two-dimensional Numerical Simulation

Figure 6.4 depicts the methodology to validate the two-dimensional model. The Viscoelastic Damping Coefficient was used in a two-dimensional numerical model using a 70 x 400 grid.

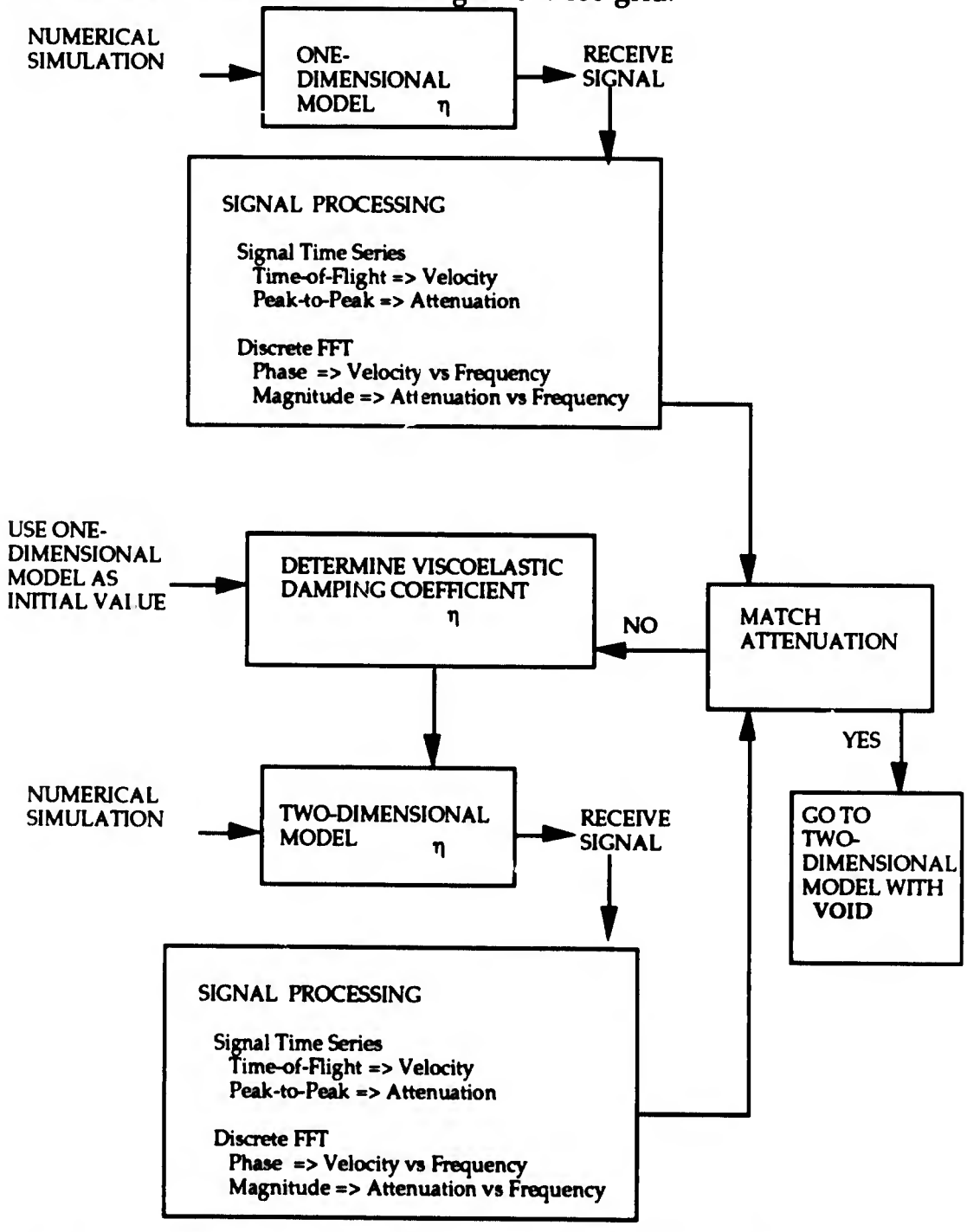

Figure 6.4. Methodology to validate the Two-dimensional Model.

The one-dimensional model indicated a Viscoelastic Damping Coefficient between -4 e -7 and -5 e -7. The discrepancy between Experimental average value of VDC (-5.7 e -7 originally, -5.6 e -7 upon revision) in Table 6.1 and the one-dimensional numerical simulation value of VDC was puzzling at first. Two factors, free surface boundary conditions and longitudinal velocity, were identified as contributing factors. The one-dimensional model did not have a free surface displacement and the longitudinal velocity was estimated. These two factors were corrected in the two-dimensional model. In the two-dimensional model, the displacement at the free surface boundary condition was twice the value of an internal location at the same distance from the source. Therefore the VDC from the one-dimensional numerical simulation would appear more attenuated than in the two-dimensional numerical simulation. In the two-dimensional numerical simulation a VDC closer to -6 e -7 matches the experimental attenuation. The longitudinal velocity was still estimated in the two-dimensional model. However this was solved and will be addressed when Figures 6.9 - 6.11 are discussed.

The experimental data A50M, B50M, C50M was compared to VDC -5.7 e -7 in Figure 6.5. The average VDC from the experimental data in Table 6.1, the combined attenuation (A50M, B50M, C50M) was -5.7 e -7 originally. This was slightly revised to -5.6 e -7, but the subsequent figures and tables still use a VDC of -5.7 e -7. The observations made are not affected by the slight difference in the VDCs.

Table 6.6 compares VDC values -5.7 e -7 and -6.3 e -7 attenuation with a graphical comparison in Figure 6.6. The attenuation for both

VDC's have a standard deviation of 0.129 db/cm, which was not shown in Figure 6.6.

The experimental values with error bounds were compared in Figures 6.7 and 6.8 to VDC -5.7 e -7 and -6.3 e -7 respectively, with excellent agreement.

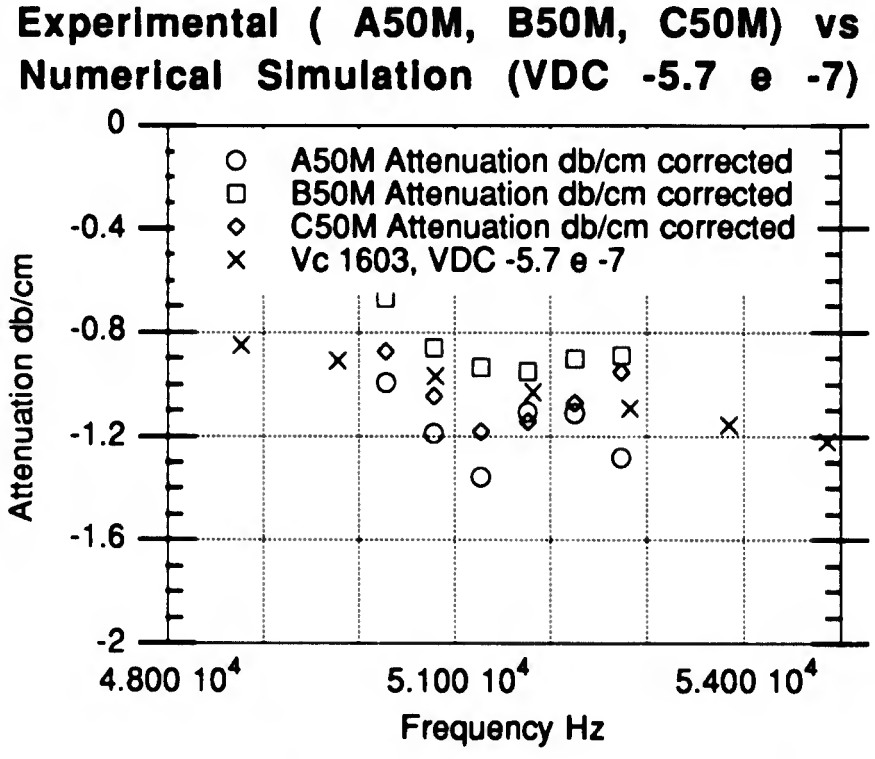

Figure 6.5 Attenuation versus Frequency, Experimental (A50M, B50M, C50M) and Numerical (Two-dimensional, no inclusion, VDC -5.7 e -7).

Again, the above Figure does not show the numerical +/- 0.129 db/cm standard deviation or the +/- 0.149 db/cm experimental data error bound. Table 6.6 and Figure 6.6 show the difference in two values of VDC. Again the experimental and numerical values of VDC differ. In the two-dimensional case the free surface boundary conditions were used, so this was not a factor. As in the one-dimensional model the longitudinal velocity was estimated. The estimate for V_C was the group velocity. This

clearly was not a close estimate. Figure 6.7 compares the numerical simulation with the average value of VDC from the experimental tests with the attenuation from the experimental tests. Figure 6.8 shows how a smaller VDC, -6.3 e -7, matches the experimental test results much closer.

Table 6.6. Attenuation versus Frequency Comparison between Experimental and Numerical, Viscoelastic Damping Coefficient (VDC) -5.7 e-7 and -6.3 e-7 at Vc 1603 m/s , Two-dimensional model.

Frequency Hz	Attenuation db/cm			
	Experimental		Numerical	
	Combined (range +/- 1 s)	Test 1 Mean values	Interpolated VDC -5.7e-7	Interpolated VDC -6.3e-7
50293	-0.66 to -0.94	-1.08	-0.94	-1.09
50781	-1.04 to -1.32	-1.11	-0.97	-1.12
51270	-1.25 to -1.53	-1.14	-1.00	-1.15
51758	-1.14 to -1.42	-1.17	-1.03	-1.18
52246	-1.06 to -1.34	-1.20	-1.05	-1.21
52734	-1.03 to -1.31	-1.23	-1.08	-1.25

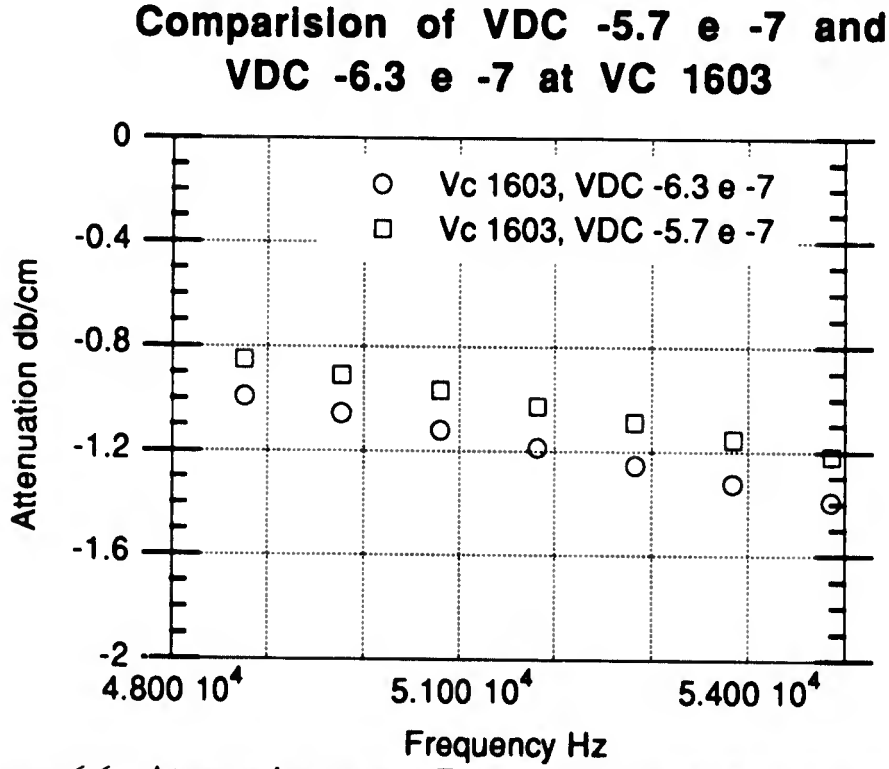

Figure 6.6. Attenuation versus Frequency Comparison between two Numerical Viscoelastic Damping Coefficients (VDC) -5.7 e-7 and -6.3 e-7 at Vc 1603 m/s , Two-dimensional model.

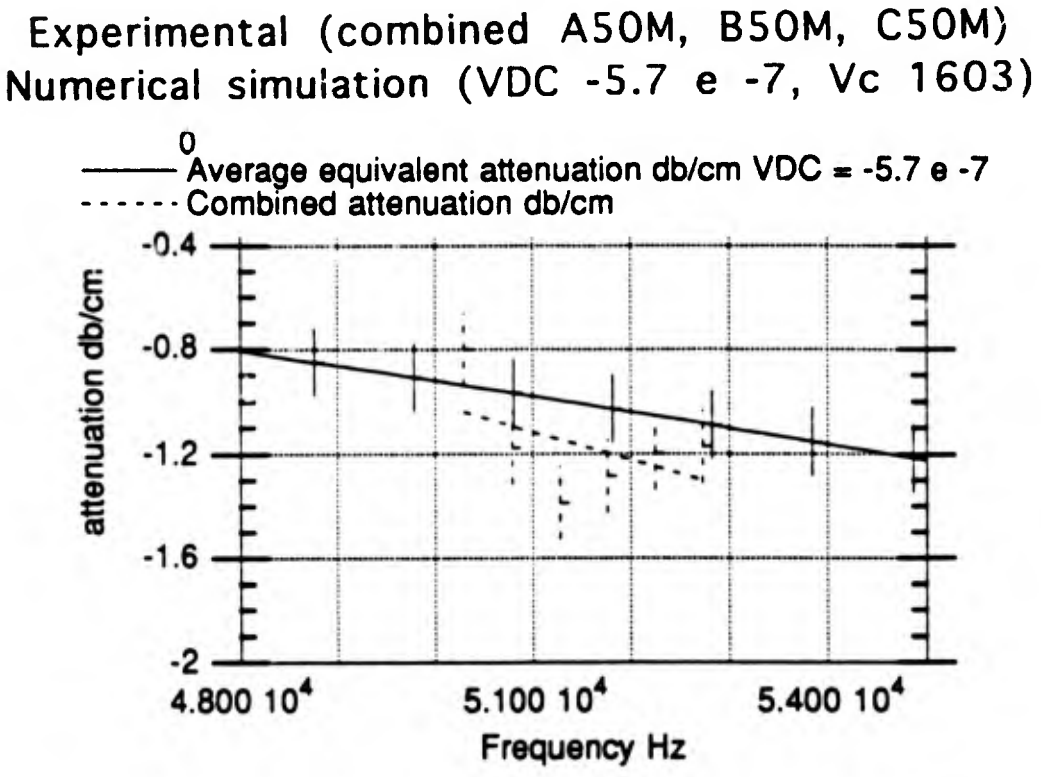

Figure 6.7. Attenuation versus Frequency Comparison between Experimental and Numerical, VDC -5.7 e -7, Two-dimensional model.

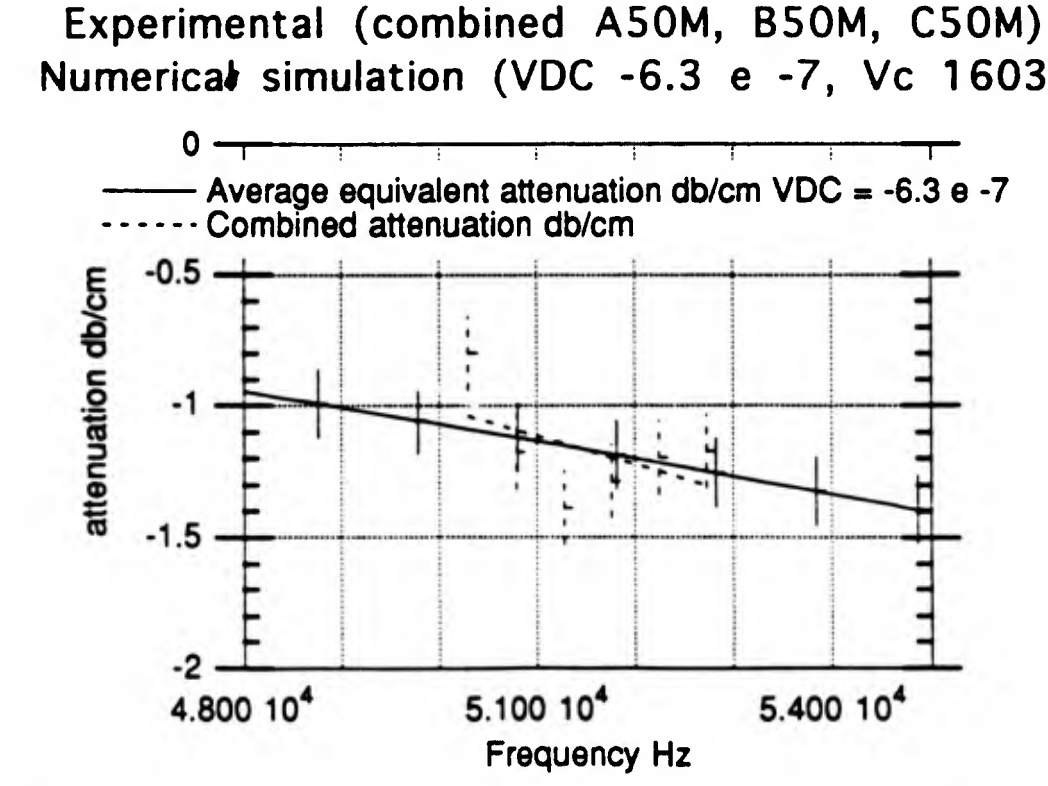

Figure 6.8. Attenuation versus Frequency Comparison between Experimental and Numerical, VDC -6.3 e -7, Two-dimensional model.

The VDC was varied in the numerical simulations with the longitudinal velocity held constant at 1603 m/s, the group velocity from Chapter V. Figure 6.9 demonstrates that, as in the one-dimensional model, the attenuation increases as the VDC gets more negative. However, since VDC and V_C are both inputs to the numerical model, Figure 6.10 was used to show how attenuation changes with a change in V_C with VDC held constant.

A V_C of 1453 m/s with a VDC of -5.7 e -7, shown in Figure 6.11 as a comparison to VC 1603 m/s VDC -6.3 e -7, matches the experimental data with the same VDC. Therefore, one must conclude that the longitudinal velocity of the SRM inert propellant has a value of approximately 1453 m/s. The numerical model determined the equivalent longitudinal velocity based on the Ricker Pulse excitation.

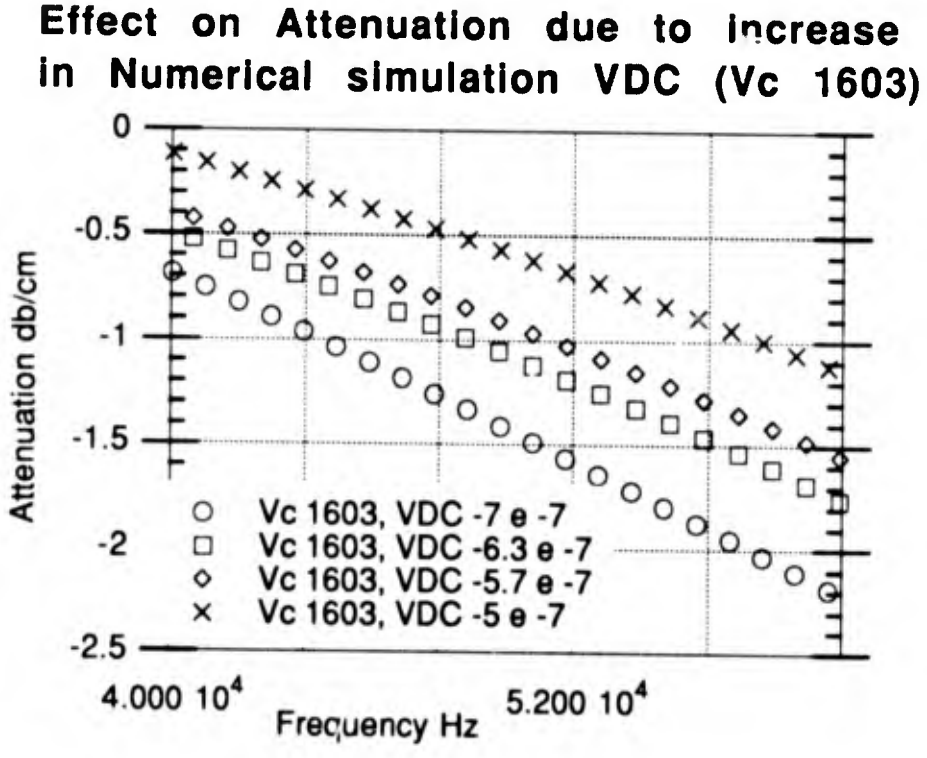

Figure 6.9. Numerical Simulation, comparison of VDCs at Vc 1603 m/s.

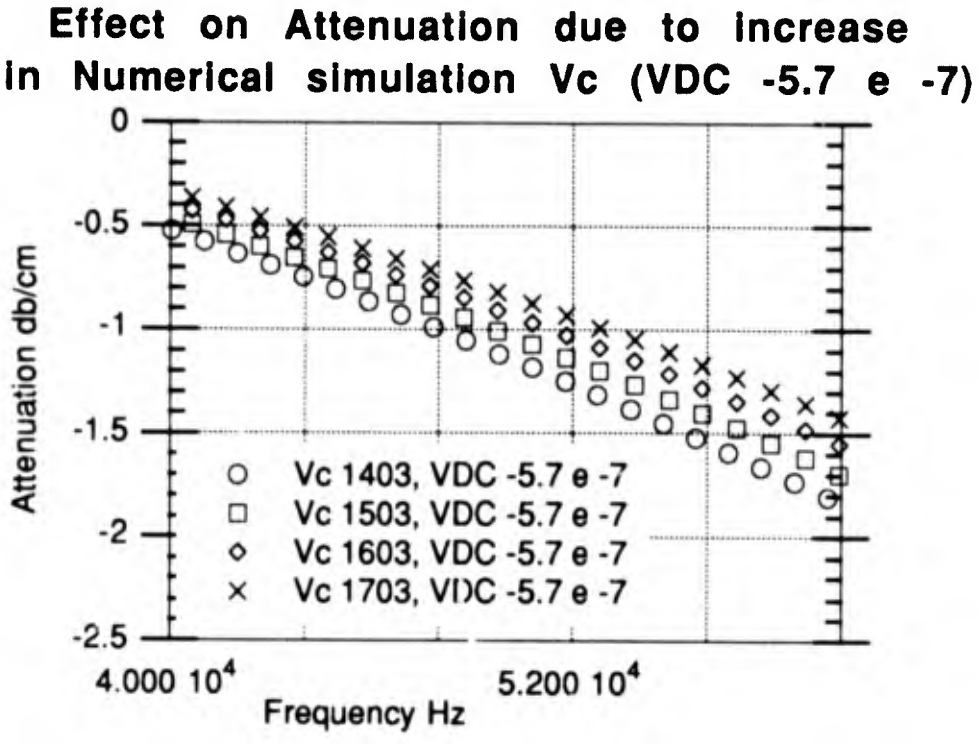

Figure 6.10. Numerical Simulation, comparison of various Longitudinal Velocity V_c, at VDC -5.7 e -7.

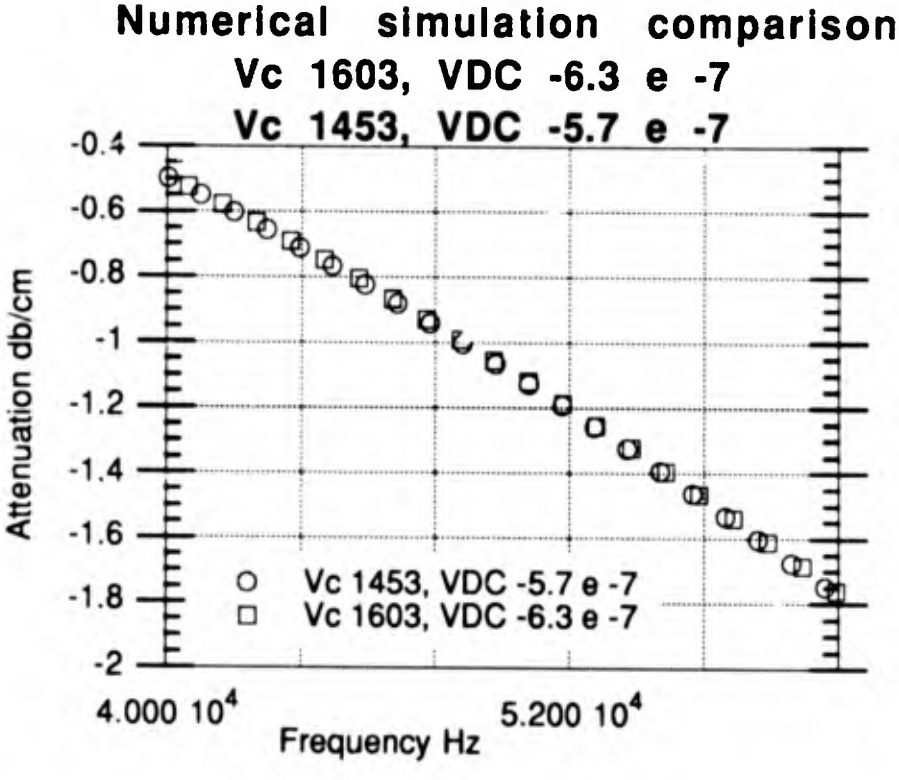

Figure 6.11. Numerical Simulation, comparison of V_C 1603 m/s, VDC -6.3 e -7 and V_C 1453 m/s, VDC -5.7 e -7.

Table 6.7. Attenuation versus Frequency Comparison between two Numerical, Viscoelastic Damping Coefficients (VDC) -6.3 e -7 at Vc 1603 m/s , and -5.7 e -7 at Vc 1453 m/s , Two-dimensional model.

Frequency Hz	Attenuation db/cm Vc 1453, VDC -5.7 e -7	Frequency Hz	Attenuation db/cm Vc 1603, VDC -6.3 e -7	Attenuation db/cm Vc 1453, VDC -5.7 e -7 (interpolated)
48844	-1.0037	48765	-0.9916	-0.9985
49820	-1.0656	49781	-1.0555	-1.0629
50797	-1.1287	50797	-1.1207	-1.1286
51774	-1.1929	51813	-1.1870	-1.1955
52751	-1.2582	52829	-1.2544	-1.2636
53728	-1.3246	53845	-1.3231	-1.3329

Table 6.7 depicts the range of values in Figure 6.11. It shows that the interpolated values of attenuation from the V_C 1453, VDC -5.7 e -7 numerical simulation match within 1% of those values from the V_C 1603, VDC -6.3 e -7 numerical simulation.

6.2. Numerical Simulation with Inclusion

The goal with the numerical simulation with inclusion was not to characterize the effect of voids but to provide an indication that the numerical simulation, like the experimental data, was affected by the void inclusion. The square void was used for convenience to match the xy grid.

A numerical simulation of a square void in a SRM inert propellant sample was compared to a numerical simulation of a sample without a void. Figure 6.12 depicts the comparison based on attenuation. The two numerical simulations used a Vc of 1603 m/s and VDC of -6.325 e -7 which closely matched the experimental data. The small square void

was located approximately where the Paddle Ball and Ping Pong Ball were in the experimental tests identified by the letters G, H, IC and IF for the Paddle Ball and J, K, LC and LF for the Ping Pong Ball. The square void was 22 x 22 grid points in the numerical grid. The void area was the equivalent of 1/9th the projection of the Paddle Ball and Ping Pong Ball on a two-dimensional surface. The scattering by the square void was different than either the Paddle Ball or the Ping Pong Ball.

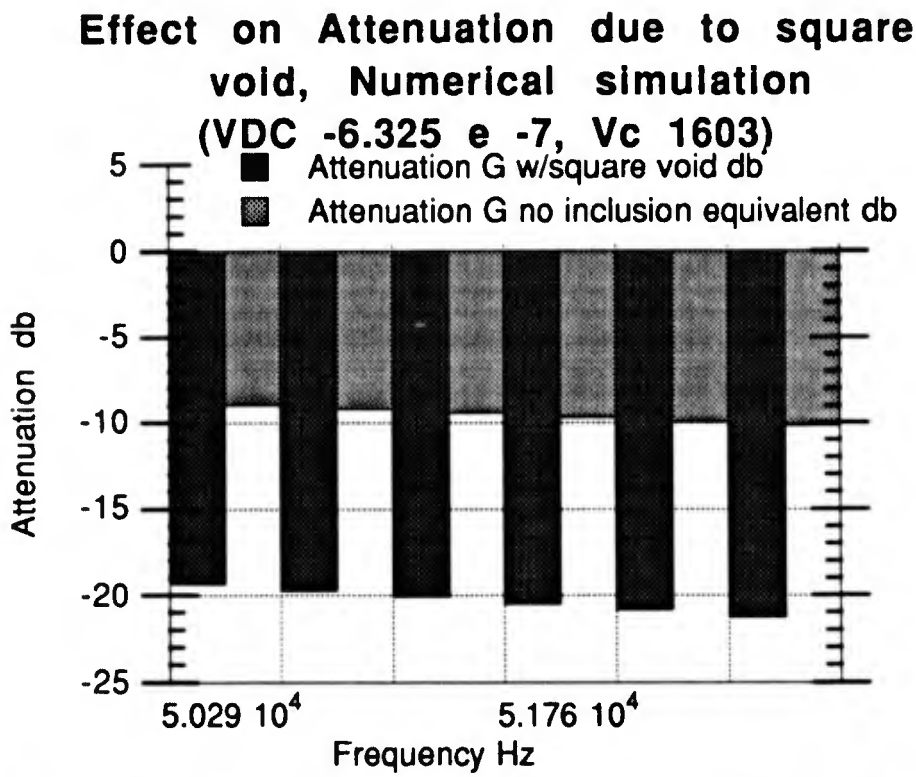

Figure 6.12. Effect on Attenuation due to Square Void inclusion, Numerical Simulation, G "no inclusion" equivalent, (VDC -6.325 e -7).

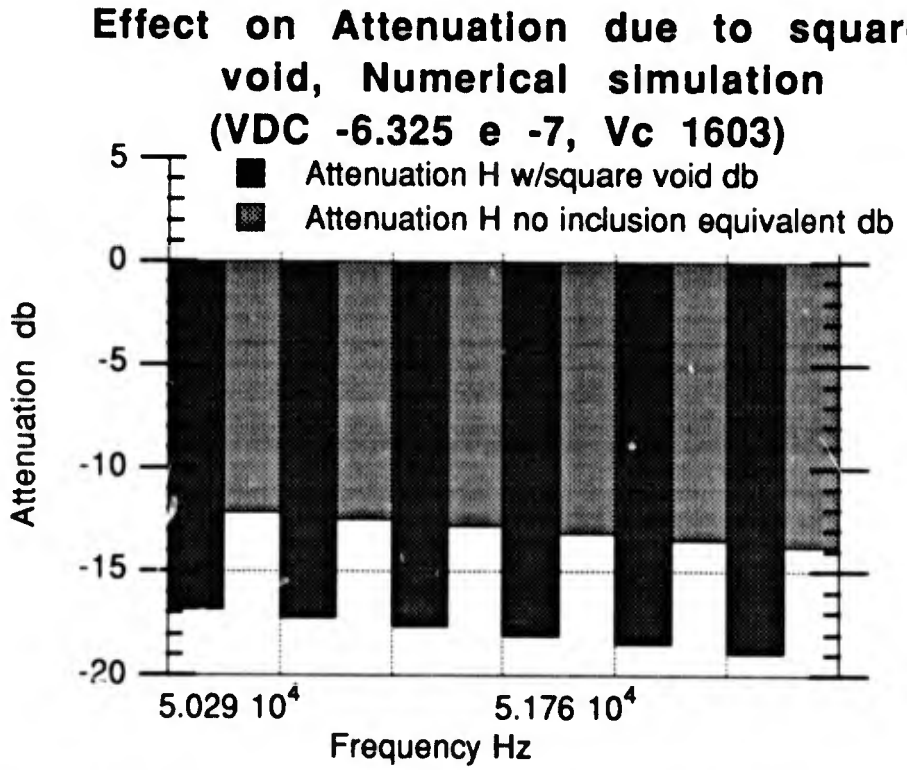

Figure 6.13. Effect on Attenuation due to Square Void inclusion, Numerical Simulation, H "no inclusion" equivalent, (VDC -6.325 e -7).

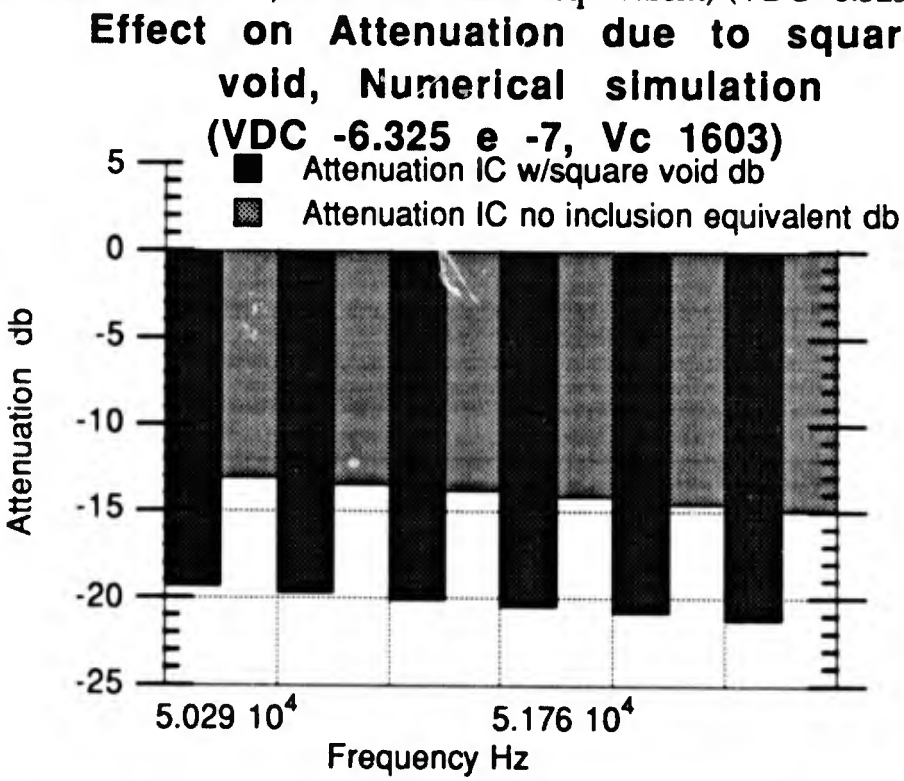

Figure 6.14. Effect on Attenuation due to Square Void inclusion, Numerical Simulation, IC "no inclusion" equivalent, (VDC -6.325 e -7).

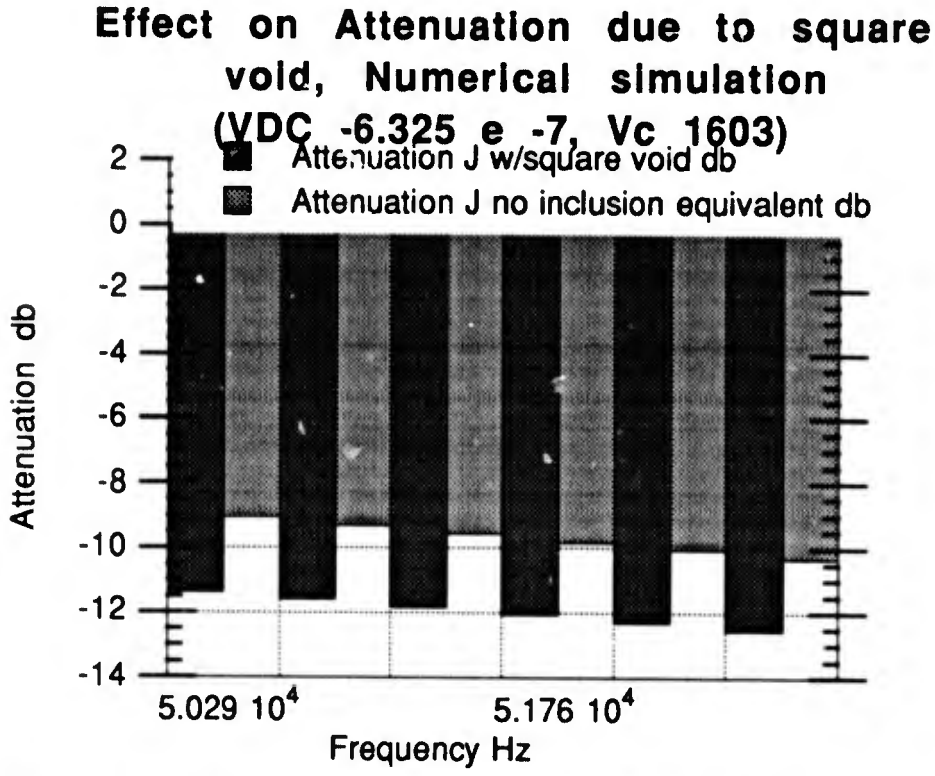

Figure 6.15. Effect on Attenuation due to Square Void inclusion, Numerical Simulation, J "no inclusion" equivalent, (VDC -6.325 e -7).

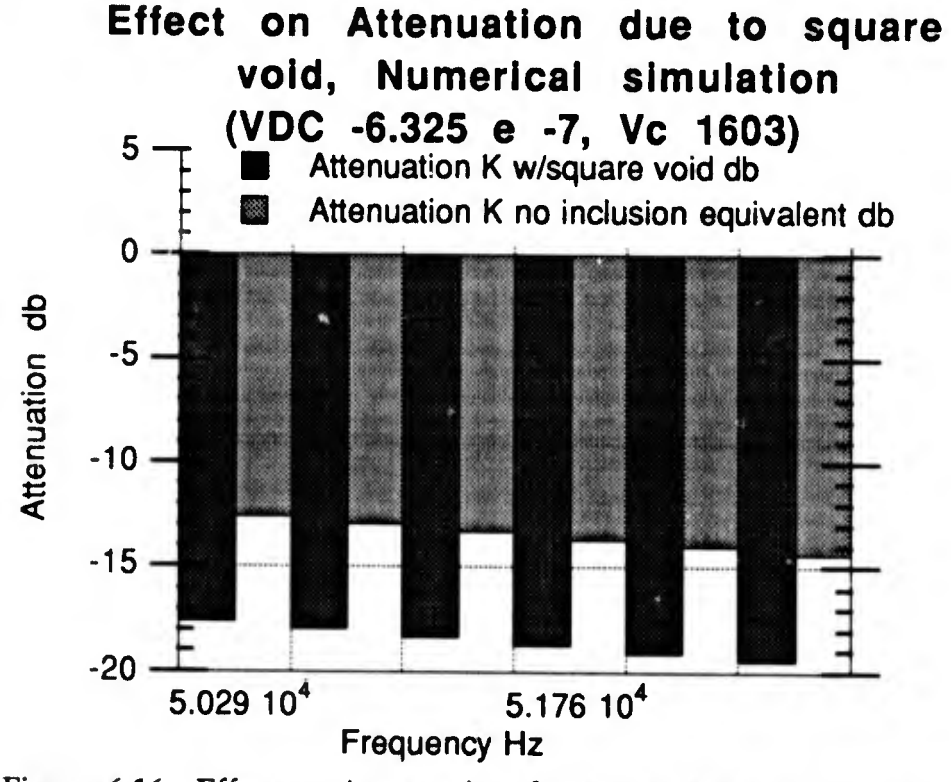

Figure 6.16. Effect on Attenuation due to Square Void inclusion, Numerical Simulation, K "no inclusion" equivalent, (VDC -6.325 e -7).

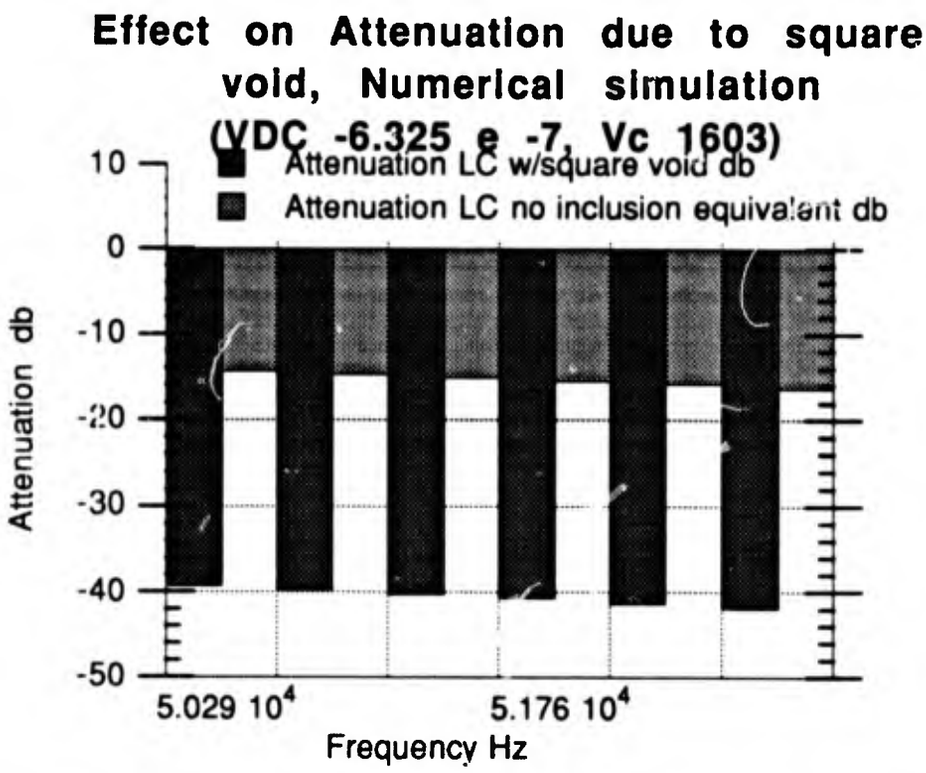

Figure 6.17. Effect on Attenuation due to Square Void inclusion, Numerical Simulation, LC "no inclusion" equivalent, (VDC -6.325 e -7).

Figures 6.18 - 6.23 compares Figures 6.12 - 6.17 to Figures 5.49 - 5.56. One can observe clearly that and how the void affects the received signal in both the experimental and numerical tests. Further, the excess attenuation holds information which should provide the means for the successful detection, location, and sizing of voids in SRM propellant segments. Even though the square void is not the same size nor shape as the inclusions in the inert propellant samples, the attenuation in db is comparable in five out of six Figures. The numerical simulation with inclusions seems to be predicting the same trend as the experiment ultrasonic NDE of the sample SRM propellant with inclusions.

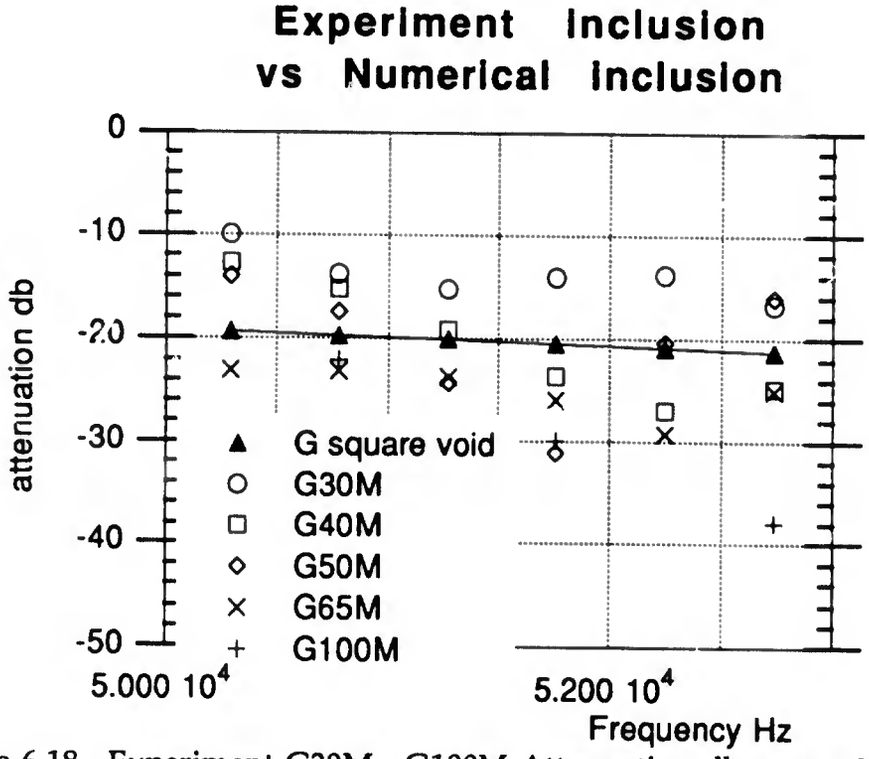

Figure 6.18. Experiment G30M - G100M Attenuation db versus Numerical Simulation G Square Void Attenuation db.

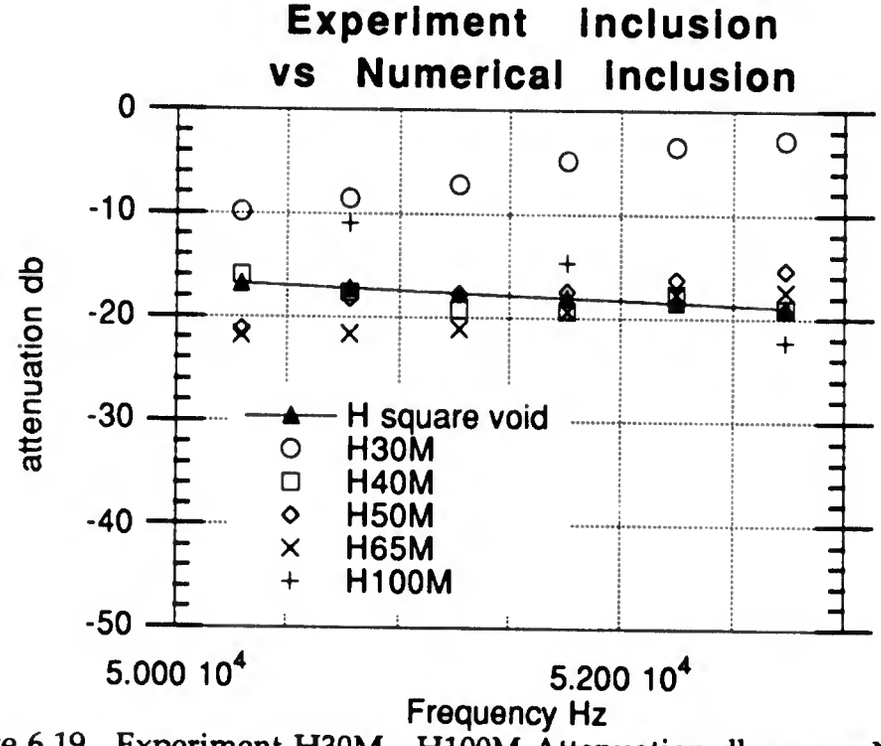

Figure 6.19. Experiment H30M - H100M Attenuation db versus Numerical Simulation H Square Void Attenuation db.

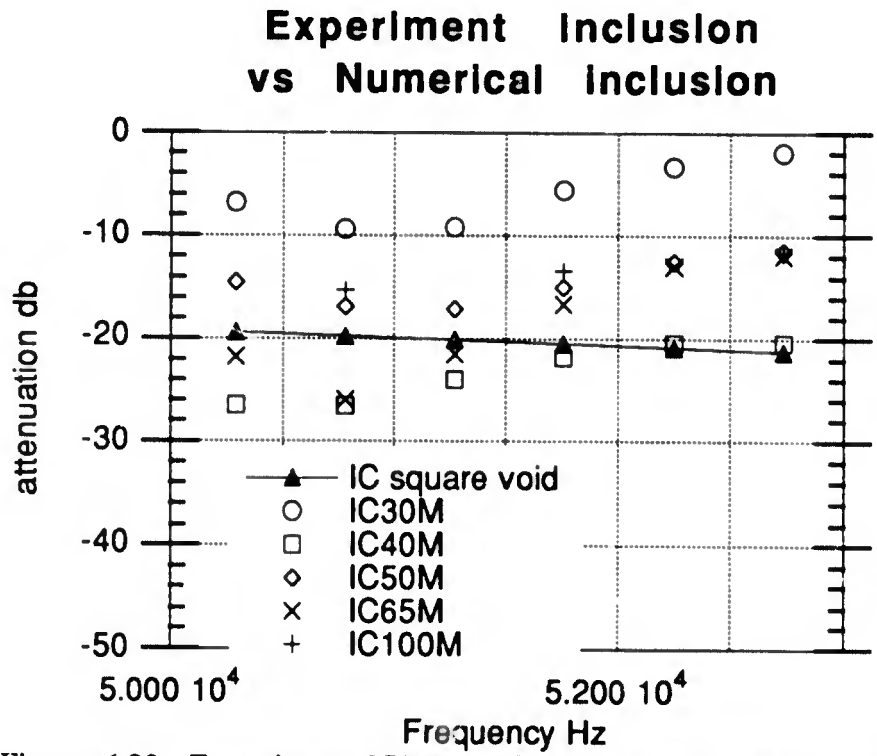

Figure 6.20. Experiment IC30M - IC100M Attenuation db versus Numerical Simulation IC Square Void Attenuation db.

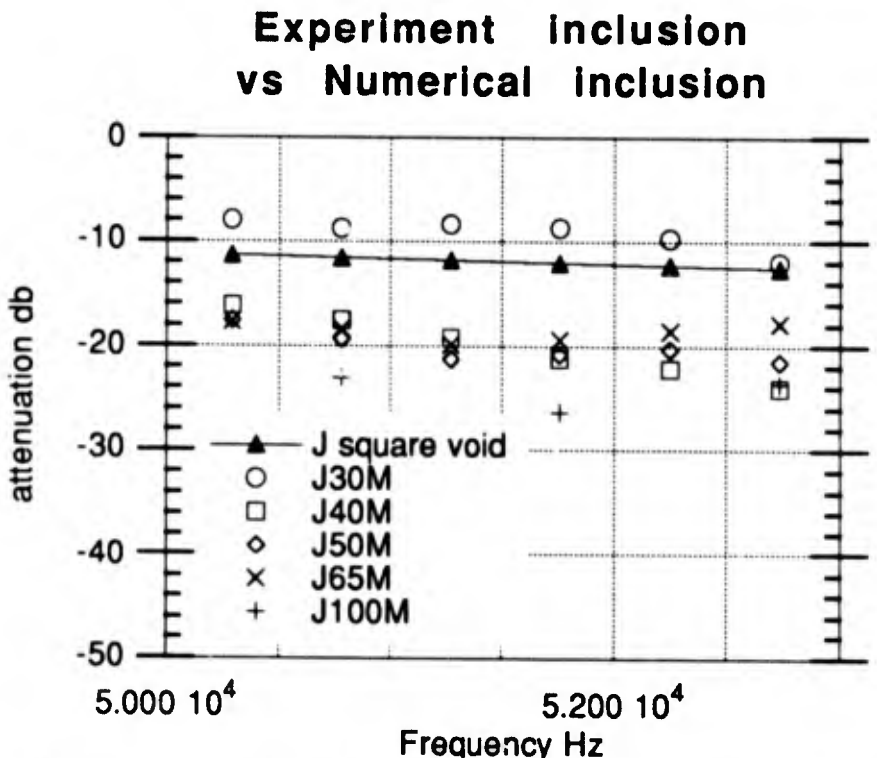

Figure 6.21. Experiment J30M - J100M Attenuation db versus Numerical Simulation J Square Void Attenuation db.

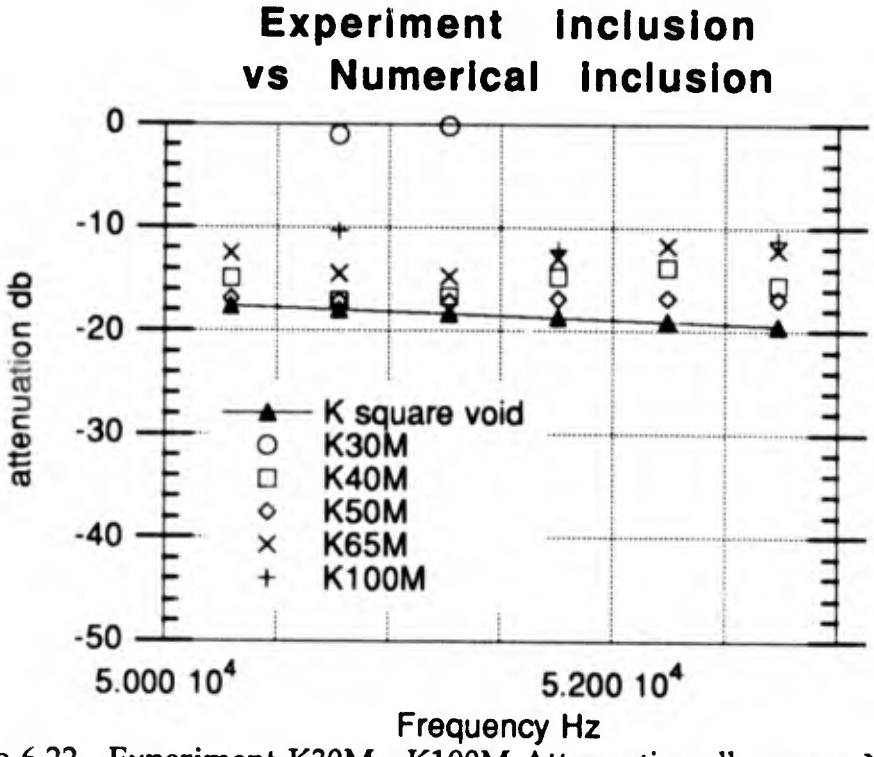

Figure 6.22. Experiment K30M - K100M Attenuation db versus Numerical Simulation K Square Void Attenuation db.

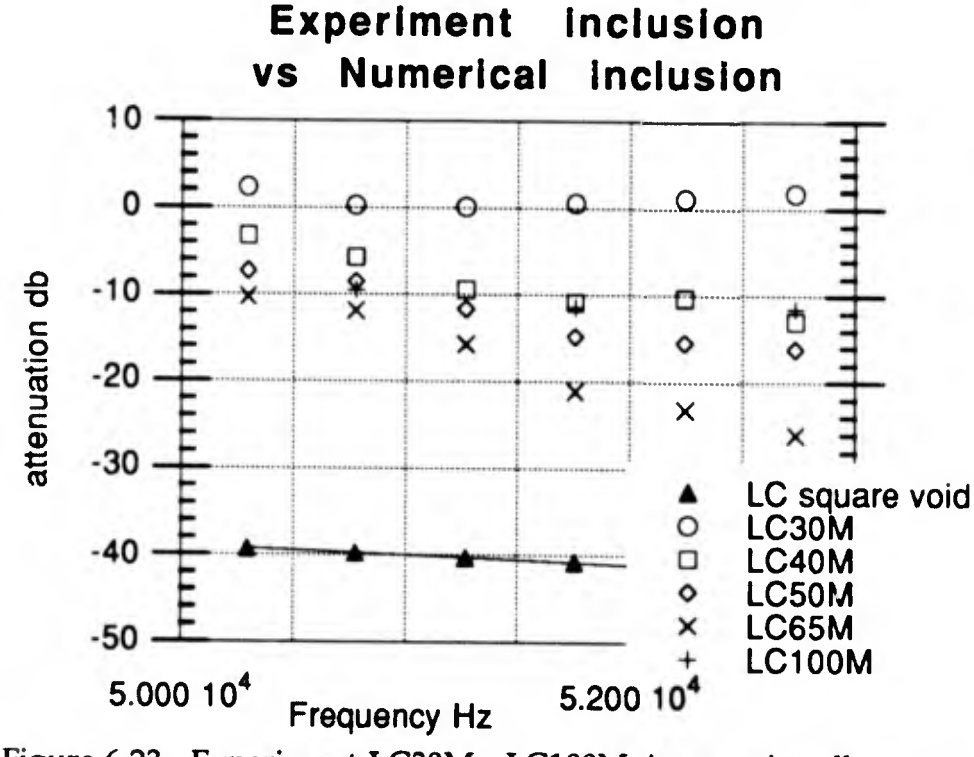

Figure 6.23. Experiment LC30M - LC100M Attenuation db versus Numerical Simulation LC Square Void Attenuation db.

CHAPTER VII

CONCLUSIONS, BENEFITS, AND FUTURE WORK

7.0 Overview

This chapter concludes the research effort by bringing together the observations from the experimental tests and numerical simulations in discussion and conclusion sections. The summary of results is followed by recommendations for improvement in the efforts to develop an ultrasonic NDE technique, as well as identifying the areas that require further examination.

7.1 Discussion

A methodology was developed during this research which appears useful for further investigation of ultrasonic NDE. The idea of casting spares or samples of material to be tested later was not new. However, the use of spares, in a non-destructive manner, to tune the ultrasonic NDE technique was unique. The current tuning involves the computation of the Viscoelastic Damping Coefficient and subsequent use in the numerical simulation. The specific numerical model chosen for the numerical simulations, Kelvin-Voigt in this research, must meet the standard of matching the characteristics of the SRM propellant. Specifically, the characteristics - attenuation and velocity, as they vary with frequency.

These characteristics were what the ultrasonic through-transmission experimental tests could measure. Flexibility in the methodology allows the use of other mechanical approximations to the stress-strain relationship if future SRM propellant compositions dictate. Further, the use of numerical simulations in a model based inversion incorporating Artificial Intelligence, Neural Networks, Knowledge based systems or other similar systems, would lessen the judgment required of the operator in the detection, location and sizing of inclusions, which the current X-Ray inspection method relies so heavily upon. Another benefit of the methodology would be the ability to conduct frequent ultrasonic NDE of the samples to monitor the effects of aging on the sample and indirectly the SRM propellant segment itself. The methodology is outlined below as steps 1 - 7, however, the last three steps were just presented, but not incorporated in this research effort.

1- When casting an SRM, cast and set aside a test specimens;
2- Conduct ultrasonic NDE of the test specimens;
3- Analyze data, compute a Viscoelastic Damping Coefficient (VDC) by the method shown in this paper;
4- Use the VDC in a numerical simulation to validate the numerical model, specifically addressing SRM propellant characteristics;
5- Conduct a numerical parametric study and include critical flaws;
6- Use a model based inversion for the accept/reject criterion;
7- Conduct periodic ultrasonic NDE of the accepted SRM propellant segments and samples to monitor for defects and aging.

Using this methodology on the test specimen identified in Chapter V, the Viscoelastic Damping Coefficient, (see Table 5.11 A, B, C, and 5.12), was determined analytically following Kino (1987) from the experimental testing attenuation versus frequency and velocity versus frequency profiles. The experimental data and the two-dimensional numerical simulations produced similar attenuation versus frequency profiles (see

Figures 6.7 and 6.8.), when the same Viscoelastic Damping Coefficient was used. The Kelvin-Voigt mechanical approximation to the stress-strain relationship adequately models the viscoelastic behavior of the SRM propellant. Two specimens contained inclusions, a Paddle Ball and a Ping Pong Ball. The ultrasonic NDE revealed a definite affect on the attenuation versus frequency profile when each of these specimen was examined (see Figures 5.46 - 5.53). Although the critical flaws were not accurately physically and geometrically modeled, the two-dimensional numerical simulation likewise exhibited a different attenuation versus frequency profile with an inclusion, a square void in this case (see Figure 6.9). The attenuation versus frequency Figures of the paddle ball and ping pong ball are generally like Figures of the square void.

The specimens with inclusions exhibit a change in the attenuation versus frequency profile which can be identified as measured attenuation. The measured attenuation consists of three parts, attenuation due to diffraction, attenuation due to viscoelastic effects (expected), and excess attenuation. It is the ability to compare the excess attenuation to the test reference which will enable the model based inversion technique to detect, locate, and size the inclusion. The problem with using just through-transmission ultrasonic NDE occurs when the ill-posed problem returns a signal with excess attenuation. Does the excess attenuation occur because there is a large inclusion near the receiver transducer, because there is a small inclusion near the transmit transducer, or because some other complex system is present? Is there possibly a medium size inclusion somewhere in between? Remember, detection, location, and sizing of volumetric flaws away from boundaries are the object of the ultrasonic NDE inspection method. Scanning or the use of a phased array of

receivers may provide more information than a simple two transducer through-transmission test. The incorporation of Artificial Intelligence, Neural Networks or a similar system into ultrasonic NDE will lessen the reliance on the ability of the operator to make judgments concerning flaw detection, location, and sizing. The excess attenuation will be the input to the signal processing problem which is beyond the scope of this research.

7.2 Conclusions

The methodology of characterizing a propellant sample for bulk viscoelastic material properties which can be matched to a numerical simulation is established. This allows each individual propellant mixture to be characterized using specific parameters of the material and this can be the basis of an inspection for voids by means of ultrasonic NDE.

The inert propellant exhibits an increasing attenuation with frequency, indicating a dissipative mechanism. The attenuation quadrupled between 50 kHz and 500 kHz. As such, any numerical simulation modelling propellant behavior must include viscoelastic effects.

The Kelvin-Voigt mechanical representation of the stress-strain relationship provides an excellent representation of the viscoelastic behavior in the inert propellant during ultrasonic NDE simulations.

The average Viscoelastic Damping Coefficient (VDC) determined from the experimental tests, with the aid of the approximation from Kino (1987), matches the value used to obtain a similar attenuation versus frequency profile in the corresponding numerical simulations. The

experimental methodology associated with the experimental tests may have caused most of the variation among the VDCs determined experimentally. Further, the numerical simulation determined an approximation to the longitudinal velocity of the SRM inert propellant, thereby providing a means for confirming predictions from experimental tests.

All current ultrasonic NDE is for defect detection on a production basis, none is used for material characterization. The characterization of propellant sample for bulk viscoelastic material properties also allows the periodic tracking of attenuation, velocity and VDC to determine the changes over time. This should provide a quantitative means of determining service-life in SRM propellant and possibly in other viscoelastic materials.

The use of the VDC in the numerical simulations with voids included, square voids in this case, clearly show excess attenuation in the attenuation versus frequency profiles, versus the simulations without voids. Similar effects are evident in the experiment tests results on the two specimen with inclusions. This trend appears to allow the detection of voids in the propellant at 50 kHz for a d/λ of 0.8.

Finally, the possibility of using ultrasonic NDE as a valid technique to detect, locate, and size voids in SRM propellant looks promising. However, a model based inversion technique, possibly incorporating Artificial Intelligence or Neural Networks, seems needed due to the ill-posed inverse problem with just single through-transmission ultrasonic NDE.

7.3 Ancillary Benefits: Monitoring Propellant Aging

Other benefits of the methodology presented herein can be found if the numerical simulation without void inclusions is used to chart how the "aging" of the SRM propellant affects the Viscoelastic Damping Coefficient. Solid Rocket Motor propellant's bulk viscoelastic material properties change with time and service history. Safety considerations preclude the use of propellant after it exceeds the estimated service life. The VDC, as used in the numerical simulation, is the ratio of viscosity to elasticity, therefore, any change can be directly related to the stiffening or hardening of the material or a change in Young's modulus. This latter event is important because the value of Young's modulus is used to determine the stresses encountered during the time the Launch Vehicle is sitting on the launch pad (propellant sagging under its own weight), during ignition, and during the actual operation of the motor.

Further, using the VDC predicted by the experimental data in the numerical simulations to match the experimental attenuation provides a means to determine the equivalent longitudinal velocity of the inert propellant. This may prove to be a tie between dynamic and static testing on SRM propellant and resultant bulk material properties determined from each test.

Batch-to-batch comparisons can be made between SRM propellant segments made of the same formulation. This would increase manufacturing reliability in a quality control aspect.

In a more futuristic thought, to alleviate the difficulty with using x-ray inspection techniques in space, the methodology could be adapted for

possible use as a model for an ultrasonic NDE technique in space during in-space construction.

7.4 Future Work

An obvious extension of this research requires a parametric study, providing both time and frequency domain information, mapping the propellant response to different void locations in the numerical simulations, specifically in line, off line, and multiple voids configurations, as well as, different void shapes.

The ill posed inverse problem of detecting, locating, and sizing flaws makes it necessary to investigate a model-based inversion. The above mentioned parametric studies may provide the background to the learning that a smart system needs. The range of critical flaw size, ka, approximately equal to 2, at 50 kHz with 3.2 cm wavelength where the flaw is slightly smaller than the wavelength, reduces the assumptions one can make in the scattering problem.

Scanning for edges, where the first indication of a 6 db loss of signal strength indicates a blocking of half the beam, should be incorporated. Further a 70 % blocking of the ultrasonic beam delivers 10 db less of signal amplitude than an unblocked collimated beam between two parallel transducers. These and other rules should be incorporated in any smart system. Again, with an expanding beam from transmitter to receiver, even with a diffraction correction, the ill-posed problem is evident and the question becomes where and what size flaw caused this blocking?

Whatever the outcome, the flaw was detected and therefore ultrasonic NDE shows promise.

Improvements in the methodology should always be investigated.

BIBLIOGRAPHY

Aki, K., and Richards, P. G., Quantitative Seismology: Theory of Methods, Volumes 1 & 2, W. H. Freeman and Co., New York, 1980.

Alford, R. M., Kelley, K. R., and Boore, D. M., "Accuracy of Finite-Difference Modelling of the Acoustic Wave Equation," Geophysics, Vol. 39, No. 6, December 1974, pp. 834-842.

Alterman, Z., and Leowenthal, D., "Computer Generated Seismograms," Methods in Computational Physics, Vol. 12, Academic Press, New York, 1972, pp. 35-164.

Atalar, A., "A Fast Method of Calculating Diffraction Loss Between Two Facing Transducers," IEEE Transactions on Ultrasonics, Ferroelectrics, and Frequency Control, Vol. 35, No. 5, September 1988, pp. 612-617.

Ayme-Bellagarda, E. J., Chang, H., and Habashy, T. M., "Forward Scattering from Solid or Fluid-Filled Inclusion Buried in Multilayered Elastic Structures," Proceedings of the IEEE 1990 Ultrasonics Symposium, Honolulu, Hawaii, December 4-7, 1990, pp. 971-974.

Bagley, R. L., and Torvik P. J., "On the Fractional Calculus Model of Viscoelastic Behavior," Journal of Rheology, Vol. 30, No. 1, 1986, pp. 133-155.

Balch, A. H., and Smolka, F. A., "Plane and Spherical Transient Voigt Waves," Geophysics, Vol. 35, No. 5, October 1970, pp. 745-761.

Blake, R. J., and Bond, L. J., "Rayleigh Wave Scattering from Surface Features: Wedges and Down-steps," Ultrasonics, Vol. 28, July 1990, pp. 214-227.

Blake, R. J., and Bond, L. J., "Rayleigh Wave Scattering from Surface Features: Upsteps and Troughs," Ultrasonics, Vol. 29, March 1991.

Blake, R. J., Bond, L. J., and Downie, A. L., "Advances in Numerical Studies of Elastic Wave Propagation and Scattering," Review of Progress in Quantitative Nondestructive Evaluation , Vol. 1, Ed.: Thompson, D. O., Chimenti, D. E., Plenum Publishing Corporation, 1982, pp. 157-165.

Bond, L. J., Surface Cracks in Metals and their Characterization Using Rayleigh Waves, Ph.D. Thesis, The City University, London, 1978.

Bond, L. J., "Numerical Techniques and Their Use to Study Wave Propagation and Scattering--A Review," Elastic Waves and Ultrasonic Nondestructive Evaluation, Ed.: Datta, S. K., Achenbach, J. D. Rajapakse, Y. S., Elsevier Science Publishers, B. V., North Holland, 1990, pp. 17-27.

Bond, L. J., Punjani, M., and Saffari, N., "Ultrasonic Wave Propagation and Scattering Using Explicit Finite Difference Methods," Mathematical Modelling in Nondestructive Testing, Ed.: Blakemore, M., Georgiou, G. A., Oxford, 1988.

Bond, L. J., Saffari, N., and Punjani, M., "Modeling Ultrasonic Waves Using Finite Difference Methods," Review of Progress in Quantitative Nondestructive Evaluation, Vol. 6A, Ed.: Thompson, D. O., Chimenti, D., E., Plenum Publishing Corporation, 1987, pp. 135-144.

Boore, D. M., "Finite-Difference Methods for Seismic Wave Propagation in Heterogeneous Materials," Academic Press, Methods in Computational Physics, Vol. 11, 1972, pp. 1-37.

Caille, G. W., The Acoustic Field Scattered from Some Approximate Pressure Release Materials Coating a Finite Cylinder, Ph. D. thesis, Georgia Institute of Technology, March 1988.

Cavicchi, T. J., "Transient High-Order Ultrasonic Scattering," Journal of the Acoustical Society of America, Vol. 88, No. 2, August 1990, pp. 1132-1141.

Cerjan, C., Kosloff, D., Kosloff, R., and Reshef, M., "A Nonreflecting Boundary Condition for Discrete Acoustic and Elastic Wave Equations," Geophysics, Vol. 50, No. 4, April 1985, pp. 705-708.

Chang, H., "3-D Reflection/Transmission Coefficients From Cylindrical Layered Elastic Media," Proceedings of the IEEE 1987 Ultrasonics Symposium, Denver, Colorado, October 14-16, 1987, pp. 455-459.

Chang, H., and D'Angelo, R. M., "Experimental Verification of Finite Difference Model for Ultrasonic Evaluation of Complex Structures," Proceedings of the IEEE 1990 Ultrasonics Symposium, Honolulu, Hawaii, 1990, pp. 965-969.

Chang, H., and Randall, C. J., "Finite-Difference Time-Domain Modelling of Elastic Wave Propagation in the Cylindrical Coordinate System," Proceedings of the IEEE 1988 Ultrasonics Symposium, Vol. 1, Chicago, Illinois, October 2-5, 1988, pp. 297-402.

Christensen, R. M., Theory of Viscoelasticity: An Introduction, Academic Press, New York, 1971.

Cooke, J. A., Determination of the Impulse Response of a Viscoelastic Beam Using a Fractional Derivative Constitutive Model, Ph.D. Thesis, North Carolina State University, Raleigh, 1988.

Craig, R. R. Jr., Structural Dynamics: An Introduction to Computer Methods, John Wiley & Sons, New York, 1981.

Daniels, C. A., Polymers: Structure and Properties, Technomic Publishing Co., Inc., Lancaster, PA, 1989.

Dean, D. S., and Young, D., "The Reduction and Display of Ultrasonic Data," Research Techniques in Nondestructive Testing, Vol. 2, Ed.: Sharpe, R. S., 1974, pp. 369-391.

Dow, J. O., Jones, M. S., and Harwood, S. A., "A Generalized Finite Difference Method for Solid Mechanics," Numerical Methods for Partial Differential Equations, Vol. 2, John Wiley and Sons, 1990, pp. 137-152.

Djordjevic, B. B, "Ultrasonic Through Body Inspection of SRM's," MMLTR 87-27, 1987.

Djordjevic, B. B, "Nondestructive Evaluation in Space," Proceedings of the IEEE 1990 Ultrasonics Symposium, Honolulu, Hawaii, December 4-7, 1990, pp. 997-1002.

Djordjevic, B. B, and Friant, C. L., "Ultrasonic Propagation and Signal Quality Estimates for Thick Multilayer Structures," Chemical Propulsion Information Agency Publication 559, May 1991, pp. 95-97.

Fortunko, C. M., Peterson, G. L., Chick, B. B., Renken, M. C., and Preis, A. L., "Absolute Measurements of Elastic-Wave Phase and Group Velocities in Lossy Materials," Rev. Sci. Instruments, Vol. 63, No. 6, June 1992, pp. 3477-3486.

Frankel, A., "A Review of Numerical Experiments on Seismic Wave Scattering," Pure and Applied Geophysics, Vol. 131, No. 4, 1989, pp. 639-685.

Fredrickson, A G., Principles and Applications of Rheology, Prentice-Hall, Englewood Cliffs, N.J., 1964.

Gammell, P. M., "Feasibility of Air Coupling for Ultrasonic Inspection of Large Solid Rocket Motors," Review of Progress in Quantitative Nondestructive Evaluation 10, Ed.: Thompson, D. O., Chimenti, D. E., Plenum Publishing Corporation, New York, 1991, pp.

Gaunaurd, G. C., Methods for Solving the Viscoelasticity Equations for Cylinder Sphere Problems, Naval Surface Weapons Center, Silver Springs, MD, NSWC/WOL/TR 76-20, 22 March 1976.

Graff, K. F., Wave Motion in Elastic Solids, Clarendon Press, Oxford, 1975.

Hall, I. H., Deformation of Solids, Barnes and Noble, New York, 1968.

Hercules Aerospace Corporation - NDE group, Private Communication, 26 September 1991.

- Staff, Private Communication, 10 February 1993.

Higdon, A., Ohlsen, E. H., Stiles, W. B., Weese, J. A., and Riley, W. F., Mechanics of Materials, 4th Edition, John Wiley and Sons, New York, 1985.

Hudson, J. A., The Excitation and Propagation of Elastic Waves, Cambridge University Press, Cambridge, Great Britain, 1980.

Ilan, A., and Weight, J. P., "The Propagation of Short Pulses of Ultrasound from a Circular Source Coupled to an Isotropic Solid," Journal of the Acoustical Society of America, Vol. 88, No. 2, August 1990, pp. 1142-1151.

Johnston, P. H., "Nondestructive Evaluation of Space Shuttle Solid Rocket Motor Field Joint," Proceedings of the IEEE 1987 Ultrasonics Symposium, Denver, Colorado, October 14-16, 1987, pp. 1087-1091.

Kline, R. A., and Egle, D. M., "Applications of Digital Methods to Ultrasonic Materials Characterization," NDT International, Vol. 19, No. 5, October 1986, pp. 341-347.

Kroll, M. and Djordjevic, B. B., "A Laser Stress-wave Probe with Sub-angstrom Sensitivity and Large Bandwidth," Proceedings of the IEEE 1982 Ultrasonics Symposium, Vol. 12, San Diego, California, October 27-29, 1982.

Lawrence, R. J., A Nonlinear Viscoelastic Equation of State for Use in Stress Propagation Calculations, SLA-73-0635, Sandia Laboratories, September 1973.

Madigosky W. M., and Scharnhorst, K. P., "Acoustic Wave Propagation in Materials with Inclusions or Voids," Sound and Vibration Damping with Polymers, Proceedings of the Symposium, National Meeting of American Chemical Society 157th, Dallas, Texas, April 9-14, 1989, Washington, D. C., American Chemical Society, 1990, pp. 229-247.

Mak, D. K., "Comparison of Various Methods for the Measurement of Reflection Coefficient and Ultrasonic Attenuation," The British Journal of Non-Destructive Testing, Vol. 33, No. 9, September 1991, pp. 441-448.

Martin Marietta Corporation, Internal Research and Development (IRAD) report R-619R, Ultrasonic Materials Characterization of Multilayer Multicomponent Structures, 1987.

Martin Marietta Corporation - Staff Engineer, Mr. Ward Rummel, Private Communication, 17 January 1992.

- Staff Engineer, Dr. B. Boro Djordjevic, Private Communication, 2 March 1992.

- Staff Engineer, Dr. Mark Langhenry, Private Communication, 10 February 1993.

- Staff Engineer, Mr. Mike Rooney, Private Communication, 25 May 1993.

Meer, A., Propagation of Longitudinal Stress Waves in Elastic and Linearly Viscoelastic Bars of Variable Cross Section, Department of the Army, USA Research Office, Durham, North Carolina, May 1969, DA-31-124-ARO(D)-358.

Morgenthaler, G. W., and Nici, R., "Development Testing, Nondestructive Evaluation and Check-out in Space Construction and its impact on Space Logistics Support," AIAA Proceedings of the Society of Logistics Engineers Fourth Annual Logistics Symposium, Cocoa Beach, Florida, November 4-6, 1991, pp. 448-456.

Mourad, K. M., The Application of the Boundary Element Method to Predict the Response of a Differential Operator Model for a Coupled Viscoelastic-Acoustic System, Ph. D. Thesis, North Carolina State University, Raleigh, 1990.

Nielsen, L. E., Mechanical Properties of Polymers and Composites, Volumes 1 & 2, Marcel Dekker Inc., New York, 1974.

Pao, Y., "Elastic Waves in Solids," Transactions of the ASME Journal of Applied Mechanics, Vol. 50, December 1983, pp. 1152-1164.

Piché, L., "Phenomena Related to the Propagation of Ultrasound in Polymers (a paradigm for disordered materials)," Proceedings of the IEEE 1989 Ultrasonics Symposium, Vol. 1, Montreal, Quebec, Canada, October 3-6, 1989, pp. 599-608.

Pipkin, A. C., Lectures on Viscoelasticity Theory, 2nd Ed., Applied Mathematical Sciences, Vol. 7, Spriger-Verlav, Berlin, 1986.

Press, W. H., Flannery, B. P., Teukolsky, S. A., and Vetterling, W. T., Numerical Recipes: The Art of Scientific Computing, Cambridge University Press, Cambridge, 1989.

Purnell, G. W., "Observations of Wave Velocity and Attenuation in Two Phase Media", Geophysics, Vol. 51, No. 12, December 1986, pp. 2193-2199.

"Radiographic Inspection Of Space Shuttle SRM Segments, Requirements for," STW7-3179A, Space Division, Morton Thiokol, Inc., 10 August 1987.

Reali, M., Rangogni, R., and Pennati, V., "Compact Analytical Expressions of Two-Dimensional Finite Difference Forms," International Journal for Numerical Methods in Engineering, Vol. 20, 1984, pp. 121-130.

Ricker, N. H., Transient Waves in Visco-Elastic Media, Elsevier Scientific Publishing, Oxford, 1977.

Roberts, D. L., and Selim, M. S., "Comparative Study of Six Explicit and Two Implicit Finite Difference Schemes for Solving One-Dimensional Parabolic Partial Differential Equations," International Journal for Numerical Methods in Engineering, Vol. 20, 1984, pp. 817-844.

Rogers, P. H., and Van Buren, A. L., "An Exact Expression for the Lommel Diffraction Correction Integral," Journal of Acoustical Society of America, Vol. 55, No. 4, April 1974, pp. 724-728.

Rooney, M., Nondestructive Evaluation of Structural Bonds for Large Solid Rocket Motor Applications, M.S. Thesis, The Johns Hopkins University, Baltimore, Maryland, November 1990.

Sachse, W., and Pao, Y., "On the Determination of Phase and Group Velocities of Dispersive Waves in Solids", Journal of Applied Physics, Vol. 49, No. 8, August 1978, pp. 4320-4327.

Schmidt, H., and Jenson, F. B., An Efficient Numerical Solution Technique for Wave Propagation in Horizontally Stratified Ocean Environments, SACLANT ASW Research Center, La Sperzia, Italy, Memorandum NATO, SACLANTCEN SM-173, 1984.

Seki, H., Granato, A, and Truell, R., "Diffraction Effects in the Ultrasonic Field of a Piston Source and Their Importance in the Accurate Measurement of Attenuation," Journal of Acoustical Society of America, Vol. 28, No. 2, 1956, pp. 230-238.

Shimizu, M., Itoh, K., Fukushima, Y., and Maniwa, T., "Swept Frequency Ultrasonic Inspection Method for Liner-Propellant Separation of the H-II SRB," IAF International Astronautical Congress 40th, Malaga, Spain, October 7-13, 1989, IAF 89-295.

Simpson, W. A. Jr., and McClung, R. W., "Quantitative Attenuation Technique for Materials Characterization," Materials Evaluation, November 1991, Vol. 49, No. 11, pp. 1409-1413.

Smith, G. D., Numerical Solution of Partial Differential Equations: Finite Difference Methods, 3rd Ed., Clarendon Press, Oxford, 1985.

Stremler, F. G., Introduction to Communication Systems, 2nd Ed., Addison-Wesley Publishing Co., London, 1982.

Sullivan, J. M Jr., Ludwig, R., and Geng, Y., "Numerical Simulation of Ultrasound Nondestructive Evaluation for Adhesive Bond Integrity," Proceedings of the IEEE 1990 Ultrasonics Symposium, Honolulu, Hawaii, December 4-7, 1990.

Sutton, G. P. Rocket Propulsion Elements: An Introduction to the Engineering of Rockets, 5th Ed., John Wiley & Sons, New York, 1986.

Thiokol Corporation - Staff, Private Communication, 4 February 1992.

Thompson, R. B., and Wadley, H. N. G., "The Use of Elastic Wave-Material Structure Interaction Theories in Nondestructive Evaluation Modelling," Critical Reviews in Solid State and Materials Science, Vol. 16, Issue 1, 1989, pp. 37-89.

Thomson, W. T., Theory of Vibration with Applications, 3rd Ed., Prentice-Hall, Engle Cliffs, New Jersey, 1988.

Truell, R., Elbaum, C., and Chick, B. B., Ultrasonic Methods in Solid State Physics, Academic Press, New York, 1969.

Tung, T., Connor, J., and Antoniadis, D. A., "A Boundary Element Method for Modeling Viscoelastic Flow in Thermal Oxidation," IEEE Transactions on Computer Aided Design," Vol. 7, No. 2, February 1988, pp. 215-224.

Virieux, J., "P-SV Wave Propagation in Heterogeneous Media: Velocity-Stress Finite-Difference Method", Geophysics, Vol. 51, No. 4, April 1987, pp. 889-901.

Weaver, R. L., Sachse, W., and Niu, L., "Transient Ultrasonic Waves in a Viscoelastic Plate: Theory," Journal of the Acoustic Society of America, Vol. 85, No. 6, June 1989, pp. 2255-2261.

Weaver, R. L., Sachse, W., and Niu, L., "Transparent Ultrasonic Waves in a Viscoelastic Plate: Applications to Materials Characterization," Journal of the Acoustic Society of America, Vol. 85, No. 6, June 1989, pp. 2262-2267.

Yang, J. C., Fernandez, R., L., and Reed, R. S., "Elastic Stress Waves Propagation in Axi-symmetric Bodies," Mechanical Behavior of Materials Proceedings, Vol. 2, Kyoto, Japan, August, 21-24, 1974. pp. 259-275.

You, Z, Lusk, M., Ludwig, R., and Lord, W., "Numerical Simulation of Ultrasonic Wave Propagation in Anisotropic and Attenuative Solid Materials," IEEE Transactions on Ultrasonics, Ferroelectrics, and Frequency Control, Vol. 38, No. 5, September 1991, pp. 436-445.

APPENDIX A

KELVIN-VOIGT THREE-DIMENSIONAL EOMS

First the elastic EOMs are developed, then the Kelvin-Voigt stress-strain relationship is introduced into the EOMs. The notational terms in equation (A1), equation (27) from Chapter III, are the gradient, ∇, the stress tensor, σ, density, ρ, and the second time-derivative of the displacement vector, $\ddot{\mathbf{u}}$.

$$\nabla \cdot \sigma = \rho \ddot{\mathbf{u}} \tag{A1}$$

The gradient, ∇ , using a Cartesian coordinate system is shown as (A2).

$$\nabla = \frac{\partial}{\partial x}\hat{i} + \frac{\partial}{\partial y}\hat{j} + \frac{\partial}{\partial z}\hat{k} \tag{A2}$$

For an elastic isotropic, homogeneous material, the three-dimensional stress-strain relationship can be expressed using the Lamé parameters, λ, and, μ, with σ_{ij} the components of the stress tensor, σ. These appear in equation (46) as (A3) and with equation (7) as (A4).

$$\sigma_{ij} = \lambda \varepsilon_{kk} + 2\mu \varepsilon_{ij} \tag{A3}$$

$$2\varepsilon_{kl} = \frac{\partial u_k}{\partial x_l} + \frac{\partial u_l}{\partial x_k} \qquad \text{(A4)}$$

Performing the indicated operations on the left hand side of equation (A1), using the above equations for the gradient, stress and strain, with the Cartesian coordinate system relating the x, y, z directions and associated with unit vectors $\hat{i}$, $\hat{j}$, $\hat{k}$ for the u, v, w displacements, one can arrive at three scalar equations. The first with strains is shown in (A5a), (A5b), (A5c), then with displacements in (A6a), (A6b), (A6c).

$$\nabla\cdot\sigma =$$

$$\hat{i}\left\{\frac{\partial}{\partial x}\left[(\lambda+2\mu)\varepsilon_{xx}+\lambda\varepsilon_{yy}+\lambda\varepsilon_{zz}\right]+\frac{\partial}{\partial y}2\mu\varepsilon_{xy}+\frac{\partial}{\partial z}2\mu\varepsilon_{xz}\right\} \qquad \text{(A5a)}$$

$$\hat{j}\left\{\frac{\partial}{\partial y}\left[(\lambda+2\mu)\varepsilon_{yy}+\lambda\varepsilon_{xx}+\lambda\varepsilon_{zz}\right]+\frac{\partial}{\partial z}2\mu\varepsilon_{yz}+\frac{\partial}{\partial x}2\mu\varepsilon_{xy}\right\} \qquad \text{(A5b)}$$

$$\hat{k}\left\{\frac{\partial}{\partial z}\left[(\lambda+2\mu)\varepsilon_{zz}+\lambda\varepsilon_{yy}+\lambda\varepsilon_{xx}\right]+\frac{\partial}{\partial x}2\mu\varepsilon_{xz}+\frac{\partial}{\partial y}2\mu\varepsilon_{yz}\right\} \qquad \text{(A5c)}$$

$$\nabla\cdot\sigma =$$

$$\hat{i}\left\{(\lambda+2\mu)\frac{\partial^2 u}{\partial^2 x}+\lambda\frac{\partial^2 v}{\partial x\partial y}+\lambda\frac{\partial^2 w}{\partial x\partial z}+\mu\left(\frac{\partial^2 u}{\partial^2 y}+\frac{\partial^2 v}{\partial x\partial y}\right)+\mu\left(\frac{\partial^2 u}{\partial^2 z}+\frac{\partial^2 w}{\partial x\partial z}\right)\right\} \qquad \text{(A6a)}$$

$$\hat{j}\left\{(\lambda+2\mu)\frac{\partial^2 v}{\partial^2 y}+\lambda\frac{\partial^2 u}{\partial x\partial y}+\lambda\frac{\partial^2 w}{\partial y\partial z}+\mu\left(\frac{\partial^2 v}{\partial^2 x}+\frac{\partial^2 u}{\partial x\partial y}\right)+\mu\left(\frac{\partial^2 v}{\partial^2 z}+\frac{\partial^2 w}{\partial y\partial z}\right)\right\} \qquad \text{(A6b)}$$

$$\hat{k}\left\{(\lambda+2\mu)\frac{\partial^2 w}{\partial^2 z}+\lambda\frac{\partial^2 v}{\partial y\partial z}+\lambda\frac{\partial^2 u}{\partial x\partial z}+\mu\left(\frac{\partial^2 w}{\partial^2 y}+\frac{\partial^2 v}{\partial z\partial y}\right)+\mu\left(\frac{\partial^2 w}{\partial^2 x}+\frac{\partial^2 u}{\partial x\partial z}\right)\right\} \quad \text{(A6c)}$$

The right hand side of equation (A1) is the second time-derivative of the displacement. The elastic EOMs, written as three scalar equations, combine equation (A6) with the right hand side of equation (A1) as equation (A7a), (A7b), (A7c).

$$\rho\frac{\partial^2 u}{\partial t^2}=(\lambda+2\mu)\frac{\partial^2 u}{\partial^2 x}+\lambda\frac{\partial^2 v}{\partial x\partial y}+\lambda\frac{\partial^2 w}{\partial x\partial z}+\mu\left(\frac{\partial^2 u}{\partial^2 y}+\frac{\partial^2 v}{\partial x\partial y}\right)+\mu\left(\frac{\partial^2 u}{\partial^2 z}+\frac{\partial^2 w}{\partial x\partial z}\right) \quad \text{(A7a)}$$

$$\rho\frac{\partial^2 v}{\partial t^2}=(\lambda+2\mu)\frac{\partial^2 v}{\partial^2 y}+\lambda\frac{\partial^2 u}{\partial x\partial y}+\lambda\frac{\partial^2 w}{\partial y\partial z}+\mu\left(\frac{\partial^2 v}{\partial^2 x}+\frac{\partial^2 u}{\partial x\partial y}\right)+\mu\left(\frac{\partial^2 v}{\partial^2 z}+\frac{\partial^2 w}{\partial y\partial z}\right) \quad \text{(A7b)}$$

$$\rho\frac{\partial^2 w}{\partial t^2}=(\lambda+2\mu)\frac{\partial^2 w}{\partial^2 z}+\lambda\frac{\partial^2 v}{\partial y\partial z}+\lambda\frac{\partial^2 u}{\partial x\partial z}+\mu\left(\frac{\partial^2 w}{\partial^2 y}+\frac{\partial^2 v}{\partial z\partial y}\right)+\mu\left(\frac{\partial^2 w}{\partial^2 x}+\frac{\partial^2 u}{\partial x\partial z}\right) \quad \text{(A7c)}$$

In order to use the scalar Kelvin-Voigt stress-strain relationship, equation (26) was repeated here as equation (A8). One must compare this to equation (1), (A9) and notice the viscoelastic modifier to Young's modulus E.

$$\sigma=\left(1+\eta/E\frac{\partial}{\partial t}\right)E\varepsilon \quad \text{(A8)}$$

$$\sigma = \quad E\varepsilon \tag{A9}$$

The viscoelastic modifier is introduced into the elastic EOMs, equation (A7), by means of the relationship between the Lamé parameters and Young's modulus, presented here as equations (A10) and (A11), where ν is Poisson's ratio.

$$\lambda = \frac{\nu E}{(1+\nu)(1-2\nu)} \tag{A10}$$

$$\mu = \frac{E}{2(1+\nu)} \tag{A11}$$

Since both of the Lamé parameters are linear with respect to Young's modulus, one modifies the λ and μ with $\left(1+\eta / E\frac{\partial}{\partial t}\right)$ in (A7) to get the three-dimensional Kelvin-Voigt EOMs. Further, one can notice that every term on the right hand side of (A7) has a Lamé parameter, so that the entire equation can be modified quite easily with the term η /E being replaced by a generic viscoelastic damping coefficient η, and presented as equations (A12a), (A12b), (A12c).

$$\rho\frac{\partial^2 u}{\partial t^2} = (\lambda+2\mu)\frac{\partial^2 u}{\partial^2 x} + \lambda\frac{\partial^2 v}{\partial x\partial y} + \lambda\frac{\partial^2 w}{\partial x\partial z} + \mu\left(\frac{\partial^2 u}{\partial^2 y} + \frac{\partial^2 v}{\partial x\partial y}\right) + \mu\left(\frac{\partial^2 u}{\partial^2 z} + \frac{\partial^2 w}{\partial x\partial z}\right) \tag{A12a}$$

$$+\eta\frac{\partial}{\partial t}\left\{(\lambda+2\mu)\frac{\partial^2 u}{\partial^2 x} + \lambda\frac{\partial^2 v}{\partial x\partial y} + \lambda\frac{\partial^2 w}{\partial x\partial z} + \mu\left(\frac{\partial^2 u}{\partial^2 y} + \frac{\partial^2 v}{\partial x\partial y}\right) + \mu\left(\frac{\partial^2 u}{\partial^2 z} + \frac{\partial^2 w}{\partial x\partial z}\right)\right\}$$

$$\rho\frac{\partial^2 v}{\partial t^2}=(\lambda+2\mu)\frac{\partial^2 v}{\partial^2 y}+\lambda\frac{\partial^2 u}{\partial x\partial y}+\lambda\frac{\partial^2 w}{\partial y\partial z}+\mu\left(\frac{\partial^2 v}{\partial^2 x}+\frac{\partial^2 u}{\partial x\partial y}\right)+\mu\left(\frac{\partial^2 v}{\partial^2 z}+\frac{\partial^2 w}{\partial y\partial z}\right) \quad \text{(A12b)}$$

$$+\eta\frac{\partial}{\partial t}\left\{(\lambda+2\mu)\frac{\partial^2 v}{\partial^2 y}+\lambda\frac{\partial^2 u}{\partial x\partial y}+\lambda\frac{\partial^2 w}{\partial y\partial z}+\mu\left(\frac{\partial^2 v}{\partial^2 x}+\frac{\partial^2 u}{\partial x\partial y}\right)+\mu\left(\frac{\partial^2 v}{\partial^2 z}+\frac{\partial^2 w}{\partial y\partial z}\right)\right\}$$

$$\rho\frac{\partial^2 w}{\partial t^2}=(\lambda+2\mu)\frac{\partial^2 w}{\partial^2 z}+\lambda\frac{\partial^2 v}{\partial y\partial z}+\lambda\frac{\partial^2 u}{\partial x\partial z}+\mu\left(\frac{\partial^2 w}{\partial^2 y}+\frac{\partial^2 v}{\partial z\partial y}\right)+\mu\left(\frac{\partial^2 w}{\partial^2 x}+\frac{\partial^2 u}{\partial x\partial z}\right) \quad \text{(A12c)}$$

$$+\eta\frac{\partial}{\partial t}\left\{(\lambda+2\mu)\frac{\partial^2 w}{\partial^2 z}+\lambda\frac{\partial^2 v}{\partial y\partial z}+\lambda\frac{\partial^2 u}{\partial x\partial z}+\mu\left(\frac{\partial^2 w}{\partial^2 y}+\frac{\partial^2 v}{\partial z\partial y}\right)+\mu\left(\frac{\partial^2 w}{\partial^2 x}+\frac{\partial^2 u}{\partial x\partial z}\right)\right\}$$

APPENDIX B

BOUNDARY CONDITIONS

B.0 Overview

In Chapter IV the finite difference formulation for a three-dimensional free surface and two-dimensional corner point were completed for the u displacement. The finite difference formulations developed below are for the three-dimensional front, back, left, right, top and bottom free surface displacements in the x, y, z directions followed by the two-dimensional A-D corner point displacements in the x and y directions.

B.1 Free Surface Finite Difference Formulations

In Section 4.2 Free Surface Boundary Conditions, the u displacement finite difference formulation in the x direction on the front side of the grid was given in equation (49) for the elastic case and in equation (50) for the Kelvin-Voigt case. Figure 4.2, repeated below depicted point R, a point on the front surface of the numerical grid. Figure B.1 depicts the three-dimensional numerical grid with point R shown on the front surface. In this figure, the x direction grid point i is indexed from 1 to n, the y direction grid point j from 1 to m, and the z direction grid point k from 1 to p. Each point on the three-dimensional numerical grid

also has an associated time step, so the displacements are identified as u(i,j,k,l) in this case a u displacement at an arbitrary point at time step l. The same format was used for displacements v and w. The three-dimensional numerical grid has six free surfaces, three of which are shown in Figure B.1, with binary pairs for each direction, i.e. Front - Back for the x direction, Left - Right for the y direction, and Top - Bottom for the z direction.

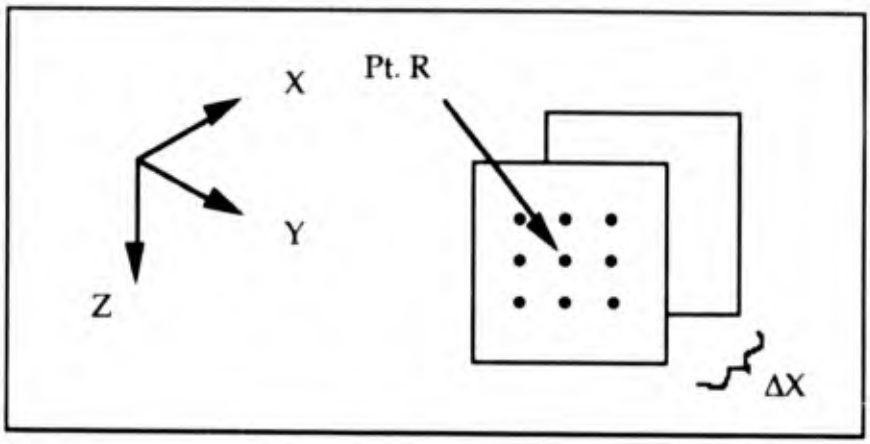

Figure 4.2. Point R on the Free Surface Grid Boundary in the X Direction.

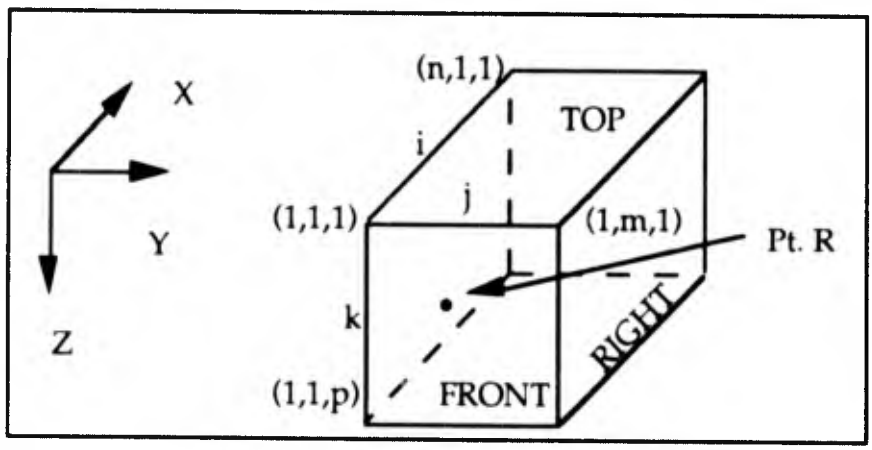

Figure B.1. Three-dimensional Numerical Grid with point R shown on the Front Surface.

The v and w displacement formulation for point R follows the same steps as did the u displacement in Section 4.2. A Taylor series approximation was the basic equation with boundary conditions and equations of motion used to substitute for the partial derivatives. Equation (44) was shown as equation (B1), was the u displacement Taylor series approximation for point R. The v and w displacements Taylor series approximation for point R just replaces u with the appropriate displacement in equation (B1).

$$u(i+1,j,k,l) = u(i,j,k,l) + h\frac{\partial u}{\partial x} + \frac{1}{2}h^2\frac{\partial^2 u}{\partial x^2} + O(h^3) \qquad \text{(B1)}$$

Where third-order terms, $O(h^3)$, were neglected, h was equal to Δx. The boundary condition σ_{xx} equal to zero was the free surface condition and shown as equation (B2). The EOM is equation (B3a).

$$\sigma_{xx} = (\lambda + 2\mu)\frac{\partial u}{\partial x} + \lambda\left(\frac{\partial v}{\partial y} + \frac{\partial w}{\partial z}\right) = 0 \qquad \text{(B2)}$$

$$\rho\frac{\partial^2 u}{\partial t^2} = (\lambda + 2\mu)\frac{\partial^2 u}{\partial^2 x} + \lambda\frac{\partial^2 v}{\partial x \partial y} + \lambda\frac{\partial^2 w}{\partial x \partial z} + \mu\left(\frac{\partial^2 u}{\partial^2 y} + \frac{\partial^2 v}{\partial x \partial y}\right) + \mu\left(\frac{\partial^2 u}{\partial^2 z} + \frac{\partial^2 w}{\partial x \partial z}\right) \qquad \text{(B3a)}$$

The other boundary conditions for all the free surface formulations, are shown in equations (B4) - (B8).

$$\sigma_{yy} = (\lambda + 2\mu)\frac{\partial v}{\partial y} + \lambda\left(\frac{\partial u}{\partial x} + \frac{\partial w}{\partial z}\right) = 0 \qquad \text{(B4)}$$

$$\sigma_{zz} = (\lambda + 2\mu)\frac{\partial u}{\partial x} + \lambda\left(\frac{\partial v}{\partial y} + \frac{\partial w}{\partial z}\right) = 0 \qquad \text{(B5)}$$

$$\sigma_{xy} = \frac{\partial u}{\partial y} + \frac{\partial v}{\partial x} = 0 \qquad \text{(B6)}$$

$$\sigma_{xz} = \frac{\partial u}{\partial z} + \frac{\partial w}{\partial x} = 0 \qquad \text{(B7)}$$

$$\sigma_{yz} = \frac{\partial v}{\partial z} + \frac{\partial w}{\partial y} = 0 \qquad \text{(B8)}$$

The equations of motion for the v and w displacements are equations (35b) and (35c), shown below as (B3b) and (B3c).

$$\rho\frac{\partial^2 v}{\partial t^2} = (\lambda + 2\mu)\frac{\partial^2 v}{\partial^2 y} + \lambda\frac{\partial^2 u}{\partial x \partial y} + \lambda\frac{\partial^2 w}{\partial y \partial z} + \mu\left(\frac{\partial^2 v}{\partial^2 x} + \frac{\partial^2 u}{\partial x \partial y}\right) + \mu\left(\frac{\partial^2 v}{\partial^2 z} + \frac{\partial^2 w}{\partial y \partial z}\right) \qquad \text{(B3b)}$$

$$\rho\frac{\partial^2 w}{\partial t^2} = (\lambda + 2\mu)\frac{\partial^2 w}{\partial^2 z} + \lambda\frac{\partial^2 v}{\partial y \partial z} + \lambda\frac{\partial^2 u}{\partial x \partial z} + \mu\left(\frac{\partial^2 w}{\partial^2 y} + \frac{\partial^2 v}{\partial z \partial y}\right) + \mu\left(\frac{\partial^2 w}{\partial^2 x} + \frac{\partial^2 u}{\partial x \partial z}\right) \qquad \text{(B3c)}$$

The task of substituting the boundary conditions and the equations of motion into the Taylor series approximations for each free surface formulation will not be shown here, however all the parts are presented above. The rest of the Kelvin-Voigt formulations for the displacements on a free surface are shown in equations (B9) - (B14), with the u, v, and w displacements corresponding to parts a, b, and c of each equation.

The Front free surface formulation corresponds to equation (B9), with the pattern for the other free surface formulations as follows: Back - (B10), Right - (B11), Left - (B12), Top - (B13), and Bottom - (B14). The Front free surface formulation for the u displacement equation (50) was shown below as equation (B9a). Before the free surface formulations are

presented the cross derivative formulations must be addressed. In equation (B3a), the equation of motion for the u displacement, the cross partial derivative terms were approximated by quasi-centered difference functions. The sign convention presented in Section 4.1 still holds. There are fifteen different formulations for the cross derivatives. The cross derivatives essentially determine a plane defined by the two directions identified in the denominator of the derivative. This plane intersects the three-dimensional numerical grid at the point where the formulation is being used to determine the displacement. For an internal grid point, the body node formulation in Section 4.1 Figure 4.1 determines the sign convention for the cross derivative centered finite difference equation. Note: there will always be eight points surrounding the point of interest in the three-dimensional numerical grid when it is an internal point. Three formulations for the cross derivatives are identified as d2xy, d2xz, and d2yz. Equation (33) defines d2xy, which is the cross derivative in the x - y plane. The functions d2xz and d2yz are defined in the x - z plane and y - z plane respectively, with the formulation the same as equation (33) except that the displacements u and w, and v and w, are used instead of u and v. The twelve other cross derivative formulations are used when the plane defined by the cross derivative intersects the free surface of the three-dimensional numerical grid. Now for two out of three planes, there are no longer eight points surrounding the point of interest, only five points. Hence the cross derivative formulations are adjusted as in equation (47) in Section 4.2. Again for a particular cross derivative, one just substitutes the appropriate grid points for each displacement in the cross derivative formulation, whether there are eight or five points surrounding the point of interest. In the following equations, for the twelve cross derivative

functions that involve the planes that intersect the free surface, dxyf as an example, are organized by the following code. The code was used to help maintain accurate formulations and provide a means of identifying the planes and free surfaces involved in each cross derivative formulation. The first check was the fact that the function started with a d, did not contain a 2, and had four letters. The last letter was the free surface, f - for front, b for back, l for left, r for right, t for top, and m for bottom. The second letter corresponded to the direction perpendicular to the free surface. The third letter would be one of the other two directions parallel to the free surface. Therefore dxyf was the front surface cross derivative formulation for the displacement in the x - y plane surrounding the point of interest. Looking at point R in Figure 4.2, the front surface, the y - z plane, shows eight points surrounding point R. However in the x - y plane and the x - z plane, only five points surround point R. In the former case the cross derivative would be d2yz, and dxyf and dxzf in the latter case.

The reason for this added level of functions was to provide modularity and a means of checking the accuracy of each formulation. Due to symmetry and using these formulations, only three minor changes are necessary in equation (B9a) to obtain (B10a).

$$
\begin{aligned}
&d2t(u) = 2\max\left(u(i+1,j,k,l) - u(i,j,k,l)\right) \\
&+\max\left(1-2rate^2\right)\begin{Bmatrix}\left[v(i,j+1,k,l) - v(i,j-1,k,l)\right] \\ +\left[w(i,j,k+1,l) - w(i,j,k-1,l)\right]\end{Bmatrix} \\
&+\max rate^2\left[d2y(u) + d2z(u)\right] \\
&+\frac{\max}{2}\left(1-rate^2\right)\left[dxyf(v) + dxzf(w)\right] \\
&+\eta\frac{\partial}{\partial t}\begin{Bmatrix}2\max\left(u(i+1,j,k,l) - u(i,j,k,l)\right) \\ +\max\left(1-2rate^2\right)\begin{Bmatrix}\left[v(i,j+1,k,l) - v(i,j-1,k,l)\right] \\ +\left[w(i,j,k+1,l) - w(i,j,k-1,l)\right]\end{Bmatrix} \\ +\max rate^2\left[d2y(u) + d2z(u)\right] \\ +\frac{\max}{2}\left(1-rate^2\right)\left[dxyf(v) + dxzf(w)\right]\end{Bmatrix}
\end{aligned}
\qquad \text{(B9a)}
$$

$$
\begin{aligned}
&d2t(v) = \max d2y(v) \\
&+\max rate^2\begin{Bmatrix}2\left[v(i+1,j,k,l) - v(i,j,k,l)\right] + d2z(v) \\ +\left[u(i,j+1,k,l) - u(i,j-1,k,l)\right]\end{Bmatrix} \\
&+\frac{\max}{2}\left(1-rate^2\right)\left[dxyf(u) + d2yz(w)/2\right] \\
&+\eta\frac{\partial}{\partial t}\begin{Bmatrix}\max d2y(v) \\ +\max rate^2\begin{Bmatrix}2\left[v(i+1,j,k,l) - v(i,j,k,l)\right] + d2z(v) \\ +\left[u(i,j+1,k,l) - u(i,j-1,k,l)\right]\end{Bmatrix} \\ +\frac{\max}{2}\left(1-rate^2\right)\left[dxyf(u) + d2yz(w)/2\right]\end{Bmatrix}
\end{aligned}
\qquad \text{(B9b)}
$$

$$
\begin{aligned}
&d2t(w) = \max d2z(w) \\
&+\max \mathrm{rate}^2 \left\{ \begin{matrix} 2\left[w(i+1,j,k,l) - w(i,j,k,l)\right] + d2y(w) \\ +\left[u(i,j,k+1,l) - u(i,j,k-1,l)\right] \end{matrix} \right\} \\
&+\frac{\max}{2}\left(1-\mathrm{rate}^2\right)\left[dxzf(u) + d2yz(v)/2\right] \\
&+\eta\frac{\partial}{\partial t}\left\{ \begin{matrix} \max d2z(w) \\ +\max \mathrm{rate}^2 \left\{ \begin{matrix} 2\left[w(i+1,j,k,l) - w(i,j,k,l)\right] + d2y(w) \\ +\left[u(i,j,k+1,l) - u(i,j,k-1,l)\right] \end{matrix} \right\} \\ +\frac{\max}{2}\left(1-\mathrm{rate}^2\right)\left[dxzf(u) + d2yz(v)/2\right] \end{matrix} \right\}
\end{aligned}
\qquad \text{(B9c)}
$$

$$
\begin{aligned}
&d2t(u) = 2\max\left(u(i-1,j,k,l) - u(i,j,k,l)\right) \\
&+\max\left(1-2\mathrm{rate}^2\right)\left\{ \begin{matrix} \left[v(i,j+1,k,l) - v(i,j-1,k,l)\right] \\ +\left[w(i,j,k+1,l) - w(i,j,k-1,l)\right] \end{matrix} \right\} \\
&+\max \mathrm{rate}^2\left[d2y(u) + d2z(u)\right] \\
&+\frac{\max}{2}\left(1-\mathrm{rate}^2\right)\left[dxyb(v) + dxzb(w)\right] \\
&+\eta\frac{\partial}{\partial t}\left\{ \begin{matrix} 2\max\left(u(i-1,j,k,l) - u(i,j,k,l)\right) \\ +\max\left(1-2\mathrm{rate}^2\right)\left\{ \begin{matrix} \left[v(i,j+1,k,l) - v(i,j-1,k,l)\right] \\ +\left[w(i,j,k+1,l) - w(i,j,k-1,l)\right] \end{matrix} \right\} \\ +\max \mathrm{rate}^2\left[d2y(u) + d2z(u)\right] \\ +\frac{\max}{2}\left(1-\mathrm{rate}^2\right)\left[dxyb(v) + dxzb(w)\right] \end{matrix} \right\}
\end{aligned}
\qquad \text{(B10a)}
$$

$$
\begin{aligned}
&d2t(v) = \max d2y(v) \\
&+\max rate^2 \begin{Bmatrix} 2\left[v(i-1,j,k,l) - v(i,j,k,l)\right] + d2z(v) \\ +\left[u(i,j+1,k,l) - u(i,j-1,k,l)\right] \end{Bmatrix} \\
&+\frac{\max}{2}\left(1 - rate^2\right)\left[dxyb(u) + d2yz(w)/2\right] \\
&+\eta\frac{\partial}{\partial t}\left\{\begin{array}{l} \max d2y(v) \\ +\max rate^2 \begin{Bmatrix} 2\left[v(i-1,j,k,l) - v(i,j,k,l)\right] + d2z(v) \\ +\left[u(i,j+1,k,l) - u(i,j-1,k,l)\right] \end{Bmatrix} \\ +\frac{\max}{2}\left(1 - rate^2\right)\left[dxyb(u) + d2yz(w)/2\right] \end{array}\right\}
\end{aligned}
\qquad \text{(B10b)}
$$

$$
\begin{aligned}
&d2t(w) = \max d2z(w) \\
&+\max rate^2 \begin{Bmatrix} 2\left[w(i-1,j,k,l) - w(i,j,k,l)\right] + d2y(w) \\ +\left[u(i,j,k+1,l) - u(i,j,k-1,l)\right] \end{Bmatrix} \\
&+\frac{\max}{2}\left(1 - rate^2\right)\left[dxzb(u) + d2yz(v)/2\right] \\
&+\eta\frac{\partial}{\partial t}\left\{\begin{array}{l} \max d2z(w) \\ +\max rate^2 \begin{Bmatrix} 2\left[w(i-1,j,k,l) - w(i,j,k,l)\right] + d2y(w) \\ +\left[u(i,j,k+1,l) - u(i,j,k-1,l)\right] \end{Bmatrix} \\ +\frac{\max}{2}\left(1 - rate^2\right)\left[dxzb(u) + d2yz(v)/2\right] \end{array}\right\}
\end{aligned}
\qquad \text{(B10c)}
$$

$$
\begin{aligned}
&d2t(u) = \max d2x(u) \\
&+\max rate^2\left\{\begin{matrix}\left[v(i+1,j,k,l)-v(i-1,j,k,l)\right]+d2z(u)\\ +2\left[u(i,j-1,k,l)-u(i,j,k,l)\right]\end{matrix}\right\} \\
&+\frac{\max}{2}\left(1-rate^2\right)\left[dxyr(v)+d2xz(w)/2\right] \\
&+\eta\frac{\partial}{\partial t}\left\{\begin{matrix}\max d2x(u)\\ +\max rate^2\left\{\begin{matrix}\left[v(i+1,j,k,l)-v(i-1,j,k,l)\right]+d2z(u)\\ +2\left[u(i,j-1,k,l)-u(i,j,k,l)\right]\end{matrix}\right\}\\ +\frac{\max}{2}\left(1-rate^2\right)\left[dxyr(v)+d2xz(w)/2\right]\end{matrix}\right\} \qquad \text{(B11a)} \\
&d2t(w) = \max d2z(w)
\end{aligned}
$$

$$
\begin{aligned}
&d2t(v) = 2\max\left(v(i,j-1,k,l)-v(i,j,k,l)\right) \\
&+\max\left(1-2rate^2\right)\left\{\begin{matrix}\left[u(i+1,j,k,l)-u(i-1,j,k,l)\right]\\ +\left[w(i,j,k+1,l)-w(i,j,k-1,l)\right]\end{matrix}\right\} \\
&+\max rate^2\left[d2x(v)+d2z(v)\right] \\
&+\frac{\max}{2}\left(1-rate^2\right)\left[dyxr(u)+dyzr(w)\right] \\
&+\eta\frac{\partial}{\partial t}\left\{\begin{matrix}2\max\left(v(i,j-1,k,l)-v(i,j,k,l)\right)\\ +\max\left(1-2rate^2\right)\left\{\begin{matrix}\left[u(i+1,j,k,l)-u(i-1,j,k,l)\right]\\ +\left[w(i,j,k+1,l)-w(i,j,k-1,l)\right]\end{matrix}\right\}\\ +\max rate^2\left[d2x(v)+d2z(v)\right]\\ +\frac{\max}{2}\left(1-rate^2\right)\left[dyxr(u)+dyzr(w)\right]\end{matrix}\right\} \qquad \text{(B11b)}
\end{aligned}
$$

$$d2t(w) = maxd2z(w)$$

$$+ max\,rate^2 \begin{Bmatrix} 2\left[w(i,j-1,k,l) - w(i,j,k,l)\right] + d2x(w) \\ +\left[v(i,j,k+1,l) - v(i,j,k-1,l)\right] \end{Bmatrix}$$

$$+ \frac{max}{2}\left(1 - rate^2\right)\left[dyzr(v) + d2xz(u)/2\right]$$

$$+\eta \frac{\partial}{\partial t} \left\{ \begin{array}{l} maxd2z(w) \\ + max\,rate^2 \begin{Bmatrix} 2\left[w(i,j-1,k,l) - w(i,j,k,l)\right] + d2x(w) \\ +\left[v(i,j,k+1,l) - v(i,j,k-1,l)\right] \end{Bmatrix} \\ + \frac{max}{2}\left(1 - rate^2\right)\left[dyzr(v) + d2xz(u)/2\right] \end{array} \right\} \qquad \text{(B11c)}$$

$$d2t(u) = maxd2x(u)$$

$$+ max\,rate^2 \begin{Bmatrix} \left[v(i+1,j,k,l) - v(i-1,j,k,l)\right] + d2z(u) \\ +2\left[u(i,j+1,k,l) - u(i,j,k,l)\right] \end{Bmatrix}$$

$$+ \frac{max}{2}\left(1 - rate^2\right)\left[dxyl(v) + d2xz(w)/2\right]$$

$$+\eta \frac{\partial}{\partial t} \left\{ \begin{array}{l} maxd2x(u) \\ + max\,rate^2 \begin{Bmatrix} \left[v(i+1,j,k,l) - v(i-1,j,k,l)\right] + d2z(u) \\ +2\left[u(i,j+1,k,l) - u(i,j,k,l)\right] \end{Bmatrix} \\ + \frac{max}{2}\left(1 - rate^2\right)\left[dxyl(v) + d2xz(w)/2\right] \end{array} \right\} \qquad \text{(B12a)}$$

$$d2t(w) = maxd2z(w)$$

$$
\begin{aligned}
&d2t(v) = 2\max\left(v(i,j+1,k,l) - v(i,j,k,l)\right) \\
&+\max\left(1-2rate^2\right)\begin{Bmatrix}\left[u(i+1,j,k,l) - u(i-1,j,k,l)\right] \\ +\left[w(i,j,k+1,l) - w(i,j,k-1,l)\right]\end{Bmatrix} \\
&+\max rate^2\left[d2x(v) + d2z(v)\right] \\
&+\frac{\max}{2}\left(1-rate^2\right)\left[dyxl(u) + dyzl(w)\right] \\
&+\eta\frac{\partial}{\partial t}\begin{Bmatrix}2\max\left(v(i,j+1,k,l) - v(i,j,k,l)\right) \\ +\max\left(1-2rate^2\right)\begin{Bmatrix}\left[u(i+1,j,k,l) - u(i-1,j,k,l)\right] \\ +\left[w(i,j,k+1,l) - w(i,j,k-1,l)\right]\end{Bmatrix} \\ +\max rate^2\left[d2x(v) + d2z(v)\right] \\ +\frac{\max}{2}\left(1-rate^2\right)\left[dyxl(u) + dyzl(w)\right]\end{Bmatrix}
\end{aligned}
\qquad \text{(B12b)}
$$

$$
\begin{aligned}
&d2t(w) = \max d2z(w) \\
&+\max rate^2\begin{Bmatrix}2\left[w(i,j+1,k,l) - w(i,j,k,l)\right] + d2x(w) \\ +\left[v(i,j,k+1,l) - v(i,j,k-1,l)\right]\end{Bmatrix} \\
&+\frac{\max}{2}\left(1-rate^2\right)\left[dyzl(v) + d2xz(u)/2\right] \\
&+\eta\frac{\partial}{\partial t}\begin{Bmatrix}\max d2z(w) \\ +\max rate^2\begin{Bmatrix}2\left[w(i,j+1,k,l) - w(i,j,k,l)\right] + d2x(w) \\ +\left[v(i,j,k+1,l) - v(i,j,k-1,l)\right]\end{Bmatrix} \\ +\frac{\max}{2}\left(1-rate^2\right)\left[dyzl(v) + d2xz(u)/2\right]\end{Bmatrix}
\end{aligned}
\qquad \text{(B12c)}
$$

$$
\begin{aligned}
&d2t(u) = maxd2x(u) \\
&+ maxrate^2 \begin{Bmatrix} [w(i+1,j,k,l) - w(i-1,j,k,l)] + d2y(u) \\ +2[u(i,j,k+1,l) - u(i,j,k,l)] \end{Bmatrix} \\
&+ \frac{max}{2}(1 - rate^2)[dzxt(w) + d2xy(v)/2] \\
&+ \eta \frac{\partial}{\partial t} \begin{Bmatrix} maxd2x(u) \\ + maxrate^2 \begin{Bmatrix} [w(i+1,j,k,l) - w(i-1,j,k,l)] + d2y(u) \\ +2[u(i,j,k+1,l) - u(i,j,k,l)] \end{Bmatrix} \\ + \frac{max}{2}(1 - rate^2)[dzxt(w) + d2xy(v)/2] \end{Bmatrix}
\end{aligned} \tag{B13a}
$$

$$
\begin{aligned}
&d2t(v) = maxd2y(v) \\
&+ maxrate^2 \begin{Bmatrix} 2[v(i,j,k+1,l) - v(i,j,k,l)] + d2x(v) \\ +[w(i,j+1,k,l) - w(i,j-1,k,l)] \end{Bmatrix} \\
&+ \frac{max}{2}(1 - rate^2)[dzyt(w) + d2xy(u)/2] \\
&+ \eta \frac{\partial}{\partial t} \begin{Bmatrix} maxd2y(v) \\ + maxrate^2 \begin{Bmatrix} 2[v(i,j,k+1,l) - v(i,j,k,l)] + d2x(v) \\ +[w(i,j+1,k,l) - w(i,j-1,k,l)] \end{Bmatrix} \\ + \frac{max}{2}(1 - rate^2)[dzyt(w) + d2xy(u)/2] \end{Bmatrix}
\end{aligned} \tag{B13b}
$$

$$
\begin{aligned}
&d2t(w) = 2\max\left(w(i,j,k+1,l) - w(i,j,k,l)\right) \\
&+\max\left(1-2rate^2\right)\left\{\begin{matrix}\left[u(i+1,j,k,l) - u(i-1,j,\kappa,l)\right] \\ +\left[v(i,j+1,k,l) - v(i,j-1,k,l)\right]\end{matrix}\right\} \\
&+\max rate^2\left[d2x(w) + d2y(w)\right] \\
&+\frac{\max}{2}\left(1-rate^2\right)\left[dzxt(u) + dzyt(v)\right] \\
&+\eta\frac{\partial}{\partial t}\left\{\begin{matrix}2\max\left(w(i,j,k+1,l) - w(i,j,k,l)\right) \\ +\max\left(1-2rate^2\right)\left\{\begin{matrix}\left[u(i+1,j,k,l) - u(i-1,j,k,l)\right] \\ +\left[v(i,j+1,k,l) - v(i,j-1,k,l)\right]\end{matrix}\right\} \\ +\max rate^2\left[d2x(w) + d2y(w)\right] \\ +\frac{\max}{2}\left(1-rate^2\right)\left[dzxt(u) + dzyt(v)\right]\end{matrix}\right\}
\end{aligned}
\qquad \text{(B13c)}
$$

$$
\begin{aligned}
&d2t(u) = \max d2x(u) \\
&+\max rate^2\left\{\begin{matrix}\left[w(i+1,j,k,l) - w(i-1,j,k,l)\right] + d2y(u) \\ +2\left[u(i,j,k-1,l) - u(i,j,k,l)\right]\end{matrix}\right\} \\
&+\frac{\max}{2}\left(1-rate^2\right)\left[dzxm(w) + d2xy(v)/2\right] \\
&+\eta\frac{\partial}{\partial t}\left\{\begin{matrix}\max d2x(u) \\ +\max rate^2\left\{\begin{matrix}\left[w(i+1,j,k,l) - w(i-1,j,k,l)\right] + d2y(u) \\ +2\left[u(i,j,k-1,l) - u(i,j,k,l)\right]\end{matrix}\right\} \\ +\frac{\max}{2}\left(1-rate^2\right)\left[dzxm(w) + d2xy(v)/2\right]\end{matrix}\right\}
\end{aligned}
\qquad \text{(B14a)}
$$

$$
\begin{aligned}
&d2t(v) = \max d2y(v) \\
&+\max rate^2 \begin{Bmatrix} 2\left[v(i,j,k-1,l) - v(i,j,k,l)\right] + d2x(v) \\ +\left[w(i,j+1,k,l) - w(i,j-1,k,l)\right] \end{Bmatrix} \\
&+\frac{\max}{2}\left(1 - rate^2\right)\left[dzym(w) + d2xy(u)/2\right] \\
&+\eta\frac{\partial}{\partial t}\begin{Bmatrix} \max d2y(v) \\ +\max rate^2 \begin{Bmatrix} 2\left[v(i,j,k-1,l) - v(i,j,k,l)\right] + d2x(v) \\ +\left[w(i,j+1,k,l) - w(i,j-1,k,l)\right] \end{Bmatrix} \\ +\frac{\max}{2}\left(1 - rate^2\right)\left[dzym(w) + d2xy(u)/2\right] \end{Bmatrix}
\end{aligned}
\qquad \text{(B14b)}
$$

$$
\begin{aligned}
&d2t(w) = 2\max\left(w(i,j,k-1,l) - w(i,j,k,l)\right) \\
&+\max\left(1 - 2rate^2\right)\begin{Bmatrix} \left[u(i+1,j,k,l) - u(i-1,j,k,l)\right] \\ +\left[v(i,j+1,k,l) - v(i,j-1,k,l)\right] \end{Bmatrix} \\
&+\max rate^2\left[d2x(w) + d2y(w)\right] \\
&+\frac{\max}{2}\left(1 - rate^2\right)\left[dzxm(u) + dzym(v)\right] \\
&+\eta\frac{\partial}{\partial t}\begin{Bmatrix} 2\max\left(w(i,j,k-1,l) - w(i,j,k,l)\right) \\ +\max\left(1 - 2rate^2\right)\begin{Bmatrix} \left[u(i+1,j,k,l) - u(i-1,j,k,l)\right] \\ +\left[v(i,j+1,k,l) - v(i,j-1,k,l)\right] \end{Bmatrix} \\ +\max rate^2\left[d2x(w) + d2y(w)\right] \\ +\frac{\max}{2}\left(1 - rate^2\right)\left[dzxm(u) + dzym(v)\right] \end{Bmatrix}
\end{aligned}
\qquad \text{(B14c)}
$$

B.2 Corner Finite Difference Formulations

In Section 4.3 the corner finite difference formulation for the u displacement at point A, in Figure 4.3 shown below, was developed. This

is for the two-dimensional simulation. For the v displacement at point A equations (B4) and (B6) are used along with the equation of motion (B3b). Again the cross derivative term in the equation of motion must be adjusted. At the corner only three points surround the corner point. Due to symmetry the u displacement finite difference formulation equation (55), shown as (B15a), mirrors the v displacement finite difference formulation. To get the v displacement finite difference formulation, the b part of each equation, just replace the u and v in equation (B15a) with v and u.

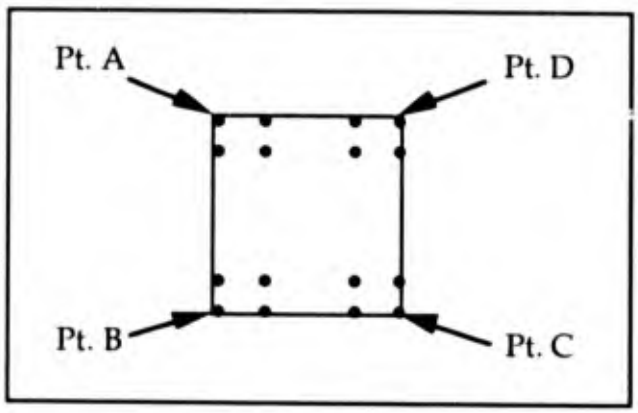

Figure 4.3. Four Corner Points for a Two-Dimensional Grid.

$$\begin{aligned} d2t(u) &= 2\max\left(1-\text{rate}^2\right)\begin{Bmatrix} v(i+1,j+1,l)+v(i,j,l) \\ -v(i+1,j,l)-v(i,j+1,l) \end{Bmatrix} \\ &+\eta\frac{\partial}{\partial t}\left[2\max\left(1-\text{rate}^2\right)\begin{Bmatrix} v(i+1,j+1,l)+v(i,j,l) \\ -v(i+1,j,l)-v(i,j+1,l) \end{Bmatrix}\right] \end{aligned} \qquad \text{(B15a)}$$

The formulations for points B, C, and D, u and v displacements are similar to equation (B15a) except the sign convention from Figure 4.1 is used. In Figure 4.1 the x direction increases from point A to point D and the y direction increases from point A to point B. As an example, the u

displacement for point B would have j in equation (B15a) replaced with j - 1, as shown in equation (B16a).

$$d2t(u) = 2\max\left(1-\text{rate}^2\right)\begin{Bmatrix} v(i+1,j,l)+v(i,j-1,l) \\ -v(i,j,l)-v(i+1,j-1,l) \end{Bmatrix}$$
$$+\eta\frac{\partial}{\partial t}\left[2\max\left(1-\text{rate}^2\right)\begin{Bmatrix} v(i+1,j,l)+v(i,j-1,l) \\ -v(i,j,l)-v(i+1,j-1,l) \end{Bmatrix}\right] \qquad \text{(B16a)}$$

For Point C formulation, replace i by i - 1, and j by j - 1, in equation (B15a). Likewise for point D, replace i by i - 1, in equation (B15a).

APPENDIX C

EXPERIMENT DATA

C.0 Overview

The following pages contain Test 1, Test 2, and Test 3 signal time series, magnitude and phase spectrum from the ultrasonic NDE of inert SRM propellant performed at Martin Marietta Laboratories, Baltimore MD. The transducer input equivalent signal were presented first, followed by the output or received signals. The D, E, and F experimental data was not presented because the sample was dissected shortly after the tests.

C.1 Coding Information

Each Figure is coded with a letter i.e. "A", followed by a number, and may have a suffix of "M" for magnitude or "P" for phase, see Table 5.2, Table 5.3 and Figure 5.2 below.

For Test 1 and Test 2, the number corresponds to the frequency of the drive signal, using three cycles for the tone burst excitation for the transducer. The frequency of the drive signals vary from 30 kHz to 500 kHz. In Test 3, there are only two drive signal frequencies used, 30 and 65 kHz. However, both drive signal frequencies used a six and ten cycles for the tone burst excitation for the transducer, identified with an S and T respectively.

Table 5.2. Sample Dimensions and Labels that Coincide with each Tests.

Test Sample	Label	Thickness cm +/- 0.01	Label	Width cm +/- 0.01	Label	Length cm +/- 0.01
3323-2 no inclusion	A	8.50	B	11.35	C	13.10
3323-1 no inclusion	D	7.33	E	7.89	F	11.10
3323-2 Paddle Ball	G	8.26	H	11.24	IC*	12.11
					IF*	
3323-2 Ping Pong Ball	J	8.38	K	11.68	LC*	13.21
					LF*	

* Refers to whether the off-center inclusion is Closer to the transmit transducer than the receive transducer or Farther from the transmit transducer than the receive transducer.

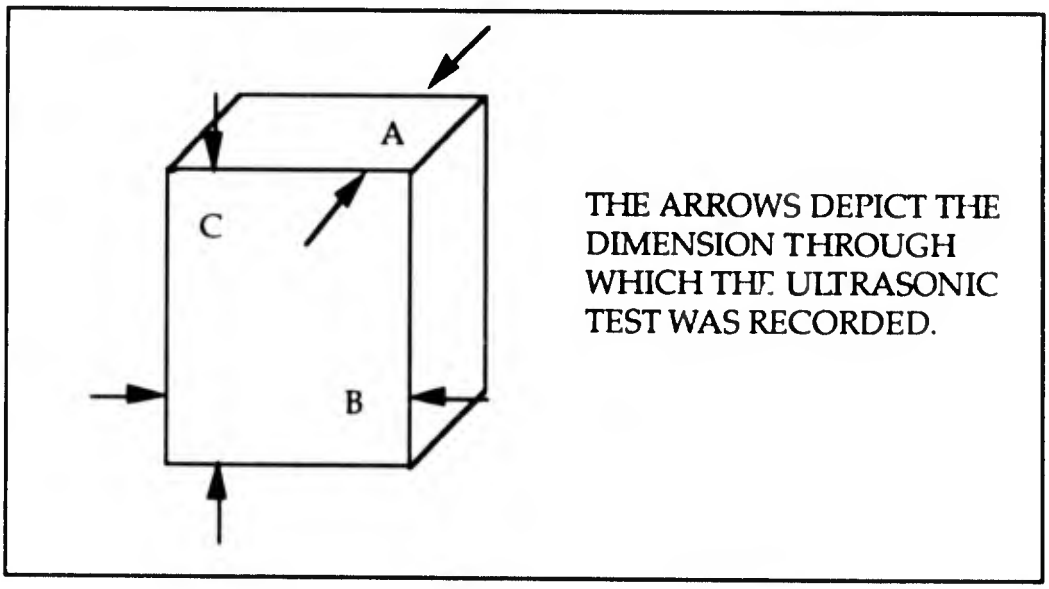

Figure 5.2. Graphic Representation of the Labels and Dimensions of Sample 3323-2 No Inclusion During Ultrasonic NDE.

Table 5.3. Test 1 Key, Identifiers used in Tables and Figures.

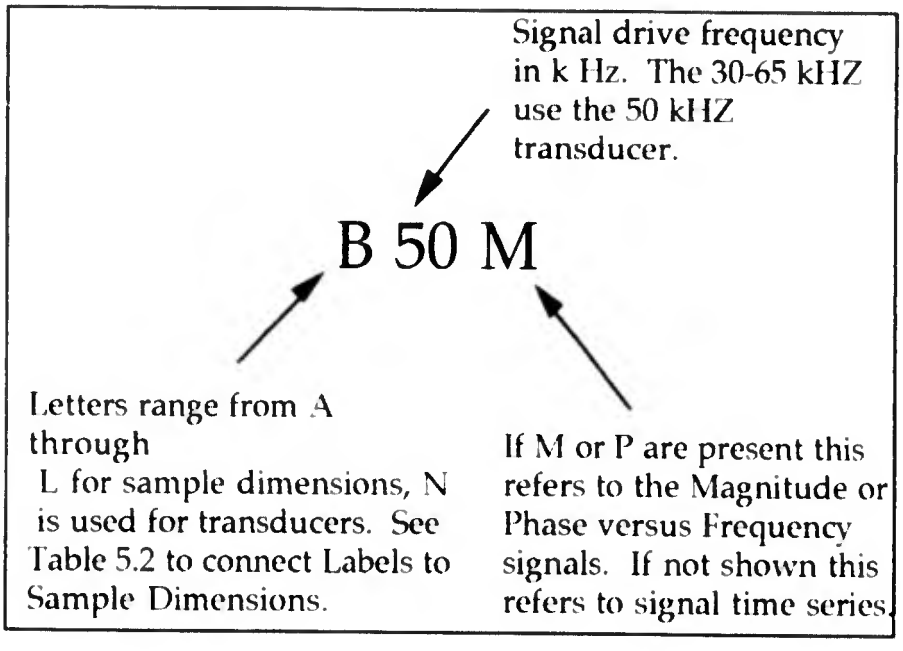

C.2 Signal Time Series and Spectrum

The signal time series obviously have an abscissa in seconds and an ordinate of volts. The DFT plots use an abscissa of frequency in Hertz. The transducers used are identified in Table C.1.

Table C.1. Transducer Frequency and Serial Number

Transducer frequency (kHz)	50	100	150	200	300	500
Transducer serial number (per pair)	M951, M953	M961, M962	M965, M968	M970, M975	MT0303, MR0302	M984, M987

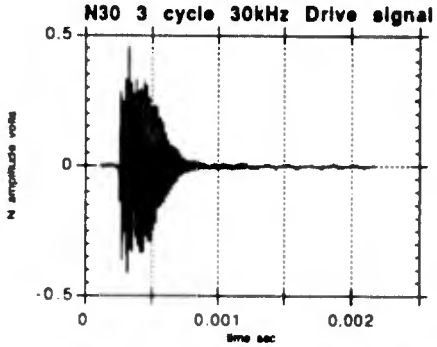
N30 3 cycle 30kHz Drive signal
0.5
0
-0.5
0
0.001
0.002

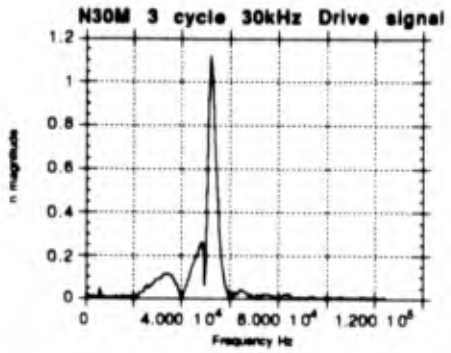
N30M 3 cycle 30kHz Drive signal
1.2
1
0.8
0.6
0.4
0.2
0
0
4.000 10^4
8.000 10^4
1.200 10^5

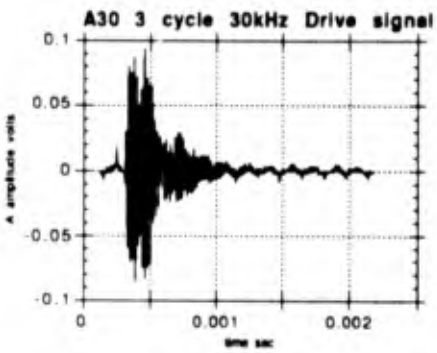
A30 3 cycle 30kHz Drive signal
0.1
0.05
0
-0.05
-0.1
0
0.001
0.002

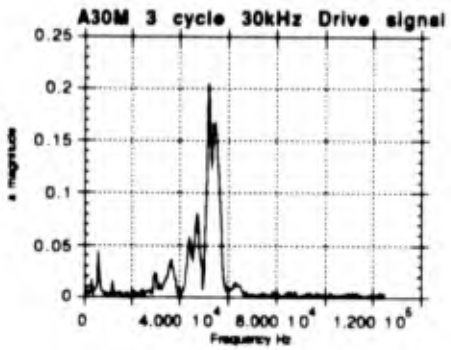
A30M 3 cycle 30kHz Drive signal
0.25
0.2
0.15
0.1
0.05
0
0
4.000 10^4
8.000 10^4
1.200 10^5

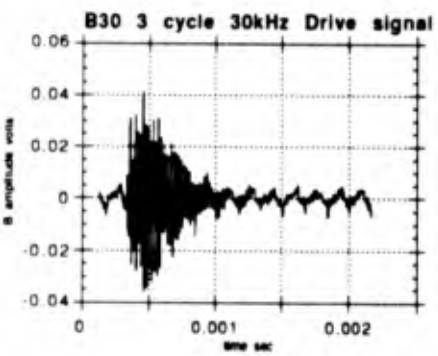
B30 3 cycle 30kHz Drive signal
0.06
0.04
0.02
0
-0.02
-0.04
0
0.001
0.002

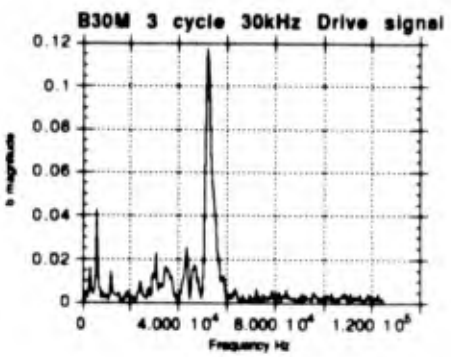
B30M 3 cycle 30kHz Drive signal
0.12
0.1
0.08
0.06
0.04
0.02
0
0
4.000 10^4
8.000 10^4
1.200 10^5

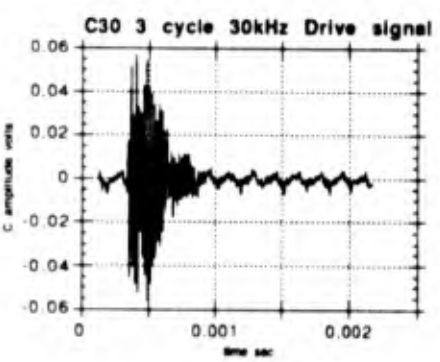
C30 3 cycle 30kHz Drive signal
0.06
0.04
0.02
0
-0.02
-0.04
-0.06
0
0.001
0.002

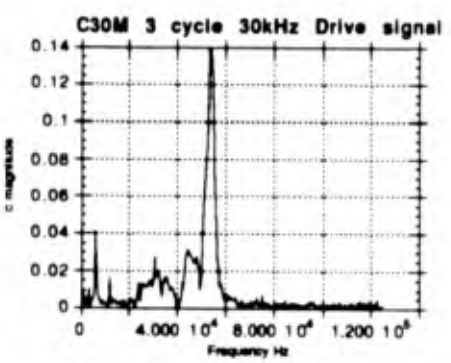
C30M 3 cycle 30kHz Drive signal
0.14
0.12
0.1
0.08
0.06
0.04
0.02
0
0
4.000 10^4
8.000 10^4
1.200 10^5

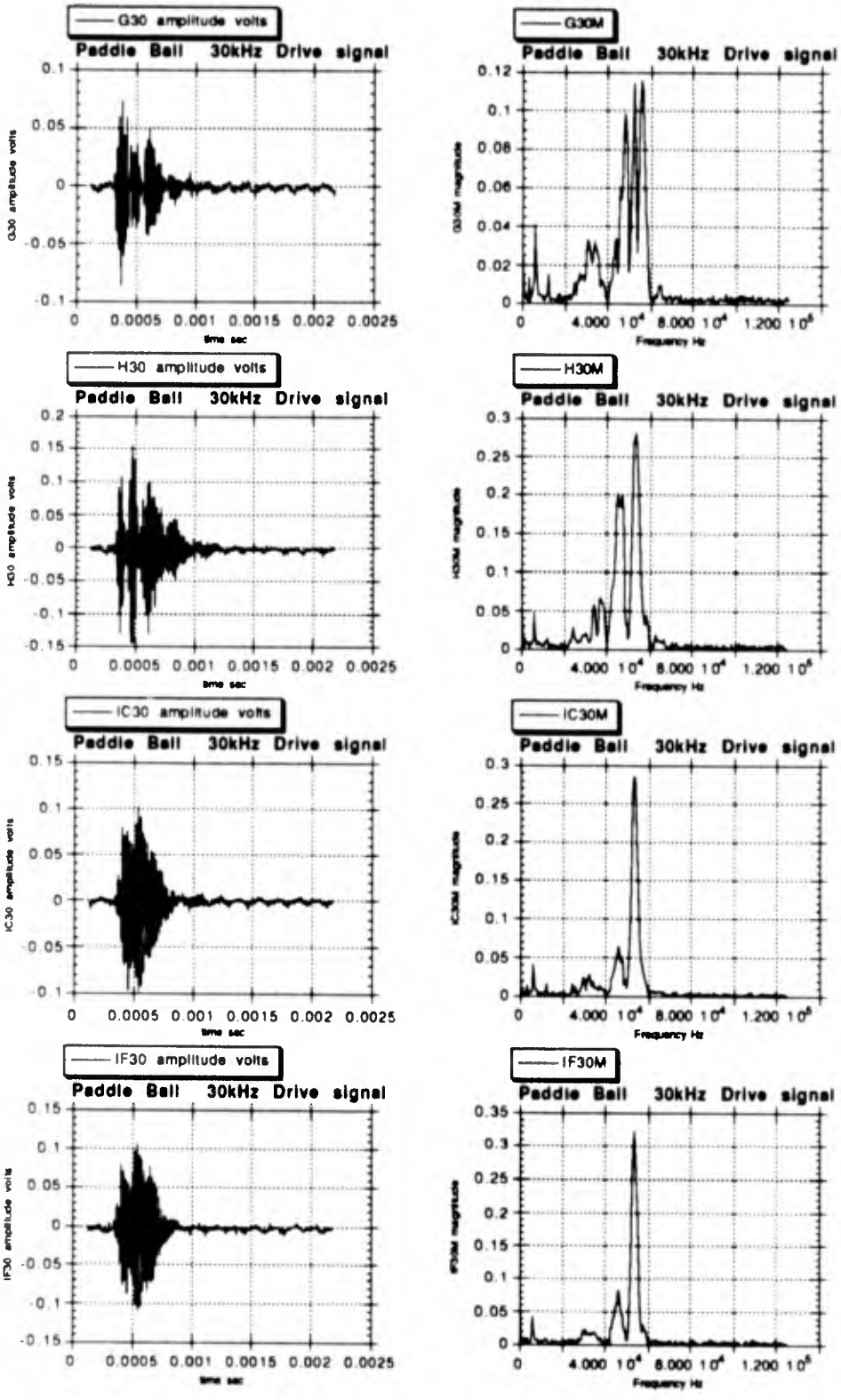
G30 amplitude volts
Paddle Ball 30kHz Drive signal
G30 amplitude volts
time sec
G30M
Paddle Ball 30kHz Drive signal
G30M magnitude
Frequency Hz
H30 amplitude volts
Paddle Ball 30kHz Drive signal
H30 amplitude volts
time sec
H30M
Paddle Ball 30kHz Drive signal
H30M magnitude
Frequency Hz
IC30 amplitude volts
Paddle Ball 30kHz Drive signal
IC30 amplitude volts
time sec
IC30M
Paddle Ball 30kHz Drive signal
IC30M magnitude
Frequency Hz
IF30 amplitude volts
Paddle Ball 30kHz Drive signal
IF30 amplitude volts
time sec
IF30M
Paddle Ball 30kHz Drive signal
IF30M magnitude
Frequency Hz

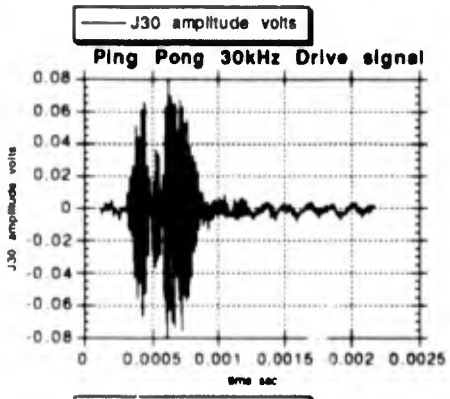
J30 amplitude volts
Ping Pong 30kHz Drive signal
J30 amplitude volts
time sec

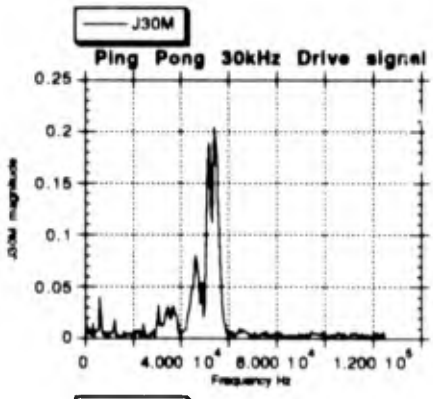
J30M
Ping Pong 30kHz Drive signal
J30M magnitude
Frequency Hz

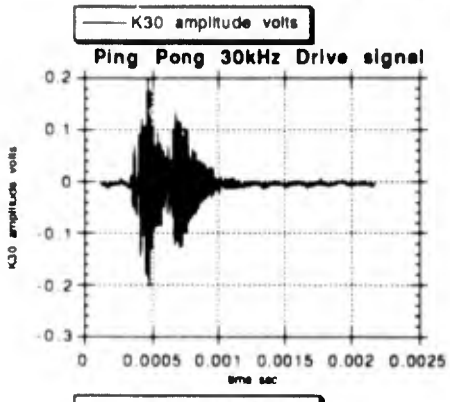
K30 amplitude volts
Ping Pong 30kHz Drive signal
K30 amplitude volts
time sec

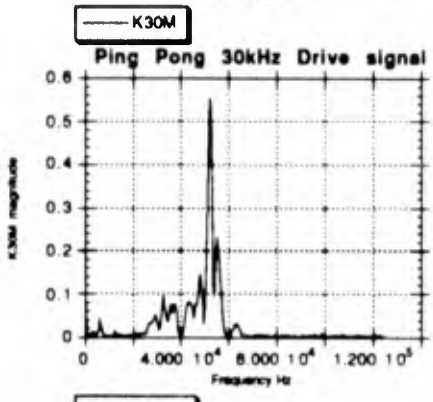
K30M
Ping Pong 30kHz Drive signal
K30M magnitude
Frequency Hz

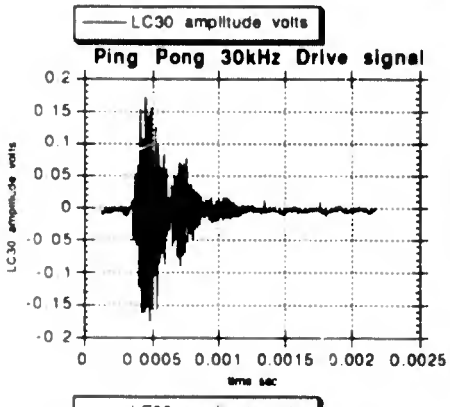
LC30 amplitude volts
Ping Pong 30kHz Drive signal
time sec

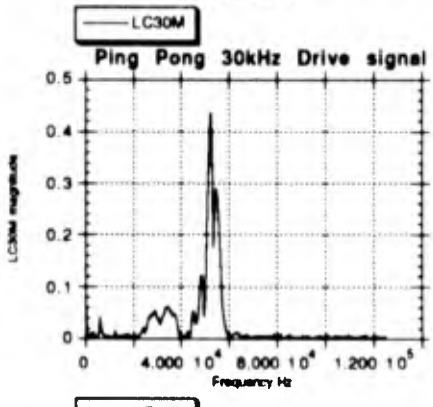
LC30M
Ping Pong 30kHz Drive signal
LC30M magnitude
Frequency Hz

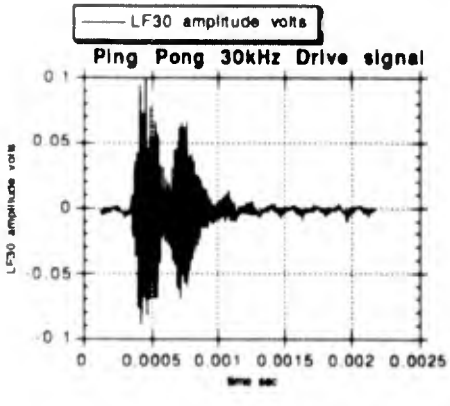
LF30 amplitude volts
Ping Pong 30kHz Drive signal
LF30 amplitude volts
time sec

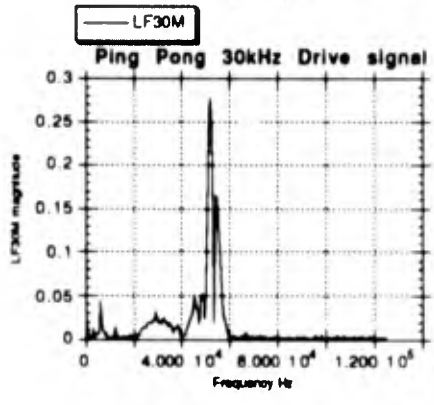
LF30M
Ping Pong 30kHz Drive signal
LF30M magnitude
Frequency Hz

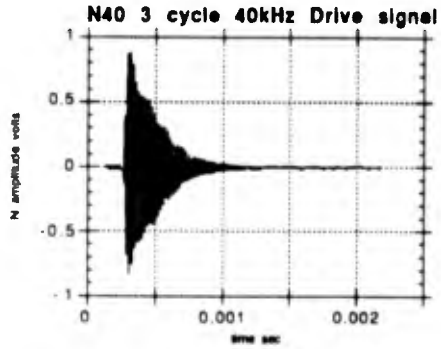
N40 3 cycle 40kHz Drive signal
N amplitude volts
1
0.5
0
-0.5
-1
0
0.001
0.002
time sec

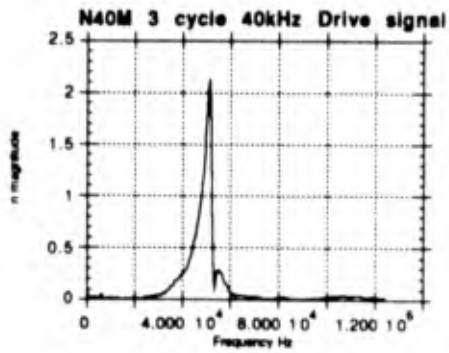
N40M 3 cycle 40kHz Drive signal
n magnitude
2.5
2
1.5
1
0.5
0
0
4.000 10^4
8.000 10^4
1.200 10^5
Frequency Hz

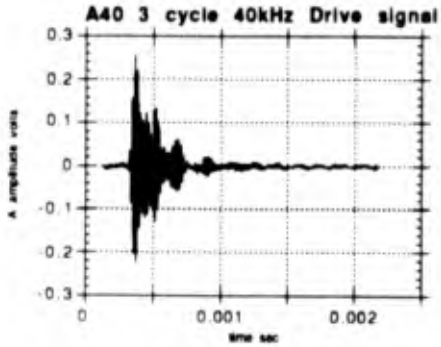
A40 3 cycle 40kHz Drive signal
A amplitude volts
0.3
0.2
0.1
0
-0.1
-0.2
-0.3
0
0.001
0.002
time sec

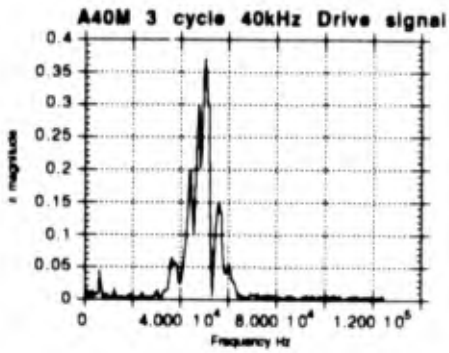
A40M 3 cycle 40kHz Drive signal
a magnitude
0.4
0.35
0.3
0.25
0.2
0.15
0.1
0.05
0
0
4.000 10^4
8.000 10^4
1.200 10^5
Frequency Hz

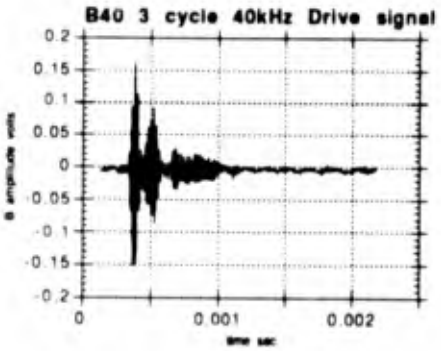
B40 3 cycle 40kHz Drive signal
B amplitude volts
0.2
0.15
0.1
0.05
0
-0.05
-0.1
-0.15
-0.2
0
0.001
0.002
time sec

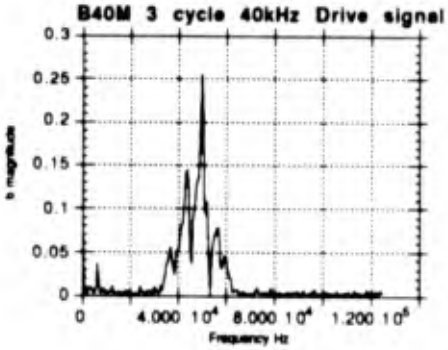
B40M 3 cycle 40kHz Drive signal
b magnitude
0.3
0.25
0.2
0.15
0.1
0.05
0
0
4.000 10^4
8.000 10^4
1.200 10^5
Frequency Hz

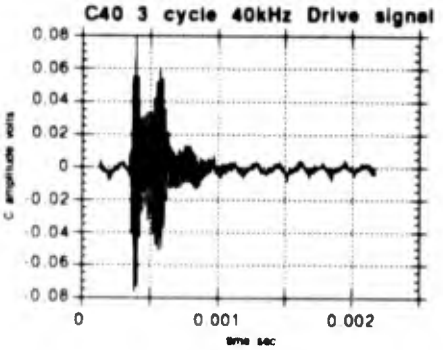
C40 3 cycle 40kHz Drive signal
C amplitude volts
0.08
0.06
0.04
0.02
0
-0.02
-0.04
-0.06
-0.08
0
0.001
0.002
time sec

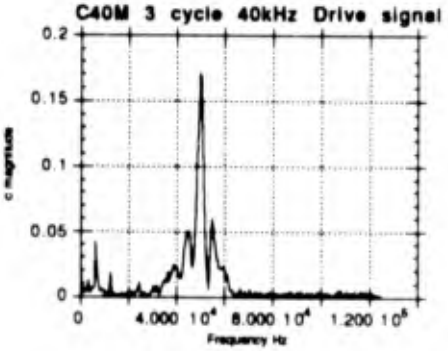
C40M 3 cycle 40kHz Drive signal
c magnitude
0.2
0.15
0.1
0.05
0
0
4.000 10^4
8.000 10^4
1.200 10^5
Frequency Hz

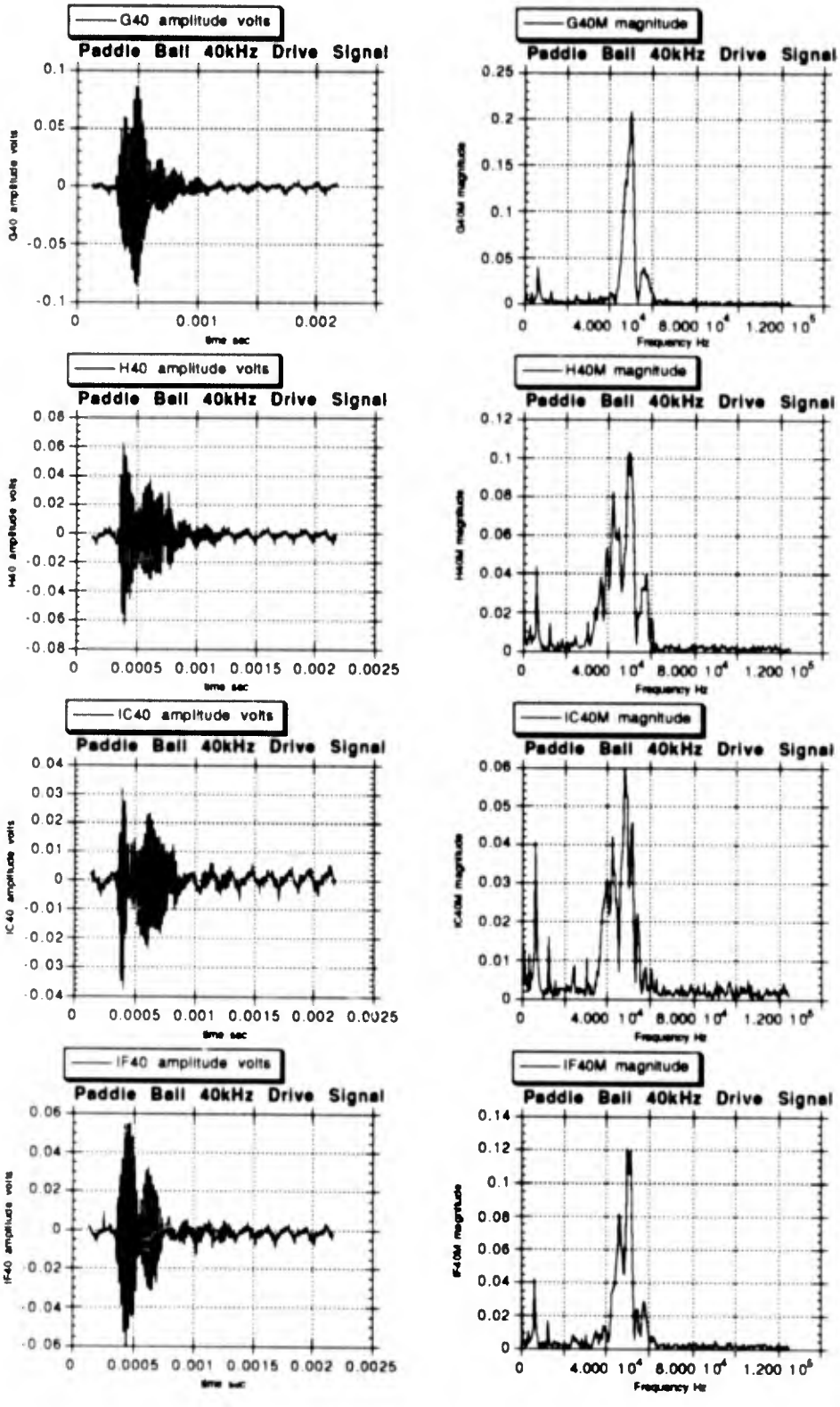
G40 amplitude volts
Paddle Ball 40kHz Drive Signal
G40 amplitude volts
time sec
G40M magnitude
Paddle Ball 40kHz Drive Signal
G40M magnitude
Frequency Hz
H40 amplitude volts
Paddle Ball 40kHz Drive Signal
H40 amplitude volts
time sec
H40M magnitude
Paddle Ball 40kHz Drive Signal
H40M magnitude
Frequency Hz
IC40 amplitude volts
Paddle Ball 40kHz Drive Signal
IC40 amplitude volts
time sec
IC40M magnitude
Paddle Ball 40kHz Drive Signal
IC40M magnitude
Frequency Hz
IF40 amplitude volts
Paddle Ball 40kHz Drive Signal
IF40 amplitude volts
time sec
IF40M magnitude
Paddle Ball 40kHz Drive Signal
IF40M magnitude
Frequency Hz

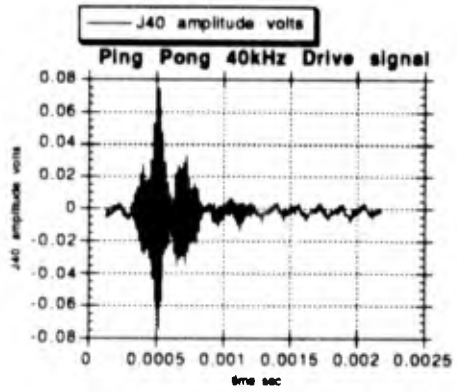
J40 amplitude volts
Ping Pong 40kHz Drive signal
J40 amplitude volts
0.08
0.06
0.04
0.02
0
-0.02
-0.04
-0.06
-0.08
0
0.0005
0.001
0.0015
0.002
0.0025
time sec

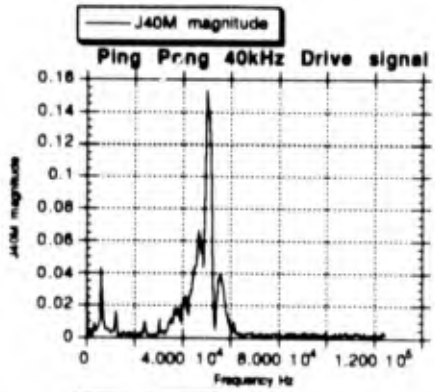
J40M magnitude
Ping Pong 40kHz Drive signal
J40M magnitude
0.16
0.14
0.12
0.1
0.08
0.06
0.04
0.02
0
0
4.000 10^4
8.000 10^4
1.200 10^5
Frequency Hz

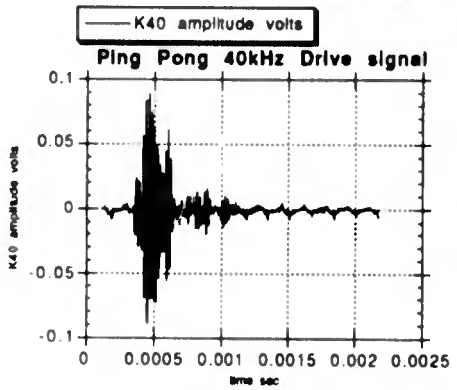
K40 amplitude volts
Ping Pong 40kHz Drive signal
K40 amplitude volts
0.1
0.05
0
-0.05
-0.1
0
0.0005
0.001
0.0015
0.002
0.0025
time sec

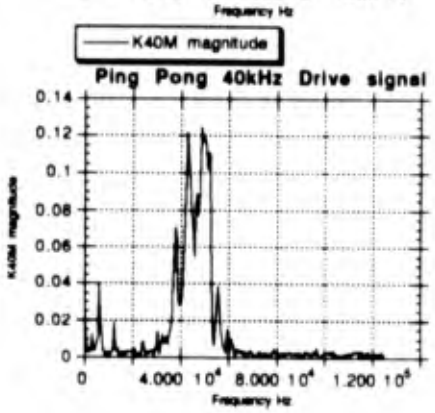
K40M magnitude
Ping Pong 40kHz Drive signal
K40M magnitude
0.14
0.12
0.1
0.08
0.06
0.04
0.02
0
0
4.000 10^4
8.000 10^4
1.200 10^5
Frequency Hz

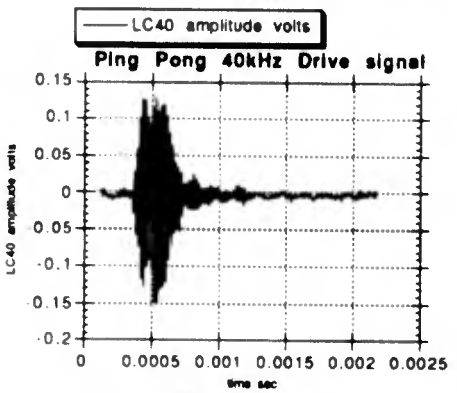
LC40 amplitude volts
Ping Pong 40kHz Drive signal
LC40 amplitude volts
0.15
0.1
0.05
0
0.05
-0.1
-0.15
-0.2
0
0.0005
0.001
0.0015
0.002
0.0025
time sec

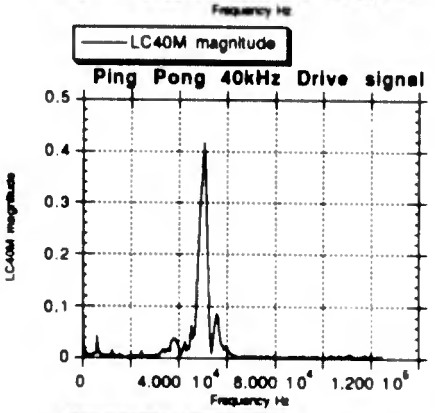
LC40M magnitude
Ping Pong 40kHz Drive signal
LC40M magnitude
0.5
0.4
0.3
0.2
0.1
0
0
4.000 10^4
8.000 10^4
1.200 10^5
Frequency Hz

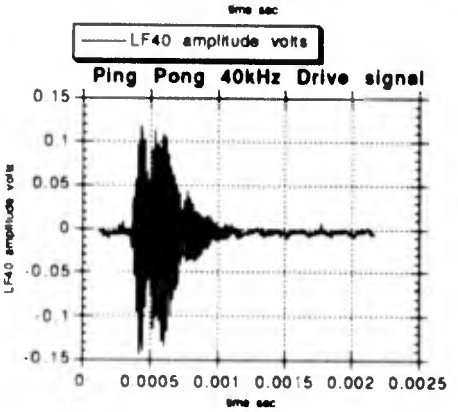
LF40 amplitude volts
Ping Pong 40kHz Drive signal
LF40 amplitude volts
0.15
0.1
0.05
0
-0.05
-0.1
-0.15
0
0.0005
0.001
0.0015
0.002
0.0025
time sec

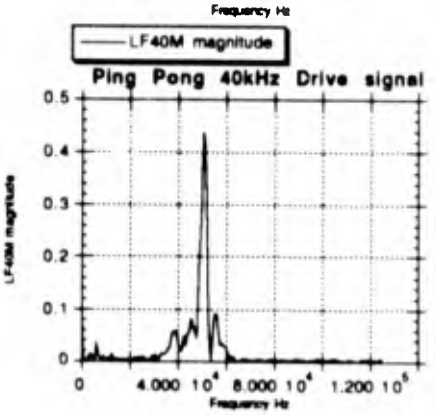
LF40M magnitude
Ping Pong 40kHz Drive signal
LF40M magnitude
0.5
0.4
0.3
0.2
0.1
0
0
4.000 10^4
8.000 10^4
1.200 10^5
Frequency Hz

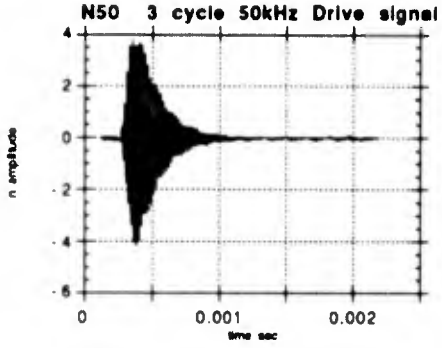
N50 3 cycle 50kHz Drive signal
n amplitude
4
2
0
-2
-4
-6
0
0.001
0.002
time sec

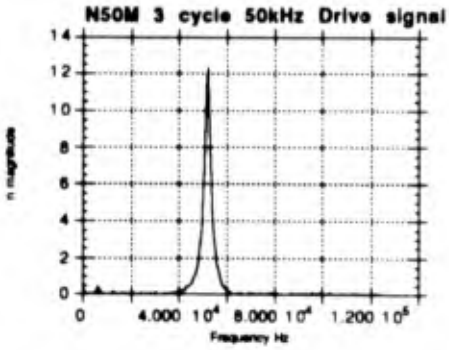
N50M 3 cycle 50kHz Drive signal
n magnitude
14
12
10
8
6
4
2
0
0
4.000 10^4
8.000 10^4
1.200 10^5
Frequency Hz

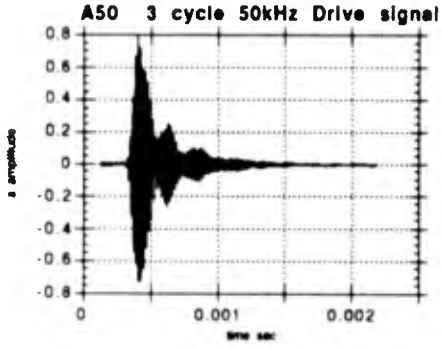
A50 3 cycle 50kHz Drive signal
a amplitude
0.8
0.6
0.4
0.2
0
-0.2
-0.4
-0.6
-0.8
0
0.001
0.002
time sec

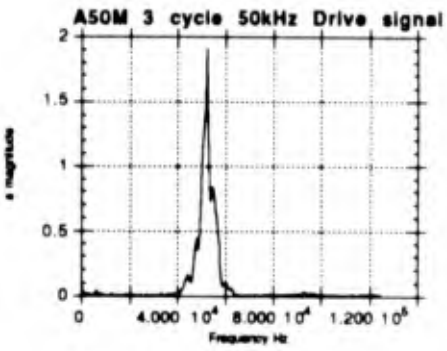
A50M 3 cycle 50kHz Drive signal
a magnitude
2
1.5
1
0.5
0
0
4.000 10^4
8.000 10^4
1.200 10^5
Frequency Hz

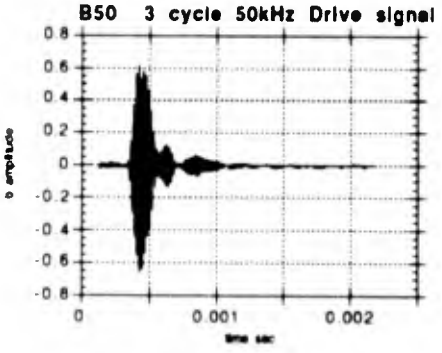
B50 3 cycle 50kHz Drive signal
b amplitude
0.8
0.6
0.4
0.2
0
-0.2
-0.4
-0.6
-0.8
0
0.001
0.002
time sec

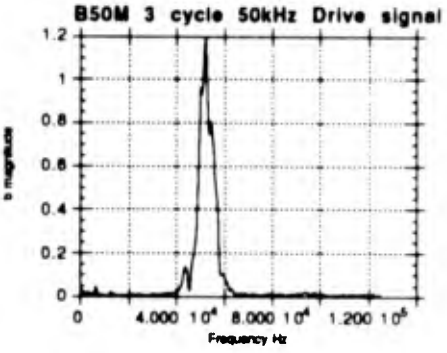
B50M 3 cycle 50kHz Drive signal
b magnitude
1.2
1
0.8
0.6
0.4
0.2
0
0
4.000 10^4
8.000 10^4
1.200 10^5
Frequency Hz

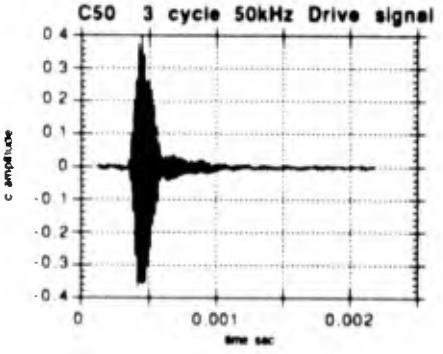
C50 3 cycle 50kHz Drive signal
c amplitude
0.4
0.3
0.2
0.1
0
-0.1
-0.2
-0.3
-0.4
0
0.001
0.002
time sec

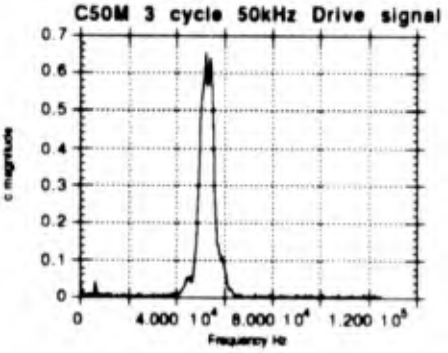
C50M 3 cycle 50kHz Drive signal
c magnitude
0.7
0.6
0.5
0.4
0.3
0.2
0.1
0
0
4.000 10^4
8.000 10^4
1.200 10^5
Frequency Hz

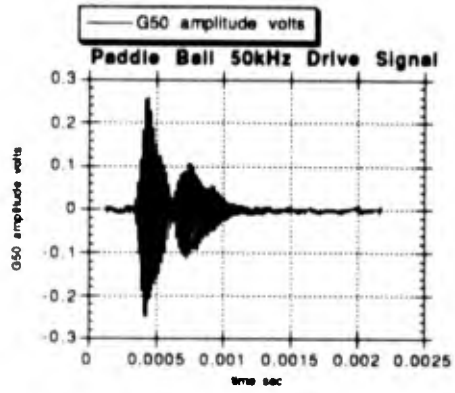
G50 amplitude volts
Paddle Ball 50kHz Drive Signal
G50 amplitude volts
0.3
0.2
0.1
0
-0.1
-0.2
-0.3
0
0.0005
0.001
0.0015
0.002
0.0025
time sec

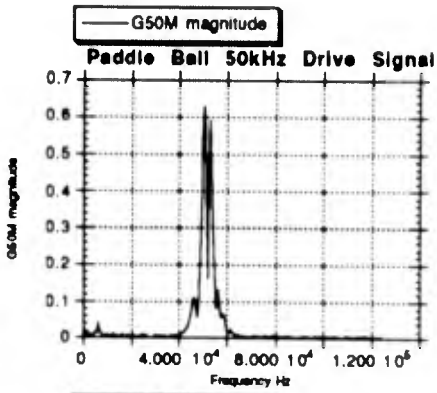
G50M magnitude
Paddle Ball 50kHz Drive Signal
G50M magnitude
0.7
0.6
0.5
0.4
0.3
0.2
0.1
0
0
4.000 10^4
8.000 10^4
1.200 10^5
Frequency Hz

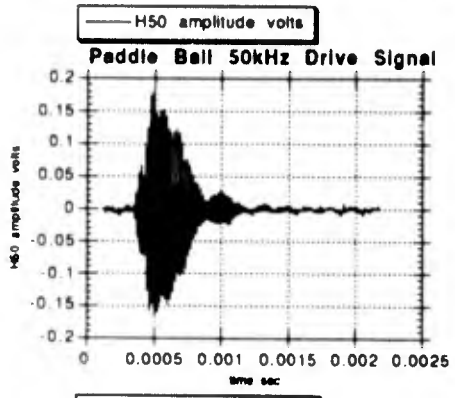
H50 amplitude volts
Paddle Ball 50kHz Drive Signal
H50 amplitude volts
0.2
0.15
0.1
0.05
0
-0.05
-0.1
-0.15
-0.2
0
0.0005
0.001
0.0015
0.002
0.0025
time sec

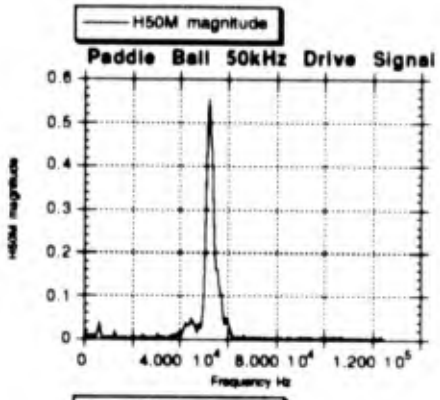
H50M magnitude
Paddle Ball 50kHz Drive Signal
H50M magnitude
0.6
0.5
0.4
0.3
0.2
0.1
0
0
4.000 10^4
8.000 10^4
1.200 10^5
Frequency Hz

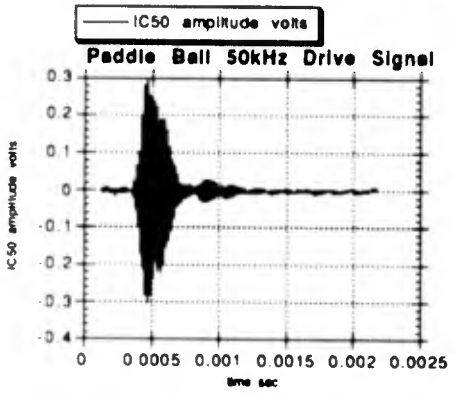
IC50 amplitude volts
Paddle Ball 50kHz Drive Signal
IC50 amplitude volts
0.3
0.2
0.1
0
-0.1
-0.2
-0.3
-0.4
0
0.0005
0.001
0.0015
0.002
0.0025
time sec

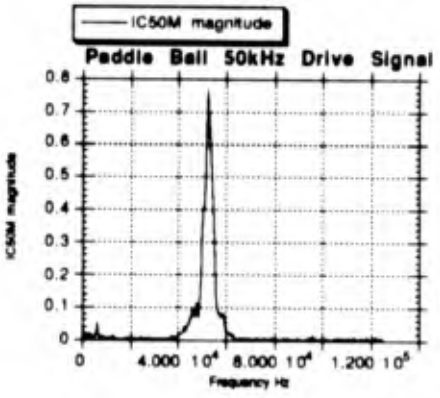
IC50M magnitude
Paddle Ball 50kHz Drive Signal
IC50M magnitude
0.8
0.7
0.6
0.5
0.4
0.3
0.2
0.1
0
0
4.000 10^4
8.000 10^4
1.200 10^5
Frequency Hz

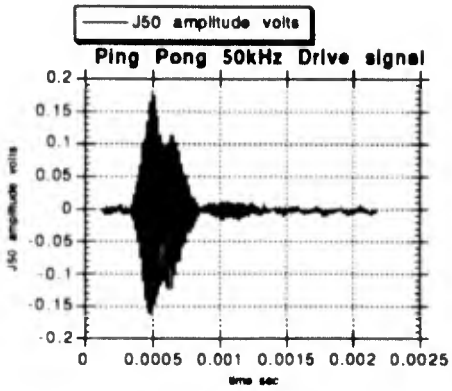
J50 amplitude volts
Ping Pong 50kHz Drive signal
0.2
0.15
0.1
0.05
0
-0.05
-0.1
-0.15
-0.2
0
0.0005
0.001
0.0015
0.002
0.0025
time sec

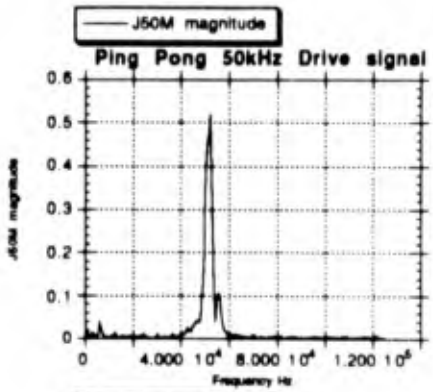
J50M magnitude
Ping Pong 50kHz Drive signal
0.6
0.5
0.4
0.3
0.2
0.1
0
4.000 10^4
8.000 10^4
1.200 10^5
Frequency Hz

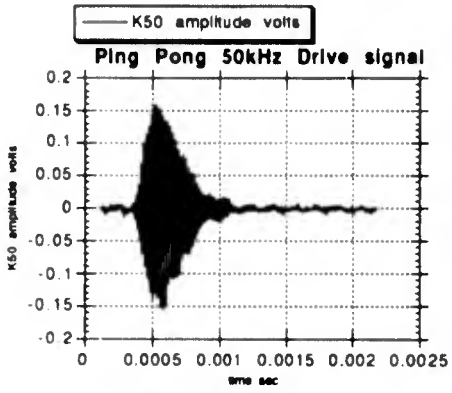
K50 amplitude volts
Ping Pong 50kHz Drive signal
0.2
0.15
0.1
0.05
0
-0.05
-0.1
-0.15
-0.2
0
0.0005
0.001
0.0015
0.002
0.0025
time sec

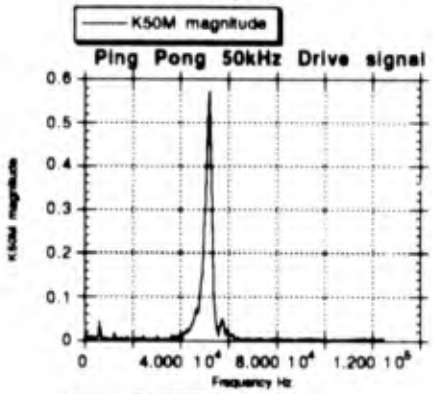
K50M magnitude
Ping Pong 50kHz Drive signal
0.6
0.5
0.4
0.3
0.2
0.1
0
4.000 10^4
8.000 10^4
1.200 10^5
Frequency Hz

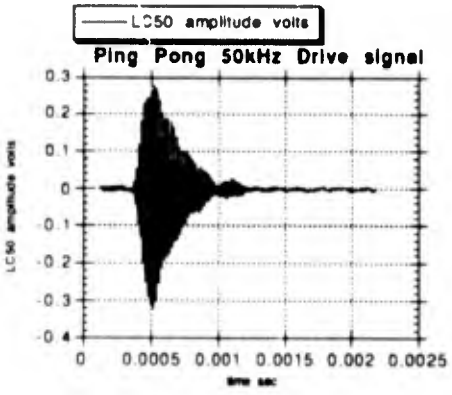
LC50 amplitude volts
Ping Pong 50kHz Drive signal
0.3
0.2
0.1
0
-0.1
-0.2
-0.3
-0.4
0
0.0005
0.001
0.0015
0.002
0.0025
time sec

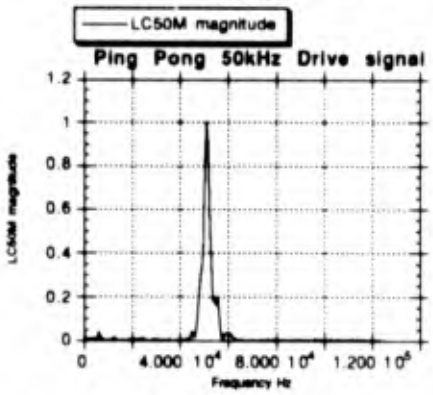
LC50M magnitude
Ping Pong 50kHz Drive signal
1.2
1
0.8
0.6
0.4
0.2
0
4.000 10^4
8.000 10^4
1.200 10^5
Frequency Hz

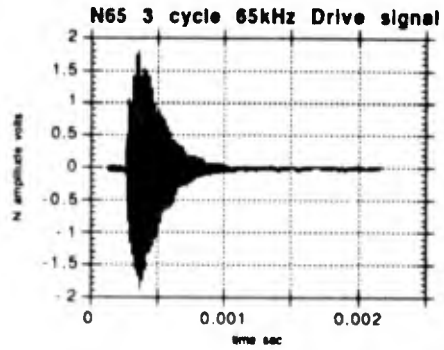
N65 3 cycle 65kHz Drive signal
N amplitude volts
2
1.5
1
0.5
0
-0.5
-1
-1.5
-2
0
0.001
0.002
time sec

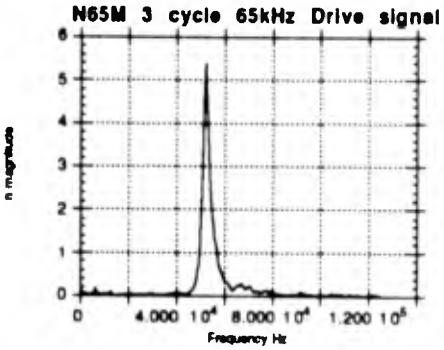
N65M 3 cycle 65kHz Drive signal
n magnitude
6
5
4
3
2
1
0
0
4.000 10^4
8.000 10^4
1.200 10^5
Frequency Hz

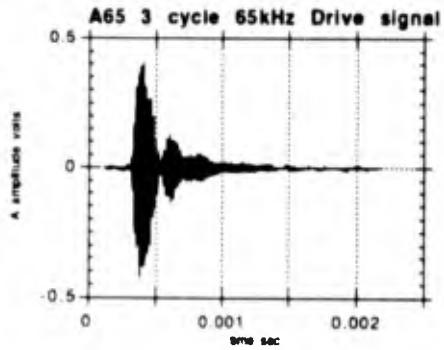
A65 3 cycle 65kHz Drive signal
A amplitude volts
0.5
0
-0.5
0
0.001
0.002
time sec

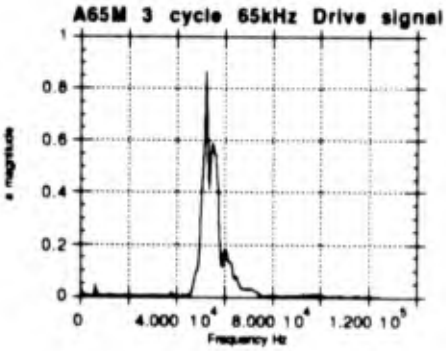
A65M 3 cycle 65kHz Drive signal
a magnitude
1
0.8
0.6
0.4
0.2
0
0
4.000 10^4
8.000 10^4
1.200 10^5
Frequency Hz

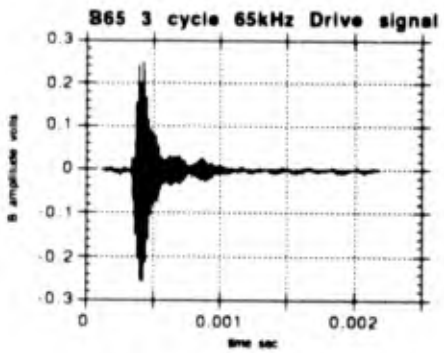
B65 3 cycle 65kHz Drive signal
B amplitude volts
0.3
0.2
0.1
0
-0.1
-0.2
-0.3
0
0.001
0.002
time sec

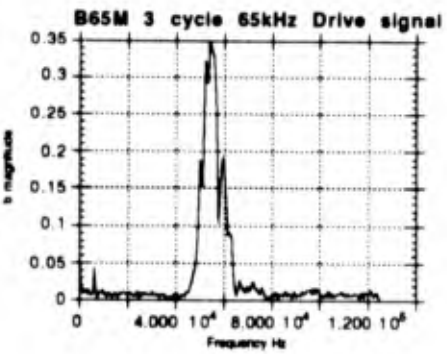
B65M 3 cycle 65kHz Drive signal
b magnitude
0.35
0.3
0.25
0.2
0.15
0.1
0.05
0
0
4.000 10^4
8.000 10^4
1.200 10^5
Frequency Hz

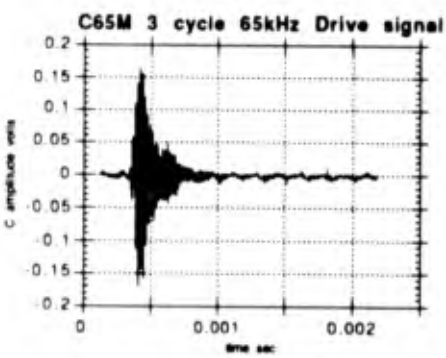
C65M 3 cycle 65kHz Drive signal
C amplitude volts
0.2
0.15
0.1
0.05
0
-0.05
-0.1
-0.15
-0.2
0
0.001
0.002
time sec

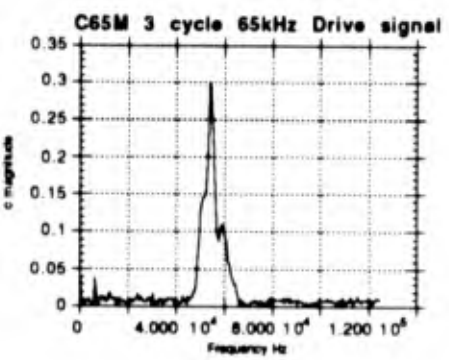
C65M 3 cycle 65kHz Drive signal
c magnitude
0.35
0.3
0.25
0.2
0.15
0.1
0.05
0
0
4.000 10^4
8.000 10^4
1.200 10^5
Frequency Hz

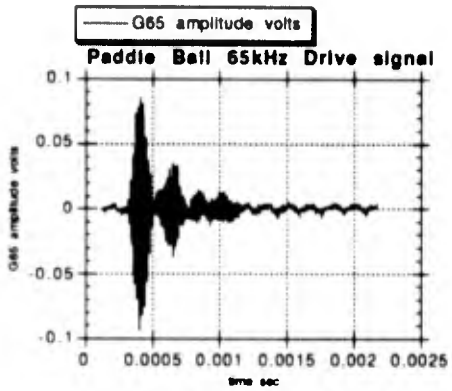
G65 amplitude volts
Paddle Ball 65kHz Drive signal
time sec

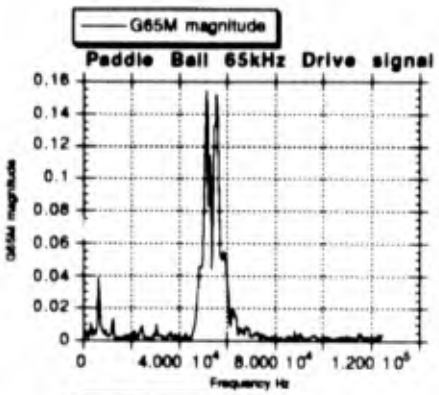
G65M magnitude
Paddle Ball 65kHz Drive signal
Frequency Hz

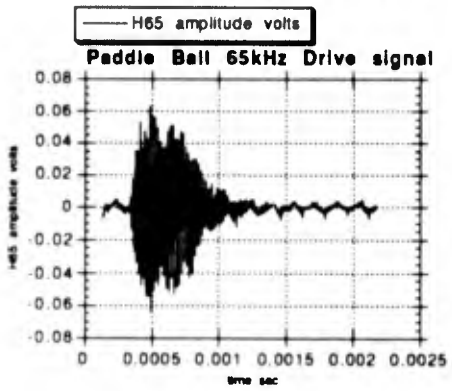
H65 amplitude volts
Paddle Ball 65kHz Drive signal
time sec

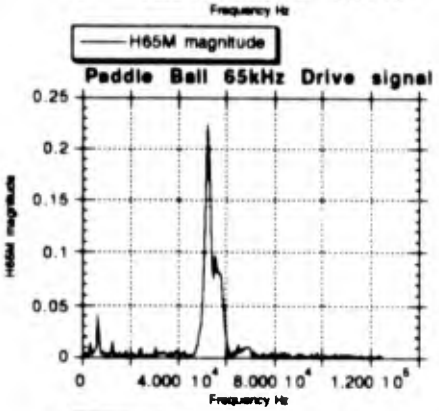
H65M magnitude
Paddle Ball 65kHz Drive signal
Frequency Hz

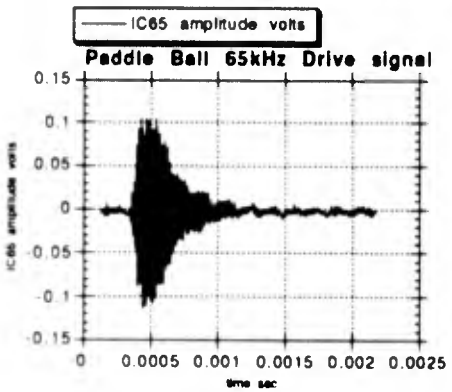
IC65 amplitude volts
Paddle Ball 65kHz Drive signal
time sec

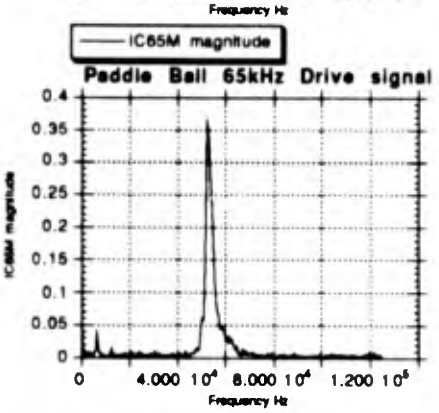
IC65M magnitude
Paddle Ball 65kHz Drive signal
Frequency Hz

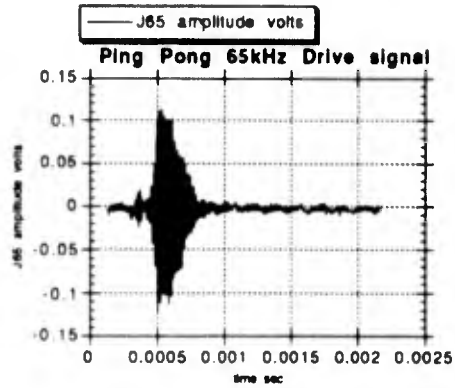
J65 amplitude volts
Ping Pong 65kHz Drive signal
0.15
0.1
0.05
0
-0.05
-0.1
-0.15
0
0.0005
0.001
0.0015
0.002
0.0025
time sec

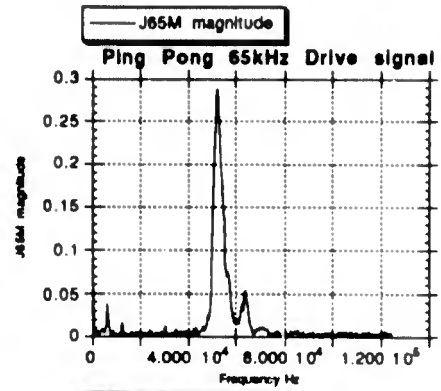
J65M magnitude
Ping Pong 65kHz Drive signal
0.3
0.25
0.2
0.15
0.1
0.05
0
4.000 10^4
8.000 10^4
1.200 10^5
Frequency Hz

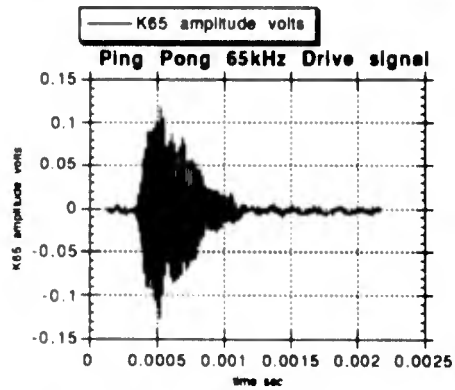
K65 amplitude volts
Ping Pong 65kHz Drive signal
0.15
0.1
0.05
0
-0.05
-0.1
-0.15
0
0.0005
0.001
0.0015
0.002
0.0025
time sec

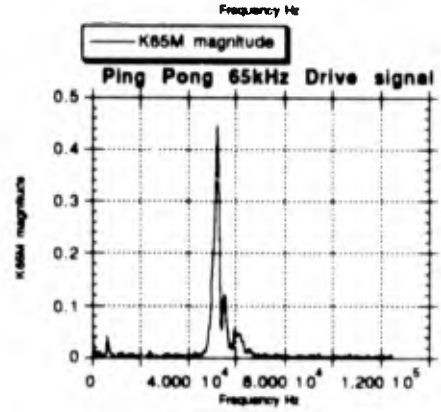
K65M magnitude
Ping Pong 65kHz Drive signal
0.5
0.4
0.3
0.2
0.1
0
4.000 10^4
8.000 10^4
1.200 10^5
Frequency Hz

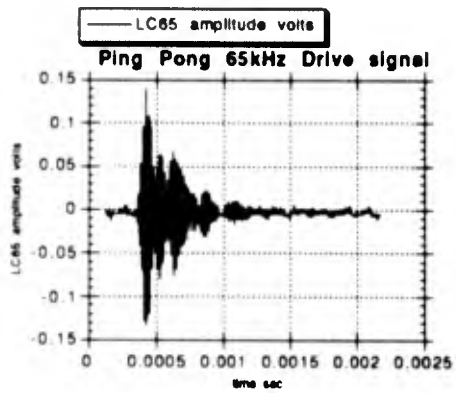
LC65 amplitude volts
Ping Pong 65kHz Drive signal
0.15
0.1
0.05
0
-0.05
-0.1
-0.15
0
0.0005
0.001
0.0015
0.002
0.0025
time sec

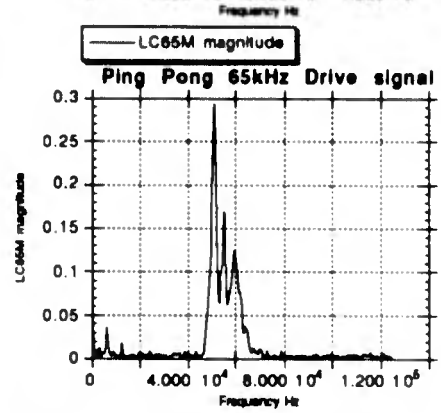
LC65M magnitude
Ping Pong 65kHz Drive signal
0.3
0.25
0.2
0.15
0.1
0.05
0
4.000 10^4
8.000 10^4
1.200 10^5
Frequency Hz

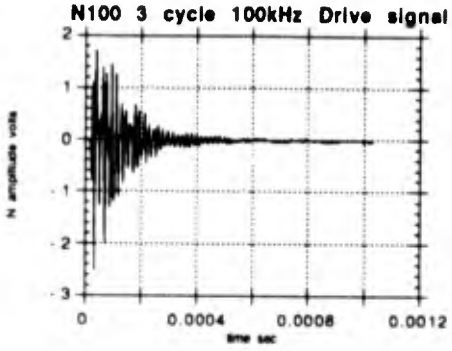
N100 3 cycle 100kHz Drive signal
N amplitude volts
time sec
0
0.0004
0.0008
0.0012

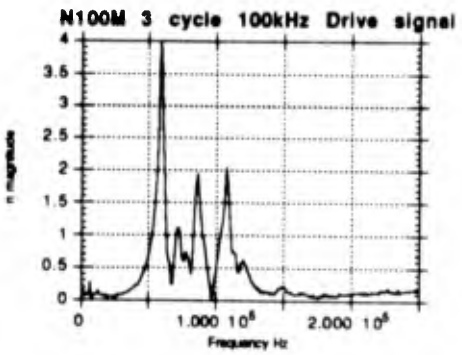
N100M 3 cycle 100kHz Drive signal
n magnitude
Frequency Hz
0
1.000 10^5
2.000 10^5

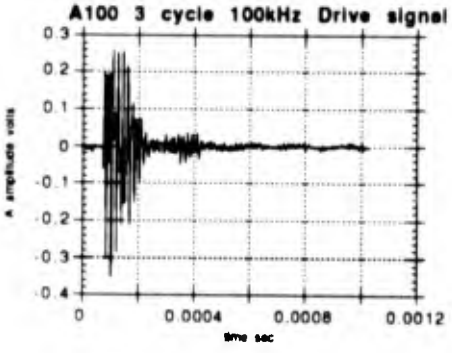
A100 3 cycle 100kHz Drive signal
A amplitude volts
time sec
0
0.0004
0.0008
0.0012

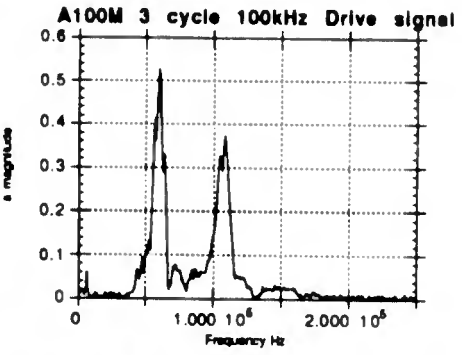
A100M 3 cycle 100kHz Drive signal
a magnitude
Frequency Hz
0
1.000 10^5
2.000 10^5

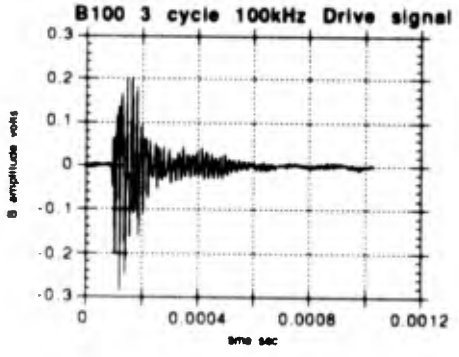
B100 3 cycle 100kHz Drive signal
B amplitude volts
time sec
0
0.0004
0.0008
0.0012

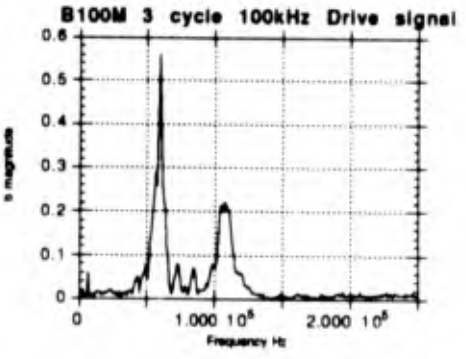
B100M 3 cycle 100kHz Drive signal
b magnitude
Frequency Hz
0
1.000 10^5
2.000 10^5

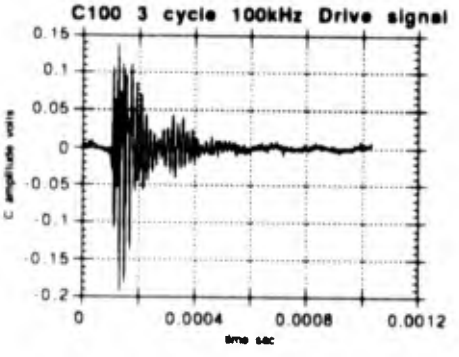
C100 3 cycle 100kHz Drive signal
C amplitude volts
time sec
0
0.0004
0.0008
0.0012

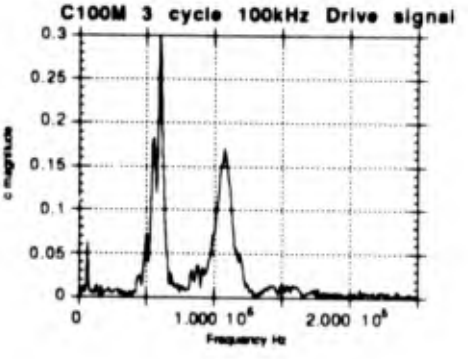
C100M 3 cycle 100kHz Drive signal
c magnitude
Frequency Hz
0
1.000 10^5
2.000 10^5

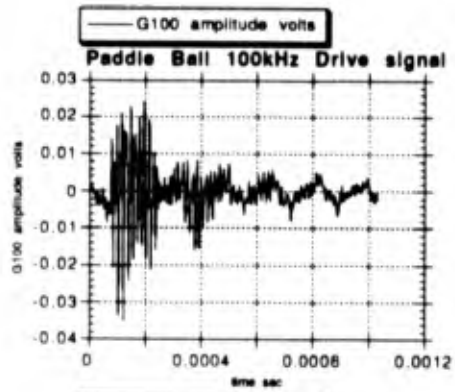
G100 amplitude volts
Paddle Ball 100kHz Drive signal
G100 amplitude volts
0.03
0.02
0.01
0
-0.01
-0.02
-0.03
-0.04
0
0.0004
0.0008
0.0012
time sec

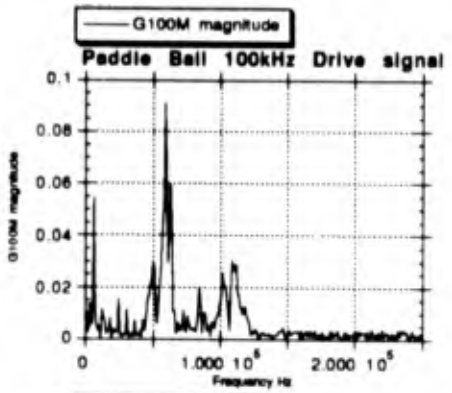
G100M magnitude
Paddle Ball 100kHz Drive signal
G100M magnitude
0.1
0.08
0.06
0.04
0.02
0
0
1.000 10^5
2.000 10^5
Frequency Hz

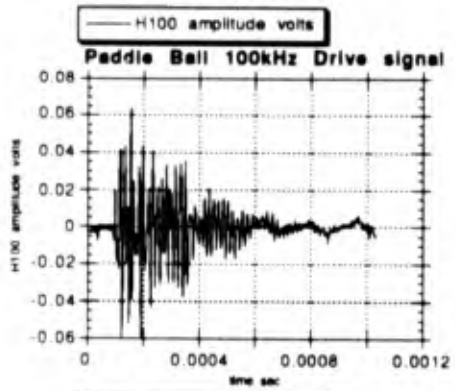
H100 amplitude volts
Paddle Ball 100kHz Drive signal
H100 amplitude volts
0.08
0.06
0.04
0.02
0
-0.02
-0.04
-0.06
0
0.0004
0.0008
0.0012
time sec

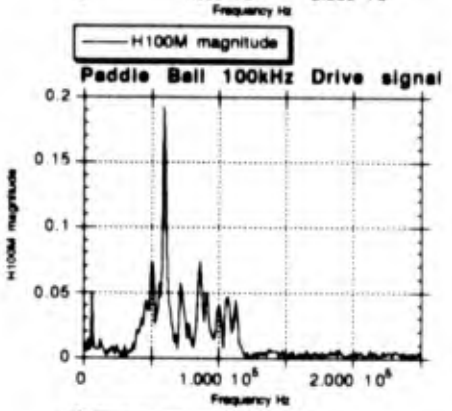
H100M magnitude
Paddle Ball 100kHz Drive signal
H100M magnitude
0.2
0.15
0.1
0.05
0
0
1.000 10^5
2.000 10^5
Frequency Hz

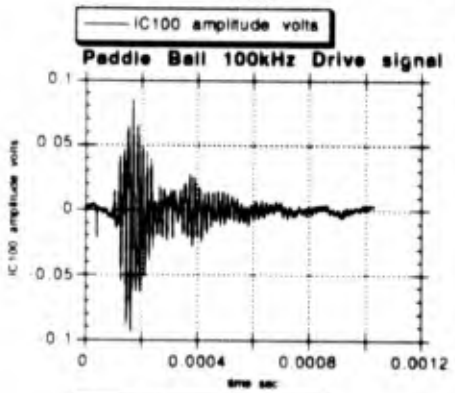
IC100 amplitude volts
Paddle Ball 100kHz Drive signal
IC100 amplitude volts
0.1
0.05
0
-0.05
-0.1
0
0.0004
0.0008
0.0012
time sec

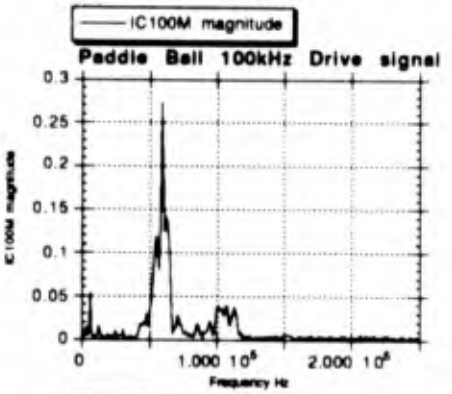
IC100M magnitude
Paddle Ball 100kHz Drive signal
IC100M magnitude
0.3
0.25
0.2
0.15
0.1
0.05
0
0
1.000 10^5
2.000 10^5
Frequency Hz

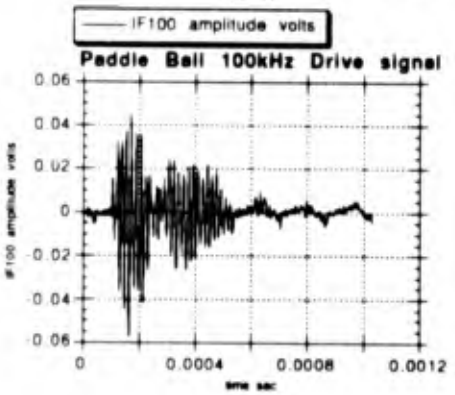
IF100 amplitude volts
Paddle Ball 100kHz Drive signal
IF100 amplitude volts
0.06
0.04
0.02
0
-0.02
-0.04
-0.06
0
0.0004
0.0008
0.0012
time sec

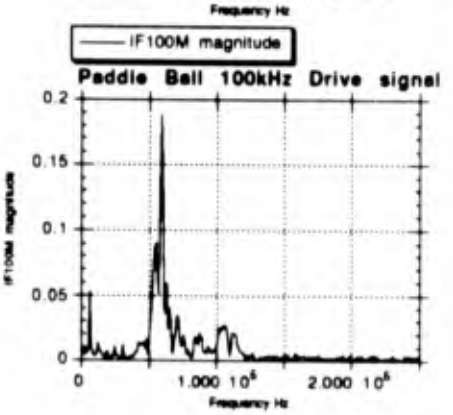
IF100M magnitude
Paddle Ball 100kHz Drive signal
IF100M magnitude
0.2
0.15
0.1
0.05
0
0
1.000 10^5
2.000 10^5
Frequency Hz

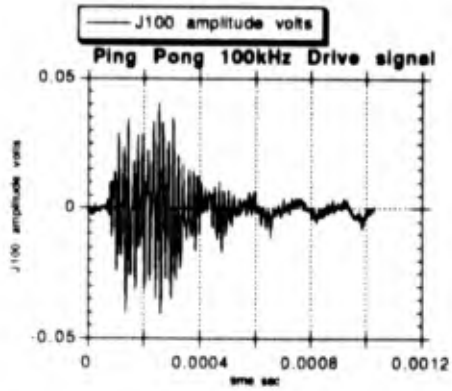
J100 amplitude volts
Ping Pong 100kHz Drive signal
0.05
0
-0.05
0
0.0004
0.0008
0.0012

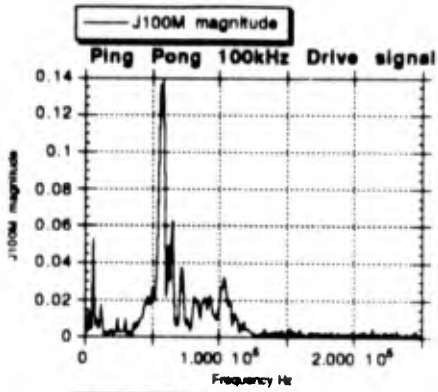
J100M magnitude
Ping Pong 100kHz Drive signal
0.14
0.12
0.1
0.08
0.06
0.04
0.02
0
1.000 10^5
2.000 10^5

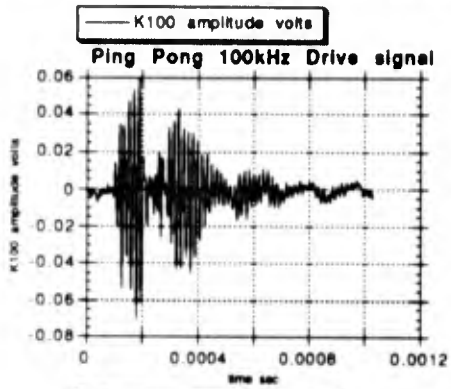
K100 amplitude volts
Ping Pong 100kHz Drive signal
0.06
0.04
0.02
0
-0.02
-0.04
-0.06
-0.08
0
0.0004
0.0008
0.0012

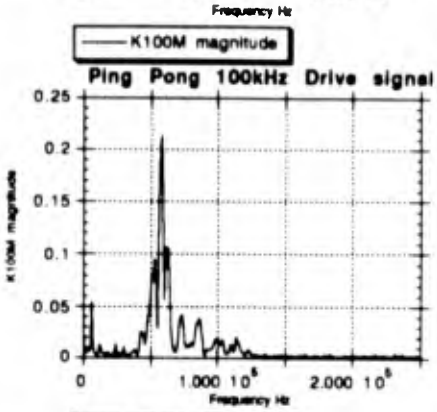
K100M magnitude
Ping Pong 100kHz Drive signal
0.25
0.2
0.15
0.1
0.05
0
1.000 10^5
2.000 10^5

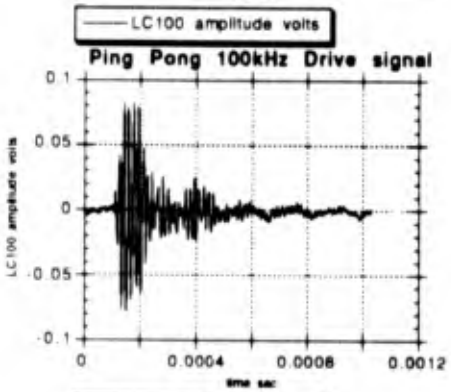
LC100 amplitude volts
Ping Pong 100kHz Drive signal
0.1
0.05
0
-0.05
-0.1
0
0.0004
0.0008
0.0012

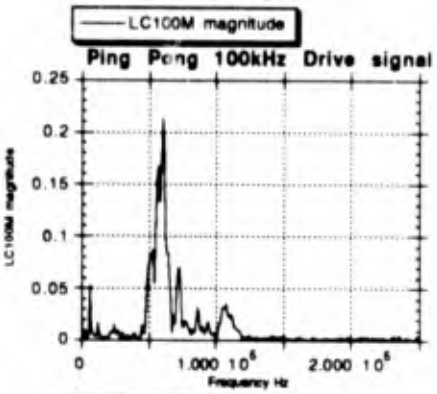
LC100M magnitude
Ping Pong 100kHz Drive signal
0.25
0.2
0.15
0.1
0.05
0
1.000 10^5
2.000 10^5

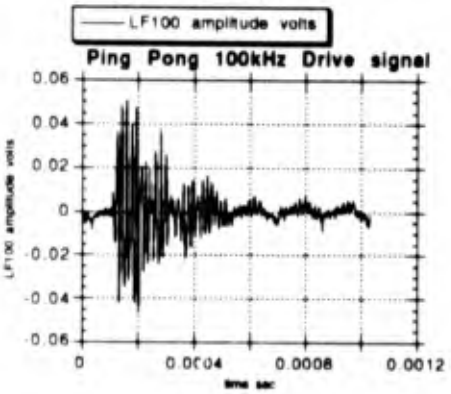
LF100 amplitude volts
Ping Pong 100kHz Drive signal
0.06
0.04
0.02
0
-0.02
-0.04
-0.06
0
0.0004
0.0008
0.0012

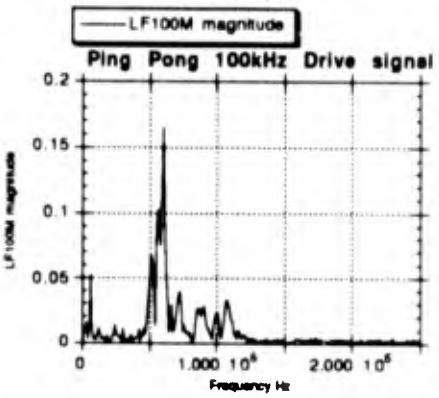
LF100M magnitude
Ping Pong 100kHz Drive signal
0.2
0.15
0.1
0.05
0
1.000 10^5
2.000 10^5

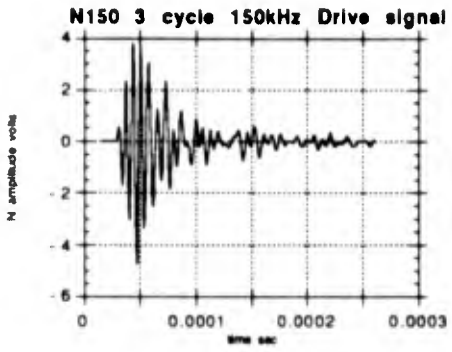
N150 3 cycle 150kHz Drive signal
N amplitude volts
4
2
0
-2
-4
-6
0
0.0001
0.0002
0.0003
time sec

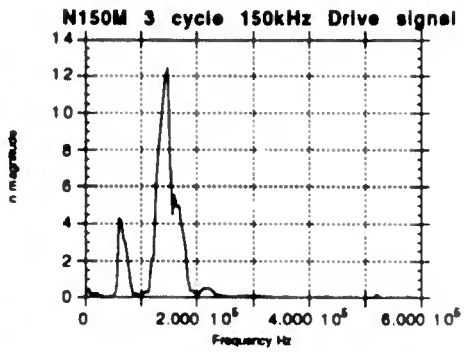
N150M 3 cycle 150kHz Drive signal
n magnitude
14
12
10
8
6
4
2
0
0
2.000 10^5
4.000 10^5
6.000 10^5
Frequency Hz

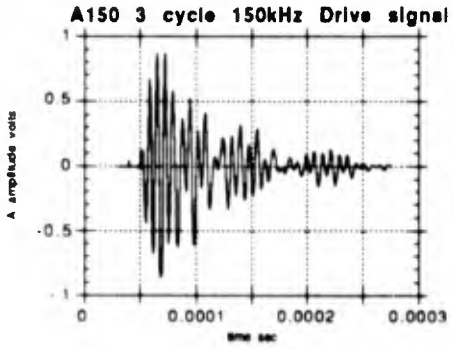
A150 3 cycle 150kHz Drive signal
A amplitude volts
1
0.5
0
-0.5
-1
0
0.0001
0.0002
0.0003
time sec

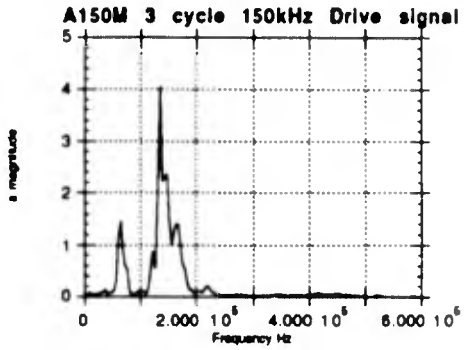
A150M 3 cycle 150kHz Drive signal
a magnitude
5
4
3
2
1
0
0
2.000 10^5
4.000 10^5
6.000 10^5
Frequency Hz

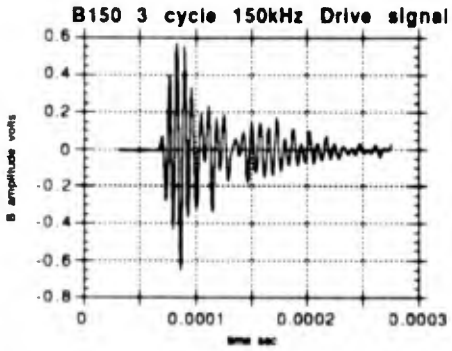
B150 3 cycle 150kHz Drive signal
B amplitude volts
0.6
0.4
0.2
0
-0.2
-0.4
-0.6
-0.8
0
0.0001
0.0002
0.0003
time sec

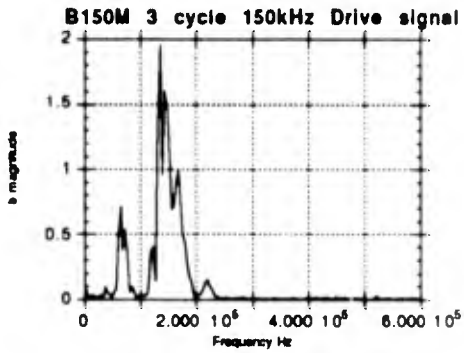
B150M 3 cycle 150kHz Drive signal
b magnitude
2
1.5
1
0.5
0
0
2.000 10^5
4.000 10^5
6.000 10^5
Frequency Hz

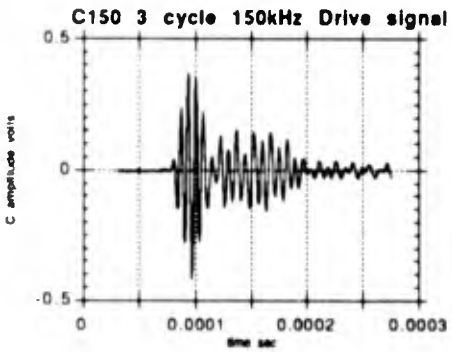
C150 3 cycle 150kHz Drive signal
C amplitude volts
0.5
0
-0.5
0
0.0001
0.0002
0.0003
time sec

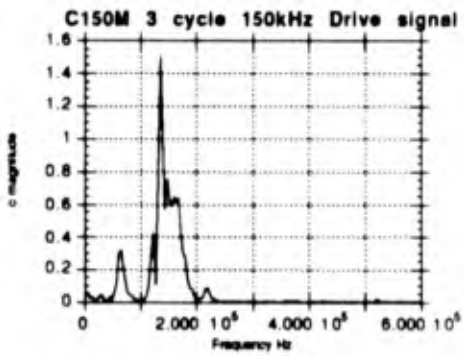
C150M 3 cycle 150kHz Drive signal
c magnitude
1.6
1.4
1.2
1
0.8
0.6
0.4
0.2
0
0
2.000 10^5
4.000 10^5
6.000 10^5
Frequency Hz

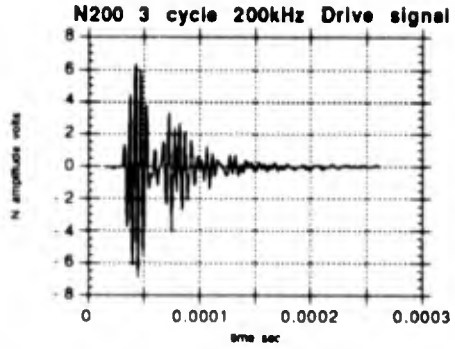
N200 3 cycle 200kHz Drive signal
N amplitude volts
8
6
4
2
0
-2
-4
-6
-8
0
0.0001
0.0002
0.0003
time sec

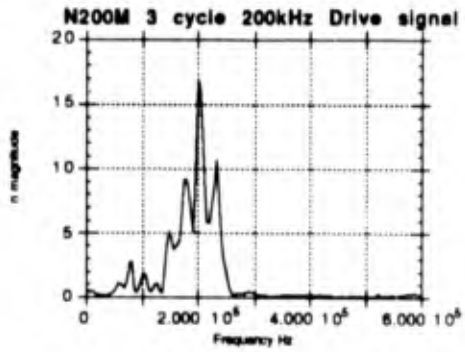
N200M 3 cycle 200kHz Drive signal
n magnitude
20
15
10
5
0
0
2.000 10^5
4.000 10^5
6.000 10^5
Frequency Hz

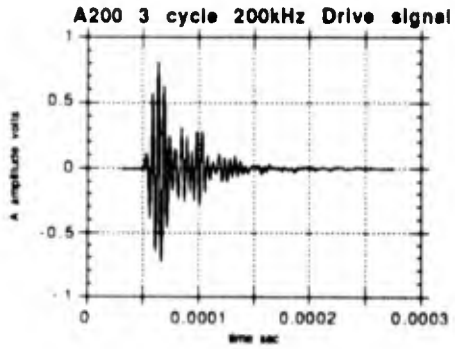
A200 3 cycle 200kHz Drive signal
A amplitude volts
1
0.5
0
-0.5
-1
0
0.0001
0.0002
0.0003
time sec

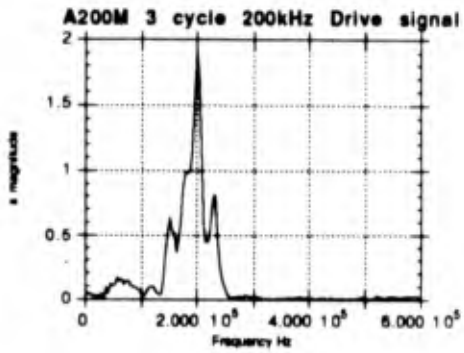
A200M 3 cycle 200kHz Drive signal
a magnitude
2
1.5
1
0.5
0
0
2.000 10^5
4.000 10^5
6.000 10^5
Frequency Hz

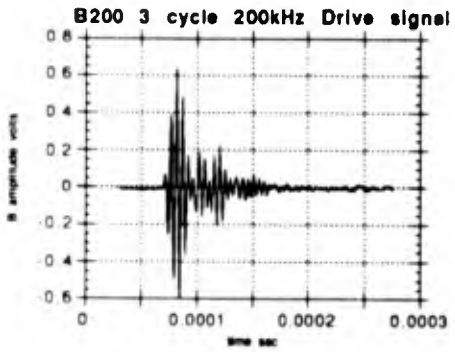
B200 3 cycle 200kHz Drive signal
B amplitude volts
0.8
0.6
0.4
0.2
0
-0.2
-0.4
-0.6
0
0.0001
0.0002
0.0003
time sec

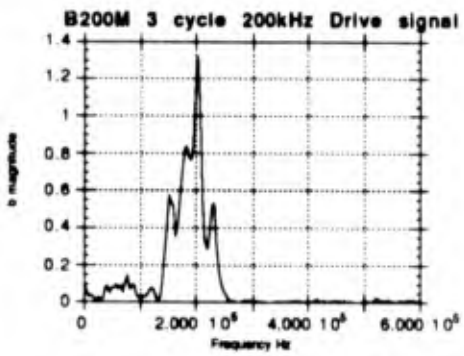
B200M 3 cycle 200kHz Drive signal
b magnitude
1.4
1.2
1
0.8
0.6
0.4
0.2
0
0
2.000 10^5
4.000 10^5
6.000 10^5
Frequency Hz

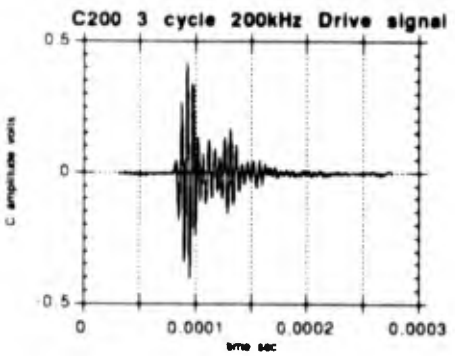
C200 3 cycle 200kHz Drive signal
C amplitude volts
0.5
0
-0.5
0
0.0001
0.0002
0.0003
time sec

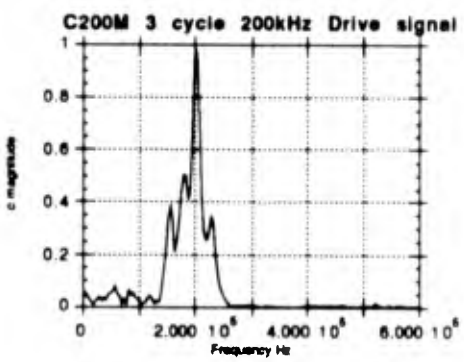
C200M 3 cycle 200kHz Drive signal
c magnitude
1
0.8
0.6
0.4
0.2
0
0
2.000 10^5
4.000 10^5
6.000 10^5
Frequency Hz

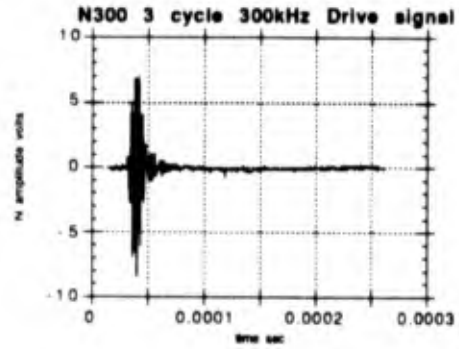
N300 3 cycle 300kHz Drive signal
N amplitude volts
10
5
0
-5
-10
0
0.0001
0.0002
0.0003
time sec

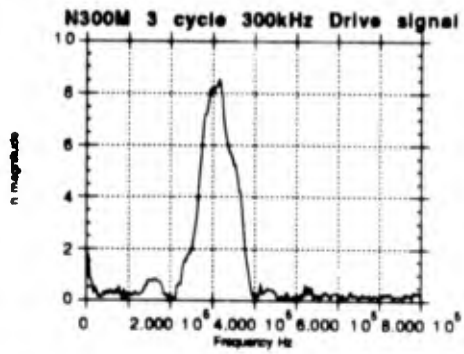
N300M 3 cycle 300kHz Drive signal
n magnitude
10
8
6
4
2
0
0
2.000 10^5
4.000 10^5
6.000 10^5
8.000 10^5
Frequency Hz

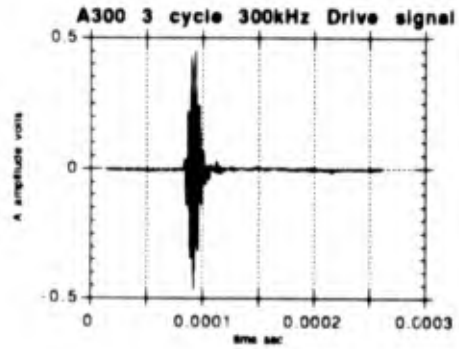
A300 3 cycle 300kHz Drive signal
A amplitude volts
0.5
0
-0.5
0
0.0001
0.0002
0.0003
time sec

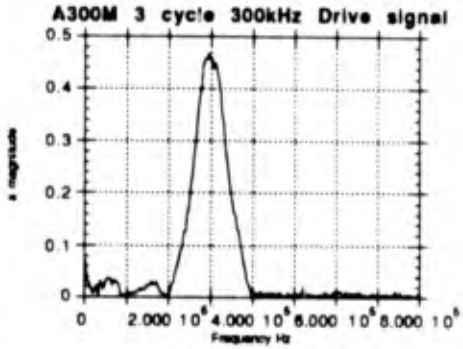
A300M 3 cycle 300kHz Drive signal
a magnitude
0.5
0.4
0.3
0.2
0.1
0
0
2.000 10^5
4.000 10^5
6.000 10^5
8.000 10^5
Frequency Hz

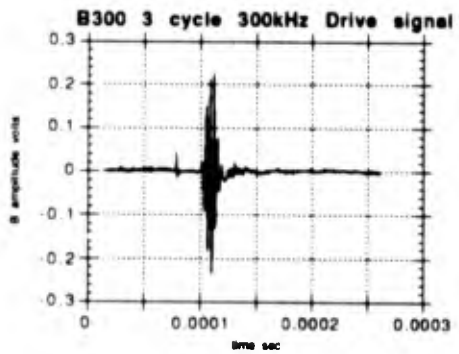
B300 3 cycle 300kHz Drive signal
B amplitude volts
0.3
0.2
0.1
0
-0.1
-0.2
-0.3
0
0.0001
0.0002
0.0003
time sec

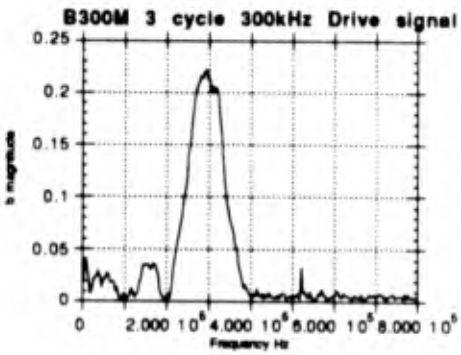
B300M 3 cycle 300kHz Drive signal
b magnitude
0.25
0.2
0.15
0.1
0.05
0
0
2.000 10^5
4.000 10^5
6.000 10^5
8.000 10^5
Frequency Hz

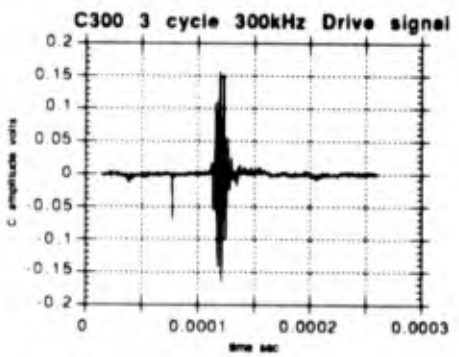
C300 3 cycle 300kHz Drive signal
C amplitude volts
0.2
0.15
0.1
0.05
0
-0.05
-0.1
-0.15
-0.2
0
0.0001
0.0002
0.0003
time sec

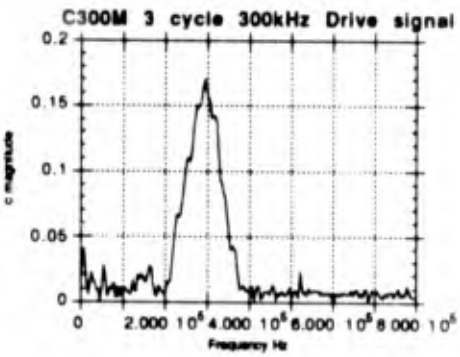
C300M 3 cycle 300kHz Drive signal
c magnitude
0.2
0.15
0.1
0.05
0
0
2.000 10^5
4.000 10^5
6.000 10^5
8.000 10^5
Frequency Hz

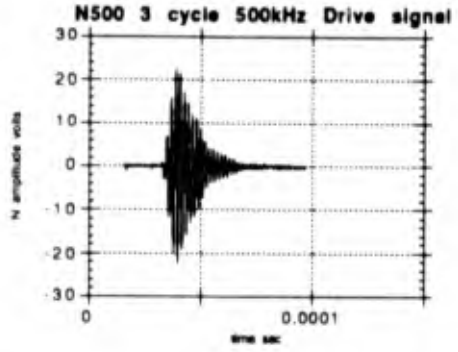
N500 3 cycle 500kHz Drive signal
30
20
10
0
-10
-20
-30
0
0.0001
time sec

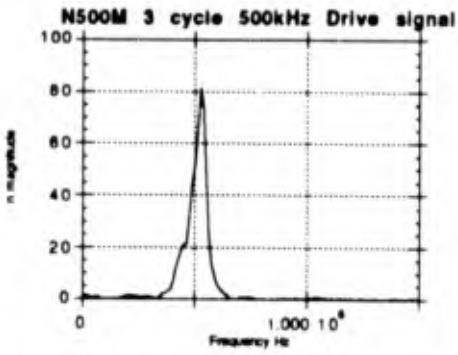
N500M 3 cycle 500kHz Drive signal
100
80
60
40
20
0
0
1.000 10^6
Frequency Hz

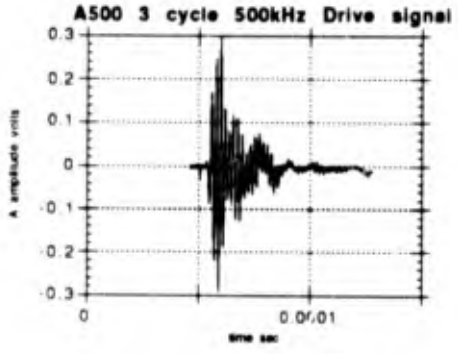
A500 3 cycle 500kHz Drive signal
0.3
0.2
0.1
0
-0.1
-0.2
-0.3
0
0.0001
time sec

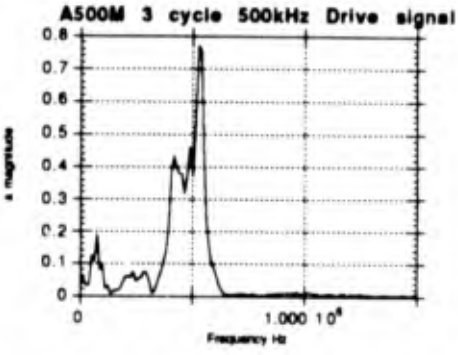
A500M 3 cycle 500kHz Drive signal
0.8
0.7
0.6
0.5
0.4
0.3
0.2
0.1
0
0
1.000 10^6
Frequency Hz

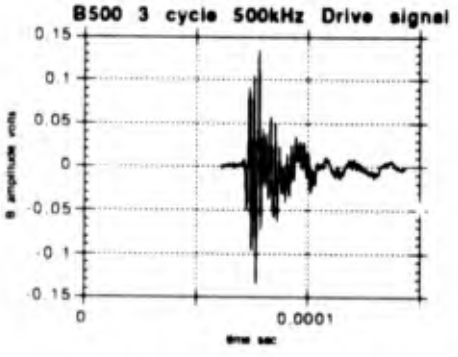
B500 3 cycle 500kHz Drive signal
0.15
0.1
0.05
0
-0.05
-0.1
-0.15
0
0.0001
time sec

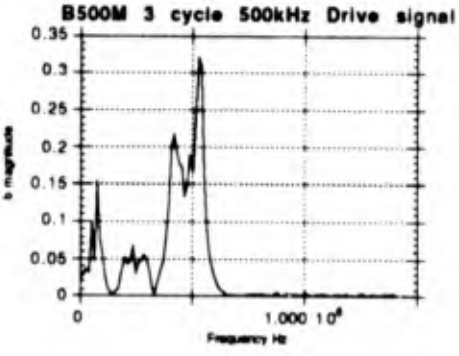
B500M 3 cycle 500kHz Drive signal
0.35
0.3
0.25
0.2
0.15
0.1
0.05
0
0
1.000 10^6
Frequency Hz

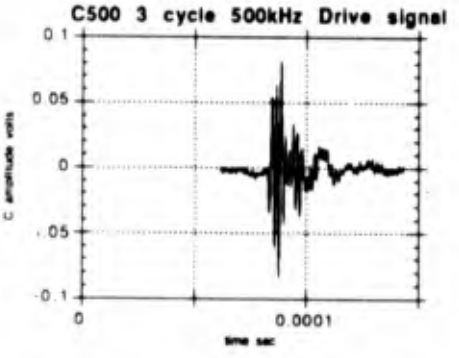
C500 3 cycle 500kHz Drive signal
0.1
0.05
0
-0.1
0
0.0001
time sec

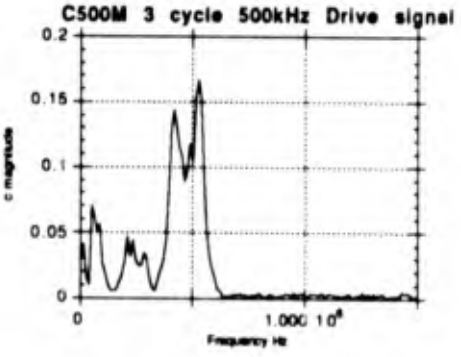
C500M 3 cycle 500kHz Drive signal
0.2
0.15
0.1
0.05
0
0
1.000 10^6
Frequency Hz

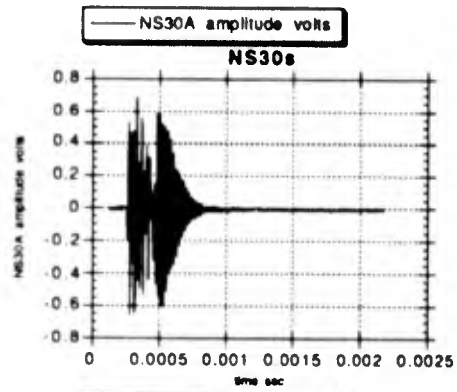
NS30A amplitude volts
NS30s
0.8
0.6
0.4
0.2
0
-0.2
-0.4
-0.6
-0.8
0
0.0005
0.001
0.0015
0.002
0.0025
time sec

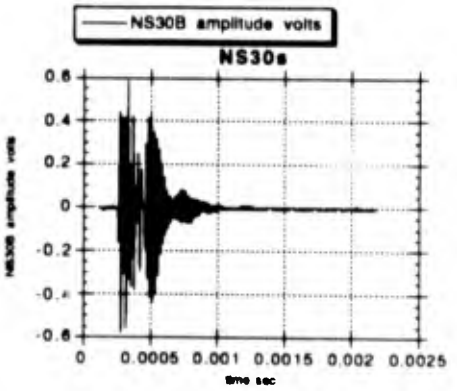
NS30B amplitude volts
NS30s
0.6
0.4
0.2
0
-0.2
-0.4
-0.6
0
0.0005
0.001
0.0015
0.002
0.0025
time sec

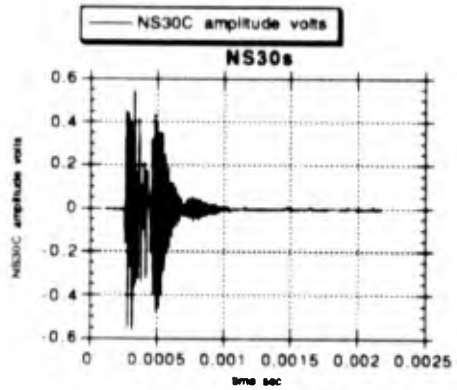
NS30C amplitude volts
NS30s
0.6
0.4
0.2
0
-0.2
-0.4
-0.6
0
0.0005
0.001
0.0015
0.002
0.0025
time sec

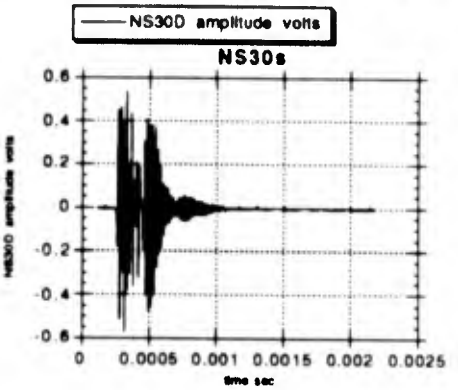
NS30D amplitude volts
NS30s
0.6
0.4
0.2
0
-0.2
-0.4
-0.6
0
0.0005
0.001
0.0015
0.002
0.0025
time sec

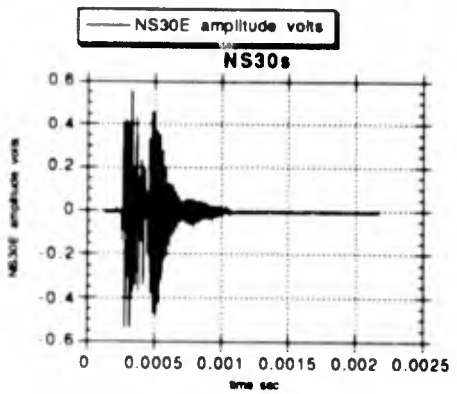
NS30E amplitude volts
NS30s
0.6
0.4
0.2
0
-0.2
-0.4
-0.6
0
0.0005
0.001
0.0015
0.002
0.0025
time sec

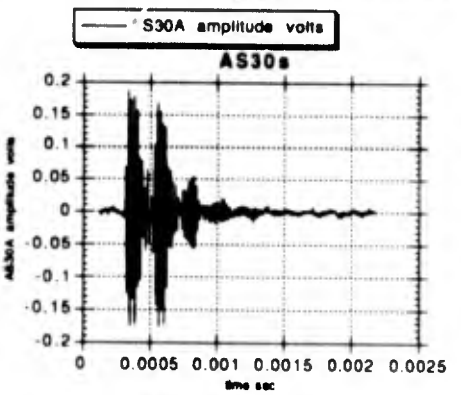
S30A amplitude volts
AS30s
0.2
0.15
0.1
0.05
0
-0.05
-0.1
-0.15
-0.2
0
0.0005
0.001
0.0015
0.002
0.0025
time sec

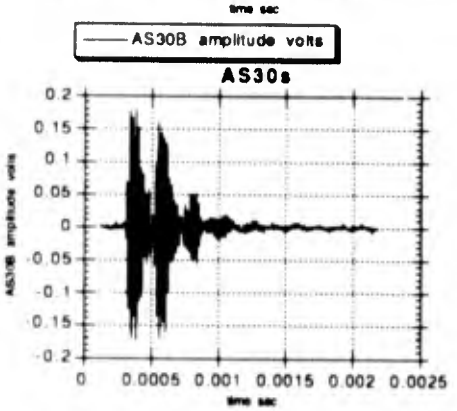
AS30B amplitude volts
AS30s
0.2
0.15
0.1
0.05
0
-0.05
-0.1
-0.15
-0.2
0
0.0005
0.001
0.0015
0.002
0.0025
time sec

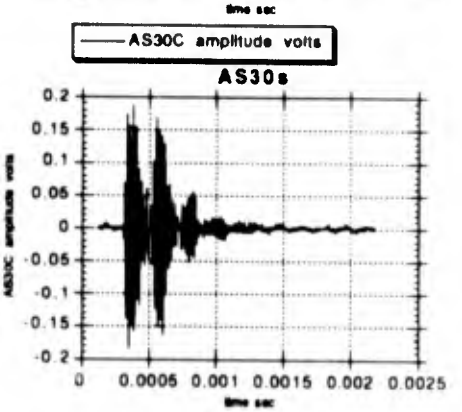
AS30C amplitude volts
AS30s
0.2
0.15
0.1
0.05
0
-0.05
-0.1
-0.15
-0.2
0
0.0005
0.001
0.0015
0.002
0.0025
time sec

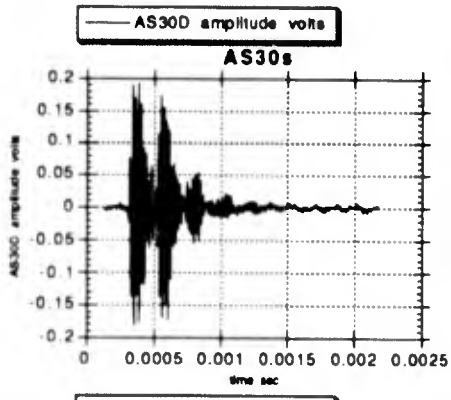
AS30D amplitude volts
AS30s
0.2
0.15
0.1
0.05
0
-0.05
-0.1
-0.15
-0.2
0
0.0005
0.001
0.0015
0.002
0.0025
time sec

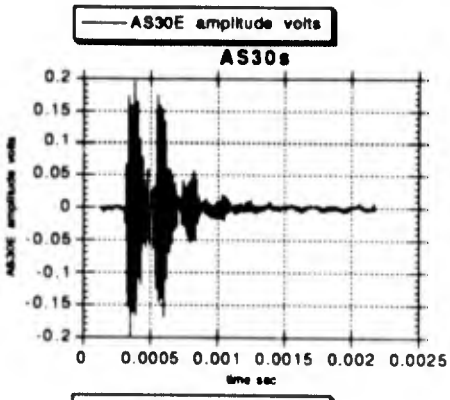
AS30E amplitude volts
AS30s
0.2
0.15
0.1
0.05
0
-0.05
-0.1
-0.15
-0.2
0
0.0005
0.001
0.0015
0.002
0.0025
time sec

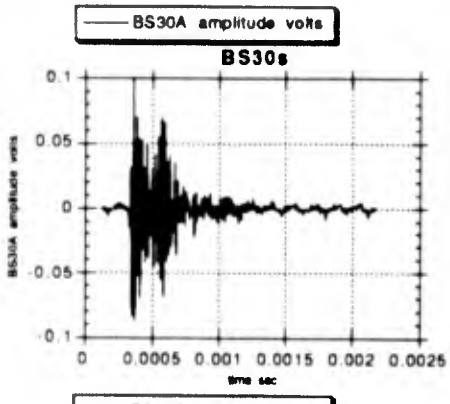
BS30A amplitude volts
BS30s
0.1
0.05
0
-0.05
-0.1
0
0.0005
0.001
0.0015
0.002
0.0025
time sec

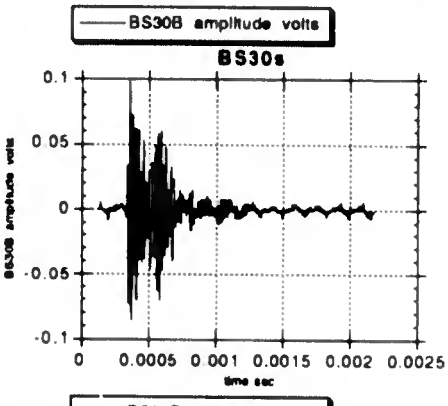
BS30B amplitude volts
BS30s
0.1
0.05
0
-0.05
-0.1
0
0.0005
0.001
0.0015
0.002
0.0025
time sec

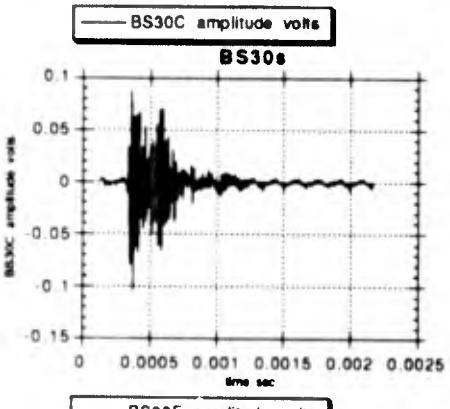
BS30C amplitude volts
BS30s
0.1
0.05
0
-0.05
-0.1
-0.15
0
0.0005
0.001
0.0015
0.002
0.0025
time sec

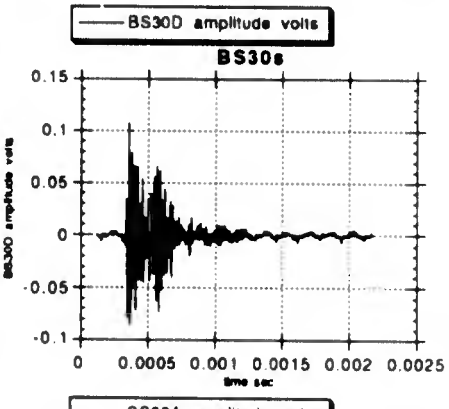
BS30D amplitude volts
BS30s
0.15
0.1
0.05
0
-0.05
-0.1
0
0.0005
0.001
0.0015
0.002
0.0025
time sec

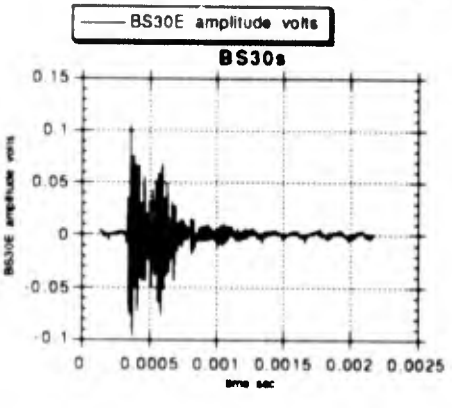
BS30E amplitude volts
BS30s
0.15
0.1
0.05
0
-0.05
-0.1
0
0.0005
0.001
0.0015
0.002
0.0025
time sec

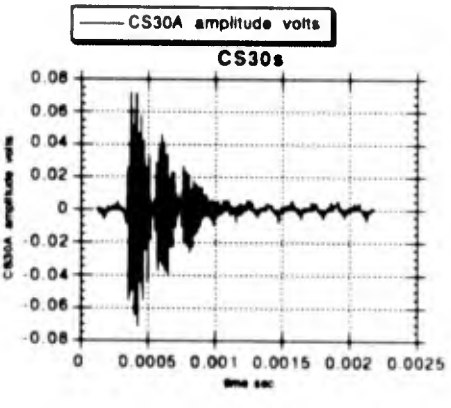
CS30A amplitude volts
CS30s
0.08
0.06
0.04
0.02
0
-0.02
-0.04
-0.06
-0.08
0
0.0005
0.001
0.0015
0.002
0.0025
time sec

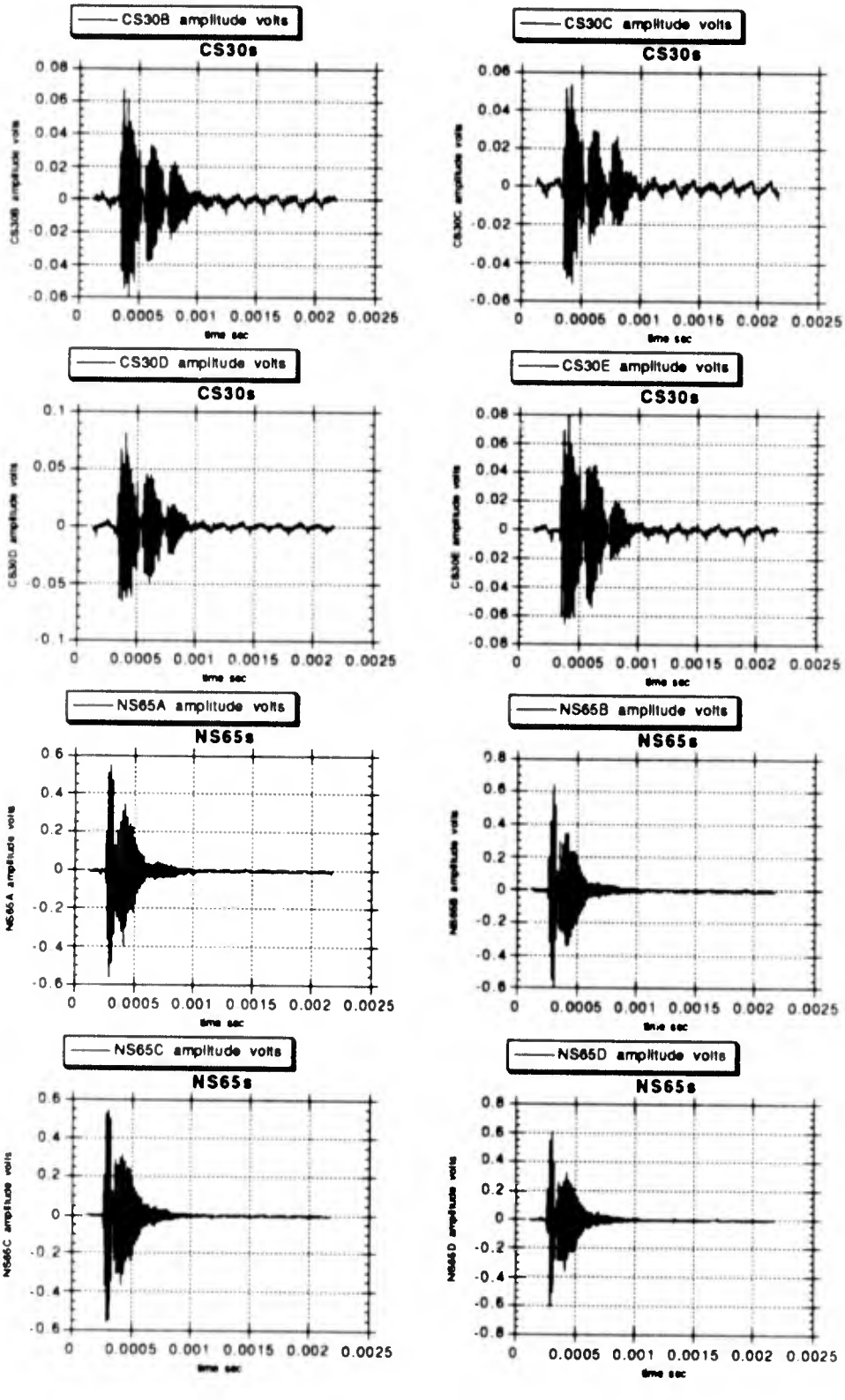
CS30B amplitude volts
CS30s
CS30B amplitude volts
time sec
CS30C amplitude volts
CS30s
CS30C amplitude volts
time sec
CS30D amplitude volts
CS30s
CS30D amplitude volts
time sec
CS30E amplitude volts
CS30s
CS30E amplitude volts
time sec
NS65A amplitude volts
NS65s
NS65A amplitude volts
time sec
NS65B amplitude volts
NS65s
NS65B amplitude volts
time sec
NS65C amplitude volts
NS65s
NS65C amplitude volts
time sec
NS65D amplitude volts
NS65s
NS65D amplitude volts
time sec

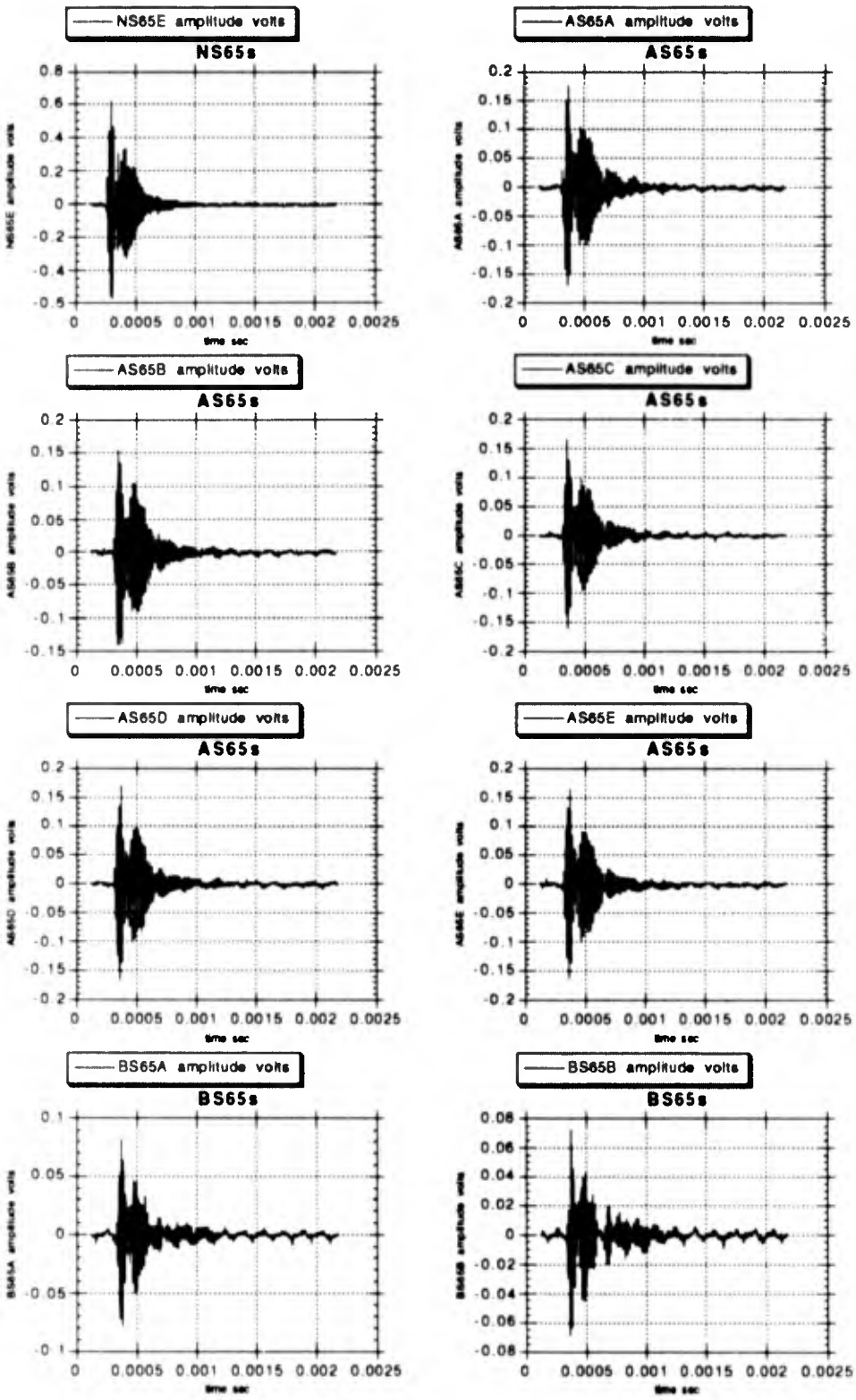
NS65E amplitude volts
NS65s
AS65A amplitude volts
AS65s
AS65B amplitude volts
AS65s
AS65C amplitude volts
AS65s
AS65D amplitude volts
AS65s
AS65E amplitude volts
AS65s
BS65A amplitude volts
BS65s
BS65B amplitude volts
BS65s
time sec

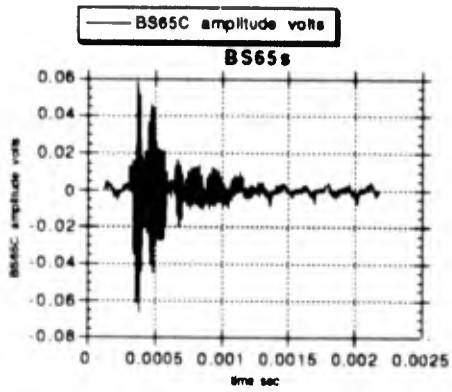
BS65C amplitude volts
BS65s
0.06
0.04
0.02
0
-0.02
-0.04
-0.06
-0.08
0
0.0005
0.001
0.0015
0.002
0.0025
time sec

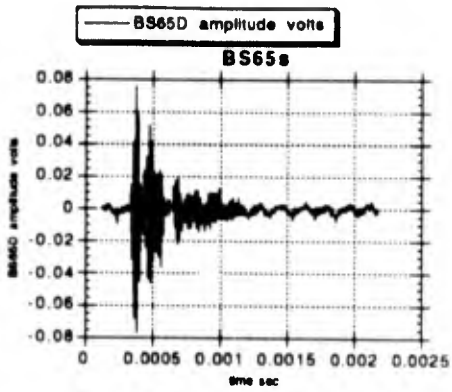
BS65D amplitude volts
BS65s
0.08
0.06
0.04
0.02
0
-0.02
-0.04
-0.06
-0.08
0
0.0005
0.001
0.0015
0.002
0.0025
time sec

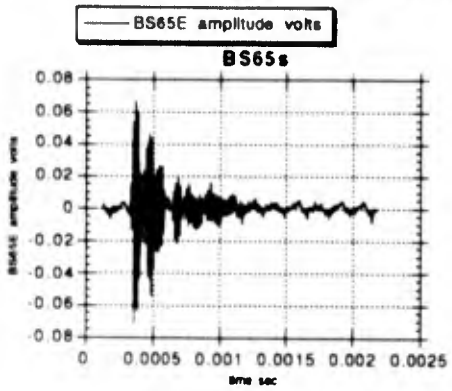
BS65E amplitude volts
BS65s
0.08
0.06
0.04
0.02
0
-0.02
-0.04
-0.06
-0.08
0
0.0005
0.001
0.0015
0.002
0.0025
time sec

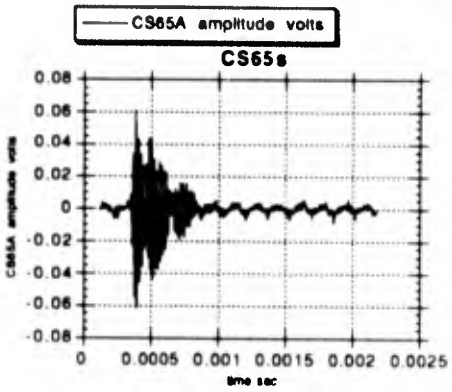
CS65A amplitude volts
CS65s
0.08
0.06
0.04
0.02
0
-0.02
-0.04
-0.06
-0.08
0
0.0005
0.001
0.0015
0.002
0.0025
time sec

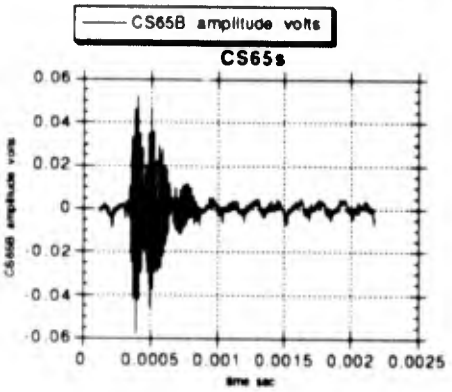
CS65B amplitude volts
CS65s
0.06
0.04
0.02
0
-0.02
-0.04
-0.06
0
0.0005
0.001
0.0015
0.002
0.0025
time sec

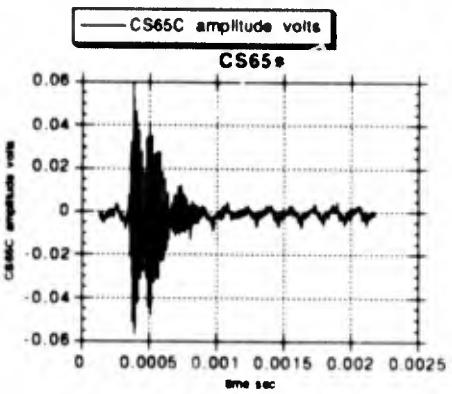
CS65C amplitude volts
CS65s
0.06
0.04
0.02
0
-0.02
-0.04
-0.06
0
0.0005
0.001
0.0015
0.002
0.0025
time sec

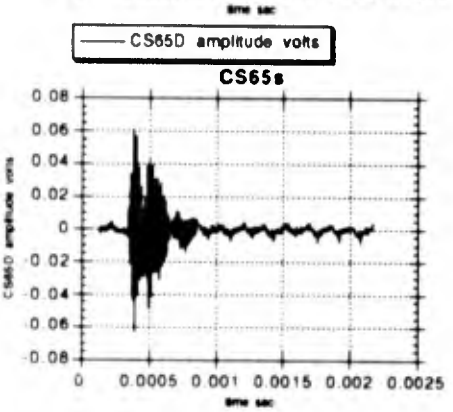
CS65D amplitude volts
CS65s
0.08
0.06
0.04
0.02
0
-0.02
-0.04
-0.06
-0.08
0
0.0005
0.001
0.0015
0.002
0.0025
time sec

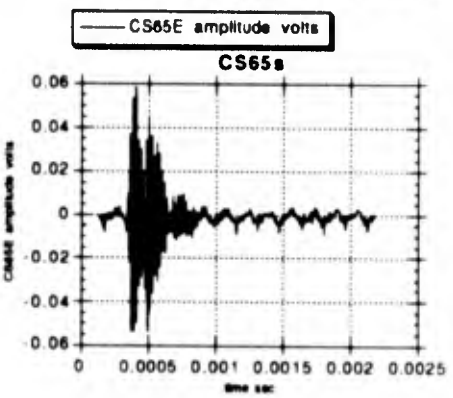
CS65E amplitude volts
CS65s
0.06
0.04
0.02
0
-0.02
-0.04
-0.06
0
0.0005
0.001
0.0015
0.002
0.0025
time sec

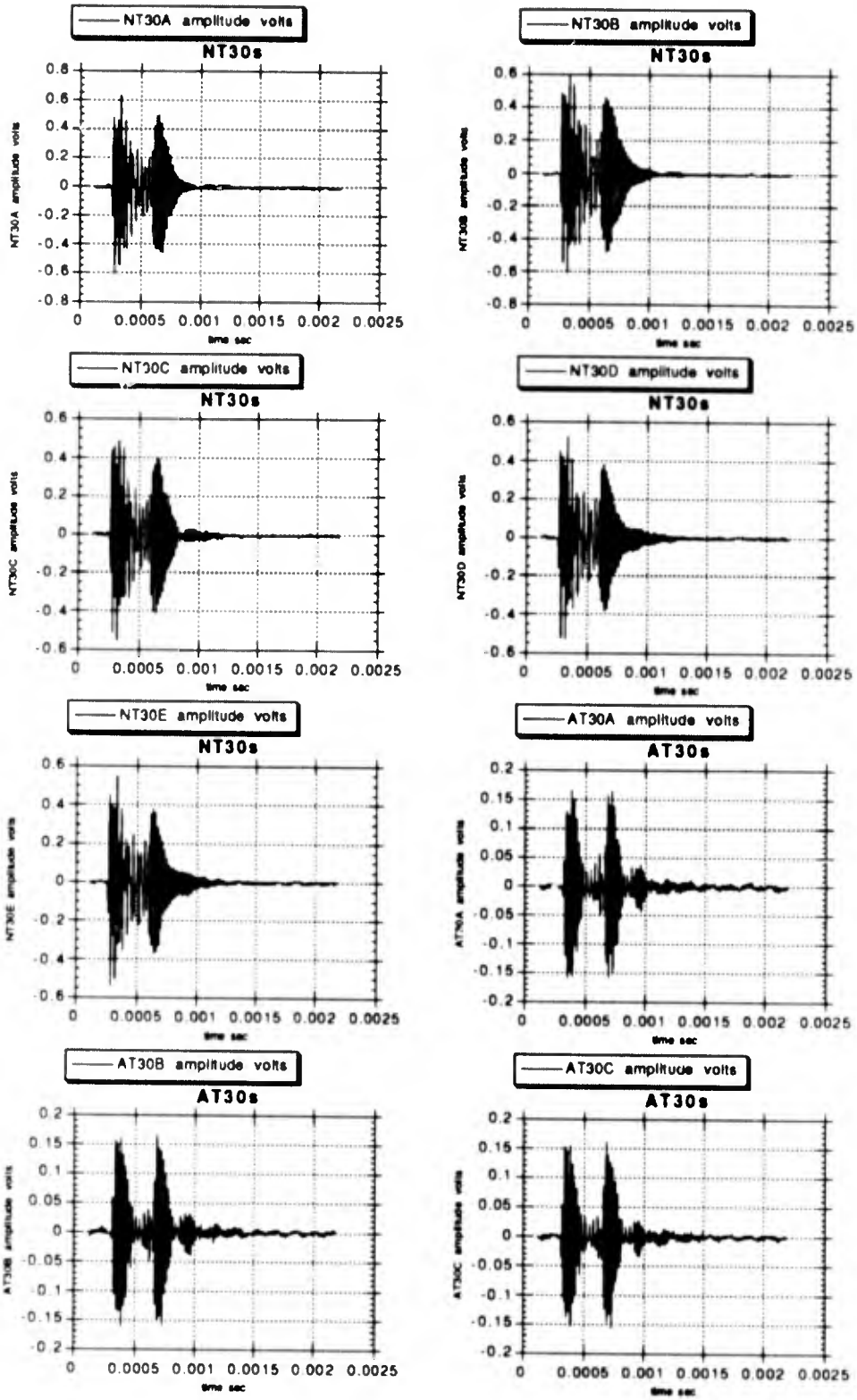
NT30A amplitude volts
NT30s
NT30A amplitude volts
time sec
NT30B amplitude volts
NT30s
NT30B amplitude volts
time sec
NT30C amplitude volts
NT30s
NT30C amplitude volts
time sec
NT30D amplitude volts
NT30s
NT30D amplitude volts
time sec
NT30E amplitude volts
NT30s
NT30E amplitude volts
time sec
AT30A amplitude volts
AT30s
AT30A amplitude volts
time sec
AT30B amplitude volts
AT30s
AT30B amplitude volts
time sec
AT30C amplitude volts
AT30s
AT30C amplitude volts
time sec

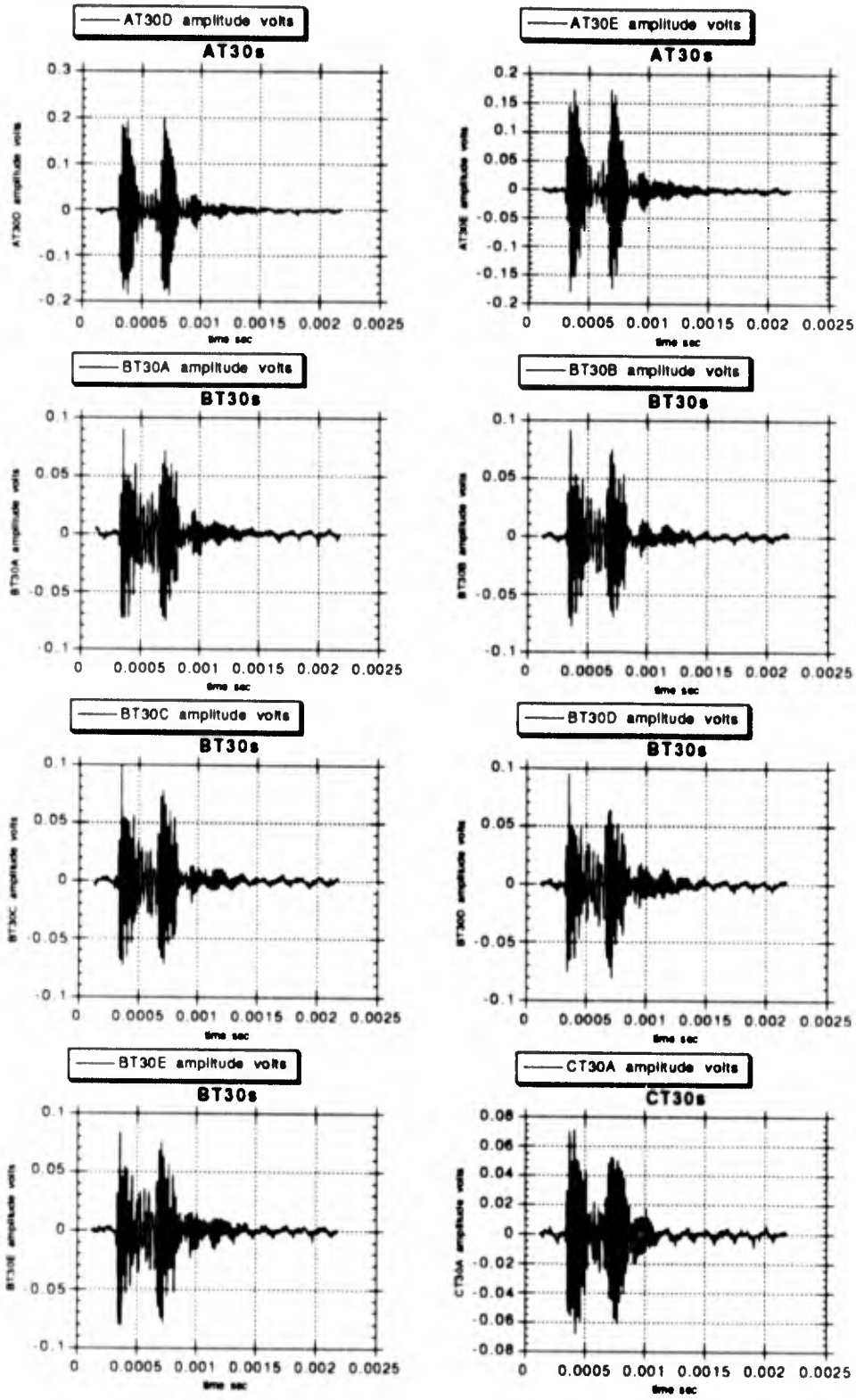
AT30D amplitude volts
AT30s
AT30E amplitude volts
AT30s
BT30A amplitude volts
BT30s
BT30B amplitude volts
BT30s
BT30C amplitude volts
BT30s
BT30D amplitude volts
BT30s
BT30E amplitude volts
BT30s
CT30A amplitude volts
CT30s
time sec

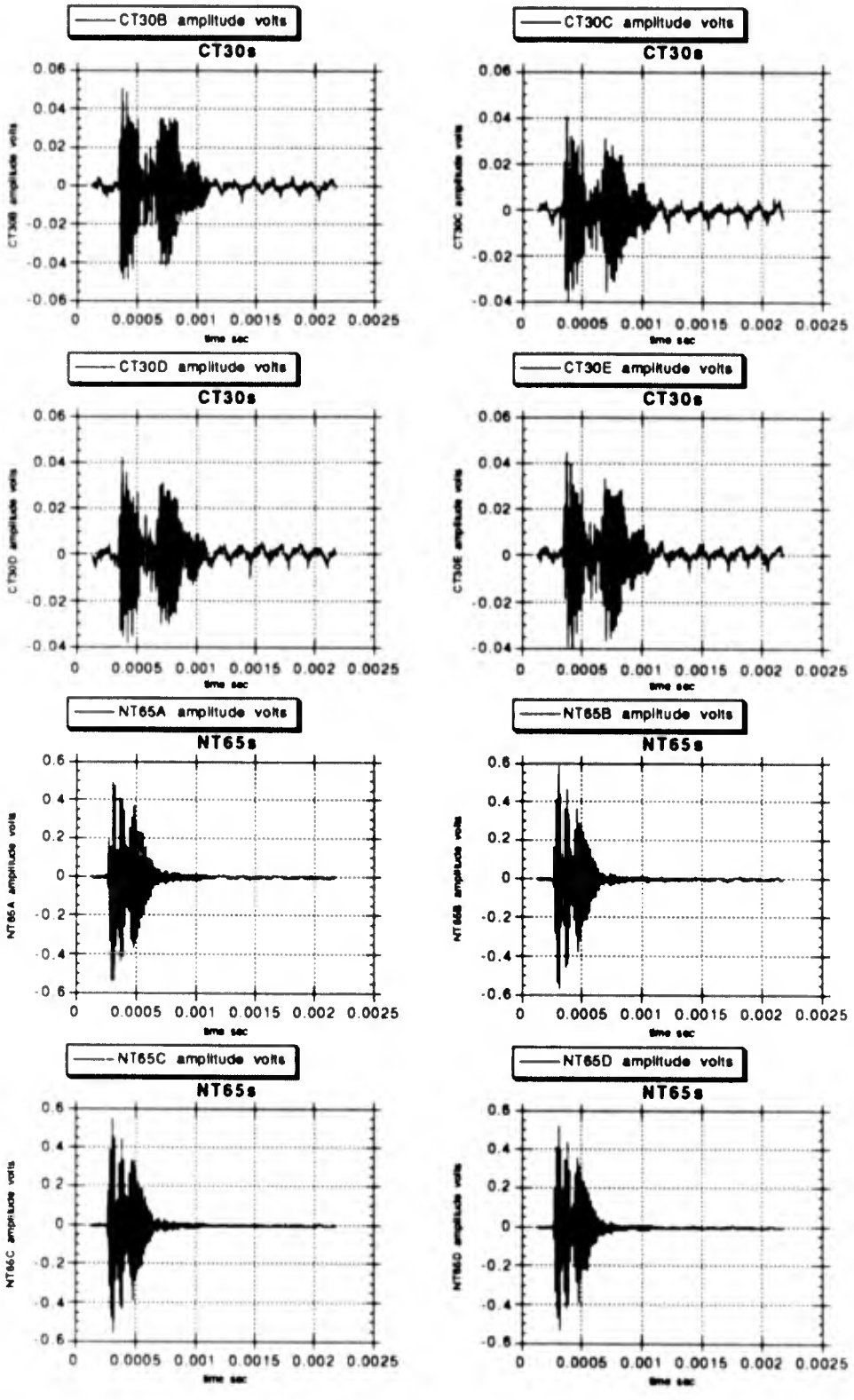
CT30B amplitude volts
CT30s
CT30B amplitude volts
time sec
CT30C amplitude volts
CT30s
CT30C amplitude volts
time sec
CT30D amplitude volts
CT30s
CT30D amplitude volts
time sec
CT30E amplitude volts
CT30s
CT30E amplitude volts
time sec
NT65A amplitude volts
NT65s
NT65A amplitude volts
time sec
NT65B amplitude volts
NT65s
NT65B amplitude volts
time sec
NT65C amplitude volts
NT65s
NT65C amplitude volts
time sec
NT65D amplitude volts
NT65s
NT65D amplitude volts
time sec

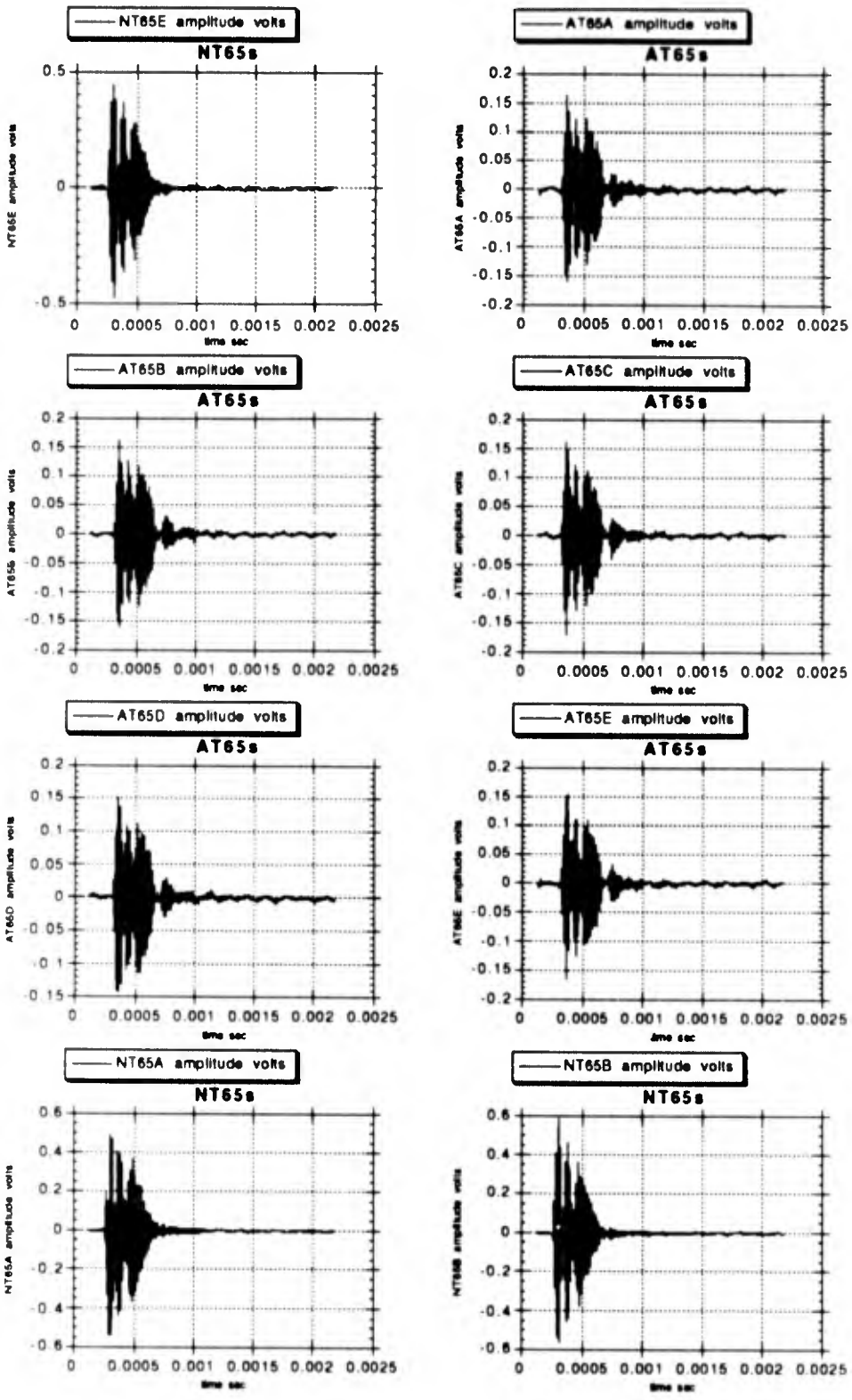
NT65E amplitude volts
NT65s
NT65E amplitude volts
time sec
AT65A amplitude volts
AT65s
AT65A amplitude volts
time sec
AT65B amplitude volts
AT65s
AT65B amplitude volts
time sec
AT65C amplitude volts
AT65s
AT65C amplitude volts
time sec
AT65D amplitude volts
AT65s
AT65D amplitude volts
time sec
AT65E amplitude volts
AT65s
AT65E amplitude volts
time sec
NT65A amplitude volts
NT65s
NT65A amplitude volts
time sec
NT65B amplitude volts
NT65s
NT65B amplitude volts
time sec

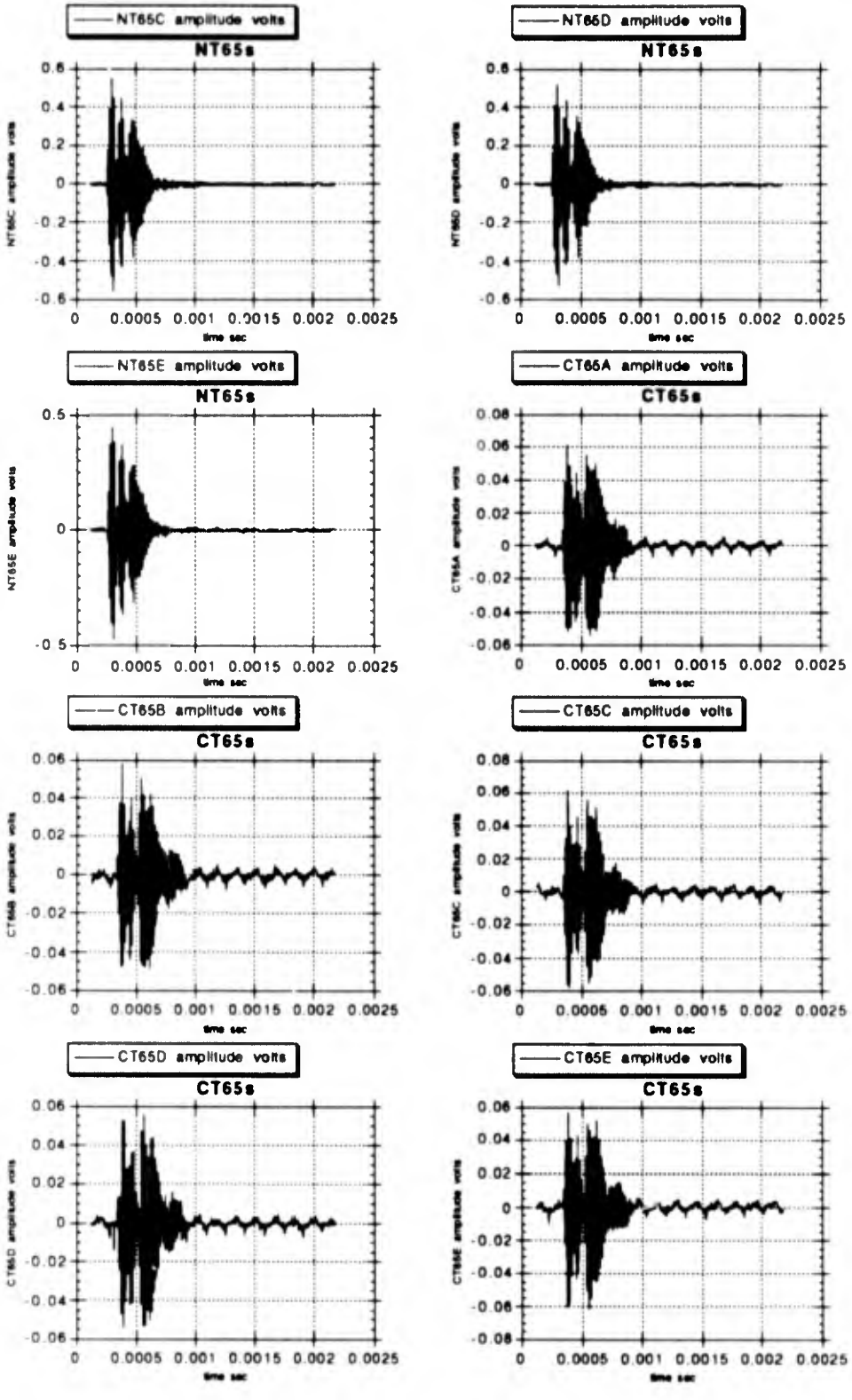
NT65C amplitude volts
NT65s
NT65C amplitude volts
time sec
NT65D amplitude volts
NT65s
NT65D amplitude volts
time sec
NT65E amplitude volts
NT65s
NT65E amplitude volts
time sec
CT65A amplitude volts
CT65s
CT65A amplitude volts
time sec
CT65B amplitude volts
CT65s
CT65B amplitude volts
time sec
CT65C amplitude volts
CT65s
CT65C amplitude volts
time sec
CT65D amplitude volts
CT65s
CT65D amplitude volts
time sec
CT65E amplitude volts
CT65s
CT65E amplitude volts
time sec